Distribution Agreement

In presenting this thesis or dissertation as a partial fulfillment of the requirements for an advanced degree from Emory University, I hereby grant to Emory University and its agents the non-exclusive license to archive, make accessible, and display my thesis or dissertation in whole or in part in all forms of media, now or hereafter known, including display on the world wide web. I understand that I may select some access restrictions as part of the online submission of this thesis or dissertation. I retain all ownership rights to the copyright of the thesis or dissertation. I also retain the right to use in future works (such as articles or books) all or part of this thesis or dissertation.

_____ _____

Emily Rose Summerbell Date

The transcriptional regulation and novel functions of the filopodia motor protein MYO10 during collective lung cancer invasion

By

Emily Rose Summerbell

Doctor of Philosophy

Graduate Division of Biological and Biomedical Sciences

Cancer Biology

| | |
|---|---|
| Adam I. Marcus, PhD<br>Advisor | Paula Vertino, PhD<br>Committee Member |
| Melissa Gilbert-Ross, PhD<br>Committee Member | David Weiss, PhD<br>Committee Member |
| Gabriel Sica, MD, PhD<br>Committee Member | Wei Zhou, PhD<br>Committee Member |

Accepted:

Lisa A. Tedesco, PhD
Dean of the James T. Laney School of Graduate Studies

Date

# The transcriptional regulation and novel functions of the filopodia motor protein MYO10 during collective lung cancer invasion

By

Emily Rose Summerbell

B.A., Vanderbilt University, 2014

Advisor:

Adam I. Marcus, Ph.D.

An abstract of

A dissertation submitted to the Faculty of the

James T. Laney School of Graduate Studies of Emory University

in partial fulfillment of the requirements for the degree of

Doctor of Philosophy

in

Graduate Division of Biological and Biomedical Sciences

Cancer Biology

2020

Abstract

The transcriptional regulation and novel functions of the filopodia motor protein MYO10 during collective lung cancer invasion

By Emily Rose Summerbell

Tumor heterogeneity drives disease progression, treatment resistance, and patient relapse, yet many questions remain regarding its contributions to tumor invasion and metastasis. Here, we investigated how heterogeneous DNA methylation and gene expression promote specialized myosin-X (MYO10)-expressing filopodia in leader cells to direct collective cancer cell invasion.

We investigated heterogeneity within collective cancer invasion by integrating DNA methylation and gene expression analysis in rare purified lung cancer leader and follower cells. Our results showed global DNA methylation rewiring in leader cells and phenotype-specific gene expression that differentiated both leader cells and follower cells from their parental population. Integration of DNA methylation and transcriptome analyses revealed that promoter hypermethylation silenced the tumor suppressor gene *HTATIP2* in leader cells. Analysis also identified the filopodial motor *MYO10* as a critical gene at the intersection of epigenetic heterogeneity and 3D collective invasion, being hypomethylated and overexpressed in leader cells. We further identified the Notch ligand JAG1 as a previously unknown upstream activator of MYO10 expression in leader cells. Using 3D live cell imaging of invading leader cells, we discovered that MYO10 drives filopodial persistence necessary for micropatterning extracellular fibronectin into linear tracks at the edge of 3D collective invasion. We further show that filopodia-directed fibronectin alignment is dependent upon the MYO10 cargo protein integrin β1. Our data fit a model where epigenetic heterogeneity and JAG1 signaling jointly drive collective cancer invasion through *MYO10* upregulation in epigenetically permissive leader cells, which induces filopodia dynamics and long-term stability necessary for linearized fibronectin micropatterning.

In addition to localizing at the tips of long-lived leader cell filopodia at the front of collective invasion, MYO10 also localizes to additional subcellular compartments. Here, we show that MYO10 also localizes to filopodia-like structures including regions of cell-cell contact, retraction fibers, and the cleavage midbody in mitotic cells, but it does not localize with spindle poles. Thus, our data suggest that MYO10 acts not only within filopodia at the front of collective invasion and ECM remodeling but also regulates filopodia and filopodia-like structures in multiple cellular contexts necessary to coordinate collective cancer invasion.

# The transcriptional regulation and novel functions of the filopodia motor protein MYO10 during collective lung cancer invasion

By

Emily Rose Summerbell

B.A., Vanderbilt University, 2014

Advisor:

Adam I. Marcus, Ph.D.

A dissertation submitted to the Faculty of the

James T. Laney School of Graduate Studies of Emory University

in partial fulfillment of the requirements for the degree of

Doctor of Philosophy

in

Graduate Division of Biological and Biomedical Sciences

Cancer Biology

2020

**Acknowledgements**

I saved this page for last, as I knew writing these words of gratitude would be the hardest part of my dissertation. Six years has felt like forever and yet like no time at all. These words of gratitude may seem small when compared to the magnitude of all your support, but know that every single one of you mean more to me than I can ever describe.

To my labmates past and present: Carol, Janna, Liza, Jerry, Rachel x2, Brian, Jamie, Christina, Joseph, Tala, Antonios, Zach, Wendy, Ale, Scott, Jessica. Thank you all for making the best lab environment I have ever worked in. A lot of people consider their lab a place of work and nothing more, but the Marcus lab knows that lab is a family. Thank you for everything, from the cute sticky notes on my bench, to birthday cards and baked goods, to sharing the secrets of SDS (even if it was two years too late, oops), to 10-hour 5-person photoconversion marathons, to microscope & pizza parties. Although the cast of characters has changed completely from when I first joined the lab, you have all been a wonderful help throughout the many seasons of grad school.

To Adam: Thank you for being an outstanding mentor and a constant supporter. You have given me so much encouragement and freedom and support in everything I've attempted from the very beginning. Thank you for your kindness when life was tough, and thank you for encouraging me to aim higher than I ever though I could achieve. I hope our paths continue to cross in years ahead.

To my committee: Thank you for your constant guidance, support, and enthusiastic encouragement, especially as the direction of my project shifted over the years. And thank you for your flexibility and patience as we have navigated the past couple months of virtual meetings.

To Ben and Josh: Thank you for letting me constantly bother you both with coding questions as I learned a new language. I feel like I have gained a superpower now that I know enough R to be "the computational person" in the Marcus lab (ha). I hope I can pass down all that you've both taught me to other fledgling coders who are completely out of their native element.

To Nael McCarty: Thank you for your unwavering support and mentorship of graduate students. During my time serving on DSAC with you, you showed what selfless leadership truly looks like, and I thank you for setting such a stellar example of how students and administrators can work together to build a better academic community. The graduate student community thanks you for your leadership through it all.

To the greater Emory and Winship communities: Thank you for making Emory a place that I was proud and excited to work at. As a native of Atlanta, I know that Atlantans are the best kinds of people. Thank you to all the students, faculty, research staff, bus drivers, custodial staff, admins, etc. that formed a truly welcoming Emory community. I miss seeing you all on a daily basis more than you know.

To COVID-19: Absolutely not, you can get lost. To the orange Jeep Wrangler: Likewise.

To ALL the cats (so many cats) that have lived with me over the past six years: Thank you for maintaining my sanity with your adorable little furry faces. I could not have survived grad school without all your kitten cuddles.

To Scott: Thank you. Thank you for everything. Out of every person I have met during my time at Emory, you are by far the person who has impacted me the most. You have made me a better scientist and a better human. I truly don't deserve all the support you've given me over the years, and I don't tell you enough how important you are to me. Even when life is difficult and complicated (especially when it's difficult and complicated), I know I can depend on you always. I truly could not have survived grad school without you. Thank you a million times more.

To my parents and my sister: Thank you for letting me live in your basement for the past five years, you are too kind. Most parents would not tolerate that, and most kids my age would have moved out 4.99 years ago, but I have genuinely loved having another five years living with you all. It has been a gift in the best and most surprising ways; most people never get this opportunity. I am forever grateful to be genetically related to people that I genuinely like and want to spend

time with. To my mother in particular, thank you for being a constant example of unconditional love. I don't say enough how much I appreciate all the hard and invisible work that you do for our family on a daily basis, especially now that all four of us are stuck under the same roof 24/7. I hope one day that I can be even just a fraction of the amazing mother that you are to me and Sarah. You are more than welcome to crash on my couch any time you want to visit my kittens and/or Ben Stuart.

This is certainly not the time nor the place that I envisioned for the end of my graduate education. At this moment, we are two months into the extended quarantine during the COVID-19 pandemic, and the world as we know it has changed forever. And yet, despite the current chaos, my gratitude for the constant love and support I have received from you all over the past six years grows exponentially. I don't have enough words to properly express my thanks to you all or describe how profoundly you have shaped my life thus far, both during and beyond grad school. I eagerly await the day when I can celebrate with each and every one of you in person and convey the full force of my socially un-distanced gratitude, no matter how long the wait may be.

**Table of Contents**

**List of Figures**

**List of Abbreviations**

*In alphabetical order:*

**CAF** – Cancer-Associated Fibroblast

**CGI –** CpG Island

**CpG –** Cytosine-phosphate-Guanine, i.e. a cytosine followed by a guanine in a DNA sequence

**CTC –** Circulating tumor cells

**CTCFL or BORIS** – CCCTC-Binding Factor Like

**DAC** – 5-aza-2'-deoxycytidine, or Decitabine

**ECD** – Extracellular domain

**ECM** – Extracellular matrix

**EMT** – Epithelial to Mesenchymal Transition

**FN or FN1** – Fibronectin

**HTATIP2** – HIV-1 Tat Interactive Protein 2

**ICD** – Intracellular domain

**IL13RA2** – Interleukin-13 receptor $\alpha$-2

**JAG1** – Jagged1

**MET** – Mesenchymal to Epithelial Transition

**MYO10** – Myosin-X

**rBM** – recombinant basement membrane

**NICD** – Notch intracellular domain

**NSCLC** – Non-small cell lung carcinoma

**SCLC –** Small cell lung carcinoma

**TM/ICD** – Transmembrane domain/intracellular domain

# Chapter 1: Introduction

## 1.1 Cancer metastasis: A complex biological conundrum

### *1.1.1 Cancer by the numbers*

Cancer remains the second leading cause of death in the United States, causing an estimated 1,762,450 new cases and 606,880 deaths in 2019 (*1, 2*). As a result of significant advances in cancer research, early diagnosis, and advanced clinical care, the cancer death rate has steadily declined each year by 1.4% for females and 1.8% for males over the past decade (*1*). This increase in patient survival has resulted in an estimated 2,629,200 fewer deaths than would be expected if the survival rates had not changed from 2007 (*1*).

However, despite an overall increase in patient survival, the spread of tumor cells to distant secondary sites (i.e. metastasis) remains the most common cause of cancer-related deaths, ultimately causing about 90% of cancer-related deaths from solid tumor types (*3*). Metastatic tumors are highly lethal because they are often inoperable, resistant to therapy, and difficult to diagnose before they have grown to dangerously large sizes within vital organs (*4, 5*). In order to develop new diagnostic biomarkers and therapeutic tactics aimed to increase survival of patients with metastatic tumors, we must first look to the basic cell biology of cancer metastasis in order to understand the mechanisms that drive this process.

### *1.1.2 Lung cancer*

For the past several decades, lung cancer has been responsible for the most patient deaths of any cancer type (*1, 2*). Although lung cancer constitutes only 12.9% of new cancer cases in the

U.S, it is responsible for almost 25% of cancer-related deaths; lung cancer kills more people annually than breast, prostate, and colorectal cancers combined (*2*). There are two main histological classes of lung cancer, small cell lung carcinoma (SCLC) and non-small cell lung carcinoma (NSCLC), comprising approximately 15% and 85% of lung cancer cases respectively (*6*). NSCLC encompasses three additional subtypes that each arise from different cells of origin within the lung and are variably associated with patient smoking history: adenocarcinoma, squamous cell carcinoma, and large cell carcinoma (*6*).

As with most solid tumor types, NSCLC patient survival is particularly dependent upon the staging at diagnosis. The overall 5-year survival of patients with NSCLC is about 20% (*2*). However, patients diagnosed when the tumor is localized only to the primary site have a 59% 5-year survival rate, and patient diagnosed when the primary tumor has infiltrated the local lymph nodes have a 31.7% 5-year survival rate. Together, these early-stage patients comprise 39% of new NSCLC diagnoses. In comparison, 57% of NSLSC cases are diagnosed when cancer has already metastasized to a distant site, and these patients have only a 5.8% 5-year survival rate (*2*). Thus, further studies of lung cancer invasion and metastasis are warranted in order to improve survival for the vast number of lung cancer patients who initially present with metastases.

### *1.1.3 The process of metastasis*

Metastasis is responsible for approximately 90% of cancer-related deaths (*3*), and yet the highly complex functional regulation of metastasis remain poorly understood, despite an explosive increase in recent research efforts to decode metastasis. The full metastatic process requires tumor cells to balance many complicated events; the tumor cells must invade out of the primary tumor, navigate through the stroma, enter into a blood vessel or lymphatic vessel, travel through the

circulatory system, exit the vasculature, and begin to proliferate at the new site (*7, 8*). Even though the metastatic spread of tumors is ultimately lethal for almost all patients, the process of metastasis is itself incredibly inefficient on a cellular level; estimates predict that only ~0.01% of tumor cells that initiate metastasis will survive the entire process (*9, 10*).

Metastasis begins with selective pressures within a rapidly growing primary tumor. As tumor cells rapidly proliferate, these cells consume far more energy and metabolites than nonmalignant cells. Once tumors grow over the size of approximately $1cm^3$, cells in the center of the tumor are far from any blood vessels and thus undergo a lack of oxygen (*i.e*. hypoxia) (*11*). Hypoxia in cancer cells then induces expression of the transcription factor HIF1α (Hypoxia-inducible factor 1α), which in turn induces expression of vascular endothelial growth factor (VEGF) (*12, 13*). Cancer cells secrete VEGF into the surrounding stroma and will bind to its corresponding receptor, VEGFR2, on the surface of blood vessels, and once VEGF stimulates VEGFR2, these blood vessel cells begin the process of angiogenesis, wherein new blood vessels are formed by the collective migration and proliferation of existing vascular cells (*14*). One cell at the leading edge of the new blood vessel is termed the "tip" cell, and this cell coordinates the collective migration of "stalk" cells behind it (*14, 15*). These tip cells respond to the gradient of VEGF as a chemotactic guidance cue to migrate towards the tumor; as the new blood vessel moves closer to the tumor cells, more VEGF is present in the stroma (*16, 17*). Inevitably, this new blood vessel will reach the tumor cells, thus providing a new source of nutrients and oxygen for the growing tumor.

However, these newly-formed blood vessels also provide a direct highway for tumor cells to escape the primary tumor. In response to the ever-growing lack of resources and selective pressures inside a crowded tumor, tumor cells will often invade outwards away from the primary

tumor and into the nearby stroma, eventually penetrating the basement membrane that separates epithelial tissues from blood vessels (*18, 19*). The specific signaling events that stimulate tumor cells to leave the primary tumor and direct their outward migration are not yet fully understood. Tumor cells can utilize several modes of invasion to escape the primary tumor, which will be outlined in more detail below. Regardless of which migration method tumor cells use, these cells will ultimately enter into a blood vessel or a lymphatic vessel, a process termed intravasation (*20*). Cell migration directly through the stroma is a slow and cumbersome process, whereas traveling through the vasculature allows for speedy dissemination of cancer cells to distant parts of the body.

While in circulation, tumor cells experience yet more selective pressures, including high shear flow pressures and cell death from becoming detached from a solid surface (termed anoikis) (*21*). In addition, tumor cells in the vasculature face an increased risk of being detected and eliminated by immune surveillance cells (*21*). Most cells in circulation will die before ever reaching a secondary site, but some rare cells will attach to a distant blood vessel and invade through the blood vessel into the stroma of the new secondary site (termed extravasation) (*22*). Once again, not all tumor cells who reach a secondary site will survive and thrive to become a secondary tumor. Most tumor cells that have extravasated will remain as single cells or very small clusters of cells that can remain dormant for years (*i.e.* micrometastases) (*9, 10*). Some micrometastases will gain the ability to begin proliferating once more and expand into a larger tumor that can threaten the normal function of the secondary organ site (*i.e.* macrometastases) (*22*). Invariably, metastasis is a complicated cellular process, and any single cancer cell has a very low chance of successfully completing the entire metastatic cascade.

### *1.1.4 Single cell invasion*

As outlined above, the metastatic cascade begins when tumor cells leave the primary site and invade through the surrounding stroma. However, cancer cells utilize a spectrum of different invasion mechanisms, which can be simplistically divided into two broad categories of single cell invasion and collective invasion (*23, 24*).

*Mesenchymal cell invasion*

Within the category of single cell invasion are two main modes of movement, each with distinct physical features and signaling pathways. Mesenchymal cells are highly elongated cells with a "front/back" polarity (rather than apical/basal polarity of stationary epithelial cells that form polarized tissue layers) (*25*). These mesenchymal cells utilize focal adhesions as "cellular feet" to sense the composition, stiffness, and orientation of the extracellular matrix (ECM) and then create traction forces to propel forward migration (*26*). Focal adhesions contain a combination of several proteins, including actin stress fibers within the cell body, several classes of linking proteins, focal adhesion kinase (FAK), the intermediate filament vimentin, and integrins which span the plasma membrane and anchor the cell to the ECM (*27-29*). Mesenchymal cells maintain strong directional persistence as they process forward in a mostly linear path (*25*).

Since focal adhesions link the cytoskeleton to the extracellular matrix, mesenchymal cells are capable of not only stepping through the ECM but also of restructuring the ECM into linear patterns (*30, 31*). The ECM is comprised of many different connective proteins that normally resemble a mesh-like pattern; integrins within focal adhesions will attach to ECM components such as collagens and fibronectin (FN), and actomyosin contractility within the cell will transmit traction forces that will pull on the ECM "mesh" and align them into linear bundles parallel with the direction of the applied force (*30, 32*). Mesenchymal cells are also capable of degrading the

ECM with digestive enzymes called matrix metalloproteases (MMPs), which allow the cancer cell to "carve" a path forward and invade through the basement membrane (*33*). Mesenchymal cancer cells often resemble the morphology of fibroblasts, which are a key cell type responsible for forming the connective tissues and ECM within the body during wound healing and development, as well as restructuring the ECM during cancer invasion (*34, 35*).

*Amoeboid cell invasion*

In addition to the mesenchymal morphology, single cells can also invade utilizing an amoeboid morphology (*36*). Amoeboid movement was named after the class of single-celled eukaryotes called amoebas, which migrate using bleb-like movements; this movement pattern was best characterized using the slime mold Dictyostelium discoidium, which can migrate as single blebbing amoeboid cells or as a massive cooperative conglomerate of cells that form a sprouting stalk (*37*). Within the normal human body, leukocytes also migrate utilizing amoeboid movement (*38*). In stark contrast to mesenchymal cancer cells, amoeboid cancer cells lack linear directionality. Amoeboid cells have a rounded amorphous shape and display more membrane blebbing that mesenchymal cells. Instead of forming linear actin stress fibers, amoeboid cells will often form large bleb-like structures at the leading edge that lack focal adhesions, termed pseudopodia or "false feet" (*36*). Since amoeboid cells don't utilize canonical focal adhesions or secrete MMPs, they don't directly pull on the ECM to direct forward movement or remodel the stroma. Instead, amoeboid cells somewhat randomly "bleb" through gaps in the ECM (*39*). Despite the more chaotic nature of amoeboid invasion compared to the linearly-ordered mesenchymal invasion, amoeboid cells invade at a much higher velocity than mesenchymal cells (*36*). It is not well understood how amoeboid cells determine their migration path, nor even how these cells

coordinate the cytoskeleton during migration. Cancer cells can utilize either amoeboid or mesenchymal modes of motility, and the transition to one invasion mode or another is facilitated in part by LKB1, a tumor suppressor gene and a kinase with dual functions in regulating cell adhesion and cell polarity, as well as metabolic signaling pathways (*40*).

### *1.1.5 Collective cell invasion*

Cancer cell invasion requires the interplay of many factors, including the actomyosin cytoskeleton, the coordination of signaling pathways that determine cell polarity and directionality (notably the Rho-GTPase protein family), FAK and integrin activity to create and turn over focal adhesions, proliferation, maintenance or suppression of cadherin-based cell-cell contacts, ECM topography sensing, ECM degradation by MMPs, and ECM deposition and/or remodeling (*24, 41*). Invading cancer cells can modulate the specific balance of these mechanisms in order to transition between invasion modes (i.e. single vs. collective, mesenchymal vs. amoeboid) (*42*). It is not fully understood why cancer cells preferentially choose one mode of invasion over another, but the mode of invasion is most likely influenced by both cell-intrinsic factors (such as expression or loss of E-cadherin) and cell-extrinsic factors (such as a dense and unordered microenvironment vs stroma that is organized in linear patterns) (*24, 43*).

However, despite the vast range of invasion tactics available, most solid tumors rely primarily on collective invasion in the early stages of metastasis (*44*). Pathological examinations of the periphery of almost all invasive solid tumor types invariably shows clusters of cancer cells that are separate from the primary tumor and invading into the nearby stroma (*31, 44-46*). In general, collective invasion is a much slower process than single cell invasion, since coordinating

the movement of one cell is simpler than coordinating the migration, cell-cell communication, and ECM remodeling required to move a group of cells (*47*).

Despite the slower rate of invasion, cancer cells that invade collectively rather than individually are more likely to survive the treacherous metastatic journey to form viable and proliferative secondary tumors (*48-50*). Most likely, invasion as a collective unit provides a survival advantage to vulnerable cancer cells during metastasis. This hypothesis is consistent with observations of circulating tumor cells (CTCs) (*48*). Cancer cells that have intravasated and are in circulation can be detected within patient blood samples, and identification of CTCs can be an early prognostic marker for later metastasis. Both single CTCs and clusters of CTCs have been isolated from patient blood samples. However, when cancer cells are directly injected into the vasculature through the mouse tail vein, clusters of CTCs are far more likely to survive and form metastases in the lung, whereas most single CTCs were cleared from circulation without ever colonizing in the lung. Therefore, groups of collectively invading cancer cells may be more likely to survive circulation and ultimately colonize at a secondary site; there is safety in numbers.

### *1.1.6 Diversity and plasticity in migration modalities*

Not all collective invasion tactics are alike; both cancer cells and normal tissues during development and wound repair utilize a wide array of mechanisms to regulate multicellular collective invasion (*43, 44, 51*). For example, in some cases, single cells migrate in the tracks of the cells in front of them, a process called “streaming”; during cell streaming, cells do not rely on cell-cell contacts to direct movement but instead depend on chemical attractants and physical cues from the extracellular environment to determine the direction of migration while following in the path of the cells that went before (*52*). In other cases, collectively invading cells rely upon

cadherin-based cell-cell adhesions or other cell-cell contacts in order to direct migration (*53*). Depending on the biological context, adherent collective invasion patterns vary in terms of their physical characteristics, including sheet-like invasion seen in wound healing, strand-like or chain-like invasion seen in angiogenesis and tumor invasion, tubular invasion that maintains a distinct lumen as seen during branching morphogenesis in development (*54*), and isolated tumor cell clusters separated from the primary tumor.

As is seen in single cell invasion, collective cancer cell invasion has a high rate of plasticity when utilizing different modes of collective invasion in response to cell-intrinsic and cell-extrinsic characteristics (*55*). Invading tumor cells can even transition between collective and single cell invasion in certain context; a collective to amoeboid transition has been observed in melanoma (*56*). One of the most well-known and yet most controversial examples of phenotype plasticity during morphogenesis and invasion is the epithelial to mesenchymal transition (EMT) (*57, 58*). During EMT, it is thought that cells of epithelial origin undergo a shift in transcriptional programming to silence epithelial genes that promote stationary cell-cell contact (*e.g.* E-cadherin) and upregulate mesenchymal genes that promote cell migration and invasion (*e.g.* MMPs, vimentin, Twist, Snail, Slug, N-cadherin) (*59*). This switch in transcriptional activity would allow epithelial cancer cells to acquire the invasive characteristics needed to escape the primary tumor.

However, recent studies have begun to challenge the notion that EMT is a binary process, and whether EMT is necessary for metastasis at all (*60, 61*). A recent study showed that multiple genetically engineered mouse models of breast cancer require E-cadherin for metastasis to occur, dispelling the notion that loss of E-cadherin and gain of full mesenchymal transcriptional reprogramming is necessary for metastasis (*62*). Furthermore, disseminated metastatic cells require epithelial characteristics in order to survive and proliferate at the secondary site, either by

a “reversion” of EMT called the mesenchymal to epithelial transition (MET) or by maintaining an intermediate phenotype such as partial EMT that retains certain proliferative characteristics (*63-65*). Although many questions remain as to what specific mechanisms regulate this high degree of phenotypic plasticity in metastatic cancer cells, evidence strongly suggests that epigenetic regulation of transcription plays an essential role in creating and maintaining highly adaptable phenotypes within metastatic cancer cells (*66, 67*).

### *1.1.7 Epigenetic regulation of phenotype plasticity and its implications for cancer invasion and metastasis*

During development, all multicellular organisms begin as a single embryonic stem cell, which contains the same DNA that will be passed on to every single daughter cell in the developing organism. However, different daughter cells must differentiate into one of the thousands of potential cell types within a fully-formed embryo without changing the DNA sequence. Cells navigate the process of differentiation and phenotype determination through epigenetics, the process of regulating gene expression through heritable molecular modifications to the structure of chromatin that do not change the DNA sequence (*68, 69*). Epigenetic regulation of gene expression has been studied thoroughly in the context of development, but we now know that aberrant epigenetic modifications play a critical role in adapting cellular functions during human disease, including cancer (*70, 71*).

As discussed above, tumorigenesis and metastasis are incredibly complex processes, and cancer cells undergoing the metastatic cascade face extreme cell-intrinsic and -extrinsic selective pressures. In order to survive such selective pressures as a lack of oxygen, immune surveillance, or successfully colonizing a secondary tumor, cancer cells must adopt new behaviors at every turn.

Ever-increasing DNA mutations within cancer cells provide a window of opportunity for cancer cells to adopt advantageous mutations (i.e. silencing a tumor suppressor gene) over time through tumor evolution, but gaining advantageous genetic mutations is a relatively slow, random, and inflexible way for cancer cells to change their behavior. Instead, epigenetic regulation of transcription allows cancer cells to adapt to ever-changing selective pressures in a speedier and potentially reversible manner. In fact, studies of the epigenetic landscape in cancer show that DNA methylation and chromatin structure are profoundly altered across essentially all cancers (*71*).

The involvement of epigenetic regulators as a key component of cancer cell phenotypic plasticity is widely known to contribute to many aspects of tumor initiation and progression. For example, several epigenetic alterations play crucial roles in the emergence of tumor drug resistance (*72, 73*), and aberrant epigenetic modifications are implicated in the emergence of metastasis (*74-76*). Thus, scientists have attempted to target epigenetic dysregulation in cancer for decades, and pharmacological inhibitors of epigenetic modifiers are used clinically as part of certain cancer therapeutic regimens (*77-83*).

DNA methylation is perhaps the best studied chromatin modification and is implicated in many aspects of development, aging, gene silencing, and cancer (*84-86*). DNA methylation occurs when one of the DNA methyltransferases (DNMTs; namely DNMT1, DNMT3A, and DNMT3B) add a methyl group to the 5-carbon of the DNA base cytosine within cytosine-guanine (CpG) dinucleotides (*87*). The addition of a methyl group to a CpG interrupts the binding availability of many transcription factors; thus CpG methylation is often associated with regions of gene silencing (*88, 89*). CpGs tend to cluster together near gene promoters and enhancers in regions known as CpG Islands (CGI). CGI are critical regulatory elements of transcription, since unmethylated CGI

predominantly localize to regions of actively-transcribed chromatin and are highly evolutionarily conserved (*90*).

Much like genetic and phenotypic heterogeneity observed in cancer, recent studies of tumor DNA methylation now reveal that many tumors exhibit intratumor DNA methylation heterogeneity, and that this intratumor methylation heterogeneity may also undergo evolutionary adaptation alongside the evolution of DNA mutations (*91-95*). However, further studies are needed in order to form a more complete picture of how intratumor DNA methylation produces functional consequences for tumor formation, progression, and metastasis, and how this intratumor DNA methylation coordinates with histone modifications and chromatin structure to drive variable phenotypic changes among heterogeneous groups of cancer cells.

### *1.1.8 Heterogeneity in cancer invasion and metastasis*

In addition to transcriptional plasticity within individual cells, another way for cancer cells to achieve the phenotypic adaptability necessary for metastasis is by creating multiclonal groups of cells with different individual characteristics. In this way, multiple clones of cells that have undergone only some of the molecular changes necessary for metastatic success can form a larger unit with collectively diverse and adaptable abilities. Heterogeneous mixes of cells (i.e. originating from multiple clones within the primary tumor, or polyclonal) are more successful at forming metastases than groups of cells that originated from a single clone (*49, 50*). By performing lineage tracing experiments of mouse tumor cells of the same genetic background but labeled with two different fluorescent proteins, it was shown that metastases preferentially formed from collective groups containing mixes of two cancer cell lineages (i.e. both red and green cells) rather than from cells of the same clone (*50*). Since these cells maintained identical genomic backgrounds minus

the fluorescent label, it can be inferred that collective invasion of heterogeneous mixes of cells provides an advantage for establishing metastasis over homogeneous groups (*50*). Thus, there is strength not only in numbers but also in diversity.

Interestingly, when examining the genetic diversity of metastatic tumors, most metastases remain remarkably homogeneous in terms of the mutational landscape (*96-98*). In particular, most metastases are strongly homogeneous in terms of which driver mutations are present when compared to all driver mutations within the primary tumor, suggesting that only one or a small number of clones from the primary tumor are present in metastases. (*99-101*). However, metastatic tumors (especially lung cancer) maintain high degrees of functional heterogeneity beyond merely driver mutations (*102*). Lung tumors and metastases often contain vast cellular heterogeneity in terms of cell morphology, metabolism, and immune response (*103, 104*). In addition, in the mouse tumor lineage tracing experiments above, the two tumor cell populations maintained identical genetic backgrounds minus the addition of a fluorescent marker, and yet these tumors formed more metastases from polyclonal groups rather than from monoclonal groups (*50*). Therefore, heterogeneity that benefits metastasis likely originates not only from genetic drivers but also from epigenetic, phenotypic, and/or metabolic heterogeneity.

In fact, phenotypic heterogeneity commonly exists not only within metastases but also within the initial collective invasion pack at the primary tumor. Observations of patient tumor samples almost 30 years ago revealed that the invasive cells within these tumors did not all look or act the same (*45*). When pieces of tumor samples were cultured in a collagen matrix to mimic the 3D extracellular environment inside the body, these tumor cells began to invade out from the tumor and into the collagen in collective chains. However, the cell at the tip of the chain was very mesenchymal in morphology (elongated, with clear MMP activity), whereas the cells further back

in the chain remained more epithelial-like in morphology. Further examination of tumor samples from multiple cancer types revealed that this pattern of distinct front/back cells was common within collective invasion. The elongated cells at the front were ultimately termed "leader" cells, and the cells adherent to the back end of the leader cells were termed "follower" cells (*23, 31, 44, 45*). Leader and follower cells have been best characterized in breast cancer. Within multiple models of collective breast cancer invasion, leader and follower cells maintain distinct transcriptional programs and morphologies (*105-108*). For example, breast cancer leader cells maintain a basal-like transcriptional profile indicated by high expression of genes such as keratin-14 (KRT14) (*105*) and low expression of EpCAM (*107*). These breast cancer leader and follower cells demonstrate rapid phenotypic plasticity, as leader and follower cells can switch phenotypes within a short time frame (*105, 109*).

### *1.1.9 Leader and follower cells in lung cancer*

Although leader and follower cells have been thoroughly characterized in breast cancer, similar leader and follower phenotypes exist within other solid tumors, including lung cancers. Interestingly, NSCLC tumors often present with high degrees of heterogeneity, meaning that multiple cellular lineages co-exist within individual tumors (*66, 104, 110, 111*). Lung cancer leader and follower cells were first characterized in the Marcus lab using spheroid invasion assays, wherein 3D spheres of lung cancer cells were embedded into either collagen or matrigel in order to induce chainlike 3D collective invasion (*112*). However, it quickly became clear that lung cancer leader and follower cells depend on different signaling mechanisms than those in breast cancer. For example, lung cancer leader cells do not show any change in expression of keratin-14 or other basal keratins (*112*).

In order to characterize the biomarkers of lung leader and follower cells, it was necessary to develop reliable methods to isolate the purified populations of leader cells or follower cells from the bulk of an invading spheroid. Within models of breast cancer collective invasion, leader and follower cells have been isolated by FACS for cell surface protein markers of leaders or followers (*105, 107*) or by roughly isolating invasive versus noninvasive cells (*107, 108*). However, lung cancer leader and follower cells cannot be isolated using the biomarkers seen in breast cancer leader and follower cells, and the physical isolation methods used previously do not fully discriminate between leader and follower cells but instead collect larger populations of invasive cells that contain both phenotypic populations. Therefore, in order to collect purified leader and follower cells for downstream molecular and cellular analysis, the Marcus lab developed a new technique to optically highlight and isolate specific cells based purely on phenotypes and not on pre-determined biomarkers, termed Spatiotemporal Genomic and Cellular Analysis (*i.e.* SaGA) (*112*).

In SaGA, cells are stably transduced to express the photoconvertible protein Dendra2 with an added palmitoylation domain that localizes Dendra2 to the plasma membrane (*i.e.* Dendra2-pal) (*112, 113*). Dendra2 is a fluorescent protein that emits green light in its nascent state, but when exposed to ultraviolet light (405nm wavelength), Dendra2 undergoes a permanent protein conformation change that causes it to emit red light (*113*). Using SaGA, spheroids expressing Dendra2-pal are embedded into matrigel. After approximately 24 hours of spheroid collective invasion, leader cells or follower cells are identified based on phenotypic characteristics and are selectively exposed to UV light using a confocal microscope, allowing for specific photomarking at a single cell level (*112*). Once many leader cells or follower cells from the same plate are photomarked, the matrigel matrix is degraded, the spheroids are dissociated to a single-cell

suspension, and the photoconverted leader or follower cells are isolated using fluorescence-activated cell sorting (FACS) (*112*). These purified leader and follower cells can be sorted either as single cells to be immediately processed for single-cell RNAseq (*114*) or as a pooled population to be maintained in cell culture and expanded for downstream molecular and cellular analysis (*112, 114-116*).

Leader cells and follower cells isolated from the NSCLC cell line H1299 display remarkable phenotypic stability over time, even when maintained in culture for several weeks. Lung cancer leader and follower cell phenotypes resemble those of breast cancer leader and follower cells, in that leader cells remain highly invasive and follower cells are poorly-invasive on their own (*105, 106, 108, 112*). In addition to differences in proliferation and invasion, leader and follower cells display divergent metabolic profiles. In lung cancer cells, leader cells are dependent upon pyruvate dehydrogenase (PDH) to drive mitochondrial respiration, whereas follower cells depend upon high rates of glucose uptake and subsequent glycolysis (*115*). One breast cancer model of collective invasion shows the opposite pattern, wherein leader-like cells utilize higher rates of glycolysis than follower-like cells (*117*). These metabolic differences once again emphasize that breast cancer and lung cancer collective invasion display many molecular differences that remain to be identified.

In addition to differences in biomarker expression and metabolic profiles between breast cancer and lung cancer collective invasion, these two invasive cancers also display important differences in how individual cells contribute to the phenotype of the larger population. In breast cancer collective invasion, individual cells undergo high rates of phenotypic plasticity, wherein leader cells and follower cells can rapidly change their position within the invasive strand or even switch phenotypes entirely (*105, 118-122*). In contrast, within heterogeneous lung cancer

populations, individual lung cancer leader cells or follower cells remain phenotypically stable over long periods of time (*112*). As further evidence that lung cancer leader and follower cells are phenotypically stable and maintained within the larger population, H1299 leader and follower cells isolated by SaGA contain 14 unique expressed mutations that are present in only one of the two phenotypes (*114*). Furthermore, when variant calling was performed on the original parental H1299 cell line, small populations of cells expressing either the leader-specific mutations or the follower-specific mutations were identified, suggesting that genomic heterogeneity underlies the distinct lineages of leader and follower cells.

Since invasive NSCLC tumors frequently display high rates of intratumoral genetic heterogeneity, this suggests that intratumor heterogeneity may functionally benefit tumor progression and invasion (*96-98*). These observations further highlight the unique biology of lung cancer collective invasion compared to breast cancer collective invasion and the importance of further profiling the key cancer-specific differences regulating leader cells and follower cells. By dissecting the molecular events that drive lung cancer leader and follower cell phenotypic determination, transcriptional plasticity, and intercellular cooperation, we can identify potential avenues to target lung cancer invasion and metastasis. In this dissertation, we identify some of the epigenetic and transcriptional events that promote the leader cell phenotype, and we characterize how these events lead to the formation of uniquely stable cytoskeletal protrusions to promote leader cell invasion and ECM remodeling.

## 1.2 The filopodia and its motor protein MYO10

### *1.2.1 The actin cytoskeleton: many forms and many functions*

The cellular cytoskeleton comprises three main categories of structures, namely actin-based microfilaments, intermediate filaments such as keratins and vimentin, and tubulin-based microtubules (*123*). Each cytoskeletal component provides structural or mechanical support for the internal structures of the cell, and all three components contribute to cell motility and invasion. However, forces generated by growing and shrinking actin-based structures play particularly critical roles in regulating cell function, shape, division, and motility in response to both intracellular and extracellular cues (*124, 125*). Among the many shapes that bundled actin microfilaments form inside of cells, three structures play outsized roles in regulating cell motility: stress fibers, which are long linear bundles that connect focal adhesions to the interior of the cell (*126*), lamellipodia, which are wide fan-shaped protrusions with highly-branched actin that pushes against the leading edge of migrating cells (*127*), and filopodia, which are thin protrusions that extend out from the cell body.

Extensive research has focused on the roles of stress fibers and lamellipodia in directed cell migration and cancer invasion, but less is known about the role of filopodia, likely in part because filopodia are much smaller and more transient than other bundled actin structures and because filopodia produce only minimal traction forces on their own. In this dissertation, transcriptomic analysis and functional studies in leader and follower cells reveal the particular importance of filopodia in facilitating collective invasion and highlights multiple previously unknown functions of filopodia within collective cancer invasion.

### *1.2.2 Filopodia: The fingers of the cell*

Filopodia are slender finger-like projections extending out from the plasma membrane that contain a core of parallel fascin-bundled actin filaments, with the fast-growing (+) end of the filaments oriented towards the filopodia tip and protected from depolymerization by actin capping proteins (*128*). Unlike larger actin-based cellular protrusions and focal adhesions, a single filopodium produces only minute traction forces (*129, 130*). Canonically, filopodia are recognized as sensors of the extracellular environment, which is crucial for several developmental processes, such as angiogenesis and neuronal axon guidance (*128*). In addition, filopodia can form nascent adhesion sites that allow the cell to adhere to the extracellular matrix (*131-134*). These filopodial adhesions sites differ from canonical focal adhesions in several ways, including a lack of paxillin, and FAK is not necessary for filopodial adhesions (*133*). Under 2D cell culture conditions, filopodia are short-lived structures, with a typical lifetime of approximately 1-2 minutes (*131, 135, 136*). However, little is known about filopodial dynamics within a 3D context and how their behavior in a confined 3D environment differs from behavior on a flat substrate. Furthermore, filopodia have been studied mostly in single cells, so questions remain as to how filopodia influence multicellular functions, such as collective cancer invasion.

### *1.2.3 Structure and function of MYO10*

Myosins are a large and highly diverse class of ATP-dependent proteins responsible for actin-based motility. Conventional myosins are best known for their role in muscle contractility, but unconventional myosin family members play many additional non-muscle roles, such as transporting cargo (organelles, proteins, RNA, etc.) along actin microfilaments or driving

formation of specialized structures such as stereocilia in the developing ear (*137-139*). The general myosin structure is composed of three conserved domains: the head, neck, and tail. The myosin head domain utilizes ATP hydrolysis to "walk" along actin filaments in a step-like manner. The neck domain links the head domain to the tail domain and acts like a lever to transmit mechanical forces. In addition, the neck domain often contains additional regulatory elements to modulate myosin motor activity. The myosin tail domain can contain a wide variety of functional motifs that mediate binding to other myosin molecules or to various cargos. The tail domain is highly variable among the different classes of unconventional myosins, which allows for the highly diverse functions of the myosin superfamily (*140*).

Myosin-X (MYO10) is an unconventional myosin that contains unique properties not seen in any other myosin. MYO10 does not participate in actomyosin contractility, but instead processes along bundled actin within filopodia (*141-144*). Similar to other myosins, MYO10 uses a two-step motion to "walk" along actin microfilaments (*145*). Unlike other myosins that process along a single actin filament such as myosin-V and myosin-VI, MYO10 preferentially steps along bundled actin microfilaments found only in filopodia due to its unique head and neck geometry (*146, 147*). The tail domain of MYO10 contains multiple functional motifs, including a myosin tail homology 4 (MyTH4 domain) that binds to tubulin and a FERM domain (band 4.1/ezrin/radixin/moesin) that binds to integrins (*140-144*). Integrin-β1 is a known cargo protein of MYO10, but it is hypothesized that other integrins may be transported as well (*148*). Loss of MYO10 disrupts proper integrin localization within filopodia and decreased cell adhesion (*148-150*). MYO10 has several other confirmed or putative cargo proteins that it transports to filopodia tips, including β-integrins, VE-cadherin, the nectrin receptor DCC, and the actin anti-capping protein Mena/VASP (*142, 148, 151, 152*). However, since MYO10 is an unconventional myosin, its function and cargo proteins

have not been studied as intensely as those of conventional myosins, and it is not known if MYO10 function varies under different cellular contexts.

In addition to the full-length protein, a headless MYO10 isoform that lacks a functional motor domain exists in neurons (*153, 154*). This shorter headless MYO10 isoform acts as an endogenous dominant negative regulator of the full-length MYO10 protein, thus inhibiting filopodia initiation and elongation during neuronal migration and differentiation (*152, 155*). MYO10 also contains three pleckstrin homology (PH) domains that bind to the phospholipid phosphatidylinositol-3,4,5-triphosphate (PtdIns(3,4,5)P3) to force MYO10 into its active conformation (*156, 157*). The phospholipid PtdIns(3,4,5)P3 preferentially localizes to regions of active plasma membrane and PI3K/Akt signaling (*158*), and MYO10 is enriched in membrane regions with high PtdIns(3,4,5)P3 (*159*). Thus, MYO10 preferentially localizes to regions of active membrane dynamics through binding interactions with PtdIns(3,4,5)P3, which in turn stimulates the formation of new filopodia predominantly at the cellular leading edge.

### *1.2.4 MYO10 regulates filopodia initiation and elongation*

MYO10 does not merely localize to the tips of filopodia but instead plays a crucial role in facilitating filopodia initiation and elongation. The geometry of MYO10 is unique compared to most other myosins, in that the step size between the two motor domain lever arms in an active MYO10 dimer is 36nm on a single actin filament and 52-57nm on fascin-bundled actin (*146*). Since MYO10 can move 1.5x farther per step on bundled actin than on a single actin filament, MYO10 travels much faster along the fascin-bundled actin filaments found in filopodia than on other actin microfilament-based structures, thus explaining why MYO10 preferentially localizes to filopodia (*146*). In addition, single molecule live cell imaging revealed that this unique dimer

step size allows MYO10 to step horizontally across different microfilaments within a larger filament bundle, and it is hypothesized that this horizontal stepping allows MYO10 to facilitate the convergence of actin filaments together during filopodia initiation (*145, 147*). Furthermore, MYO10 facilitates multi-cycle extension and retraction to create long filopodia. In this process, MYO10 initiates a new filopodia that extends approximately 2.4μm forward. MYO10 travels with the growing tip of the filopodia, and β-integrins and the actin branching protein Arp2/3 both travel concomitantly to the filopodia tip (*160*). Once Arp2/3 and β-integrins have accumulated at the filopodia tip, MYO10 is able to initiate a second "step" forward in any direction, resulting in long, angled filopodia with multiple integrin-based adhesion sites attaching the filopodia to the extracellular substrate (*160*). These initial studies of MYO10 function in filopodia initiation and elongation were performed almost exclusively in 2D cell culture, so elucidating the function of MYO10 within a 3D biological context will be crucial to fully understanding the role of filopodia in development, cell migration, and cancer invasion.

### *1.2.5 MYO10 regulates collective migration during development*

Until recently, the role of MYO10 in development and cellular homeostasis was unknown, due in part to the fact that MYO10 is a low abundance protein in endogenous tissues and is thus difficult to isolate (*142, 161*). Between 2017 and 2019, five *Myo10* knockout mouse models from three independent labs were produced that provided the first evidence for the many diverse roles of MYO10 in developing embryos (*162-164*). Importantly, all three *Myo10* knockout models provide consistent evidence that MYO10 regulates collective migration during multiple developmental processes. For example, all three studies reported that homozygous *Myo10* deletion or loss-of-function resulted in 25-70% incidence of exencephaly, a fatal error in the closure of the

neural tube due to decreased collective migration of neural crest cells. Furthermore, these homozygous *Myo10* knockout mice consistently presented with white belly spots at 100% penetrance and syndactyly (digits that are fused together) at over 50% penetrance, both derived from inhibited collective migration of neural crest cells or neural crest lineage progeny. These mice also showed severe defects in retinal vascular formation in 75-100% of mice. Angiogenesis within developing retinas requires collective migration of vascular cells, and one mouse model confirmed that *Myo10* knockout mice had significantly fewer filopodia in retinal vascular cells (*164*). Since *Myo10* is crucial for developmental processes that depend upon collective migration, this raises the intriguing possibility that MYO10 could regulate cancer collective invasion as well.

### *1.2.6 Filopodia and MYO10 in cancer*

Within the past few years, several studies have produced growing evidence that high levels of MYO10 expression promotes tumor progression and metastasis. For example, elevated expression of MYO10 correlated with tumor aggressiveness and metastasis in both *in vivo* models of breast cancer and in breast cancer patients (*149, 165*). Upregulation of MYO10 has also been seen in lung adenocarcinoma and prostate cancer (*166-168*). Although these studies show a correlation between high MYO10 expression and tumor progression and/or metastasis, these studies provide very little evidence to explain the mechanism(s) by which MYO10 promotes metastasis. One study shows that MYO10 is necessary for the formation of invadopodia in breast cancer models, consistent with prior evidence that MYO10 facilitates invadopodia formation (*165, 169*). While these studies provide thought-provoking evidence that MYO10 plays an important role in cancer progression and metastasis, we still lack a mechanistic understanding of how MYO10-expressing filopodia regulate cancer cell migration and invasion. Furthermore, there is

essentially nothing known about the transcriptional regulation of MYO10. MYO10 is highly expressed in many aggressive cancer cells, so identifying the mechanisms that regulate MYO10 expression may provide new insight into how to inhibit filopodia during cancer invasion and metastasis.

### 1.3 Dissertation Goals

Tumors are complex 4D structures composed of many distinct populations of cancer cells and stromal cells that are capable of working together to coordinate multicellular functions, such as collective cancer cell invasion and metastasis. While the biological intricacies of tumor heterogeneity and metastasis are difficult to fully understand, the human impact of cancer metastasis is starkly straightforward; metastasis ultimately causes 90% of cancer-related deaths. In order to discover clinically actionable methods to target metastasis in patients, it is first necessary to understand how tumor invasion originates from within highly complex and heterogeneous primary tumors. In this dissertation, we utilize an *in vitro* model of tumor invasion to explore how epigenetic transcriptional regulation within leader cells and follower cells enables filopodia-driven collective cancer cell invasion.

Chapter 2 of this dissertation combines an analysis of DNA methylation and gene expression to identify how transcriptional regulation of leader and follower cells contributes to their distinct phenotypes. This analysis revealed that DNA methylation within leader cells is in stark contrast to DNA methylation patterns within follower cells and the parental cell line of origin, with leader cells showing an overall shift towards DNA hypermethylation. We identified a subset of genes that were differentially expressed between leader cells and follower cells that also contained differentially methylated promoters. Of particular interest, the tumor suppressor HTATIP2 was hypermethylated and silenced in leader cells, while the filopodial motor protein MYO10 was hypomethylated at the promoter and overexpressed in leader cells compared to follower cells.

In Chapter 3, we demonstrate how MYO10 regulates filopodial elongation and stability that promotes 3D collective invasion of lung cancer cells. Although MYO10 has been implicated

in cancer invasion and metastasis previously, very little is known about how it is transcriptionally regulated or how it functions within heterogeneous collective invasion packs. To that end, JAG1 was identified as an upstream regulator of MYO10 expression, in conjunction with the promoter demethylation described in Chapter 2. We also identified a surprising new role by which MYO10 regulates collective cancer cell invasion; MYO10-expressing filopodia direct extracellular fibronectin remodeling into linear fibrils at the leading edge, effectively paving a straight path forward for collective invasion.

In addition to its role in filopodia at the leading edge of collective invasion, MYO10 has been implicated in the regulation of both cell-cell adhesion and mitosis. In Chapter 4, we discuss these two additional roles that MYO10 may contribute to leader cells. Through this, we also demonstrate that follower cells provide a proliferative advantage to leader cells, supporting the idea of symbiotic cooperation between the two cell populations. Taken together, this work suggests many potential avenues for continued research into how tumor heterogeneity functionally promotes cancer invasion and metastasis.

# Chapter 2: Epigenetic heterogeneity between leader and follower cells reveals functional regulators of collective cancer invasion

## 2.1 Author's Contribution and Acknowledgement of Reproduction

Portions of this chapter, including Figures 1-4, were reproduced with edits from:
E.R. Summerbell*, J.K. Mouw*, J.S.K. Bell, C.M. Knippler, B. Pedro, J. Arnst, T.O. Khatib, R. Commander, J. Konen, B.G. Barwick, B. Dwivedi, J. Kowalski, P. Vertino, A.I. Marcus. Epigenetically heterogeneous tumor cells direct collective invasion through filopodia-driven fibronectin micropatterning. *Science Advances*. 2020; **6**: eaaz6197.

E.R.S., J.K.M., P.V., and A.I.M. designed the experiments. J.M.K. performed the initial experiments related to the RNAseq data. E.R.S. performed the initial experiments related to the DNA methylation microarray. E.R.S., J.S.K.B., B.G.B., B.D., S.S., and J.Kowalski contributed to the bioinformatics and statistical analysis of the genomics and epigenomics data. E.R.S., J.K.M., and R.C. drafted the manuscript. All authors provided input and feedback during manuscript preparation and edited the manuscript.

## 2.2 Abstract

Tumor heterogeneity drives disease progression, treatment resistance, and patient relapse, yet remains largely under-explored in invasion and metastasis. Since epigenetic mechanisms, such as DNA methylation, regulate phenotypic plasticity and cell differentiation in many cellular contexts, we hypothesize that leader and follower cell phenotypes can emerge through epigenetic reprogramming of lung cancer cells. Here, we investigated heterogeneity within collective cancer invasion by integrating DNA methylation and gene expression analysis in rare purified lung cancer leader and follower cells. Our results showed that the transcriptional programs of leader cells, follower cells, and the H1299 NSCLC parental population differ significantly between all three phenotypes, while leader cells alone showed substantial genome-wide shifts in DNA methylation compared to both follower cells and the parental population. By integrating the DNA methylome analysis, RNAseq analysis, and subsequent functional studies, we find that the filopodial motor protein *MYO10* and the transcriptional regulator *HTATIP2* are two genes at the functional intersection of epigenetic heterogeneity and 3D collective invasion. In addition, nonspecific inhibition of DNA methylation using 5-aza-2'-deoxycytidine (DAC) significantly abrogated collective invasion of H1299 parental cells and leader cells and induced expression of the silenced tumor suppressor *HTATIP2* in leader cells. Our data suggest a mechanism wherein aberrant DNA methylation functionally contributes to the leader cell phenotype by modulating downstream leader cell gene expression. Subsequent validation of differentially methylated target genes may identify additional functionally-relevant genes that drive leader cell-dependent collective cancer invasion.

## 2.3 Introduction

Tumor heterogeneity drives disease progression and treatment resistance, yet most cancer research and therapy decisions are carried out at the whole-population level (*97, 170*). The polyclonal nature of metastatic lesions suggests they originate from heterogeneous clusters of collectively invading cells, rather than clonally from singular disseminated cells (*50, 96, 171, 172*). During the initial steps of tumor invasion, many solid tumors of epithelial origin rely on collective invasion, in which packs of cells invade into the adjacent stroma while maintaining cell-cell contacts (*44, 105*). Collective invasion packs correlate with higher histologic tumor grade and increased metastatic potential, demonstrating the importance of understanding how intratumoral heterogeneity propagates invasion and metastasis (*44, 48, 173*). Nevertheless, the molecular mechanisms underlying the formation and function of heterogeneous collective invasion packs remain poorly understood.

Heterogeneous collective invasion packs can contain phenotypically-distinct invasive "leader" and noninvasive "follower" cell populations (*45, 105, 107, 112, 114*). Although the specific markers of leader and follower cells may vary based on the tissue of origin, effective cooperation between leader and follower subpopulations invariably promotes the survival and invasion of collectively invading cancer cells (*105, 112*). Cooperation between leader and follower cells frequently necessitates hijacking developmental cell-cell signaling pathways, including the Notch pathway and VEGF-dependent non-canonical angiogenic mimicry (*174, 175*). Despite a growing understanding of the underlying genetic and transcriptomic differences between tumor subpopulations, little is known about the epigenetic factors that underlie heterogeneous phenotype determination and plasticity within the collective invasion pack.

We sought to utilize epigenetic heterogeneity to identify key regulators of phenotypic heterogeneity, cell-cell cooperation, and collective tumor invasion. To do this, we integrated DNA methylation array data with RNAseq expression data on purified populations of lung cancer leader and follower cells. We found vast rewiring of the DNA methylome and transcriptome unique to leader cells compared with follower cells or the parental population, including significant enrichment for differential DNA methylation and gene expression across several pathways that fundamentally regulate multicellular collective invasion. Here, we identified the transcriptional regulator HTATIP2 and the unconventional filopodia motor protein MYO10 as two genes of interest that have differentially methylated promoters and are differentially expressed between leader and follower cells. Performing additional functional studies will allow us to determine the functional role of these two genes in regulating collective invasion.

## 2.4 Methods

### Cell culture conditions

H1299 human NSCLC cells (ATCC, Manassas, VA) were cultured in Roswell Park Memorial Institute (RPMI-1640) media supplemented with 10% fetal bovine serum and 100 units $ml^{-1}$ of penicillin/streptomycin and maintained at 37°C and 5% $CO_2$. Leader and follower cell subpopulations were isolated from H1299 cells transfected with Dendra2 via SaGA as previously described (*112*). Briefly, H1299 cells were transfected with plasma-membrane targeted Dendra2, a photoconvertible fluorophore, allowing for visualization of individual cells during imaging. Prior to photoconversion, all cells have green fluorescence (maximum excitation 490, maximum emission 507); upon excitation with a 405 laser, the Dendra2 within the selected cell is

photoconverted to emit red fluorescence (maximum excitation 553, maximum emission 573). During 3D invasion, singular leader cells or groups of follower cells were photoconverted separately without any measurable fluorescence conversion in neighboring cells. Subsequently, the cells were extracted from the 3D matrices and sorted out using flow cytometry. All primary cells and cell lines were authenticated by ATCC (where applicable), or by analysis of morphological and phenotypic characteristics as well as gene and protein expression. No cell lines used in this study were found in the database of commonly misidentified cell lines that is maintained by ICLAC and NCBI Biosample. All primary cells and cell lines were tested for mycoplasma contamination using a commercially available kit (PCR-Mycoplasma Test Kit I/C, Promokine PK-CA91-1024), according to the manufacturer's instructions, at the onset of the work (tested negative) and have never exhibited contamination symptoms after initial testing.

**Plasmids, transfections and transductions**

Derivative cells were transfected using Lipofectamine 3000 (Thermo Fisher, Waltham, MA), per the manufacturer's instructions, or transduced using lentiviral supernatants derived from HEK 293T cells using the psPAX2-PMD2.G system. The $p^{CMV}$LifeAct-TagRFP plasmid was obtained from Ibidi (Gräfelfing, Germany; 60102). The gd2PAL-Dendra2 plasmid was obtained from Dr. Gary Bassell (Emory University) and transfected into H1299 cells as previously described (*112*). The GFP-MYO10 and mCherry-MYO10 constructs were a kind gift from Dr. Richard Cheney (UNC Chapel Hill) (*154*). The human JAG1 shRNA (HSH004470-LVRU6P) and ORF (EX-M0722-Lv105-B) constructs were purchased from GeneCopoeia (Rockville, MD). The human

MYO10 siRNA constructs (Silencer Select siRNA s9224 and s9225) were purchased from Thermo Fisher (Waltham, MA).

**Reagents and antibodies**

*Primary and secondary antibodies for immunoblotting:* MYO10 (Novus Biologicals, NBP1-87748) was used at 1:2000. HTATIP2 (LSBio, LS-B10900) was used at 1:1000. Actin (Sigma A2066) was used at 1:5000. Tubulin (Millipore, MAB1864) was used at 1:20,000. Peroxidase AffiniPure Goat Anti-Mouse IgG (H+L)(Jackson ImmunoResearch, 115-035-003) was used at 1:10,000. Peroxidase AffiniPure Goat Anti-Rabbit IgG (H+L)(Jackson ImmunoResearch, 111-035-144) was used at 1:10,000. Peroxidase AffiniPure Goat Anti-Rat IgG (H+L)(Jackson ImmunoResearch, 112-035-003) was used at 1:10,000.

**DNA methylation microarray**

DNA methylation status was assessed in triplicate on H1299 parental, leader and follower cells. For parental cells, three different passages were used. For follower cells, three separately-isolated populations were used. For leader cells, two separately-isolated populations were used: one passage of one population, and two passages of the other. Cells were grown to 70% confluency then trypsinized and homogenized using QIAshredder (Qiagen, 79654; Hilden, Germany). DNA and RNA were isolated in tandem using the AllPrep DNA/RNA Mini Kit (Qiagen, 80204). Fluorescent DNA quantification was performed using the Quant-iT dsDNA broad range assay (Invitrogen, Q33130; Carlsbad, CA). Quality was assessed on a 2% agarose gel. 500 ng of DNA was bisulfite converted using the Zymo EZ-96 DNA Methylation Kit using the protocol suggested by the Illumina Infinium Methylation guide (Illumina, 150191519; San Diego, CA). The bisulfite-

converted DNA was then used with the Illumina Infinium HD Methylation Assay in a whole genome amplification (WGA). After WGA, the DNA was fragmented, precipitated, resuspended, and hybridized to the Illumina MethylationEPIC BeadChip array (Illumina, WG-317-1001), which was then washed to remove any unbound DNA. The bound DNA underwent extension and staining according to the manufacturer protocol. The BeadChip was then coated and scanned on the Illumina HiScan to obtain the raw data.

Array data were processed and analyzed in R using the package ChAMP (*176*). Probe data were filtered according to the standard ChAMP settings, with the exception of not filtering out probes on the X and Y chromosomes. Beta values were normalized using the BMIQ method and standard settings. Differentially methylated probes (DMPs) were determined using the champ.DMP() command, which calculates Benjamini-Hochberg adjusted p-values using the limma package . DMPs with a beta difference > 0.2 and an adjusted p-value < 0.05 were considered significant. Differentially methylated regions (DMRs) were determined using the champ.DMR() command, utilizing the ProbeLasso algorithm with a minimum DMR size of 50 bp and a minimum of 2 probes. DMRs with a beta difference > 0.2 and an adjusted p-value < 0.05 were considered significant. Overlaps of DMPs or DMRs with genomic features was performed using the GenomicRanges package. Gene set enrichment analysis of DMPs was performed using the methylGSA package, using the methylRRA method and standard settings (*177*). Bonferroni adjusted p-values < 0.05 were considered significant. Gene sets used for enrichment analysis included the Molecular Signatures Database (MSigDB v6.2) Hallmark gene set collection, KEGG Pathway Database, and Reactome Pathway Database. DMPs were annotated based on their relationship with GenCode (V27, hg19) transcripts with the following hierarchy: 1) CpG within a protein-coding TSS (TSS200 and TSS1500); 2) within a protein-coding gene (intergenic); 3)

within 2kb of a protein-coding gene (perigenic); 4) lncRNA; 5) other ncRNA (miRNA, rRNA, scRNA, snRNA, snoRNA, ribozyme, sRNA, antisense RNA, or scaRNA); 6) pseudogenes. All other CpG were considered intergenic. CpG islands (CGI) were defined according to UCSC hg19.

**RNA-sequencing and Gene Set Enrichment Analysis**

RNA-sequencing was performed in triplicate on H1299 parental, leader, and follower cells. RNA library preparation and sequencing were performed by the Emory Integrated Genomics Core and Omega Bio-Tek, Inc. as previously described (*114*). Data processing, read alignment, quality control, and statistical analyses were performed by the Emory Biostatistics and Bioinformatics Shared Resource as previously described (*114*). RNAseq expression raw counts for human hg19 RefSeq annotated genes were measured using HTSeq v0.6.1 (*178*). Count normalization and pairwise differential analysis was determined using DESeq (*179*), which uses a negative binomial distribution statistic with a Benjamini-Hochberg-corrected false discovery rate. Data was log2(normalized count+1) transformed for all downstream analysis. Unsupervised hierarchical clustering and the resulting heatmaps were created using NOJAH (*180*).

Gene Set Enrichment Analysis (*181*) javaGSEA desktop application was used to identify gene expression profiles that were enriched in either leader or follower cells. Gene sets were selected from the Molecular Signatures Database (MSigDB v6.2), including the Hallmark gene set collection, KEGG Pathway Database, and Reactome Pathway Database. Enrichment scores were calculated using a weighted signal-to-noise ratio with 1000 permutations and randomization by gene set to account for a small sample size (N=3 for each cell type). Gene sets were considered

significantly enriched in either leaders or followers with a normalized enrichment score (NES) > 1.5, a nominal p-value < 0.05, and an FDR q-value < 0.25.

**3-D invasion assays, spheroid microscopy and image analysis**

Spheroids were generated as previously described (*112*) and embedded in Matrigel recombinant basement membrane (Corning, 356237). Images were taken using an Olympus CKX41 microscope with an Infinity 1-3C camera (×4 air, 0.13 NA, UPlanFL N). For mixed population spheroid experiments, cells were plated together in low-adhesion wells at the indicated ratios with 3000 total cells per spheroid. Invasive area and spheroid circularity were measured using ImageJ as previously described (*112*).

**Quantitative PCR**

Quantitative real-time PCR was performed in triplicate with iTaq Universal SYBR Green Supermix (BioRad, catalogue no1725121) using a CFX96 real-time PCR detection system (BioRad), and the relative amount of complementary DNA was calculated using a standard dilution curve, based on human GAPDH mRNA or human tubulin mRNA. Primer sequences for all qPCR reactions are: MYO10 forward (TGAGAGGGAGCTGCTCTTTG), MYO10 reverse (GTCGTGCTGTAGCGCTTCTTC), HTATIP2 forward (TTCCAAAGTCACGCTCATTGG), HTATIP2 reverse (TGAAAGGCAGAGGCGTAGTC), GAPDH forward (GGTGGTCTCCTCTGACTTCAACA), GAPDH reverse (GTTGCTGTAGCCAAATTCGTTGT), tubulin forward (CTTCGGCCAGATCTTCAGAC), tubulin reverse (AGAGAGTGGGTCAGCTGGAA).

**Immunoblotting**

For immunoblotting, total cellular protein expression was assessed via western blotting. Briefly, adherent cells were rinsed twice with 1X PBS containing Ca2+ and Mg2+ and lysed with 2% SDS lysis buffer (50mM Tris pH 8.0, 2% SDS, 100mM NaCl, 50mM DTT) supplemented with Halt Protease and Phosphatase Inhibitor Cocktail (Thermo Fisher, 78442). Samples were subsequently sonicated briefly to shear the DNA and reduce lysate viscosity. Sample protein content was quantified using a BCA protein assay kit (Thermo Fisher, 23225) prior to SDS-PAGE.

**Statistical analysis**

All quantitative results were analyzed with the test indicated in the figure legends, after confirming that the data met appropriate assumptions (normality, homogeneous variance and independent sampling). Unless otherwise stated, all indicated p-values are two-tailed and all data are plotted as the mean with error bars indicating standard error of the mean. All results were reproduced at least twice in the laboratory. The figure legends indicate the number of independent biological replicates and sample size for each experiment. Microsoft Excel and Graphpad Prism software were used to conduct statistical analyses of the data. P-values less than 0.05 were considered significant.

## 2.5 Results

### Epigenetic heterogeneity between lung cancer leader cells and follower cells reveals functionally relevant determinants of phenotype heterogeneity

We purified leader and follower cell subpopulations from invading spheroids of the H1299 lung cancer cell line using SaGA (*112*). To explore the epigenetic differences that underlie leader and follower behavior, we performed an Illumina Infinium MethylationEPIC 850K DNA methylation microarray on purified leader and follower cells, as well as on the parental population from which these cells were derived (Fig. 2.1 & 2.2). The 5000 most variant CpG sites (*i.e.* differentially methylated probes, or DMPs) clustered independently by cell type (Fig. 2.1A). Interestingly, leader cells displayed a significant shift towards hypermethylation across all CpG sites, with a 10% increase in the genome-wide median beta value compared to follower and parental cells (Fig. 2.2A-B).

We identified 3,322 differentially methylated regions (DMRs) with a beta value difference ≥ 0.2 between two of the three populations (Fig. 2.1B). While only one DMR was differentially methylated in follower cells compared to parental cells, 3,308 DMRs were differentially methylated in leader cells compared to follower cells and/or the parental population, and 13 DMRs differed between all three groups (with all 13 showing mean beta values in the order of followers < parental < leaders). In addition, 79% of the 3308 DMRs were hypermethylated in leader cells compared to follower and/or parental cells, while the remaining 21% were hypomethylated in leader cells (Fig. 2.2C). DMPs between leader and follower cells were enriched for noncoding regulatory elements and intergenic regions and were less frequent in proximal promoters and intragenic regions (Fig. 2.1C). Overall, our data showed that DNA methylation within follower

cells and parental cells was remarkably similar, but leader cells expressed unique patterns of DNA methylation compared to follower or parental cells.

We next performed RNAseq on isolated leader and follower cells and the parental population to assess gene expression differences (*114*) (Fig. 2.1-2.3). Principal component analysis of gene expression showed that parental, leader, and follower cells all clustered separately by cell type (Fig. 2.2D). To identify the subset of genes that were the most differentially expressed between each phenotype, we identified the 98$^{th}$ percentile most variant genes (499 genes) between all three cell types (Fig. 2.1D). Within the top 15 most differentially expressed genes, myosin-X (*MYO10*), fibronectin (*FN1*), and the Notch ligand Jagged-1 (*JAG1*) were highly expressed in leader cells compared to follower cells (Fig. 2.1E). Interestingly, among the differentially expressed genes were regulators of DNA cytosine methylation, with leader cells expressing a distinctive pattern of these genes compared to follower and parental cells (Fig. 2.2E).

Since DNA methylation at CpG islands within gene promoters negatively regulates gene expression (*83, 182*), we identified 123 genes that exhibited both a significant difference in gene expression (2-fold normalized gene count difference and adjusted p-value $< 0.01$) and differentially methylated CpG islands overlapping the proximal promoter when comparing leader cells and follower cells (Fig. 2.1F). Of the genes identified, 72 exhibited hypermethylation of the promoter and were underexpressed in leader cells relative to followers, whereas 13 showed the opposite relationship (*e.g.* a hypomethylated promoter and overexpressed in leaders compared to follower cells), consistent with the well-described negative correlation between promoter methylation and gene expression (*83, 182*) (Fig. 2.1F). When we looked beyond the promoter and searched for DMRs that overlap any portion of expressed genes, we identified 905 DMRs that overlap the promoter and/or gene body of differentially expressed genes (Fig. 2.2F). Gene set

enrichment analysis (GSEA) of genes differentially expressed between leaders and followers independent of DNA methylation aligned with previous transcriptome analysis by microarray (*112*) and emphasized many pathways critical for collective migration in cancer, angiogenesis, and axon guidance (*50, 177, 181, 183, 184*) (Fig. 2.1G & 2.3). However, GSEA performed on DNA methylation instead of gene expression between leaders and followers revealed that only leader cells but not follower cells enriched for differentially methylated gene sets (Fig. 2.1G). The combined gene expression and DNA methylation GSEA analyses in leader cells compared to follower cells overlapped at several key pathways relevant to collective migration in both cancer and normal physiology, such as Notch1 signaling, axon guidance, angiogenesis, and ECM-receptor interactions (Fig. 2.1G). These data demonstrate significant heterogeneity across both DNA methylation and gene expression between leader cells and follower cells that overlaps with many biologically relevant pathways, recapitulating intratumor heterogeneity observed in primary patient samples.

**The filopodia motor protein Myosin-X is differentially methylated and enriched in leaders**

From our integrated DNA methylation and gene expression analysis, we identified myosin-X (*MYO10*) as the gene most significantly upregulated and hypomethylated at the promoter in leader cells compared to follower cells (Fig. 2.1F). MYO10 is an unconventional myosin that localizes to filopodia tips and drives filopodia elongation (*144, 160*). Annotation of the *MYO10* DMPs revealed that CpG probes within 1500bp of the promoter and the first exon were hypomethylated in leader cells compared to follower cells, whereas almost all CpG probes within the gene body were hypermethylated compared to follower cells (Fig. 2.4A-B). Since promoter methylation acts as a transcriptional repressor (*83, 182*) and gene body methylation positively

correlates with gene expression (*185, 186*), these data suggest that shifts in MYO10 DNA methylation may enable MYO10 overexpression in leader cells. Overexpression of *MYO10* in leader cells observed by RNAseq was validated by qPCR and Western blot (Fig. 2.4C-D). We performed extensive functional studies to determine how high MYO10 expression regulates the leader cell phenotype and drives collective invasion, which will be presented and discussed in Chapters 3 and 4 of this dissertation.

**The putative tumor suppressor HTATIP2 is underexpressed and contains a hypermethylated promoter in leader cells compared to follower cells**

In addition to *MYO10*, we identified 122 additional genes that are significantly overexpressed or underexpressed in leader cells compared to follower cells that also contain differentially methylated promoters (Fig. 2.1F). Over half of these genes (72 out of 123) were underexpressed and contained a hypermethylated promoter in leader cells compared to follower cells, consistent with the role of promoter DNA methylation enabling gene silencing (*83, 182*). Since aberrant promoter hypermethylation is a common mechanism of tumor suppressor silencing, we hypothesized that some of these 72 genes may be known or putative tumor suppressors that were silenced in leader cells, which could contribute to the invasive/metastatic potential of leader cells. Thus, from this subset, we prioritized genes of interest by those with potential tumor suppressor activity.

From this, we identified the gene HIV-1 Tat Interactive Protein 2 (*HTATIP2*, also known as *TIP30* or *CC3)* as a top gene of interest with high promoter methylation and gene silencing in leader cells (Fig. 2.1F). *HTATIP2* is an oxidoreductase that can block nuclear import when bound to NADPH, and it is a known tumor suppressor gene and a putative metastasis suppressor with

antiangiogenic and proapoptotic functions (*187-189*). Downregulation of *HTATIP2* correlates with increased tumor aggression and poor patient prognosis in several cancer types, including hepatocellular carcinoma (HCC), glioblastoma, pancreatic cancer, melanoma, and both non-small cell lung carcinoma (NSCLC) and small cell lung carcinoma (SCLC) (*190-194*). Interestingly, high promoter methylation and gene silencing of HTATIP2 has been observed in medulloblastoma and esophageal squamous cell carcinoma patients (*195, 196*). However, these previous studies examined HTATIP2 expression or silencing within cell lines or bulk tumor samples, thus it is not known how HTATIP2 silencing in a small population of heterogeneous tumor cells (i.e. leader cells) may affect tumor progression and invasion of the larger tumor.

Within the CGI that overlaps the *HTATIP2* promoter (N = 20 CpG probes), *HTATIP2* was highly methylated in leader cells compared to follower cells or parental cells, with median beta values of 0.92 in leaders, 0.09 in followers, and 0.32 in parental cells (Fig. 2.5A-B). There were too few CpG probes outside of this CGI and within the gene body of *HTATIP2* to analyze gene body methylation (N = 3 probes; Fig. 2.5A). *HTATIP2* is binarily expressed between leaders and followers; *HTATIP2* is highly expressed in follower cells and the parental H1299 cells, but *HTATIP2* showed zero expression in leader cells, both by RNAseq and qPCR validation (Fig. 2.5C-D). Western blots performed on parental, follower, and leader cells showed that parental and follower cells had high expression of a double band around the predicted molecular weight of HTATIP2 (~27kDa), while leader cell protein samples showed only a single band at the lower molecular weight and no expression of the upper band (Fig. 2.5E).

Next, we performed preliminary functional studies to determine if HTATIP2 regulates collective invasion within leader and follower cells. Since loss-of-function of the tumor suppressor HTATIP2 correlates with increased tumor progression and metastasis in patients (*191*), we

predicted that knocking down HTATIP2 in follower cells would increase their invasive potential. We performed spheroid invasion assays of follower cells expressing a control siRNA (siCtrl) or one of two independent siRNAs targeting HTATIP2 (Fig. 2.5F-H). HTATIP2 knockdown significantly increased the collective chain-like invasion of follower cell spheroids, both in terms of the total invasive area and the presence of multicellular chains branching off of the spherical center (measured by spheroid circularity; decreased circularity indicates a less spherical and more branched shape) (Fig. 2.5F-G). These results suggest that HTATIP2 promoter methylation and gene silencing in leader cells may contribute functionally to the highly invasive behavior of leader cells, although further functional studies will be needed to fully assess the function of HTATIP2 in leader and follower cells.

**Nonspecific inhibition of DNA methylation abrogates the collective invasion of leader cells by rescuing HTATIP2 expression**

Since leader cells displayed phenotype-specific shifts in DNA methylation across the genome, we hypothesized that maintenance of DNA methylation is necessary to maintain the leader cell phenotype. To test this, we treated parental, leader, and follower cell spheroids with 5-aza-2'-deoxycytidine (DAC). DAC is nonspecific inhibitor of DNA methylation maintenance that works by incorporating into nascent DNA strands and irreversibly binding to DNA methyltransferases (DNMTs) (*77*). After 72 hours of treatment with vehicle control or DAC, the collective invasion of leader cell spheroids treated with DAC decreased significantly, both in terms of total invasive area and the amount of branching within the invasive front (Fig. 2.6A-B). Follower cell spheroids, which are poorly invasive under control conditions, were not affected by treatment with DAC (Fig. 2.6A-B). Interestingly, parental cell spheroids treated with DAC only

moderately decreased the total invasive area but significantly decreased the total amount of branch-like invasive chains (Fig. 2.6A-B). Furthermore, all three cell types showed an equivalent dose-independent decrease in cell viability across a range of DAC concentrations (Fig. 2.6C), with all three groups achieving approximately 90% of growth compared to vehicle control when treated with DAC at doses of 0.3μM to 20μM. These results suggest that inhibition of DNA maintenance in pure leader cell populations or heterogeneous populations containing leader cells (i.e. parental cells) inhibits collective invasion, and that the decrease in chain-like collective invasion seen in leader cells and parental cells is not due to a decrease in proliferation but rather by inhibiting cellular processes regulated by DNA methylation that are necessary for collective invasion.

Since DAC treatment causes a genome-wide decrease in DNA methylation, we predicted that DAC treatment would enable expression of genes that were previously silenced in leader cells through DNA hypermethylation at regulatory elements. As established earlier, the promoter of *HTATIP2* is hypermethylated in leader cells compared to follower and parental cells, and *HTATIP2* has no detectable expression in leader cells (Fig. 2.1, 2.5). Thus, we hypothesized that treatment with DAC would demethylate the *HTATIP2* promoter in leader cells, which would enable a more transcriptionally permissive state at the *HTATIP2* promoter and subsequently increase *HTATIP2* expression. To test this, parental, leader, and follower cells were treated with 500nM DAC 48 hours before RNA and protein was collected. In the vehicle control treated cells, HTATIP2 mRNA was expressed in parental and follower cells but not in leader cells (Fig. 2.7A), consistent with previous experiments (Fig. 2.5D). When treated with DAC, parental cells and follower cells showed a slight increase in *HTATIP2* expression, while DAC-treated leader cells now expressed *HTATIP2* at levels equivalent to control-treated parental and follower cells (Fig. 2.7A). In contrast to *HTATIP2*, *MYO10* is highly expressed and has a hypomethylated promoter in leader cells

compared to parental and follower cells (Fig. 2.1, 2.4). Thus, we would expect that DAC treatment in leader cells would not change *MYO10* expression, since the promoter is already demethylated. However, DAC-treated leader cells showed a significant increase in *MYO10* expression compared to vehicle control-treated leader cells, while *MYO10* expression remained unchanged in parental and follower cells (Fig. 2.7B). In addition, we quantified HTATIP2 and MYO10 protein expression in these cells by Western blot, and changes in protein expression for both genes mirrored the changes in mRNA expression (Fig. 2.7C-E). Taken together, these data suggest that DNA hypermethylation in leader cells is critical for maintaining the leader cell invasive phenotype at least in part by transcriptionally silencing the tumor suppressor *HTATIP2,* and that nonspecific inhibition of DNA methylation can induce expression of HTATIP2 in leader cells.

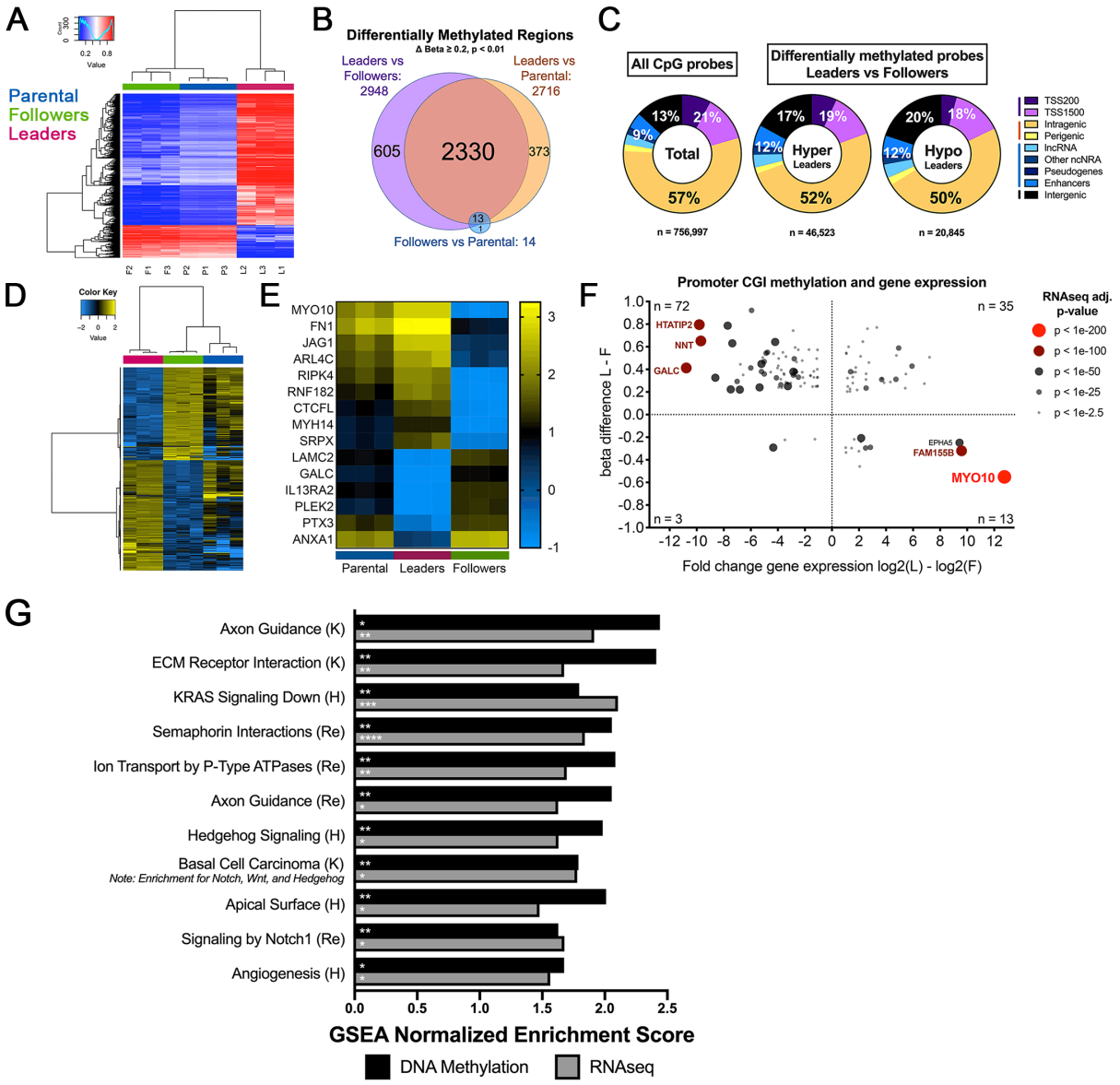


**Figure 2.1: Transcriptomic heterogeneity and DNA methylation heterogeneity between leader and follower cells reveals potential functional regulators of collective invasion.**

(**A**) Heatmap of beta values for the 5000 most differentially methylated CpG probes (DMPs) by variance across all samples from a MethylationEPIC DNA methylation array. Dendrograms represent unsupervised hierarchical clustering using Euclidean distance measures and complete-

link agglomerative clustering. (**B**) Venn diagram of differentially methylated regions (DMRs) between each pair of phenotypes with beta difference ≥ 0.2 and adjusted p-value < 0.01. (**C**) Annotation of DMPs across genomic features. All probes = all probes in MethylationEPIC array after filtering, N = 756,997 CpG probes. Hyper = probes with beta difference ≥ 0.2 and adjusted p-value < 0.01 in leaders compared to followers, N = 46,523 CpG probes. Hypo = probes with beta difference ≤ -0.2 and adjusted p-value < 0.01 in leaders compared to followers, N = 20,845 CpG probes. (**D-E**) Heatmaps of z-scores from log2 normalized RNAseq gene expression counts of most differentially expressed genes by variance across all samples based on DESeq differential expression analysis. (**D**) 98$^{th}$ percentile (499 genes) scaled by both row and column, unsupervised hierarchical clustering with Pearson distance measures and Ward's method of agglomerative hierarchical clustering. (**E**) Subset of the 15 most differentially expressed genes by variance, without clustering. (**F**) Scatter plot comparing promoter CpG island (CGI) methylation beta value differences and RNAseq log2 fold changes for all genes that are both differentially expressed (≥2-fold gene expression difference and differential expression adjusted p < 0.01) and differentially methylated at the CGI (≥0.2 difference for the mean beta value of all probes within the CGI) between leaders and followers. Size and color of dot indicate DESeq adjusted p-value for differential gene expression. **(G)** Bar plot of Gene Set Enrichment Analysis normalized enrichment scores (NES) for both differentially methylated (black bars) and differentially expressed (grey bars) gene sets enriched in leader cells compared to follower cells. H = MSigDB Hallmark gene set collection; K = KEGG Pathway Database, Re = Reactome Pathways Database. DNA methylation: Bonferroni-adjusted p-values: * p <0.05, ** p < 0.01. RNAseq: all adjusted p-values < 0.05, RNAseq FDR: * q < 0.25, ** q < 0.05, *** q < 0.01, **** q < 0.0001.

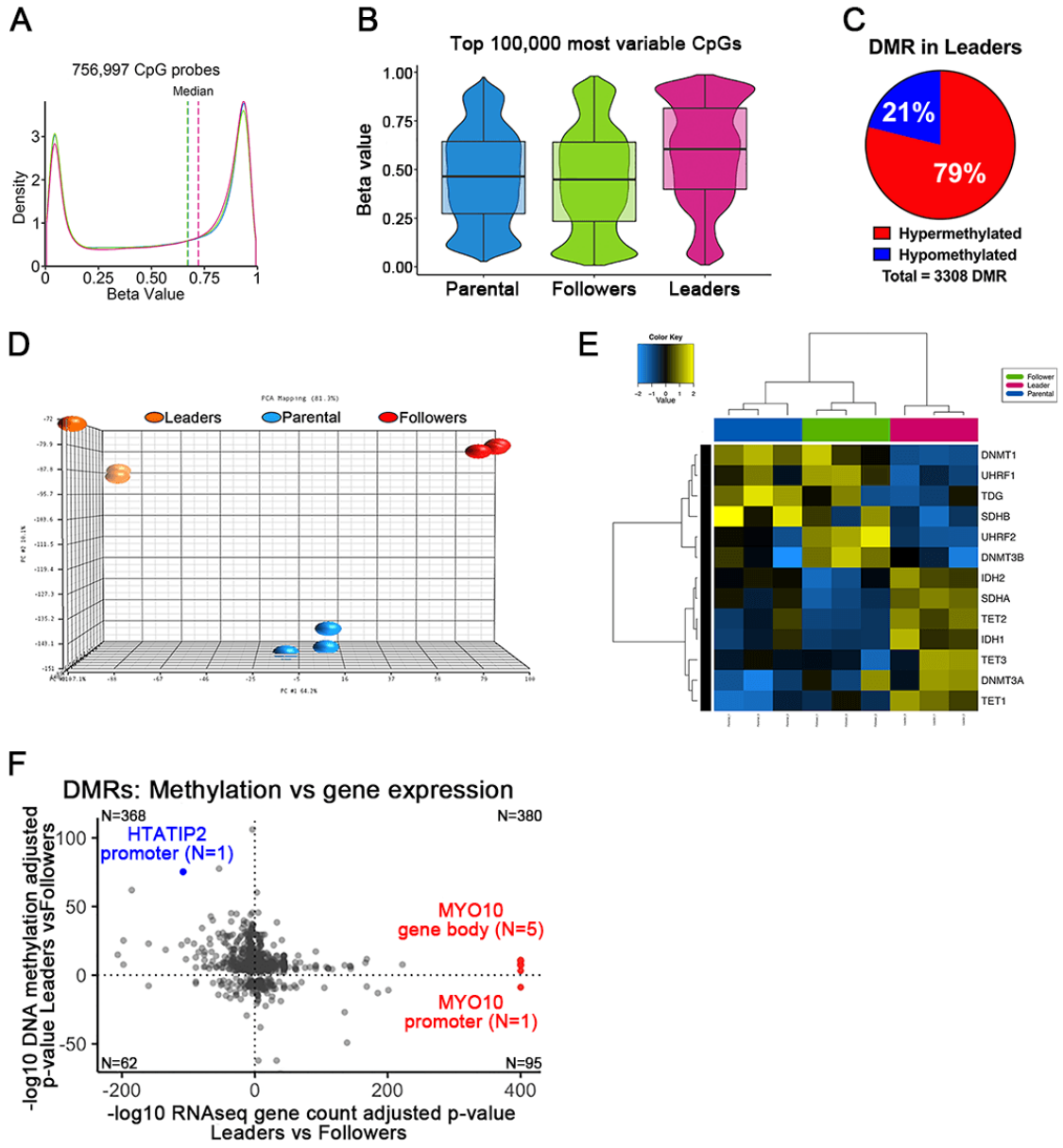


**Figure 2.2: Leader cells contain unique DNA methylation and gene expression compared to follower and parental cells.**

(**A**) Density plot of all 756,997 CpG probes after filtering. Vertical lines represent median beta value. Kruskal-Wallis rank sum test p-value < 2.2e-16. (**B**) Violin plot of beta values for the 100,000 most variable DMPs by variance across all samples. Box plot overlay represents the

median and interquartile range. (**C**) Pie chart of DMRs in (Figure 1B), hypermethylated or hypomethylated in leader cells compared to follower and parental cells. (**D**) Principal Component Analysis (PCA) of log2 normalized RNAseq gene counts. Leaders = orange, Parental = blue, Followers = red. (**E**) Heatmap of log2 normalized RNAseq gene counts (z-score scaled by column and row, Euclidean distance measure with Ward's agglomerative clustering method), showing selected genes that functionally regulate DNA methylation. (**F**) Starburst plot of 905 differentially methylated regions (DMRs) that overlap a gene or its promoter (1500 bp upstream of TSS) for leaders versus followers. n= indicates number of genes within that quadrant. -log10 adjusted p-values for both methylation and gene expression are transformed to indicate the direction of change; positive values indicate gene overexpression or DMR hypermethylation in leader cells compared to follower cells, and negative values indicate gene underexpression or DMR hypomethylation in leader cells compared to follower cells. DMR overlapping the HTATIP2 promoter is labeled in blue. DMRs overlapping the MYO10 gene body (N = 5) or MYO10 promoter (N = 1) are labeled in red.

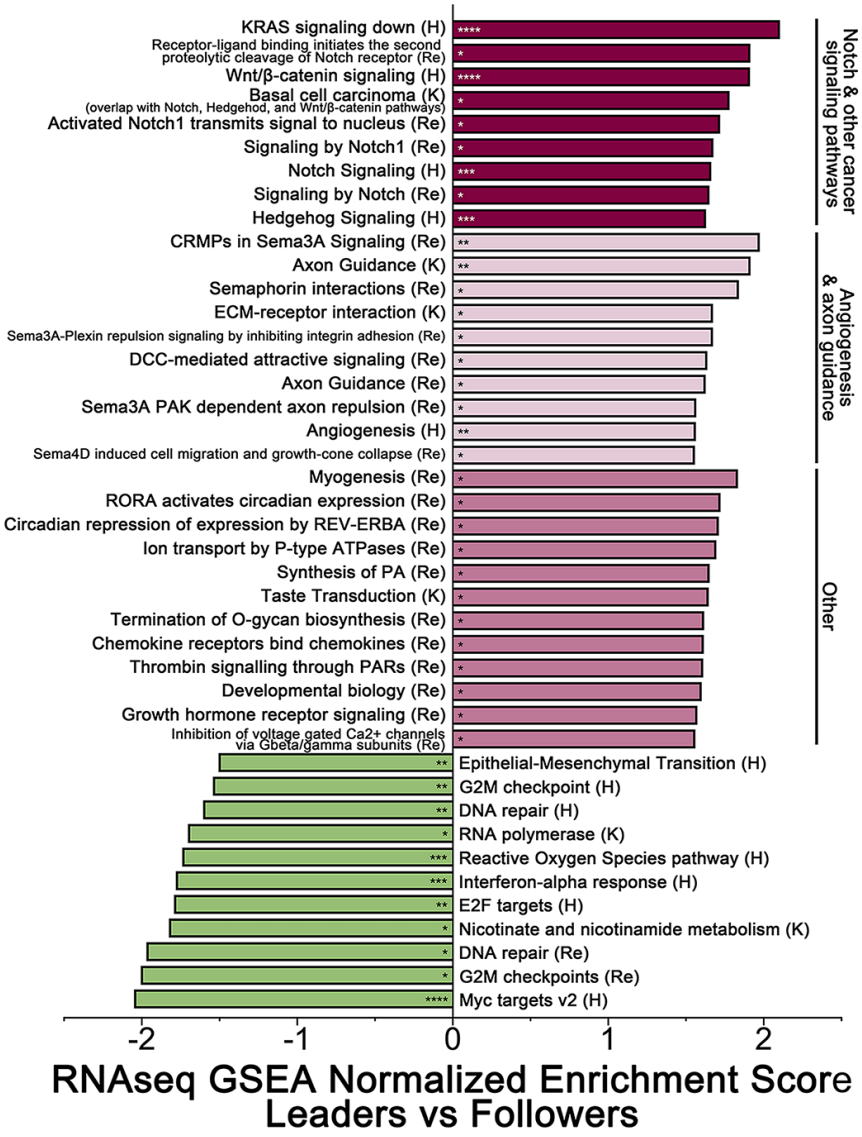


**Figure 2.3: RNAseq gene set enrichment analysis (GSEA) of leader and follower cells.**

Gene set enrichment analysis of RNAseq transcriptome data in leader and follower cells independent of DNA methylation analysis. A positive Normalized Enrichment Score (NES) indicates pathway enrichment in leader cells (pink bars); a negative NES indicates pathway enrichment in follower cells (green bars). H = MSigDB Hallmark gene set collection; K = KEGG Pathway Database, Re = Reactome Pathways Database. All $p < 0.05$; FDR: * $q < 0.25$, ** $q < 0.05$, *** $q < 0.01$, **** $q < 0.0001$.

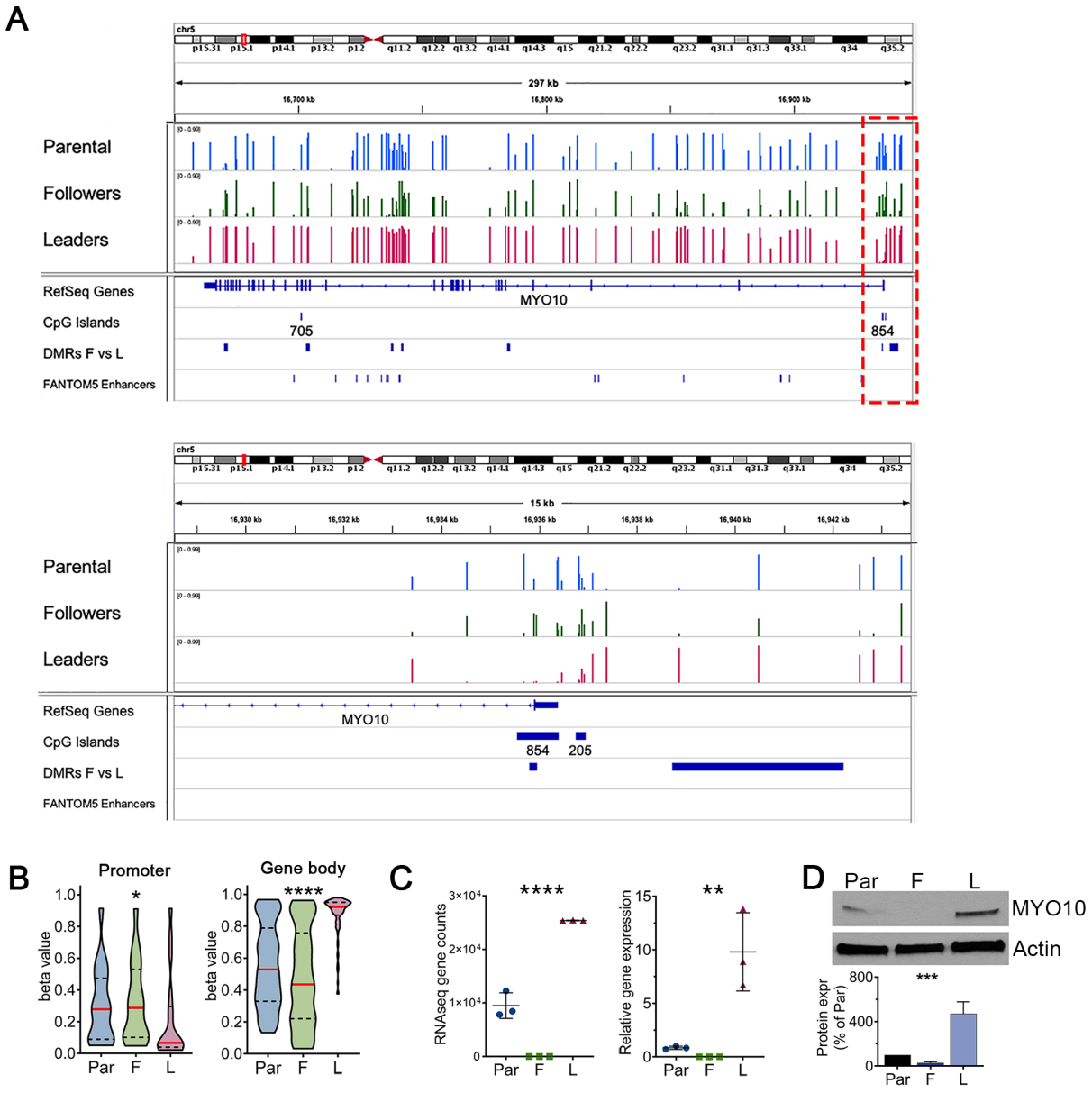


**Figure 2.4: *MYO10* is differentially methylated and overexpressed in leader cells.**

(**A**) Visualization of MethylationEPIC CpG probe methylation across parental, follower, and leader cells within *MYO10* and the surrounding genomic region using the Integrative Genomics Viewer (*197*). Each sample row (Parental in blue, Followers in green, Leaders in magenta) is the mean of three biological replicates, and vertical bars represents the beta value of each CpG probe (0-1 scale). (*Top*) View of a 297 kb region of Chr5p15.1 containing the full-length *Myo10* gene.

*Myo10* runs right-to-left 5' → 3'. Red box indicates zoom on the 15 kb region surrounding the TSS shown on the (*Bottom*). (**B**) Violin plots of beta values for all CpG probes within the MYO10 TS1500 promoter (left, N = 18 CpG probes) or the MYO10 gene body (right, N = 95 CpG probes) comparing parental (Par), follower (F), and leader (L) cells. Red line indicates the median, dashed black lines indicate the interquartile range. n = 3 biological replicates per cell type. Kruskal-Wallis test with Dunn's correction for multiple comparisons. (**C**) MYO10 mRNA expression measured by RNAseq gene counts (*left*) or by qPCR (*right*); n = 3 independent biological replicates per condition per assay. Ordinary one-way ANOVA with Tukey correction for multiple comparisons. (**D**) Western blot and quantification of protein levels in parental, follower, or leader cells for MYO10; actin as a loading control, n = 5 independent biological replicates per condition. *$p<0.05$, **$p<0.01$, ***$p<0.001$, ****$p<0.0001$.

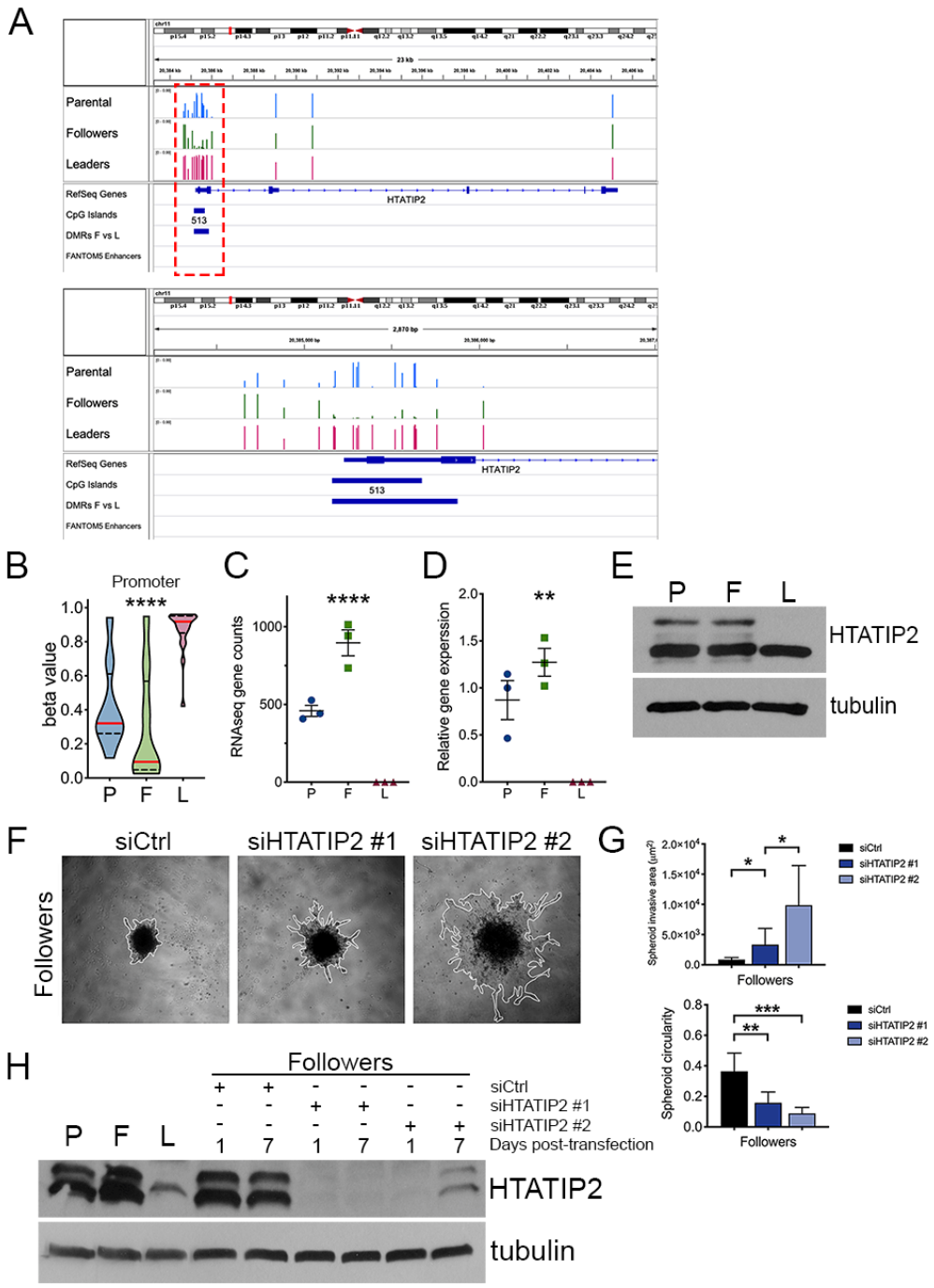


**Figure 2.5: HTATIP2 promoter methylation silences HTATIP2 expression in leader cells to promote collective invasion**

(**A**) Visualization of MethylationEPIC CpG probe methylation across parental, follower, and leader cells within *HTATIP2* and the surrounding genomic region using the Integrative Genomics

Viewer (*197*). Each sample row (Parental in blue, Followers in green, Leaders in magenta) is the mean of three biological replicates, and vertical bars represents the beta value of each CpG probe (0-1 scale). (*Top*) View of a 23 kb region of Chr11p15.1 containing the full-length *HTATIP2* gene. Red box indicates zoom on the 2.8 kb region surrounding the TSS shown on the (*Bottom*). (**B**) Violin plots of beta values for all CpG probes within the CpG island overlapping the HTATIP2 promoter (N = 20 CpG probes), comparing parental (P), follower (F), and leader (L) cells. Red line indicates the median, dashed black lines indicate the interquartile range. n = 3 biological replicates per cell type. Kruskal-Wallis test with Dunn's correction for multiple comparisons., (**C-D**) *HTATIP2* mRNA expression measured by RNAseq gene counts (**C**) or by qPCR (**D**); n = 3 independent biological replicates per condition per assay. Ordinary one-way ANOVA with Tukey correction for multiple comparisons. (**E**) Western blot in parental, follower, or leader cells for HTATIP2; tubulin as loading control, n = 2. (**F-G**) Representative images (**F**) and quantification (**G**) of 72h spheroid invasion assays in Matrigel of H1299 leaders expressing siCtrl or one of two *HTATIP2* siRNAs (siHTATIP2 #1 and siHTATIP2 #2). n = 2 biological replicates, N = 6 spheroids per condition per replicate. Kruskal-Wallis test with Dunn's correction for multiple comparisons. (**H**) Western blot in parental, follower, or leader cells, as well as siRNA knockdowns in follower cells. The number of days post-transfection (1 day or 7 days) and siRNA used (siCtrl, siHTATIP2 #1, or siHTATIP2 #2) are indicated above the blot. Tubulin as loading control. *p<0.05, **p<0.01, ***p<0.001, ****p<0.0001.

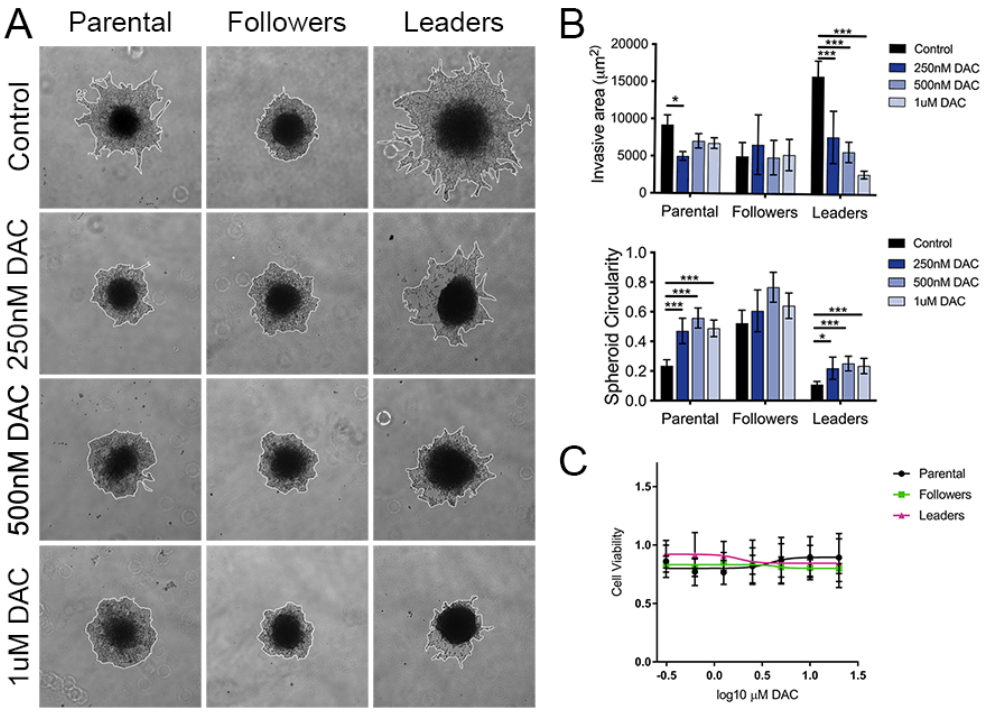


**Figure 2.6: Inhibition of DNA methylation with 5-aza-2'-deoxycytidine (DAC) abrogates leader cell-dependent collective invasion.**

**(A)** Images of spheroid invasion assays of H1299 parental, follower, and leader cells 24 hours after embedding into recombinant basement membrane. Cells treated with DAC or vehicle control (1:1 glacial acetic acid:$H_2O$) 72 hours before embedding. (B) Quantification of the invasive area and circularity of the spheroid invasion assays in (**A**). 2-way ANOVA with Sidak's multiple comparison test. n =3, N = 6 spheroids per condition per replicate. *p<0.05, ***p<0.001. (**C**) SRB cell viability assay, 72 hours after treatment with vehicle control or DAC at final concentrations from 0.3µM to 20µM. Error bars represent mean ± s.e.m. $IC_{50}$ not achieved at any tested dose of DAC. n = 3 biologically independent replicates.

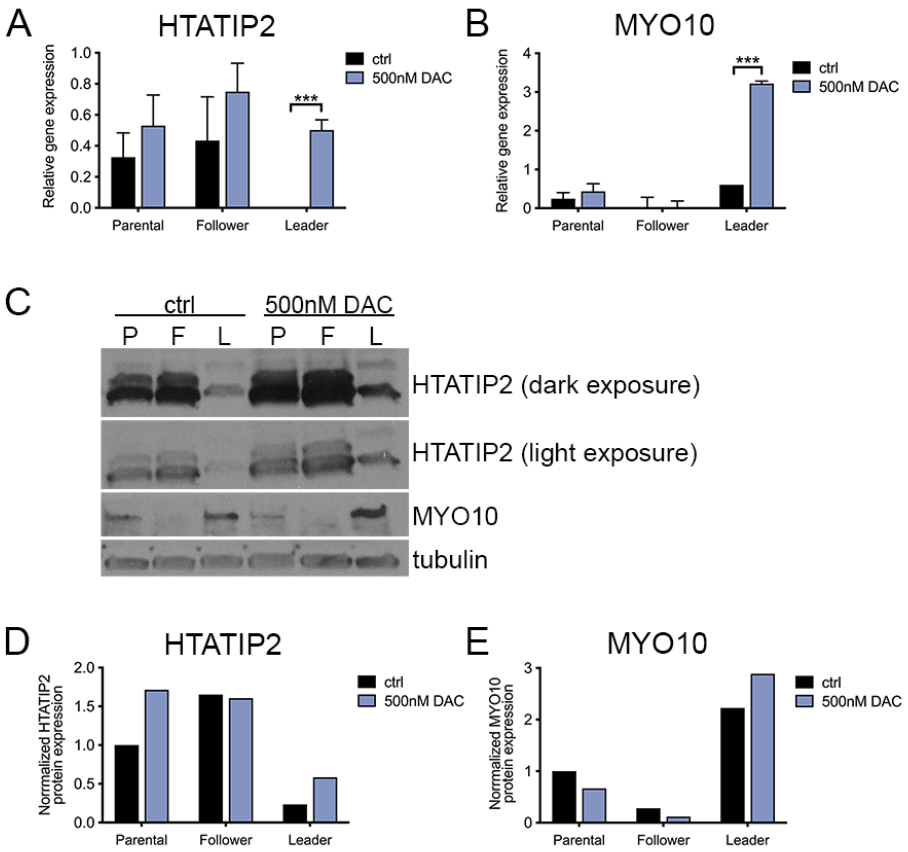


**Figure 2.7: Inhibition of DNA methylation by DAC increases expression of *HTATIP2* and *MYO10* in leader cells.**

(**A-B**) qPCR of *HTATIP2* relative mRNA expression (**A**) or MYO10 relative gene expression (**B**) in H1299 parental, follower, and leader cells 48h after treatment with 500nM DAC or vehicle control. *TUBA1A* (α-tubulin) mRNA expression as control. 2-way ANOVA with Sidak's multiple comparisons test. n = 3 independent biological replicates. (**C**) Western blot of HTATIP2 and MYO10 protein expression in H1299 parental, follower, and leader cells 48h after treatment with 500nM DAC or vehicle control. α-tubulin expression as control. n = 1 biological replicate. (**D**-**E**) Densitometry quantification of HTATIP2 and MYO10 expression normalized to α-tubulin (control) expression from the Western blot in (**C**). ***p<0.001

## 2.6 Discussion

Intratumor heterogeneity drives tumor progression and metastasis, but the epigenetic contribution to this heterogeneity remains largely unknown. Here, we found that lung cancer leader cells are a distinct cell population with unique patterns of both DNA methylation and gene expression, compared to follower cells and the parental population (Fig. 2.1-2.3). DNA methylation patterns that differed in leader cells compared to follower cells and parental cells correlated with a gene expression program enriched for pathways that drive collective invasion; these pathways included Notch signaling, angiogenesis, and cell-ECM interactions (*32, 50, 51, 112, 172, 183*) (Fig. 2.1, 2.3). In contrast, follower cells and the parental population had nearly identical DNA methylation patterns despite maintaining differences in gene expression (Fig. 2.1-2.3). Together, these data suggest that the leader cell phenotype is characterized by a distinct epigenome, providing the first evidence of heritable epigenetic rewiring that differentiates leader and follower cells beyond gene expression alone.

In addition to broad genome-wide shifts in DNA methylation within leader cells, we identified several genes of interest whose expression in leader cells may be regulated by DNA methylation at the promoter (Fig. 2.1F). Here, we identified the genes *MYO10* and *HTATIP2* as two of the genes with the most significant differences in both promoter methylation and gene expression; *MYO10* is both highly expressed and is hypomethylated at the promoter in leader cells compared to follower cells, while *HTATIP2* is not expressed in leader cells and contains a hypermethylated promoter compared to follower cells (Fig. 2.4-2.5). Functionally, both MYO10 and HTATIP2 perform functions that are necessary for collective invasion. A more substantial analysis of MYO10 functions during collective invasion will be presented in Chapters 3 and 4 of this dissertation. However, HTATIP2 is a known tumor suppressor gene that is frequently mutated,

deleted, or epigenetically silenced in several highly invasive cancer types (*189, 192, 193, 198, 199*). Our data supports the theory that HTATIP2 is a putative metastasis suppressor, in that siRNA silencing of HTATIP2 in follower cells increased spheroid collective invasion (Fig. 2.5F-H). HTATIP2 regulates nuclear import and transcriptional activity, and while the downstream effectors of HTATIP2 are not yet fully known, it is logical that a transcriptional regulator such as HTATIP2 could significantly impact the shifts in gene expression necessary for driving the follower or leader cell phenotypes. While MYO10 and HTATIP2 are only two of many genes of interest within our leader and follower cells, our analysis of these two genes show that shifts in DNA methylation between leader and follower cells has functional consequences for collective invasion.

Looking beyond changes in DNA methylation in these discrete loci, leader cells showed a genome-wide shift towards DNA hypermethylation. Leader cells were significantly hypermethylated or hypomethylated at over 67,000 CpG sites across the genome compared to follower cells, resulting in a 10% increase in the median beta value across all CpG probes in leader cells (Fig. 2.1C, 2.2A). Although the majority of these DMPs were within promoter regions or intragenic regions, approximately 30% of DMPs were within the sequences of enhancers, non-coding RNAs; since only 21% of the CpG probes within this array localize to these non-coding regions, then it can be inferred that hypermethylation or hypomethylation in leader cells occurs disproportionately in non-coding regions (Fig. 2.1C). DNA methylation at distal regulatory elements is still poorly understood, but these data raise the intriguing question as to whether DNA methylation in leader cells within distal regulatory elements and intergenic regions plays a role in regulating leader cell gene expression. In order to evaluate DNA methylation within non-coding regions and non-annotated intergenic regions, bisulfite sequencing could be utilized to provide true

genome-wide analysis of DNA methylation beyond the subset of CpG sites sampled in the MethylationEpic 850K array.

Since leader cells showed an overall shift towards DNA hypermethylation, we hypothesized that this increase in DNA methylation was a necessary component of leader cell transcriptional regulation, and that consequently, leader cells would be more sensitive to the inhibition of DNA methylation. Although there are not currently any methods to reliably reduce DNA methylation at specific loci, there are several clinically-utilized inhibitors of DNA methyltransferases (DNMTs) (*77, 81*). These inhibitors act as mimetics of cysteine and are incorporated into nascent DNA during DNA replication, wherein they permanently bind to DNMTs to inhibit these proteins from adding 5mC to the nascent DNA strand (*81*). When parental, follower, and leader cells were treated with the DNMT inhibitor DAC, leader cell spheroids and parental cell spheroids significantly decreased collective invasion, while all three cell types treated with DAC showed approximately 90% viability across a wide range of doses compared to treatment with the vehicle control (Fig. 2.6). While we did not confirm that DAC decreased the overall levels of DNA methylation in these cells, increased expression of *HTATIP2* and *MYO10* after DAC treatment suggested that DAC had induced changes in gene expression through reduced promoter DNA methylation (Fig. 2.7).

Interestingly, while leader-specific shifts in DNA methylation and gene expression (*e.g.* high expression of *MYO10* and no expression of *HTATIP2*) were significant within an isolated leader cell population compared to follower or parental cells, these patterns could not be detected in the parental cell population when pooled. However, heterogeneous protein expression was detected in single cells within the parental population by flow cytometry. The parental population contained a small percentage of leader cells (*112, 114*); patient tumors likely also contain similar

rare but genetically- or epigenetically-distinct cell populations that cannot be detected by bulk analysis of the whole tumor. Thus, we hypothesize that such rare tumor cell subpopulations might only be detected in patients using single-cell analysis techniques. Further improving and integrating single-cell technologies into clinical use will be critical for identifying those rare but functionally distinct tumor subpopulations driven by epigenetic heterogeneity, such as leader cells or cancer stem cells. In addition, we anticipate differences between leader and follower cell subpopulations in other epigenetic mechanisms that influence chromatin states and transcriptional regulation beyond DNA methylation. Continued exploration of intratumor genetic and epigenetic heterogeneity will be crucial for fully understanding tumor clonal evolution and its relationship to collective invasion.

# Chapter 3: MYO10 directs collective invasion through filopodia-driven fibronectin micropatterning by leader cells

## 3.1 Author's Contribution and Acknowledgement of Reproduction

Portions of this chapter, including Figures 1-9, 11-14, & 16, were reproduced with edits from: E.R. Summerbell*, J.K. Mouw*, J.S.K. Bell, C.M. Knippler, B. Pedro, J. Arnst, T.O. Khatib, R. Commander, J. Konen, B.G. Barwick, B. Dwivedi, J. Kowalski, P. Vertino, A.I. Marcus. Epigenetically heterogeneous tumor cells direct collective invasion through filopodia-driven fibronectin micropatterning. *Science Advances*. 2020; **6**: eaaz6197.

E.R.S., J.K.M., P.V., and A.I.M. designed the experiments. E.R.S., J.K.M., J.L.A., C.M.K., B.P., B.G.B., T.O.K., and J.Konen performed the experiments; E.R.S. performed the experiments in Figures 1-3, 9-15, and portions of the experiments in Figures 4-8. E.R.S., J.S.K.B., B.G.B., B.D., S.S., and J.Kowalski contributed to the bioinformatics and statistical analysis of the genomics and epigenomics data. E.R.S., J.K.M., and R.C. drafted the manuscript. All authors provided input and feedback during manuscript preparation and edited the manuscript.

## 3.2 Abstract

Tumor heterogeneity drives disease progression, treatment resistance, and patient relapse, yet remains largely under-explored in invasion and metastasis. Here, we investigated heterogeneity within collective cancer invasion by integrating DNA methylation and gene expression analysis in rare purified lung cancer leader and follower cells. Our results showed global DNA methylation rewiring in leader cells and revealed the filopodial motor MYO10 as a critical gene at the intersection of epigenetic heterogeneity and 3D collective invasion. We further identified JAG1 signaling as a novel upstream activator of MYO10 expression in leader cells. Using 3D live cell imaging, we discovered that MYO10 drives filopodial persistence necessary for micropatterning extracellular fibronectin into linear tracks at the edge of 3D collective invasion exclusively in leaders. We further show that filopodia-directed FN alignment is dependent upon the MYO10 cargo protein integrin β1. Our data fit a model where epigenetic heterogeneity and JAG1/Notch signaling jointly drive collective cancer invasion through MYO10 upregulation in epigenetically permissive leader cells, which induces filopodia dynamics and long-term stability necessary for linearized fibronectin micropatterning.

### 3.3 Introduction

Tumor heterogeneity drives disease progression and treatment resistance, yet most cancer research and therapy decisions are carried out at the whole-population level (*97, 170*). The polyclonal nature of metastatic lesions suggests they originate from heterogeneous clusters of collectively invading cells, rather than clonally from singular disseminated cells (*50, 171, 172*). During the initial steps of tumor invasion, many solid tumors of epithelial origin rely on collective invasion, in which packs of cells invade into the adjacent stroma while maintaining cell-cell contacts (*44, 105*). Collective invasion packs correlate with higher histologic tumor grade and increased metastatic potential, demonstrating the importance of understanding how intratumoral heterogeneity propagates invasion and metastasis (*44, 48, 173*). Nevertheless, the molecular mechanisms underlying the formation and function of heterogeneous collective invasion packs remain poorly understood.

Heterogeneous collective invasion packs can contain phenotypically-distinct invasive "leader" and noninvasive "follower" cell populations (*45, 105, 107, 112, 114*). Although the specific markers of leader and follower cells may vary based on the tissue of origin, effective cooperation between leader and follower subpopulations invariably promotes the survival and invasion of collectively invading cancer cells (*105, 112*). Cooperation between leader and follower cells frequently necessitates hijacking developmental cell-cell signaling pathways, including the Notch pathway and VEGF-dependent non-canonical angiogenic mimicry (*174*). Despite a growing understanding of the underlying genetic and transcriptomic differences between tumor subpopulations, little is known about the epigenetic factors that underlie heterogeneous phenotype determination and plasticity within the collective invasion pack.

We sought to utilize epigenetic heterogeneity to identify key regulators of phenotypic heterogeneity, cell-cell cooperation, and collective tumor invasion. To do this, we integrated DNA methylation array data with RNAseq expression data on purified populations of lung cancer leader and follower cells. We found vast rewiring of the DNA methylome and transcriptome unique to leader cells compared with follower cells or the parental population, including significant enrichment for differential DNA methylation and gene expression across several pathways that fundamentally regulate multicellular collective invasion. Integration of DNA methylation and transcriptome data identified the filopodia protein MYO10 at the intersection of epigenetic regulation and collective cancer cell invasion in leader cells. Filopodia are thin finger-like membrane protrusions at the periphery of cells that critically support cell adhesion, migration, invasion, and extracellular mechanosensing in both normal physiology and in cancer (*132*). As a filopodial motor protein that localizes to filopodia tips, MYO10 drives filopodial maintenance and function by transporting key cargo to filopodia tips, including integrins and actin anti-capping proteins (*144, 148, 150*). Since MYO10 was binarily expressed only in our leader cells, we sought to determine if MYO10 serves a previously unrecognized leader cell-specific role of both MYO10 and filopodia during collective invasion. In summary, we demonstrate that lung cancer collective invasion is facilitated by DNA methylation heterogeneity and JAG1 activity that jointly drive MYO10 overexpression and localization to the tips of filopodia within specialized leader cells, which allows stable leader cell filopodia to actively guide linear FN micropatterning and induce 3D collective cell invasion.

## 3.4 Methods

### Cell culture conditions

H1299, H23, H1792, H1975, and A549 human NSCLC cells (ATCC, Manassas, VA) were cultured in Roswell Park Memorial Institute (RPMI-1640) media supplemented with 10% fetal bovine serum and 100 units $ml^{-1}$ of penicillin/streptomycin and maintained at 37°C and 5% $CO_2$. HEK 293T cells (ATCC, Manassas, VA) were maintained in Dulbecco's Modified Eagle's Media (DMEM) supplemented with 10% fetal bovine serum and 100 units mL-1 of penicillin/streptomycin at 37°C and 5% $CO_2$. Leader and follower cell subpopulations were isolated from H1299 cells transfected with Dendra2 via SaGA as previously described (*112*). Briefly, H1299 cells were transfected with plasma-membrane targeted Dendra2, a photoconvertible fluorophore, allowing for visualization of individual cells during imaging. Prior to photoconversion, all cells have green fluorescence (maximum excitation 490, maximum emission 507); upon excitation with a 405 laser, the Dendra2 within the selected cell is photoconverted to emit red fluorescence (maximum excitation 553, maximum emission 573). During 3D invasion, singular leader cells or groups of follower cells were photoconverted separately without any measurable fluorescence conversion in neighboring cells. Subsequently, the cells were extracted from the 3D matrices and sorted out using flow cytometry. All primary cells and cell lines were authenticated by ATCC (where applicable), or by analysis of morphological and phenotypic characteristics as well as gene and protein expression. No cell lines used in this study were found in the database of commonly misidentified cell lines that is maintained by ICLAC and NCBI Biosample. All primary cells and cell lines were tested for mycoplasma contamination using a commercially available kit (PCR-Mycoplasma Test Kit I/C,

Promokine PK-CA91-1024), according to the manufacturer's instructions, at the onset of the work (tested negative) and have never exhibited contamination symptoms after initial testing.

**NSCLC patient-derived cell line**

All tissue samples were procured by the Human Tissue Procurement Service shared resource at the Winship Cancer Institute of Emory University in accordance with the approved IRB protocol. Tissues were digested for 3h in digestion buffer (DMEM/F-12 supplemented with 10mM HEPES, 2% BSA, 1x ITS, 0.5µg/ml hydrocortisone, 1x Normocin) containing 2 mg/ml Type 3 Collagenase (Worthington), 100 U/ml Hyaluronidase (Sigma) at 37°C until fully digested. Cells were pelleted for 5 min at 300xg, re-suspended in red blood cell lysis buffer (Abcam) to lyse red blood cells, and pelleted again. Cells were then re-suspended in digestion buffer containing 200µg/ml DNase 1 (Sigma) and incubated 10 min at 37°C. After DNase digestion, cells were pelleted, re-suspended in media and plated. Cells were grown in modified M87 media containing 2% FBS (*200*). The presence of the NSCLC-marker TTF1 (EP1584Y)(1:50, Abcam), and pan cytokeratin (clone PCK-26)(1:300, Abcam) as well as the absence of the fibroblast marker, S100A4 (EPR2761) (1:100, Abcam), were used to verify the purity of these lines(*201*).

**Plasmids, transfections and transductions**

Derivative cells were transfected using Lipofectamine 3000 (Thermo Fisher, Waltham, MA), per the manufacturer's instructions, or transduced using lentiviral supernatants derived from HEK 293T cells using the psPAX2-PMD2.G system. The $p^{CMV}$LifeAct-TagRFP plasmid was obtained from Ibidi (Gräfelfing, Germany; 60102). The gd2PAL-Dendra2 plasmid was obtained from Dr. Gary Bassell (Emory University) and transfected into H1299 cells as previously described (*112*).

The GFP-MYO10 and mCherry-MYO10 constructs were a kind gift from Dr. Richard Cheney (UNC Chapel Hill) (*154*). The human JAG1 shRNA (HSH004470-LVRU6P) and ORF (EX-M0722-Lv105-B) constructs were purchased from GeneCopoeia (Rockville, MD). The human MYO10 siRNA constructs (Silencer Select siRNA s9224 and s9225) were purchased from Thermo Fisher (Waltham, MA).

**Reagents and antibodies**

*Primary and secondary antibodies for immunoblotting:* MYO10 (Novus Biologicals, NBP1-87748) was used at 1:2000. JAG1 (Cell Signaling, 70109) was used at 1:2000. IL13RA2 (Abcam, ab55275) was used at 1:2000. Cleaved Notch1 (Val1744)(Cell Signaling, 4147) was used at 1:2000. α-tubulin (Millipore, MAB1864) was used at 1:5000. Actin (Sigma A2066) was used at 1:5000. Gapdh (Cell Signaling, 2118) was used at 1:5000. Peroxidase AffiniPure Goat Anti-Mouse IgG (H+L)(Jackson ImmunoResearch, 115-035-003) was used at 1:10,000. Peroxidase AffiniPure Goat Anti-Rabbit IgG (H+L)(Jackson ImmunoResearch, 111-035-144) was used at 1:10,000. Peroxidase AffiniPure Goat Anti-Rat IgG (H+L)(Jackson ImmunoResearch, 112-035-003) was used at 1:10,000.

*Primary and secondary antibodies and reagents for immunostaining*: MYO10 (Novus Biologicals, NBP1-87748) was used at 1:1000. JAG1 (Cell Signaling, 70109) was used at 1:1000. FN1 (Abcam, ab6328) was used at 1:1000. 4′,6-Diamidine-2′-phenylindole dihydrochloride (DAPI)(Sigma, D9542) was used as a nuclear counterstain at 300nM. Phalloidin-488 (Thermo Fisher, A12379) or Phalloidin-635 (Thermo Fisher, A34054) was dissolved in methanol and used at 1:100. Rhodamine-fibronectin (Cytoskeleton, FNR01) was used at 1:50, mixed with rBM. JAG1 antibody used for blocking (Sino Biological,1164-MMO3) was used at 100 ng/mL. Integrin-β1

antibody used for blocking (Abcam, ab24693) was used at 50 ng/mL. Integrin-αVβ3 antibody used for blocking (Abcam, ab78289) was used at 50 ng/mL. The following IgG Highly Cross-Adsorbed secondary antibodies were each used at 1:1000: Goat anti-mouse Alexa Fluor 568 (Invitrogen, A11031), Goat anti-mouse Alexa Fluor 647 (Invitrogen, A21235), Goat anti-rabbit Alexa Fluor 568 (Invitrogen, A11036), Goat anti-rabbit Alexa Fluor 647 (Invitrogen, A21245).

*Fluorophore-conjugated primary antibodies for fluorescence-activated cell sorting*: JAG1-PE (Sino Biological, 11648-MM03-P) was used at 5uL per 100uL, and IL13RA2-APC (Miltenyi Biotec, 130-104-505) was used at 2uL per 100uL.

**DNA methylation microarray and quantitative PCR**

DNA methylation status was assessed in triplicate on H1299 parental, leader and follower cells. For parental cells, three different passages were used. For follower cells, three separately-isolated populations were used. For leader cells, two separately-isolated populations were used: one passage of one population, and two passages of the other. Cells were grown to 70% confluency then trypsinized and homogenized using QIAshredder (Qiagen, 79654; Hilden, Germany). DNA and RNA were isolated in tandem using the AllPrep DNA/RNA Mini Kit (Qiagen, 80204). Fluorescent DNA quantification was performed using the Quant-iT dsDNA broad range assay (Invitrogen, Q33130; Carlsbad, CA). Quality was assessed on a 2% agarose gel. 500 ng of DNA was bisulfite converted using the Zymo EZ-96 DNA Methylation Kit using the protocol suggested by the Illumina Infinium Methylation guide (Illumina, 150191519; San Diego, CA). The bisulfite-converted DNA was then used with the Illumina Infinium HD Methylation Assay in a whole genome amplification (WGA). After WGA, the DNA was fragmented, precipitated, resuspended,

and hybridized to the Illumina MethylationEPIC BeadChip array (Illumina, WG-317-1001), which was then washed to remove any unbound DNA. The bound DNA underwent extension and staining according to the manufacturer protocol. The BeadChip was then coated and scanned on the Illumina HiScan to obtain the raw data.

Array data were processed and analyzed in R using the package ChAMP (*176*). Probe data were filtered according to the standard ChAMP settings, with the exception of not filtering out probes on the X and Y chromosomes. Beta values were normalized using the BMIQ method and standard settings. Differentially methylated probes (DMPs) were determined using the champ.DMP() command, which calculates Benjamini-Hochberg adjusted p-values using the limma package . DMPs with a beta difference > 0.2 and an adjusted p-value < 0.05 were considered significant. Differentially methylated regions (DMRs) were determined using the champ.DMR() command, utilizing the ProbeLasso algorithm with a minimum DMR size of 50 bp and a minimum of 2 probes. DMRs with a beta difference > 0.2 and an adjusted p-value < 0.05 were considered significant. Overlaps of DMPs or DMRs with genomic features was performed using the GenomicRanges package. Gene set enrichment analysis of DMPs was performed using the methylGSA package, using the methylRRA method and standard settings (*177*). Bonferroni adjusted p-values < 0.05 were considered significant. Gene sets used for enrichment analysis included the Molecular Signatures Database (MSigDB v6.2) Hallmark gene set collection, KEGG Pathway Database, and Reactome Pathway Database. DMPs were annotated based on their relationship with GenCode (V27, hg19) transcripts with the following hierarchy: 1) CpG within a protein-coding TSS (TSS200 and TSS1500); 2) within a protein-coding gene (intergenic); 3) within 2kb of a protein-coding gene (perigenic); 4) lncRNA; 5) other ncRNA (miRNA, rRNA,

scRNA, snRNA, snoRNA, ribozyme, sRNA, antisense RNA, or scaRNA); 6) pseudogenes. All other CpG were considered intergenic. CpG islands (CGI) were defined according to UCSC hg19.

DNA methylation was also quantified using the methyl-sensitive HpaII enzyme to digest unmethylated CCGG motifs as previously described (*202*). Briefly, DNA was aliquoted into three equal portions of 500ng for mock, HpaII (40 units; NEB R0171S), and MspI (40 units; NEB R0106S) digestion reactions with CutSmart Buffer (NEB) which were performed overnight at 37°C in a T100 thermal cycler (BioRad). Quantitative PCR primers were designed to span one CCGG site and used to quantify the DNA in each reaction. Here, the mock-digested DNA was used to quantify the total amount of DNA, the HpaII-digested reaction represents the methylated fraction of DNA, and the methyl-insensitive isoschizomer MspI serves as a digestion / negative control. DNA methylation levels were quantified as the ratio of HpaII-digested material to mock-digested material. Primer sequences for all qPCR reactions are: MYO10 forward (TGAGACGCTCGCATTTTCTA) and MYO10 reverse (CAGGGCCTCCGTTTTCTTAC).

**RNA-sequencing and Gene Set Enrichment Analysis**

RNA-sequencing was performed in triplicate on H1299 parental, leader, and follower cells. RNA library preparation and sequencing were performed by the Emory Integrated Genomics Core and Omega Bio-Tek, Inc. as previously described (*114*). Data processing, read alignment, quality control, and statistical analyses were performed by the Emory Biostatistics and Bioinformatics Shared Resource as previously described (*114*). RNAseq expression raw counts for human hg19 RefSeq annotated genes were measured using HTSeq v0.6.1 (*178*). Count normalization and pairwise differential analysis was determined using DESeq (*179*), which uses a negative binomial distribution statistic with a Benjamini-Hochberg-corrected false discovery rate. Data was

log2(normalized count+1) transformed for all downstream analysis. Unsupervised hierarchical clustering and the resulting heatmaps were created using NOJAH (*180*).

Gene Set Enrichment Analysis (*181*) javaGSEA desktop application was used to identify gene expression profiles that were enriched in either leader or follower cells. Gene sets were selected from the Molecular Signatures Database (MSigDB v6.2), including the Hallmark gene set collection, KEGG Pathway Database, and Reactome Pathway Database. Enrichment scores were calculated using a weighted signal-to-noise ratio with 1000 permutations and randomization by gene set to account for a small sample size (N=3 for each cell type. Gene sets were considered significantly enriched in either leaders or followers with a normalized enrichment score (NES) > 1.5, a nominal p-value < 0.05, and an FDR q-value < 0.25.

**3-D invasion assays, spheroid microscopy and image analysis**

Spheroids were generated as previously described (*112*) and embedded in Matrigel recombinant basement membrane (Corning, 356237). Images were taken using an Olympus CKX41 microscope with an Infinity 1-3C camera (×4 air, 0.13 NA, UPlanFL N). For mixed population spheroid experiments, cells were plated together in low-adhesion wells at the indicated ratios with 3000 total cells per spheroid. Invasive area and spheroid circularity were measured using ImageJ as previously described (*112*).

**Quantitative PCR**

Quantitative real-time PCR was performed in triplicate with iTaq Universal SYBR Green Supermix (BioRad, catalogue no1725121) using a CFX96 real-time PCR detection system (BioRad), and the relative amount of complementary DNA was calculated using a standard

dilution curve, based on human GAPDH mRNA or human tubulin mRNA. Primer sequences for all qPCR reactions are: MYO10 forward (TGAGAGGGAGCTGCTCTTTG), MYO10 reverse (GTCGTGCTGTAGCGCTTCTTC), JAG1 forward (GGCAACACCTTCAACCTCAAG), JAG1 reverse (TGATCATGCCCGAGTGAGAAG), GAPDH forward (GGTGGTCTCCTCTGACTTCAACA), GAPDH reverse (GTTGCTGTAGCCAAATTCGTTGT), tubulin forward (CTTCGGCCAGATCTTCAGAC), tubulin reverse (AGAGAGTGGGTCAGCTGGAA).

**Immunoblotting and immunostaining**

For immunoblotting, total cellular protein expression was assessed via western blotting. Briefly, adherent cells were rinsed twice with 1X PBS containing Ca2+ and Mg2+ and lysed with 2% SDS lysis buffer (50mM Tris pH 8.0, 2% SDS, 100mM NaCl, 50mM DTT) supplemented with Halt Protease and Phosphatase Inhibitor Cocktail (Thermo Fisher, 78442). Samples were subsequently sonicated briefly to shear the DNA and reduce lysate viscosity. Sample protein content was quantified using a BCA protein assay kit (Thermo Fisher, 23225) prior to SDS-PAGE.

For immunostaining, cells in 2D or spheroids embedded in rBM were rinsed twice with 1X PBS containing calcium and magnesium pre-warmed to 37°C and then immediately fixed with paraformaldehyde and glutaraldehyde (1X PBS containing calcium and magnesium with added 2% PFA and 0.001% glutaraldehyde; freshly prepared and warmed to 37°C) for 20 minutes at room temperature. For immunofluorescence staining, permeabilization, three glycine rinses, blocking, and antibody staining were performed as previously described (*203*). After primary and secondary antibody staining, cells in 2D or 3D spheroids were imaged with the Leica TCS SP8 inverted confocal microscope (×20 air HC PL APO CS2, 0.75 NA; ×40 oil HC PL APO CS2, 1.30

NA; ×63 oil HC PL APO CS2, 1.40 NA) using 1mm stack intervals for ×20 objective or 0.3 mm z-stack intervals for all other objectives, line scanning (405 nm DMOD Flexible, 488 nm argon, 561 nm DPSS, 633 nm Helium-Neon), 2x line averaging, and both Hyd GaAsP detectors and PMT detectors.

**Live cell imaging**

Cells were plated into cell culture dishes with optical glass bottoms, or spheroids were embedded in rBM as previously described (*112*) and then imaged using the Leica TCS SP8 inverted confocal microscope (×20 air HC PL APO CS2, 0.75 NA; ×40 oil HC PL APO CS2, 1.30 NA; ×63 oil HC PL APO CS2, 1.40 NA; ×100 oil HC PL APO CS2, 1.40 NA) with live cell chamber (37°C and 5% $CO_2$). using 1mm stack intervals for ×20 objective or 0.3 mm z-stack intervals for all other objectives, line scanning using a resonant galvanometric tandem scanner (8kHz; 488 nm argon, 561 nm DPSS, 633 nm Helium-Neon), 8x line averaging, and Hyd GaAsP detectors. For LifeAct-RFP imaging of filopodia dynamics in 2D, images were acquired with the ×100 objective every second for 10 minutes. For cell migration tracking in 2D, images were acquired with the ×20 objective every 5 minutes for 16 hours. For imaging of filopodia dynamics and rhodamine-fibronectin fibrillogenesis during 3D spheroid collective invasion, images were acquired with the ×63 objective every 30 seconds for approximately 1-2 hours.

**Image analysis**

Spheroid invasive area and circularity (an indirect measure of sheet-like invasion) were measured using ImageJ as previously described (*112*) . For immunofluorescence, all 3D images (x,y,z) were flattened to 2D maximum projections (x,y) using ImageJ in order to increase the intensity of dim

spheroid branches or fine filopodial structures. The maximum and minimum pixel values for each channel were thresholded to the same 8-bit values for all images within the same experiment. For 2D cell migration assays, quantification of cell migration was done using Volocity imaging software. For analysis of filopodia length in fixed 3D samples, filopodia length was manually quantified using ImageJ software. For analysis of filopodia dynamics during live 3D collective cell invasion, filopodia were manually tracked using ImageJ software.

*Analysis of the localization of Dendra2, GFP-MYO10, and rhodamine-FN along filopodia during 3D collective cell invasion:* The 4D imaged (x,y,z,t) were reduced to a 3D maximum projection (x,y,t) in order to increase the visibility of filopodia and nascent FN puncta. Quantification was performed on the time point where the nascent FN puncta was first visible. For each filopodium, a line (width = 3 pixels) was drawn on top of the filopodia from tip to base, and a line plot profile was created for each separated channel (Analyze>Plot Profile). The peak of the rhodamine-FN puncta and the peak of GFP-MYO10 were defined as the point along the line with the highest pixel intensity. Before analysis, the correct localization of the FN nascent puncta and the end of the filopodia were each visually confirmed by examining several frames before and after the time frame represented in the line plot.

*Quantification of extracellular fibronectin area:* All image analysis was performed in ImageJ. 3D images (x, y, z) were flattened to 2D maximum projections (x, y). The phalloidin channel was used to create a binary threshold the intracellular area, using Image>Adjust>Threshold. If necessary, any holes in the cell outline were filled with Process>Binary>Fill Holes. The binary threshold was eroded with a pixel count of 3 to remove background speckles (Process>Binary>Options>Count = 3 and Process>Binary>Erode). A selection was created from the remaining binary threshold encompassing the intracellular area, and the surface area was measured in order to normalize

extracellular fibronectin area. Next, the fibronectin channel of the images was smoothened to reduce nonspecific background noise (Process>Smooth). Next, the intracellular selection was pasted onto the fibronectin image, and the pixels inside of this selection were cleared (Edit>Selection>Clear), leaving behind only extracellular fibronectin. The remaining pixels were used to create a binary threshold using the same method as above for the phalloidin channel. The area and integrated density of the extracellular fibronectin within the threshold were measured (Analyze>Measure) and normalized to the intracellular area of the same image.

**Liquid chromatography–mass spectrometry (LC-MS/MS) of secreted proteins**

To produce serum-free conditioned media, cells were grown to 70% confluency on three 100mm cell culture dishes per sample. The cells were then washed twice with 1X PBS, then cultured in 8mL of serum-free RPMI-1640 for 48 hours. The collected conditioned media was centrifuged at 300 x g at 4°C for 15 minutes to remove dead cells from the media. To purify proteins secreted by the cells, 15mL of conditioned media was transferred into an Amicon Ultra-15 Centrifugal Filter Unit with a filter size of 3kDa and centrifuged at 4000 x g at 4°C for 60 minutes in a swinging bucket rotor. 15mL of RPMI 1640 without serum was also concentrated using the same method. LC-MS/MS data acquisition was performed as previously described (*204*) using a Dionex Ultimate 3000 RSLCNano and monitored on an Orbitrap Fusion mass spectrometer (ThermoFisher Scientific , San Jose, CA). Analysis of mass spectrometry data was performed as previously

described. Peptides were identified by matching the spectra with Proteome Discoverer 2.0 (ThermoFisher Scientific) against the human Uniprot database (90,300 target sequences).

**Statistical analysis**

All quantitative results were analyzed with the test indicated in the figure legends, after confirming that the data met appropriate assumptions (normality, homogeneous variance and independent sampling). Unless otherwise stated, all indicated p-values are two-tailed and all data are plotted as the mean with error bars indicating standard error of the mean. All results were reproduced at least twice in the laboratory. The figure legends indicate the number of independent biological replicates and sample size for each experiment. Microsoft Excel and Graphpad Prism software were used to conduct statistical analyses of the data. P-values less than 0.05 were considered significant.

## 3.5 Results

### Myosin-X is enriched in leader cells

From our integrated DNA methylation and gene expression analysis, we identified myosin-X (*MYO10*) as the gene most significantly upregulated and hypomethylated at the promoter in leader cells compared to follower cells (Fig. 1F). MYO10 is an unconventional myosin that localizes to filopodia tips and drives filopodia elongation (*144, 160*). Annotation of the *MYO10* DMPs revealed that CpG probes within 1500bp of the promoter and the first exon were hypomethylated in leader cells compared to follower cells, whereas almost all CpG probes within the gene body were hypermethylated compared to follower cells (Fig. 1G and Fig. S3A). Since promoter methylation acts as a transcriptional repressor (*83, 182*) and gene body methylation positively correlates with gene expression (*186*), these data suggest that shifts in *MYO10* DNA methylation may enable *MYO10* overexpression in leader cells. Overexpression of *MYO10* in leader cells observed by RNAseq was validated by qPCR and Western blot (Fig. 1H-I). Leader cells expressed endogenous MYO10 within filopodia in 2D cell culture (Fig. 1J), as well as the NSCLC parental cell lines H1299, H1792, and H1975 (Fig. 1K). During 3D spheroid collective invasion, leader cells were enriched for MYO10 compared to follower cells (Fig. 1L). Collectively invading spheroids of the parental H1299, H1792, and H1975 cell lines also showed enriched MYO10 expression in cells at the front of invasive chains compared to cells further back in these collective chains (Fig. 1M). These data suggest MYO10 is highly expressed in invasive NSCLC leader cells but not follower cells.

**MYO10 regulates filopodia length, cell motility, and collective invasion**

Since filopodia regulate many aspects of cancer cell adhesion and invasion (*132*), we wanted to determine if MYO10-driven filopodia functionally regulate leader cell migration and invasion. We quantified filopodia length in leaders and followers during 3D collective invasion (Fig. 2A). Follower cells almost exclusively displayed short filopodia (mean length 1.5μm), compared to leader cell filopodia (mean length 3.4μm). To determine how MYO10 expression impacts leader cell filopodial dynamics, we depleted *MYO10* via siRNA in leader cells (Fig. S3B) which resulted in significantly shorter filopodia (mean length 1.5μm) reminiscent of those observed in follower cells, and consistent with previous work demonstrating MYO10-driven filopodia elongation on 2D substrates (*131, 135, 136*)(Fig. 2A-C, Videos S1 and S2). Interestingly, when we assessed filopodia lifetimes in our siCtrl versus siMYO10 leader cells during 3D invasion, we observed lifetimes significantly longer than those reported in 2D (*131, 135, 136*) (Fig. 2C-D). When we assessed filopodia lifetimes in 2D, we found significantly shorter lifetimes for both siCtrl and siMYO10 leader cells (Fig. 2C-D), confirming significantly different filopodia dynamics in 3D versus 2D for our leader cell subpopulation.

To determine how MYO10 impacted 2D cell motility and 3D invasion, we modulated MYO10 expression in both leader and follower cell subpopulations (Fig. S3B-C). MYO10 knockdown in leader cells significantly decreased cell motility in 2D, while MYO10 overexpression in follower cells increased cell motility (Fig. 2E-F). MYO10 knockdown in leader cells and in three parental NSCLC cell lines significantly abrogated chain-like collective invasion (Fig. 2G-H). Conversely, ectopic mCherry-MYO10 expression in follower cells induced long

filopodia and significantly increased 3D spheroid invasion (Fig. 2I). These data suggest that MYO10 is necessary for collective invasion via its role in leader cell filopodia.

**JAG1 expression is elevated in leader cells**

The absence of *MYO10* promoter methylation in leader cells relative to followers is indicative of a more permissive chromatin environment, but in itself is not deterministic of gene expression levels. Given the significant upregulation of MYO10 in leaders, we therefore examined our transcriptome analysis for putative pathways that might impinge upon the locus to regulate MYO10 expression. The Notch signaling pathway is an evolutionarily-conserved pathway composed of four Notch receptors (Notch1-4) and five canonical ligands (JAG1, JAG2, DLL1, DLL3, and DLL4) that regulates cell-cell signaling (*205*) and is frequently dysregulated in cancer (*206, 207*). GSEA showed that the expression of Notch transcriptional targets (*177, 181, 208*), including *MYO10*, was highly enriched in leader cells compared to follower cells (Fig. S4A-B). Among all nine Notch receptors and ligands, *JAG1* was highly expressed in leader cells compared to parental and follower cells and was by far the most differentially expressed Notch family member (Fig. 3A). Upon further interrogation, we found that *JAG1* was one of the most highly differentially expressed cell surface ligands or receptors in the entire transcriptome analysis (Fig. 1E). We also identified *IL13RA2* as a cell surface marker highly expressed in follower cells compared to leader cells (Fig. 1E). Flow cytometry analysis of cell surface JAG1 revealed that the parental H1299 cell line contained approximately 7% JAG1$^{HIGH}$/IL13RA2- cells (Fig. S4C). Consistent with RNAseq data, leader cells were enriched in JAG1, whereas less than 1% of follower cells expressed cell surface JAG1 (Fig. S4C). Additionally, when we analyzed patient-derived NSCLC primary cells (EUH3174) by flow cytometry, we saw a small population of

JAG1$^{HIGH}$/IL13RA2$^{-}$ cells (~10%) and a small population of JAG1$^{LOW}$/IL13RA2$^{+}$ cells (~3%) (Fig. S4C). When we assessed protein expression by immunoblotting, both MYO10 and the JAG1 full-length protein were enriched in the leader population compared to their follower counterparts, while IL13RA2 protein expression was absent in leader cells (Fig. 3B). Parental cells that were FACS sorted for the "leader-like" JAG1$^{HIGH}$/IL13RA2$^{-}$ or "follower-like" JAG1$^{LOW}$/IL13RA2$^{+}$ subpopulations showed similar expression patterns of MYO10, JAG1 full length protein, JAG1 intracellular domain (ICD), and IL13RA2 as leader cells and follower cells respectively (Fig. 3B, S4D). When we assessed JAG1 localization during 3D invasion, we confirmed that JAG1 was expressed in leaders but not followers during spheroid collective invasion (Fig. 3C). When we compared MYO10 and JAG1 localizations in leader cells cultured in either 2D or 3D, JAG1 was primarily localized to cell-cell boundaries, while MYO10 was predominantly found at the tips of the filopodia; both proteins could also be found within cell body (Fig. S5).

To determine if JAG1 was necessary for leader cell-driven collective invasion, we performed shRNA knockdowns of JAG1 in purified leader cells (Fig. 3D-E, Fig. S6A). While reducing JAG1 expression only moderately decreased leader cell invasion in homogenous leader-only spheroids due to poor cell-cell adhesion within the spheroid, heterogeneous spheroids consisting of 10% leader cells and 90% follower cells showed significantly decreased spheroid collective invasion (Fig. S6B); similar results were observed with "leader-like" JAG1$^{HIGH}$-sorted cells alone or mixed with "follower-like" JAG1$^{LOW}$-sorted H1299 cells (Fig. S6C). Additionally, JAG1 antibody inhibition significantly decreased spheroid collective invasion and transwell invasion of multiple NSCLC cell lines and spheroids of patient-derived NSCLC primary cells EUH3174 (Fig. S7A-B). Taken together, these data suggest that JAG1 activity is necessary for rare leader cells within heterogeneous tumor populations to drive collective invasion.

**JAG1 signaling upregulates MYO10 expression**

We next investigated whether JAG1 regulates MYO10 expression. JAG1 knockdown in leader cells significantly abrogated MYO10 mRNA and protein expression (Fig. 3D-E, S6A), but MYO10 knockdown did not affect JAG1 expression (Fig. S7C). Importantly, ectopic JAG1 overexpression in follower cells, where the MYO10 promoter remained methylated, did not induce MYO10 expression (Fig. 3F, S7D) or alter *MYO10* promoter methylation (Fig. 3G), suggesting JAG1 cannot restore MYO10 expression without additional epigenetic events (*e.g*. promoter hypomethylation) observed in leader cells (Fig. 1). These data suggest that JAG1 is necessary for regulating MYO10 expression in leader cells in conjunction with a permissive DNA methylation state.

Since JAG1 critically regulates 3D collective invasion and also upregulates MYO10 expression in leader cells, and since MYO10 drives filopodia elongation necessary for collective invasion, we predicted that the effects of JAG1 during collective invasion were mediated by its effects on filopodia via inducing MYO10 expression. To determine whether JAG1 affects filopodia elongation, we quantified filopodia length after manipulating MYO10 and JAG1 expression (Fig. 3H-I). While JAG1 knockdown in leader cells significantly shortened filopodia, filopodial length was rescued with ectopic expression of MYO10 (Fig. 3H). Filopodia length in follower cells increased after JAG1 expression and further increased after expression of MYO10 (Fig. 3I). Next, we assessed whether JAG1 regulation of MYO10 expression impacted not only filopodia length but also 3D invasion (Fig. 3J-K). JAG1 knockdown in leader cells significantly abrogated spheroid collective invasion, while MYO10 expression rescued spheroid invasion (Fig. 3J) and transwell invasion (Fig. S7E). While ectopic expression of JAG1 alone in follower cells

only moderately increased spheroid collective invasion, expression of MYO10 in followers with or without JAG1 substantially increased spheroid collective invasion (Fig. 3K) and transwell invasion (Fig. S7E), far more than JAG1 alone. These data strongly suggest that JAG1 regulates MYO10 expression (and consequently filopodia length and 3D collective invasion) in epigenetically-permissive leader cells.

**MYO10 regulates ECM remodeling in leader cells through fibronectin micropatterning**

Increased fibronectin expression correlates with cancer cell invasion and metastasis, and linearized fibronectin promotes the directional migration of cancer cells (*209-211*). Our data showed that leader cells but not follower cells produced and secreted high levels of FN1 (*112*) (Fig. 3.XXX). To identify additional proteins of interest that were differentially secreted in either leader cells or follower cells, we analyzed serum free conditioned media from parental, follower, and leader cells. We detected several differentially secreted extracellular matrix proteins and TGF-β proteins (Fig. 3.XX). However, FN1 was by far the most abundant protein secreted by leader cells, with substantially more protein fragments detected in leader-conditioned media compared to follower- or parental-conditioned media (Fig. 3.XXX). In addition to producing and secreting FN, leader cells actively remodeled extracellular FN during collective invasion into parallel linear fibrils extending past the leading edge (Fig. 4D-G, 5A), resembling invasion-promoting stromal FN alignment observed at the edges of invasive tumors (*211, 212*). Since follower cells do not produce or secrete FN, follower cell spheroids in recombinant basement membrane (rBM) did not display any FN fibrils (Fig. 5B). Even when FN was added to the rBM, follower cell spheroids were not able to align the exogenous FN (Fig. 5C), suggesting that follower cells lack the ability to remodel extracellular fibronectin. Leader cell FN alignment at the invasive front was also

observed in invading spheroids of H1299, H1792, and H1975 cells, and EUH3174 patient-derived cells (Fig. S8). Thus, NSCLC leader cells not only produced and secreted FN but also aligned this FN towards the direction of collective invasion.

Since the linear FN fibrils uniquely produced by leader cells resembled the geometry of filopodia, we hypothesized that MYO10-driven filopodia regulate FN remodeling. In support of this hypothesis, invading spheroids of MYO10-knockdown leader cells still produced FN fibrils directly underneath cell bodies but created significantly fewer extracellular FN fibrils extending past the cellular leading edge (Fig. 4D-E). Similarly, since JAG1 promotes MYO10 expression in leader cells, invading spheroids of JAG1-knockdown leader cells did not produce any FN fibrils, despite these cells producing abundant globular FN inside cell bodies and coating the extracellular surface (Fig. S9). Furthermore, leader cell filopodia that co-localized with MYO10 and/or FN1 during 3D invasion were significantly longer than filopodia not co-localized with either protein (Fig. 4F-G). Therefore, these data suggest that MYO10-rich filopodia are necessary for aligning and discretely micropatterning the leading-edge extracellular FN into linearized fibrils.

**MYO10 drives filopodia persistence necessary for leading-edge FN micropatterning**

To investigate the interplay between MYO10-driven filopodia and FN micropatterning during collective invasion, we performed live cell confocal imaging of leader cell spheroids expressing membrane-bound Dendra2 that were embedded into Matrigel mixed with fluorescently-labeled FN (FN-rhodamine, Fig. 6A-C, Video S3). FN-rhodamine fibrils formed either underneath the cell body or within linearized “tracks” extending beyond the leading cell (Fig. 6A, arrows), as observed in fixed spheroids with endogenous FN (Figs. 4D-G 5A, S8, S9). When assessing how filopodia and FN interacted during fibrillogenesis, we observed that leading-

edge FN fibrils formed almost exclusively with ultra-stable filopodia with long lifetimes in a two-step process of initiation and elongation. After a filopodium tip paused without retraction for several minutes (Fig. 6B-C, arrow), FN-rhodamine nucleation puncta initiated ~2 microns behind the filopodium tip (Fig. 6B-C, arrowheads). After the filopodium retracted towards the cell body (Fig. 6B-C, asterisk), the distal end of FN fibrils remained in place, whereas the proximal end continued to grow and elongate. After this, some filopodia fully retracted into the cell body, and in other cases the filopodia remained engaged with the fibril proximal end; in either scenario, the FN fibril remained in place, now protruding beyond the cellular leading edge along the path where the filopodia once extended and retracted (Fig. 6B-C). Thus, these data suggested that leader cell filopodia are not merely sensors of the extracellular environment but also actively participate in fibronectin fibrillogenesis.

To determine MYO10 localization and function during filopodia-based FN fibrillogenesis, we performed similar imaging using spheroids of H1299 cells expressing GFP-MYO10 embedded into rBM mixed with FN-rhodamine (Fig. 6D-K, Video S4). We observed two distinct populations of MYO10-GFP filopodia: long-lived filopodia wherein the tip persisted in one location for ≥15 minutes (Fig. 6D-E, G) and short-lived filopodia that did not persist in one location (Fig. 6F). Filopodia-associated FN fibrils initiated exclusively with long-lived filopodia, following the same two-step process of fibril initiation within the filopodia shaft and subsequent fibril elongation when filopodia retracted (Fig. 6E-G). To quantify the spatial relationship between GFP-MYO10 and FN-rhodamine during this process, we drew line plots along the full length of 92 filopodia from tip to base at the moment when a new FN-rhodamine fibril was first visible. As expected, GFP-MYO10 localized to the filopodia tips, whereas the average FN-rhodamine intensity peaked around 2-2.5μm away from the tip and then slowly tapered in intensity towards the base (Fig. 6H).

The distance between the peaks of GFP-MYO10 and FN-rhodamine for each individual filopodium at the start of fibril initiation ranged from 0.3 to 6.5μm, with a median distance of 1.8μm (Fig. 6I). Since the length of leader cell filopodia during 3D invasion varies from approximately 2-20μm (Fig. 2A), we normalized the fluorescence signal intensities across a common distance from tip to base, which showed that GFP-MYO10 localized exclusively to the filopodia tip while FN fibrils formed along the shaft (Figure 6J). These data were also consistent with our observations that nascent FN puncta formed within the shafts of filopodia in cells expressing membrane-bound Dendra2 (Fig. 6B-C). Thus, these data suggest that MYO10 does not directly interact with FN but instead facilitates filopodia tip anchoring before FN fibrillogenesis begins, presumably within nascent adhesion sites along the filopodia shaft.

Interestingly, we observed two distinct pools of filopodia. In contrast to the long-lived filopodia associated with leading-edge FN fibrillogenesis, we observed short-lived filopodia that did not adhere to the matrix and would extend and retract multiple times without forming FN fibrils. (Fig. 6F). Since only a subset of the observed filopodia formed FN fibrils, we compared the lifetimes of several hundred filopodia that either formed FN fibrils or did not form fibrils during collective spheroid invasion (Figure 6K-L). In spheroids of H1299 cells expressing GFP-MYO10, filopodia that formed nascent FN fibrils displayed strikingly long lifetimes (mean lifetime = 37.2 minutes) compared to filopodia that did not participate in FN fibrillogenesis (mean lifetime = 5.77 minutes)(Fig. 6K). Similarly, filopodia in leader cell spheroids that formed FN fibrils were ultra-stable (mean lifetime = 46.3 minutes) compared to filopodia that did not form FN fibrils (mean lifetime = 5.6 minutes)(Fig. 6L). In fact, 95% of FN fibril-producing filopodia in leader cells persisted for 15 minutes or longer (Fig. 6L). Thus, our data suggest that leader cells display both

long-lived and short-lived subsets of filopodia during 3D collective invasion, and that only long-lived filopodia are capable of directing FN fibrillogenesis at the leading edge.

Since MYO10 knockdown significantly shortened the mean leader cell filopodia lifetime during 3D collective invasion from 16 minutes to 5 minutes (Fig. 2C), we hypothesized that MYO10 knockdown specifically depleted the long-lived pool of filopodia. When we re-examined the filopodial lifetimes in si-control and siMYO10 leader spheroids for the presence of ultra-stable filopodia, we observed that 35% of all si-control leader cell filopodia persisted for ≥15 minutes, but less than 5% of the total filopodia in MYO10-knockdown cells persisted for this length of time (Fig. 6M). In total, these data suggest MYO10 drives filopodial persistence for periods of time greater than 15 minutes, which is a necessary prerequisite for leading-edge FN fibrillogenesis to occur within the shafts of filopodia.

**Integrin β1 is necessary for leader cell FN micropatterning during 3D collective invasion**

Although MYO10 drives filopodial persistence necessary for FN alignment, live cell imaging of MYO10-GFP and FN-rhodamine showed that MYO10 did not directly co-localize with nascent FN puncta (Fig. 3.14G-I). Since MYO10 is a motor protein that transports cargo to filopodia tips, we hypothesized that one of these transported cargo proteins may mediate the effects of MYO10 on FN remodeling, rather than direct MYO10-FN interactions. For example, MYO10 contains a FERM (4.1/ezrin/radixin/moesin) domain that interacts with β-integrin subunits (including integrins β1, β3, and β5) and allows MYO10 to transport integrins to the tips of filopodia (*150*). Integrins are transmembrane proteins that act as crucial links between the actin cytoskeleton and the extracellular environment (*213*). All integrins act as heterodimers with one alpha subunit and one beta subunit, and the activated extracellular head domains of integrin

heterodimers can bind to extracellular matrix proteins while the intracellular tail domains interact with the actin cytoskeleton through various adapter proteins (*214*). When bound to extracellular matrix proteins, integrins are capable of transmitting intracellular forces from actomyosin contractility in order to induce extracellular matrix remodeling (*30*). In particular, integrins α5β1 and αVβ3 are known to directly participate in FN remodeling; α5β1 is largely considered the dominant participant in fibronectin fibrillogenesis, while αvβ3-mediated fibrillogenesis provides an secondary alternative pathway under specific circumstances (*210, 215, 216*).

We first assessed the mRNA expression for these two key integrin pairs important for fibronectin engagement (Fig. 3.15A) (*217*). Expression of integrins α5 (*ITGA5*) and β1 (*ITGB1*) were similar between our H1299 parental, leader and follower populations, with *ITGB1* highly expressed in all cell types as expected (*218*). Both integrin αV (*ITGAV*) and integrin β3 (*ITGB3*) were elevated in leader cells compared to both the parental and follower populations (Fig. 3.15A). Using an inhibitory antibody approach, we tested the effect of β1 or αvβ3 integrin inhibition on 3D invasion, as well as fibronectin deposition and fibrillogenesis. While blocking αvβ3 integrin minimally affected 3D collective invasion, inhibition of β1 integrin drastically reduced spheroid invasion in leader cells (Fig. 3.15B). Similarly, blocking αvβ3 integrin had minimal effects on leader cell-mediated fibronectin fibril formation in our invading spheroids, while blocking β1 integrin abolished all leader cell fibrillogenesis (Fig. 3.15C). Notably, antibody-mediated β1 integrin inhibition had no effect on fibronectin abundance; large globular pools of fibronectin appeared within the cells and at cell-cell boundaries (Fig 3.15C). These data suggest that while fibronectin organization is remarkably perturbed in the absence of β1 integrin, fibronectin production remains potentially unchanged. Thus, our data suggest that transport of β1 integrin into filopodia by MYO10 is necessary for filopodia-dependent FN linearization.

Taken together, our data suggest a model to describe the induction and activity of MYO10 within the rare leader cell population during collective cancer invasion. Aberrant DNA methylation combined with high JAG1 expression and subsequent Notch signaling induce high expression of MYO10 and FN1 in leader cells; MYO10 drives filopodial elongation and persistence in 3D and also recruits its cargo protein β1 integrin into filopodia, all of which are necessary steps to induce filopodia-dependent linearization of extracellular FN1 (Fig. 3.16).

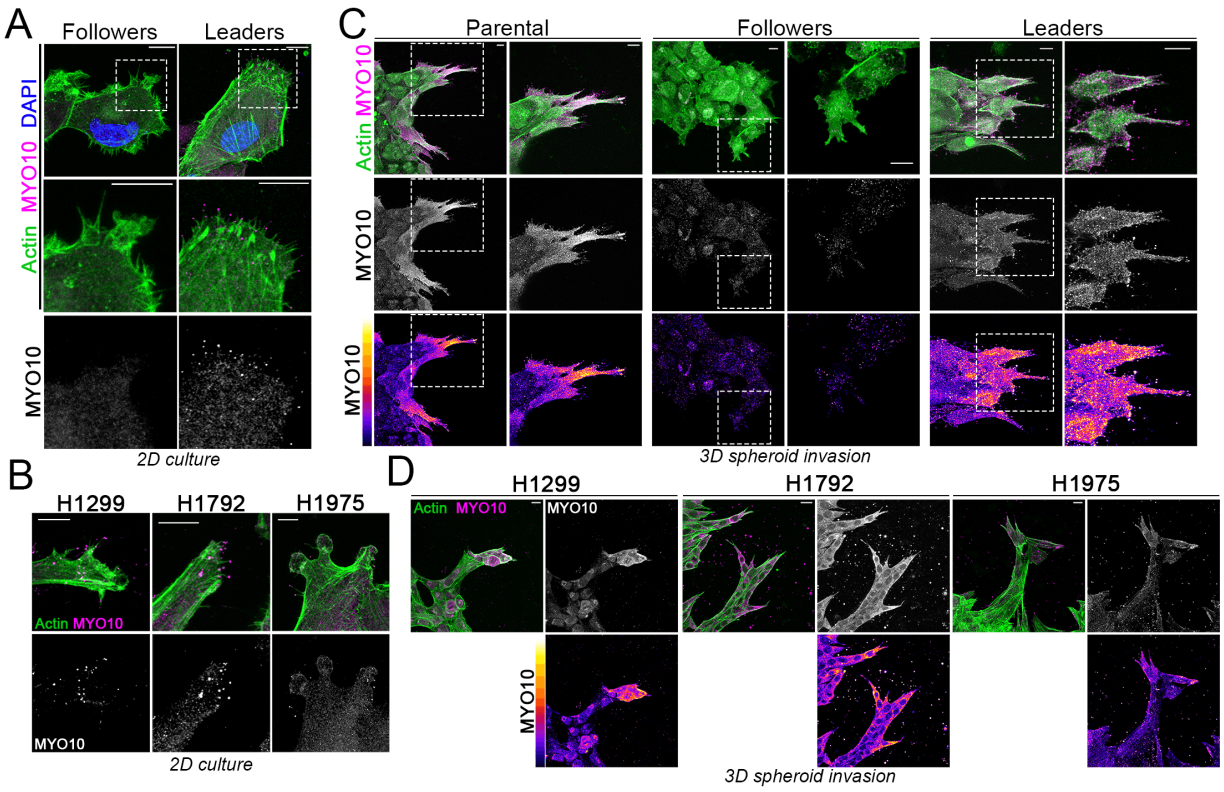


**Figure 3.1 The filopodial motor protein MYO10 is enriched in leader cells during collective lung cancer spheroid invasion.**

(**A-B**) Immunofluorescence imaging of 2D cell culture of follower and leader cells (**A**) or of parental H1299, H1792, and H1975 NSCLC cells (**B**). Scale bars, 5 μm; Representative images from n = 3 biological replicates of immunofluorescence per cell type, N = minimum of 30 cells imaged per cell type. (**C-D**) Immunofluorescence imaging of 3D spheroid invasion through Matrigel of H1299 parental, follower, and leader cells (**C**) or of H1299, H1792, and H1975 NSCLC cells (**D**). Fire LUT represents MYO10 signal intensity. Scale bars, 10 μm.

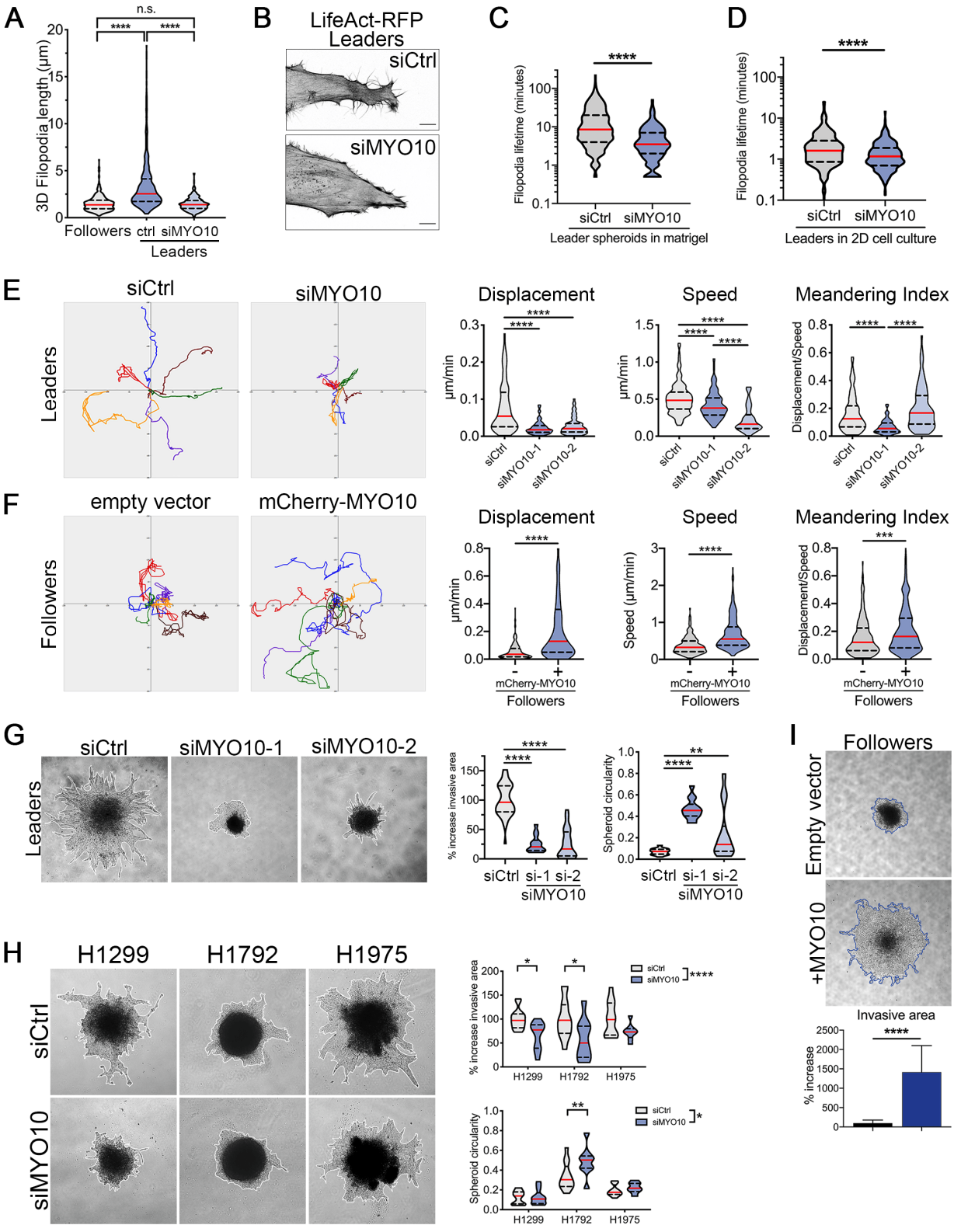
A
n.s.
****
****
3D Filopodia length (μm)
Followers
ctrl
siMYO10
Leaders
B
LifeAct-RFP
Leaders
siCtrl
siMYO10
C
****
Filopodia lifetime (minutes)
siCtrl
siMYO10
Leader spheroids in matrigel
D
****
Filopodia lifetime (minutes)
siCtrl
siMYO10
Leaders in 2D cell culture
E
siCtrl
siMYO10
Leaders
Displacement
Speed
Meandering Index
μm/min
Displacement/Speed
siCtrl
siMYO10-1
siMYO10-2
F
empty vector
mCherry-MYO10
Followers
Displacement
Speed
Meandering Index
μm/min
Speed (μm/min)
Displacement/Speed
mCherry-MYO10
Followers
G
siCtrl
siMYO10-1
siMYO10-2
Leaders
% increase invasive area
Spheroid circularity
siCtrl
si-1
si-2
siMYO10
H
H1299
H1792
H1975
siCtrl
siMYO10
% increase invasive area
Spheroid circularity
I
Followers
Empty vector
+MYO10
Invasive area
% increase

**Figure 3.2: MYO10 regulates cell motility and collective invasion.**

(**A**) Violin plot of filopodia lengths during 3D invasion of follower cells, si-control leader cells (ctrl), and siMYO10 leader cells. Red line indicates the median, dashed black lines indicate the interquartile range. n = 3 biological replicates, followers N = 459 filopodia, siCtrl leaders N = 688 filopodia, siMYO10 leaders N = 490 filopodia, 12 fields of view per condition per replicate. Kruskal-Wallis test with Dunn's correction for multiple comparisons. (**B**) Representative images from live cell imaging of LifeAct-RFP filopodia dynamics in leader cells expressing siCtrl or siMYO10. Scale bars, 10 μm. (**C**) Violin plot of filopodia lifetimes during 3D spheroid invasion of si-control leader cells (siCtrl), and siMYO10 leader cells. Red line indicates the median, dashed black lines indicate the interquartile range (IQR). n = 3 biological replicates and N = 824 filopodia quantified (517 siCtrl filopodia and 307 siMYO10 filopodia). For siCtrl filopodia: median = 8.5 minutes, IQR = 4 – 20 minutes. For siMYO10 filopodia: median = 3.5 minutes, IQR = 2 – 7 minutes. Kruskal-Wallis test with Dunn's correction for multiple comparisons. (**D**) Violin plot of filopodia lifetimes on 2D substrates of si-control leader cells (siCtrl), and siMYO10 leader cells. Red line indicates the median, dashed black lines indicate the IQR. N = 2 biological replicates and N = 584 filopodia quantified (298 siCtrl filopodia and 286 siMYO10 filopodia). For siCtrl filopodia: median = 1.61 minutes, IQR = 0.86 – 2.83 minutes. For siMYO10 filopodia: median = 1.17 minutes, IQR = 0.70 – 1.88 minutes. Kruskal-Wallis test with Dunn's correction for multiple comparisons. (**E-F**) Live cell tracking analysis and quantification of 2D cell migration of leader cells expressing siCtrl or siMYO10 (**E**) or in follower cells expressing a control mCherry vector or mCherry-MYO10 (**F**). For (**E**), n = 4 biological replicates for siCtrl cells and n = 2 for each MYO10 siRNA, and N = 186, 148, and 86 cell paths quantified per siRNA, respectively, Kruskal-Wallis test with Dunn's correction for multiple comparisons. For **(F)**, n = 3 biological replicates,

N = 237 and 259 cell paths quantified per condition, respectively. Mann-Whitney U-test, two-tailed. (**G**) Representative images and quantification of 72h spheroid invasion assays in Matrigel of H1299 leaders expressing siCtrl or one of two MYO10 siRNAs (siMYO10-1 and siMYO10-2). For siCtrl: n = 5 biological replicates and N = 45 spheroids. For siMYO10-1, n = 2 biological replicates and N = 14 spheroids. For siMYO10-2, n = 3 biological replicates and N = 31 spheroids. Kruskal-Wallis test with Dunn's correction for multiple comparisons. (**H**) Representative images and quantification of 72h spheroid invasion assays of parental H1299, H1792 and H1975 cells expressing siCtrl one of two MYO10 siRNAs (siMYO10-1 and siMYO10-2). For H1299: n = 4 biological replicates and N = 29 spheroids. For H1792: n = 3 and N = 22 spheroids. For H1975: n = 2 and N = 20 spheroids. Two-way ANOVA with Sidak's multiple comparison test. Effect of the siRNA indicated to the right of the key. (**I**) Representative images and quantification of 48h spheroid invasion assays in Matrigel of follower cells expressing a control empty vector or mCherry-MYO10. Mann-Whitney U-test, two-tailed. For all panels, * $p < 0.05$, ** $p < 0.01$, *** $p < 0.001$, and **** $p < 0.0001$.

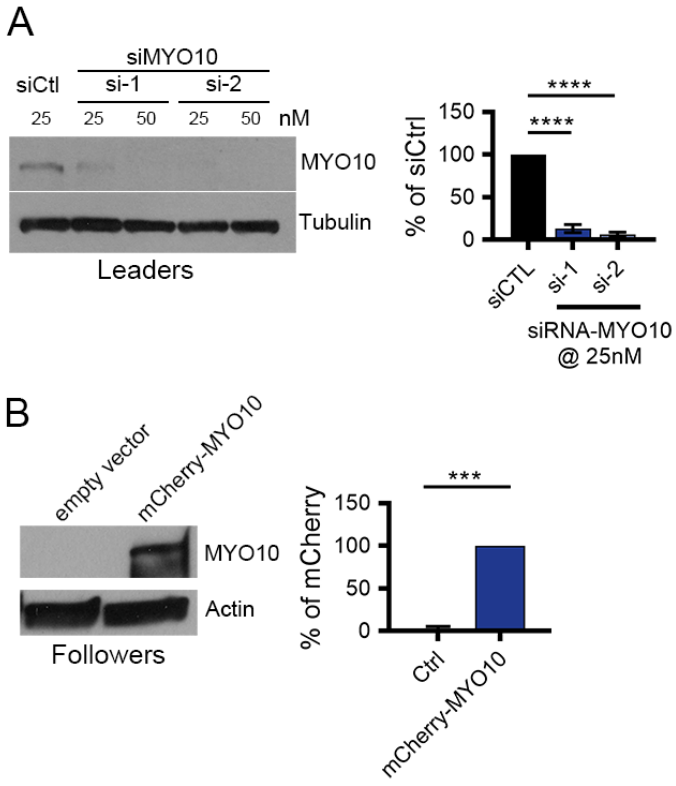


**Figure 3.3: Validation of MYO10 siRNA knockdowns and mCherry-MYO10 transient overexpression.**

(**A**) Western blots and quantification for H1299 leader cells treated with either an si-control (siCtrl) or one of two different siRNA targeting MYO10 (si-1, si-2); tubulin as a loading control. n = 2 independent biological replicates for si-1; n = 5 independent biological replicates for siCtl and si-2. (C) Western blots and quantification for H1299 follower cells ectopically expressing either an mCherry-only vector control (empty vector) or mCherry-tagged MYO10 (mCherry-MYO10); actin as a loading control. n = 3 independent biological replicates. *** $p < 0.001$, and **** $p < 0.0001$.

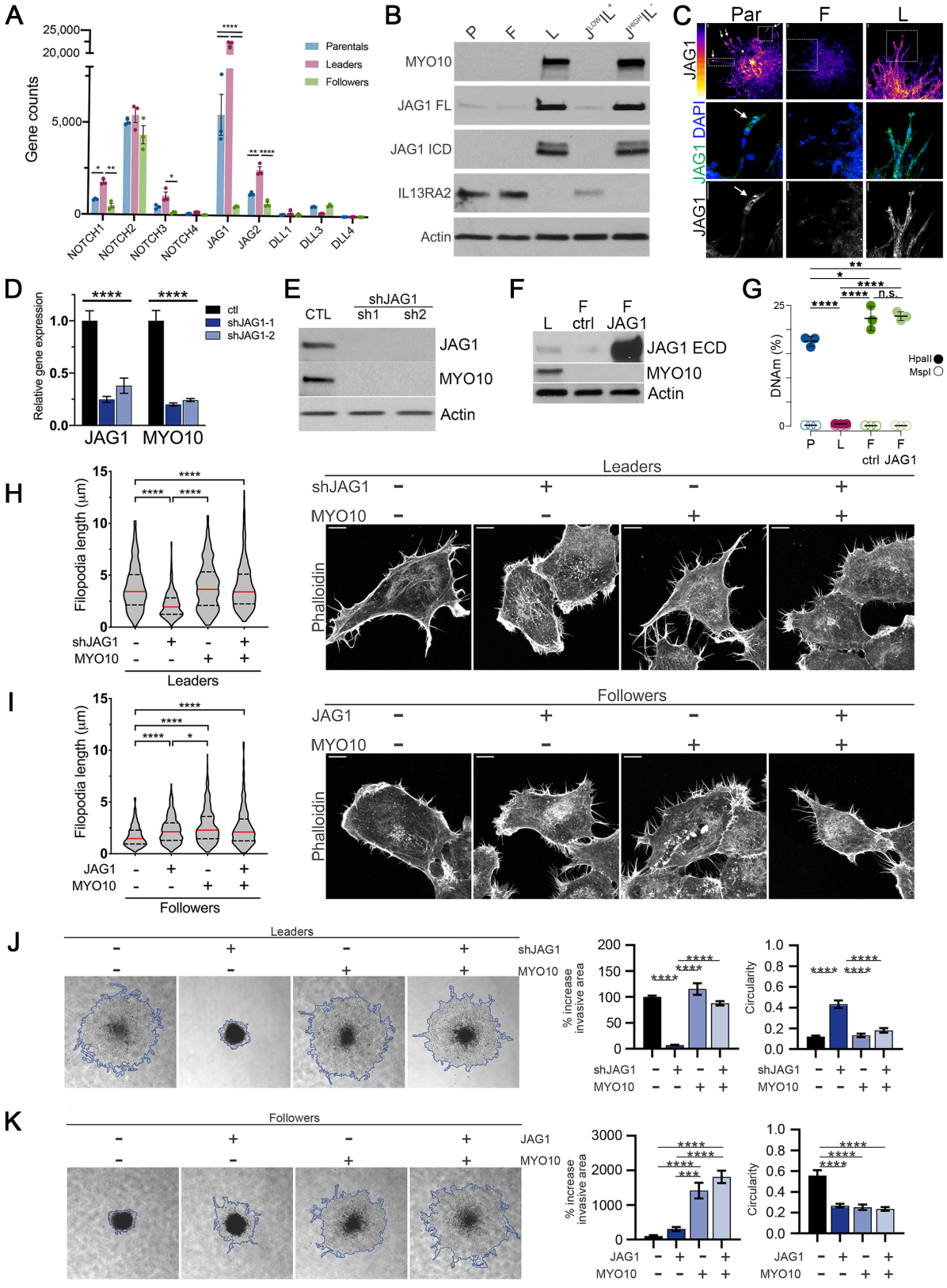
A
Gene counts
25,000
20,000
5,000
0
Parentals
Leaders
Followers
NOTCH1
NOTCH2
NOTCH3
NOTCH4
JAG1
JAG2
DLL1
DLL3
DLL4
B
P
F
L
MYO10
JAG1 FL
JAG1 ICD
IL13RA2
Actin
C
Par
F
L
JAG1
JAG1 DAPI
D
Relative gene expression
ctl
shJAG1-1
shJAG1-2
JAG1
MYO10
E
CTL
shJAG1
sh1
sh2
JAG1
MYO10
Actin
F
L
F ctrl
F JAG1
JAG1 ECD
MYO10
Actin
G
DNAm (%)
HpaII
MspI
P
L
F ctrl
F JAG1
n.s.
H
Filopodia length (µm)
shJAG1
MYO10
Leaders
Phalloidin
I
Filopodia length (µm)
JAG1
MYO10
Followers
Phalloidin
J
Leaders
shJAG1
MYO10
% increase invasive area
Circularity
K
Followers
JAG1
MYO10
% increase invasive area
Circularity

**Figure 3.4: JAG1 signaling is upstream of MYO10 expression in leader cells.**

(**A**) Bar graph of the mean RNAseq normalized gene counts for the four Notch receptors and five canonical Notch ligands, showing strong overexpression of JAG1 in leader cells compared to follower cells. Error bars indicate s.e.m, dots indicate individual replicates. N = 3 independent biological replicates per condition. Ordinary two-way ANOVA with Tukey's correction for multiple comparisons. (**B**) Western blots of H1299 parental, follower, and leader cells and H1299 cells sorted for the JAG1$^{LOW}$/IL13RA2+ "follower-like" population and the JAG1$^{HIGH}$/IL13RA2- "leader-like" population; probed for MYO10, JAG1 full-length (FL), JAG1 intracellular domain (ICD), and IL13RA2.; actin as loading control. N = 3 independent biological replicates per condition; quantification shown in Figure S4D. (**C**) Immunofluorescence of 3D invasion of H1299 parental, follower, or leader cell spheroids stained for JAG1. N = 3 independent biological replicates per condition. (**D**) qPCR of mRNA extracted from leader cells expressing a control shRNA or shRNA-JAG1, normalized to actin expression. N = 3 independent biological replicates per condition. (**E**) Western blot of JAG1 and MYO10 expression in H1299 leader cells ectopically expressing either an shRNA control or an shRNA targeting JAG1 (sh1, sh2); actin as the loading control. N = 3 independent biological replicates per condition; quantification shown in Figure S6A. (**F**) Western blot probing for JAG1 and MYO10 with H1299 leader cells (L), follower cells (F) expressing a control empty vector (Ctrl), or follower cells expressing JAG1; actin as the loading control. N = 4 independent biological replicates per condition; quantification shown in Figure S7D. (**G**) Quantification of MYO10 methylation status using qPCR. HpaII = methyl-sensitive restriction enzyme, MspI = methyl-insensitive restriction enzyme. Percent of DNA methylation (%DNAm) calculated as the ratio of digested material amplified to mock-digested material amplified. n = 3 independent biological replicates per condition. (**H**) Violin plots quantifying 2D filopodia length

with representative images of leader cell filopodia in leader cells expressing shRNA-JAG1 and/or mCherry-MYO10. Cells in 2D cultures and stained with phalloidin to visualize actin. Red line indicates median, dashed black lines indicate interquartile ranges. N = 2 biological replicates and N = 300+ filopodia quantified per condition from a minimum of 12 fields of view per condition per replicate. Kruskal-Wallis test with Dunn's multiple comparison test. Scale bar, 10 μm. (**I**) Violin plots quantifying 2D filopodia length with representative images of follower cells expressing JAG1 and/or mCherry-MYO10. Cells in 2D cultures and stained with phalloidin to visualize actin. Red line indicates median, dashed black lines indicate interquartile ranges. N = 2 biological replicates and N = 500+ filopodia quantified per condition from 12 fields of view per condition per replicate. Kruskal-Wallis test with Dunn's multiple comparison test. (**J**) Representative images and quantification of 3D collective spheroid invasion of leader cells expressing shRNA-JAG1 and/or mCherry-MYO10. Ordinary one-way ANOVA with Tukey's correction for multiple comparisons. N = 4 independent biological replicates and N = 24 spheroids per condition. (**K**) Representative images and quantification of 3D collective spheroid invasion follower cells expressing JAG1 and/or mCherry-MYO10. n = 3 independent biological replicates and N = 18 spheroids per condition. Ordinary one-way ANOVA with Tukey's correction for multiple comparisons. For all panels, n.s. = not significant, * $p < 0.05$, ** $p < 0.01$, *** $p < 0.001$, and **** $p < 0.0001$.

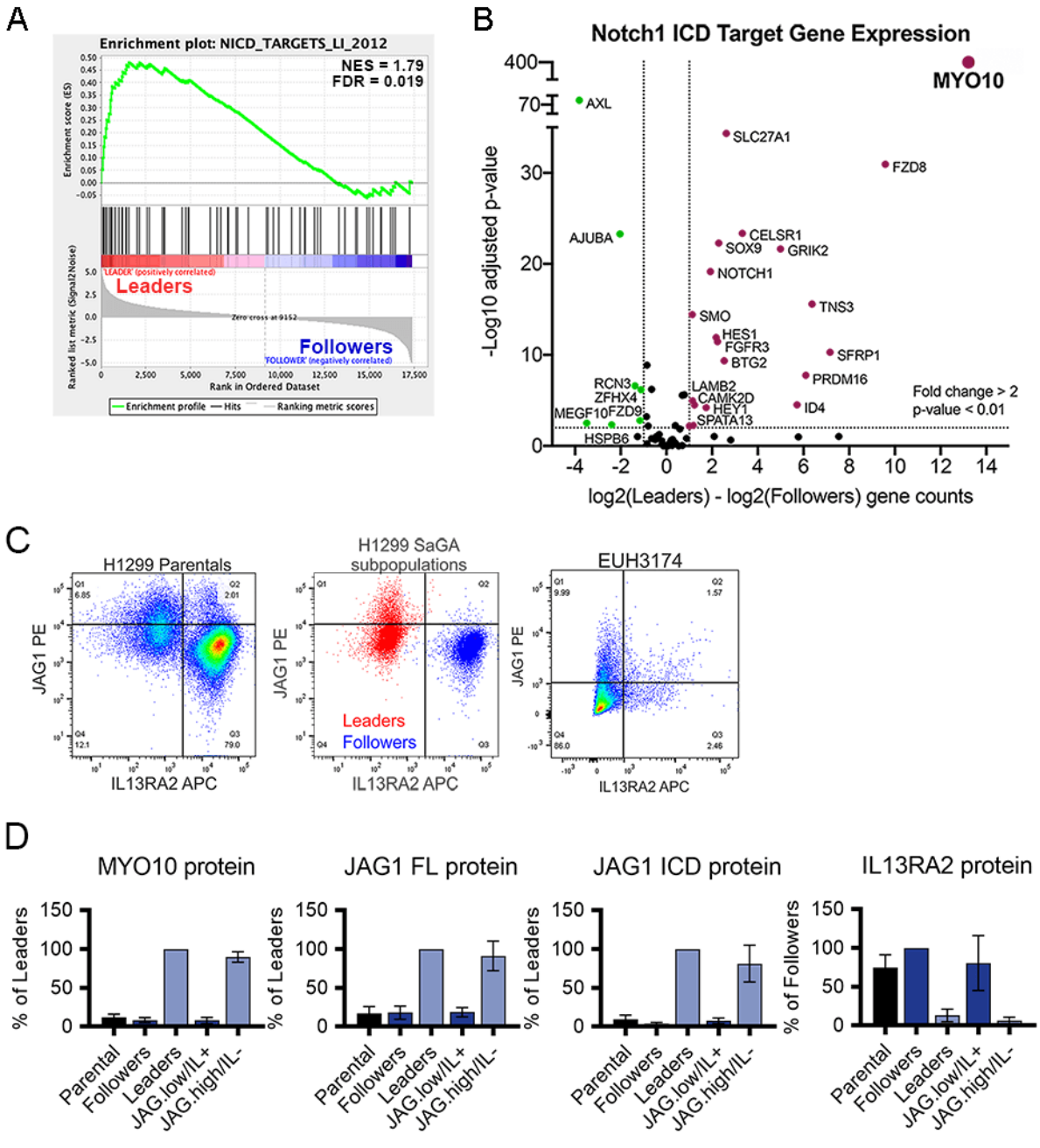


**Figure 3.5: Notch1 signaling upstream of MYO10 is enriched in leader cells, and JAG1 is highly expressed in leader-like cells within heterogeneous cancer cell populations.**

(**A**) Gene set enrichment analysis plot for RNAseq gene expression in leader cells (red) versus follower cells (blue), showing enrichment in leader cells for transcriptional targets of the Notch

intracellular domain (NICD) previously identified by ChIP-seq and gene expression analysis, including MYO10 (*208*). NES = 1.78, FDR = 0.019. (**B**) Volcano plot of the NICD targets in (**A**) significantly expressed in leader cells (magenta) or follower cells (green). (**C**) *Left*: Representative scatter plot of flow cytometry analysis of H1299 parental cells probed for the leader cell marker JAG1 (y-axis) or the follower cell marker IL13RA2 (x-axis), showing multiple populations with variable expression. Rainbow pseudo-coloring indicates density of cells on the plot. n = 3 independent biological replicates. *Center*: Scatter plot of flow cytometry of leader cells (red) and follower cells (cyan) probed for the leader cell marker JAG1 (y-axis) and the follower cell marker IL13RA2 (x-axis), showing separation of the two populations resembling the populations seen within the parental population. n = 3 independent biological replicates. *Right*: Scatter plot of flow cytometry of the EUH3174 patient-derived cells probed for the leader cell marker JAG1 (y-axis) and the follower cell marker IL13RA2 (x-axis), showing rare populations expressing these markers. Rainbow pseudo-coloring indicates density of cells on the plot. n = 2 independent biological replicates. (**D**) Quantification of Western blots in (**Fig. 3.4B**) of parental, follower, and leader cells as well as H1299 parental cells sorted for JAG1 and IL13RA2; blots probed for MYO10, JAG1 full length protein (FL), JAG1 intracellular domain (ICD), and IL13RA2, actin as the loading control. n = 3 independent biological replicates per condition.

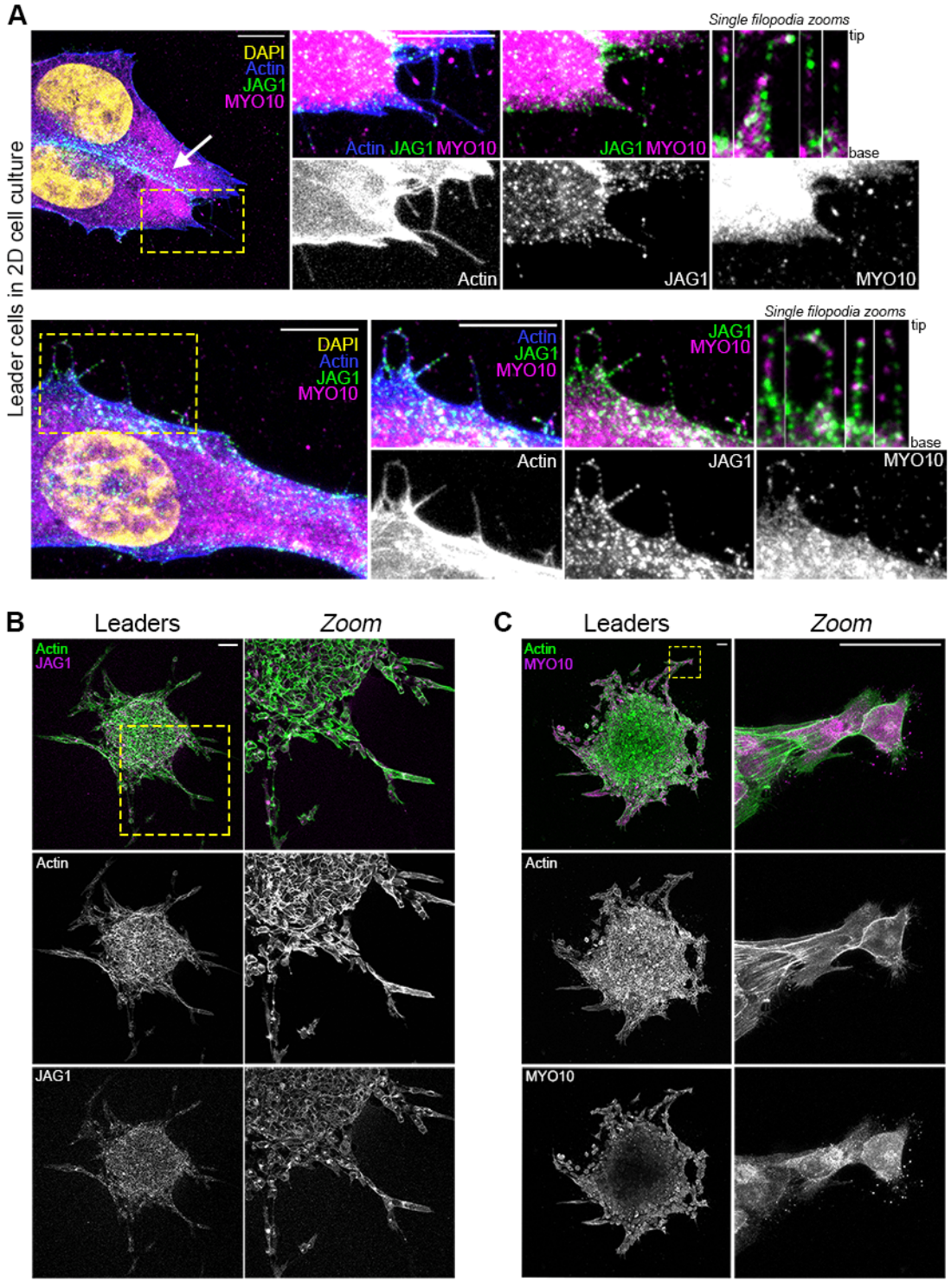


**Figure 3.6: MYO10 and JAG1 localization in leaders in 2D and 3D.**

(**A**) Two representative images of immunofluorescence for MYO10 and JAG1 in leader cells in 2D cell culture. Actin stained with phalloidin, and DNA stained with DAPI. Yellow dashed box indicates area of zoom. Yellow = DAPI, blue = actin, green = JAG1, magenta = MYO10; greyscale images labeled individually. Brightness uniformly enhanced post-acquisition in all digital zoom images to increase visibility of faint filopodial structures. Additional zoomed images of four filopodia from each cell are shown, in order from left to right according to their location in the first zoomed image. n = 2 biological replicates, N = 22 fields of view. Scale bar = 10 μm. (**B**) Representative maximum projection z-stack images showing JAG1 immunofluorescence within a whole leader cell spheroid collectively invading through Matrigel. Actin stained with phalloidin. Yellow dashed box shows location of optical zoom. n = 3 independent experiments, 6 spheroids per replicate. Scale bar = 50 μm. (**C**) Representative maximum projection z-stack images showing MYO10 immunofluorescence within a whole leader cell spheroid collectively invading through Matrigel. Actin stained with phalloidin. Yellow dashed box shows location of optical zoom. n = 3 independent experiments, 6 spheroids per replicate. Scale bar = 50 μm.

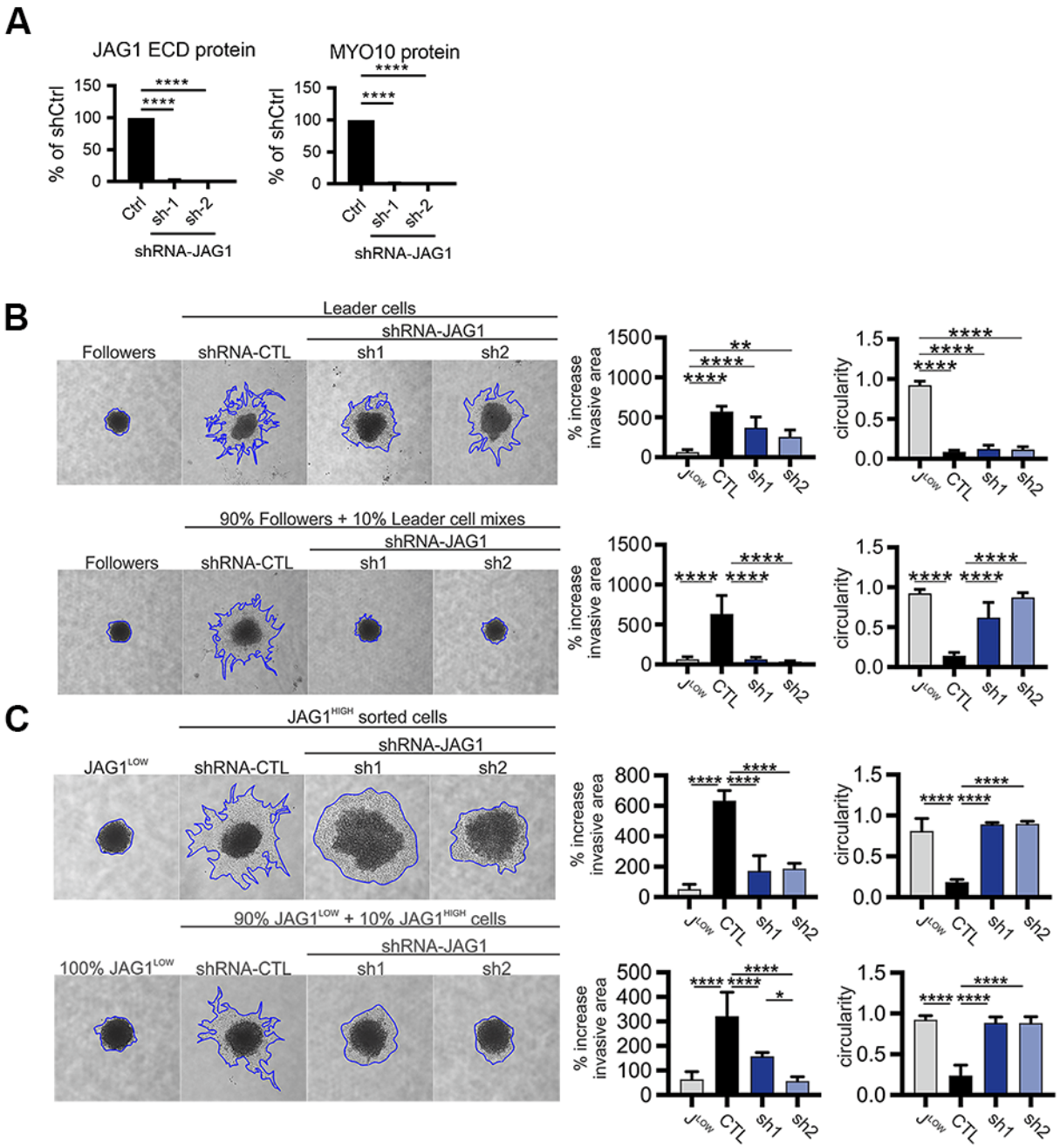


**Figure 3.7: JAG1 is essential for leader-driven collective invasion.**

(**A**) Quantification of western blots in (**Figure 3.4E**) assessing JAG1 and MYO10 expression in H1299 leader cells ectopically expressing either a control shRNA (Ctrl) or one of two different

shRNAs targeting JAG1 (sh-1, sh-2); actin as a loading control. (**B**) *Top*: Representative images and quantification of spheroid invasion assays of follower cells or 100% leader cells with control shRNA (shRNA-CTL) or shJAG1. *Bottom*: Representative images and quantification of spheroid invasion assays of 100% follower cells or mixes of 90% follower cells plus 10% leader cells. The 10% leader cells in each mixed population were expressing the indicated shRNA. n = 3 independent biological replicates. (**C**) *Top*: Representative images and quantification of spheroid invasion assays of 100% $JAG1^{LOW}$ FACS sorted H1299 cells or 100% $JAG1^{HIGH}$ FACS sorted H1299 cells expressing control shRNA or shRNA-JAG1. *Bottom*: Representative images and quantification of spheroid invasion assays of 100% $JAG1^{LOW}$ FACS sorted H1299 cells or with mixes of 90% $JAG1^{LOW}$ sorted cells plus 10% $JAG1^{HIGH}$ sorted cells. The 10% $JAG1^{HIGH}$ sorted cells in each mixed population were expressing the indicated shRNA (quantified in **Fig. 3.4E** and **3.7A**). (**A-C**) For all panels unless otherwise indicated: n = 3 independent biological replicates. Ordinary one-way ANOVA with Tukey's correction for multiple comparisons. For all panels, * $p < 0.05$, ** $p < 0.01$, *** $p < 0.001$, and **** $p < 0.0001$.

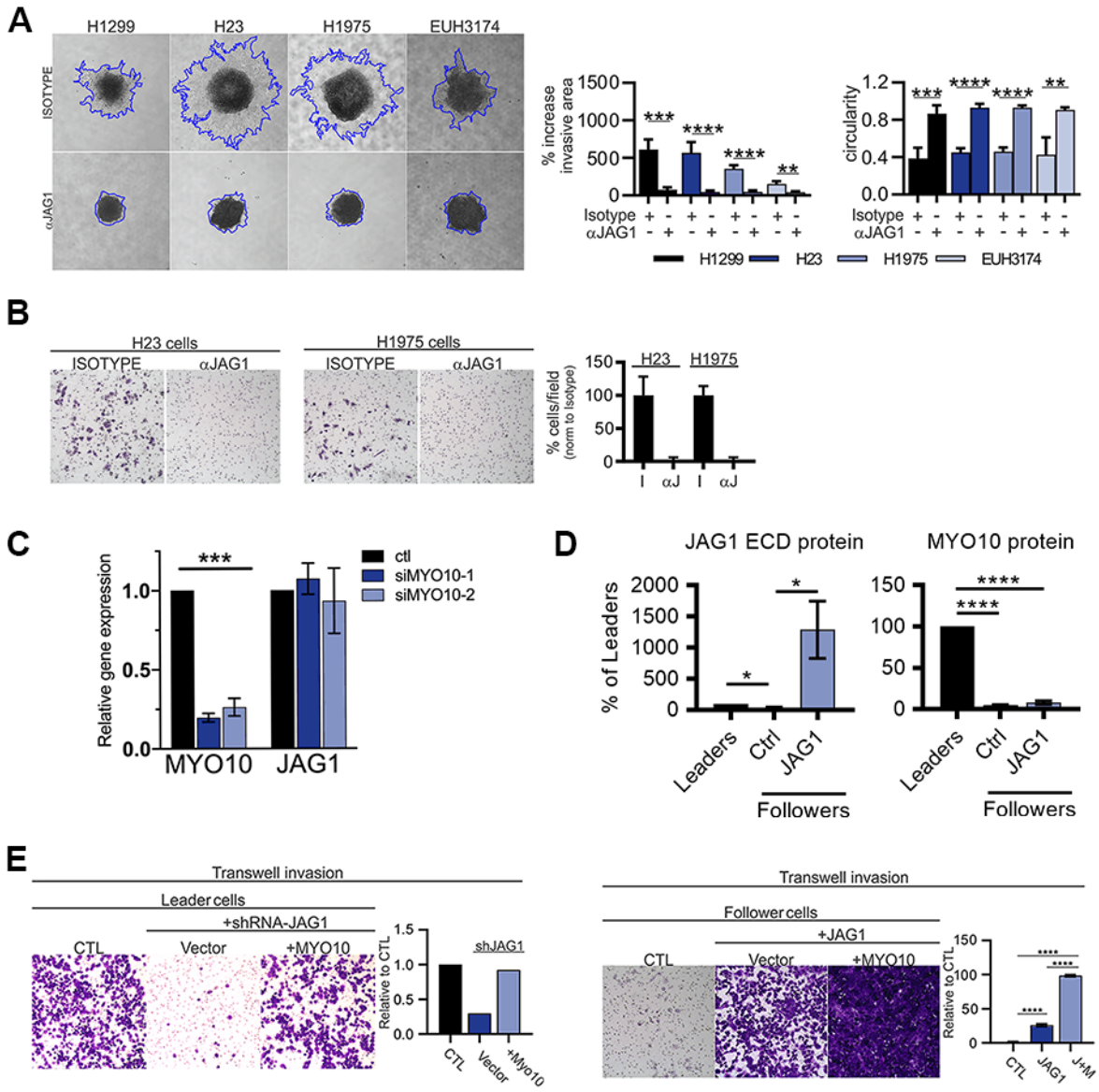


**Figure 3.8: JAG1 regulates collective invasion through MYO10.**

(**A**) Representative images and quantification of spheroid invasion assays of three NSCLC cell lines and one NSCLC patient-derived organoid (EUH3174) with an isotype control antibody or an anti-JAG1 blocking antibody (αJAG1). Two-tailed unpaired t-test between each cell type pair. (**B**) Representative images and quantification of transwell invasion assays of H23 and H1975 cells

with isotype control antibody (Isotype or I) or an anti-JAG1 blocking antibody (αJAG1 or αJ). (**C**) qPCR of mRNA extracted from leader cells expressing a control siRNA or siRNA-MYO10, showing decreased expression of MYO10 but not JAG1, normalized to GAPDH expression. n = 3 independent biological replicates. (**D**) Quantification of western blots in (**Fig. 3.4F**) assessing protein expression of JAG1 and MYO10 in H1299 leader cells, or follower cells ectopically expressing either an empty vector control (Ctrl) or JAG1 (JAG1); actin as the loading control. n = 3 independent biological replicates per condition. (**E**) Left: Representative images and quantification of transwell invasion assays of leader cells expressing a control empty vector alone, empty vector plus shRNA-JAG1, or GFP-MYO10 plus shRNA-JAG1. n = 1 independent biological replicate. Right: Representative images and quantification of transwell invasion assays of follower cells expressing a control empty vector alone, empty vector plus JAG1 overexpression, or GFP-MYO10 plus JAG1 overexpression. n = 3 independent biological replicates. Ordinary one-way ANOVA with Tukey's correction for multiple comparisons. For all panels, * $p < 0.05$, ** $p < 0.01$, *** $p < 0.001$, and **** $p < 0.0001$.

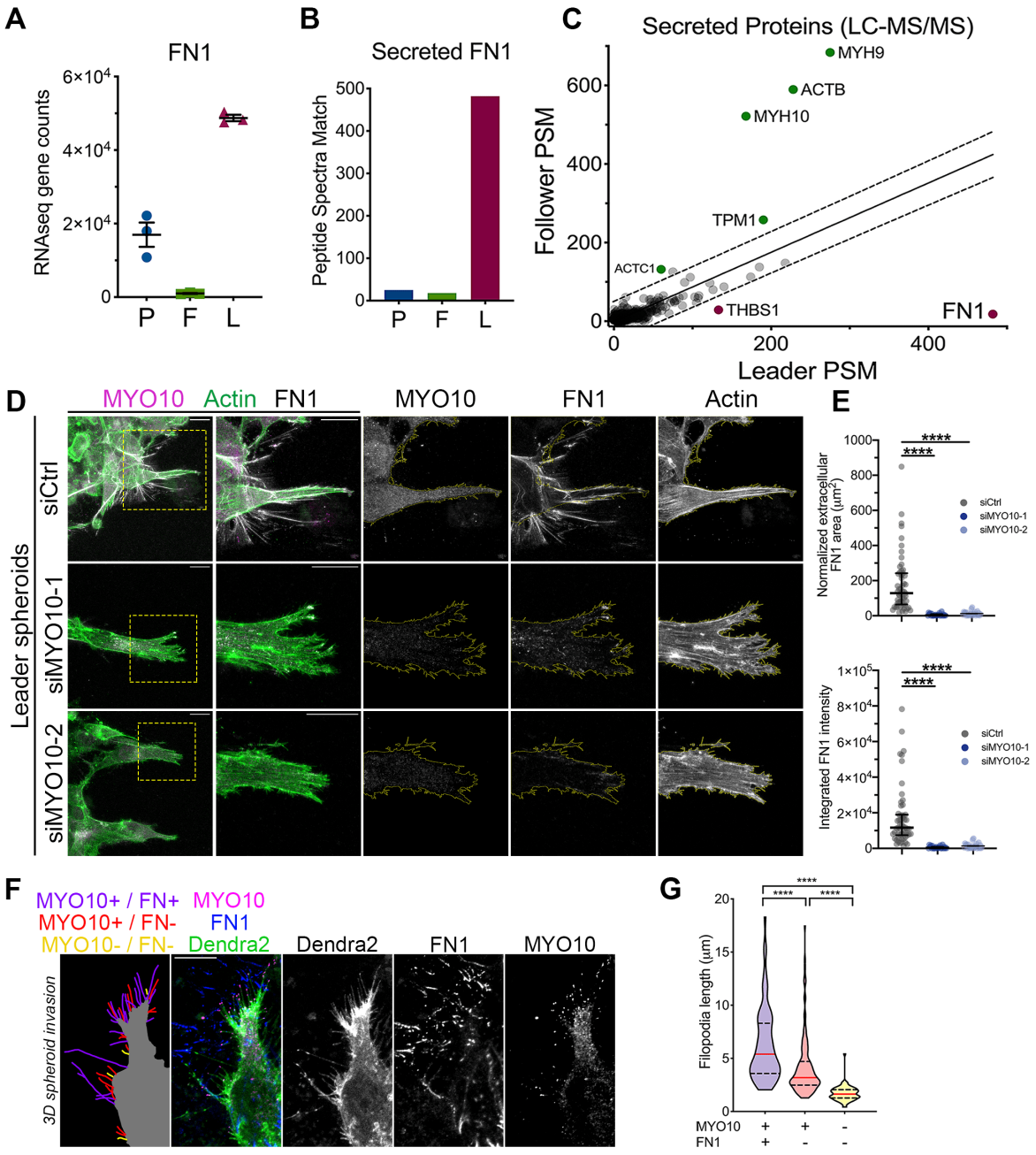


**Figure 3.9: MYO10 regulates alignment of extracellular fibronectin at the leading edge of 3D invasion**

(**A**) Representative FN1 immunofluorescence image and optical zooms of a H1299 leader cell spheroid invading through Matrigel. Actin was stained with phalloidin. Box indicates location of

zoom. Arrowheads indicate locations of linear extracellular FN micropatterning (**B**) Representative FN1 immunofluorescence images and optical zoom of a representative H1299 follower cell spheroid cultured in Matrigel. (**C**) Representative FN1 immunofluorescence images and optical zoom of a H1299 follower cell spheroid cultured in Matrigel mixed with 10 μg/mL human plasma FN. **(A-C)** Box indicates location of zoom. n = 3 biological replicates per condition, N = 6 spheroids imaged per condition per replicate. Scale bar, 20 μm.

| Protein | Symbol | PSM Leaders | PSM Followers |
|---|---|---|---|
| Fibronectin (WT and isoform 15) | FN1 | 482 | 18 |
| Thrombospondin-1 | THBS1 | 133 | 29 |
| Laminin subunit gamma 2 | LAMC2 | 0 | 30 |
| Fibrillin-1 | FBN1 | 0 | 14 |
| Collagen alpha-1 (VI) | COL6A1 | 13 | 40 |
| Transforming growth factor b2 | TGFB2 | 6 | 1 |
| TGF-b induced protein | TGFBI | 0 | 15 |
| Latent-TGFb-binding protein 2 | LTBP2 | 0 | 8 |
| Latent-TGFb-binding protein 4 | LTBP4 | 0 | 8 |
| Matrix metalloproteinase-2 | MMP2 | 38 | 7 |
| uPAR | PLAUR | 5 | 14 |
| VEGF-C | VEGFC | 1 | 6 |
| Jagged-1 | JAG1 | 8 | 0 |

**Figure 3.10: Proteomics of secreted proteins from leader cells and follower cells reveals potential pathways to regulate collective invasion.**

Table listing a subset of approximately 1800 proteins identified in the conditioned media of leader cells or follower cells. Briefly, parental cells, leader cells, or follower cells were cultured in serum-free media for 48 hours before the media was removed, purified, concentrated, and processed by LC/MS-MS. PSM = Peptide Spectral Match, a semi-quantitative measure of protein detected in each sample. PSM shown here is the sum of all PSM for each isoform of the protein detected in leader or follower samples minus the PSM detected in serum-free media alone. Orange rows = extracelluar matrix proteins; grey rows = TGFb-related proteins; green rows = other.

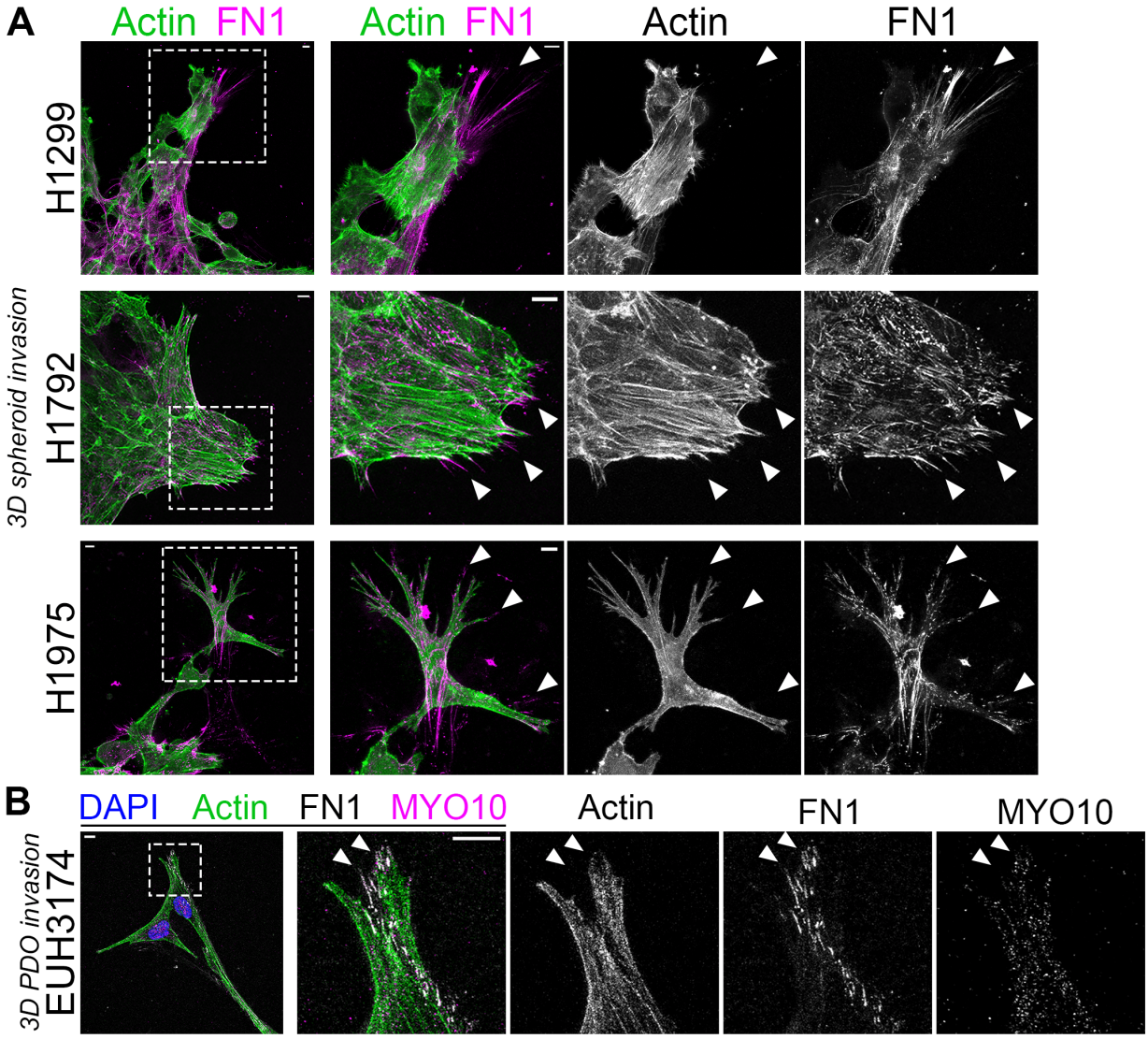


**Figure 3.11: NSCLC leader cells micropattern endogenous FN at the leading edge of 3D collective invasion.**

(**A**) Representative immunofluorescence images of FN1 in spheroid invasion assays of H1299, H1792, and H1975 cell lines. Actin was stained with phalloidin. Scale bar, 10 μm. n = 3 independent biological replicates with at least 6 spheroids per replicate. (**B**) Representative immunofluorescence images of FN1 and MYO10 in spheroid invasion assays of the NSCLC

patient-derived EUH3174 cells. Actin was stained with phalloidin. DNA was stained with DAPI. n = 2 independent biological replicates with at least 3 spheroids per replicate. (**A-B**) Box indicates zoomed region of image. Arrowheads indicate examples of linear FN micropatterning extending past the leader cells within collective invasion chains. Scale bar, 10 μm.

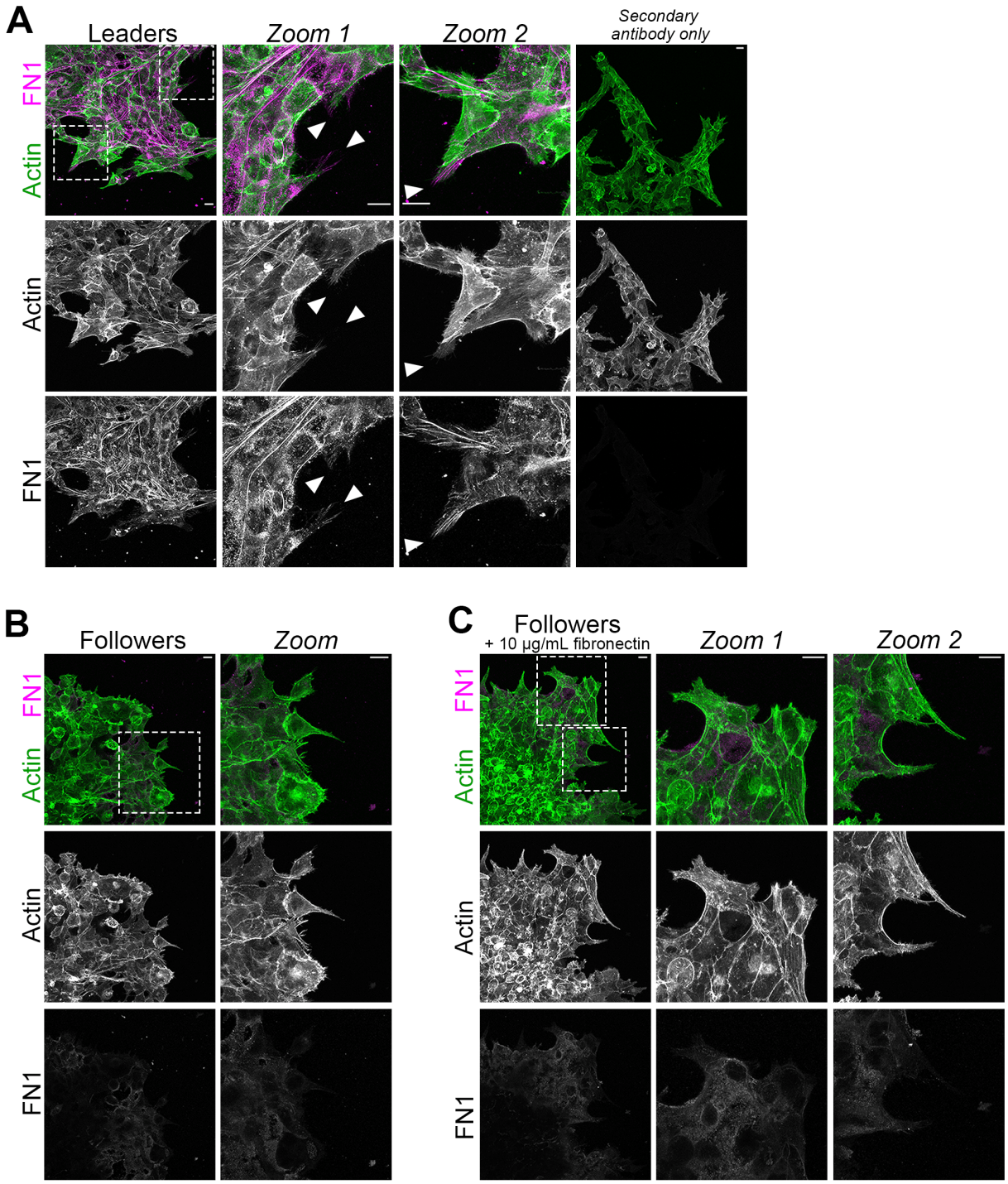


**Figure 3.12: Follower cells lack the ability to align extracellular fibronectin.**

(**A**) Representative FN1 immunofluorescence image and optical zooms of a H1299 leader cell spheroid invading through Matrigel. Actin was stained with phalloidin. Box indicates location of

zoom. Arrowheads indicate locations of linear extracellular FN micropatterning (**B**) Representative FN1 immunofluorescence images and optical zoom of a representative H1299 follower cell spheroid cultured in Matrigel. (**C**) Representative FN1 immunofluorescence images and optical zoom of a H1299 follower cell spheroid cultured in Matrigel mixed with 10 μg/mL human plasma FN. (A-C) Box indicates location of zoom. n = 3 biological replicates per condition, N = 6 spheroids imaged per condition per replicate. Scale bar, 20 μm.

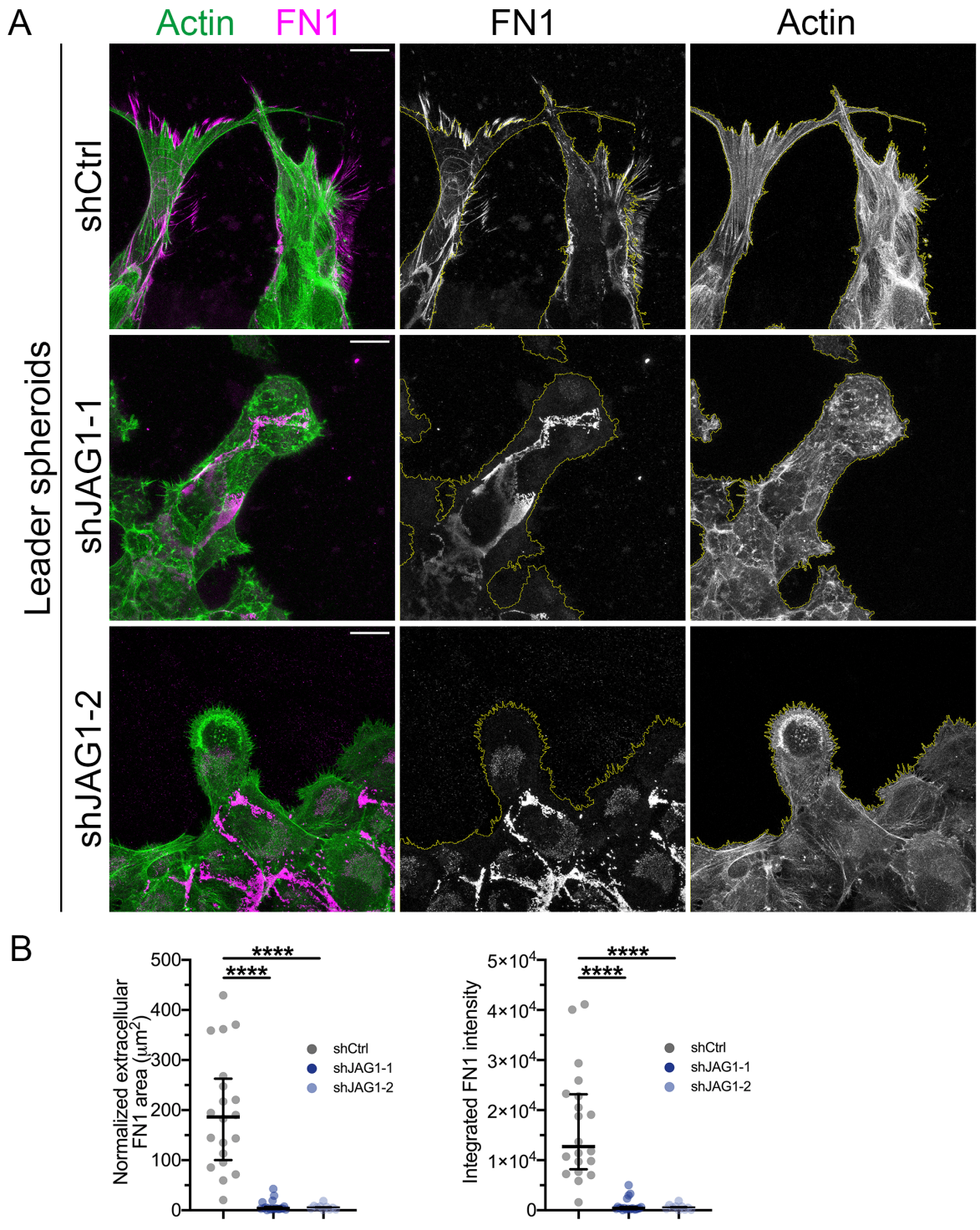


**Figure 3.13: Loss of JAG1 inhibits fibronectin fibrillogenesis.**

(**A**) Representative immunofluorescence images of FN1 in spheroid invasion assays of H1299 leader cells ectopically expressing either an shRNA control vector (shCtrl) or shRNA targeting

JAG1 (shJAG1-1, shJAG1-2). Actin was stained with phalloidin. Scale bar, 10 μm. Yellow outline indicates cell borders detected by thresholding the phalloidin signal. (**B**) Quantification of normalized extracellular FN1 area (left) or integrated FN1fluorescence intensity (right; FN1 surface area multiplied by 8-bit fluorescence signal intensity within that area) within the extracellular area excluded from the phalloidin thresholding outlined in (**A**). Kruskal-Wallis test with Dunn's multiple comparison test. n = 2 biological replicates with N = 20 fields of view per condition. **** $p < 0.0001$.

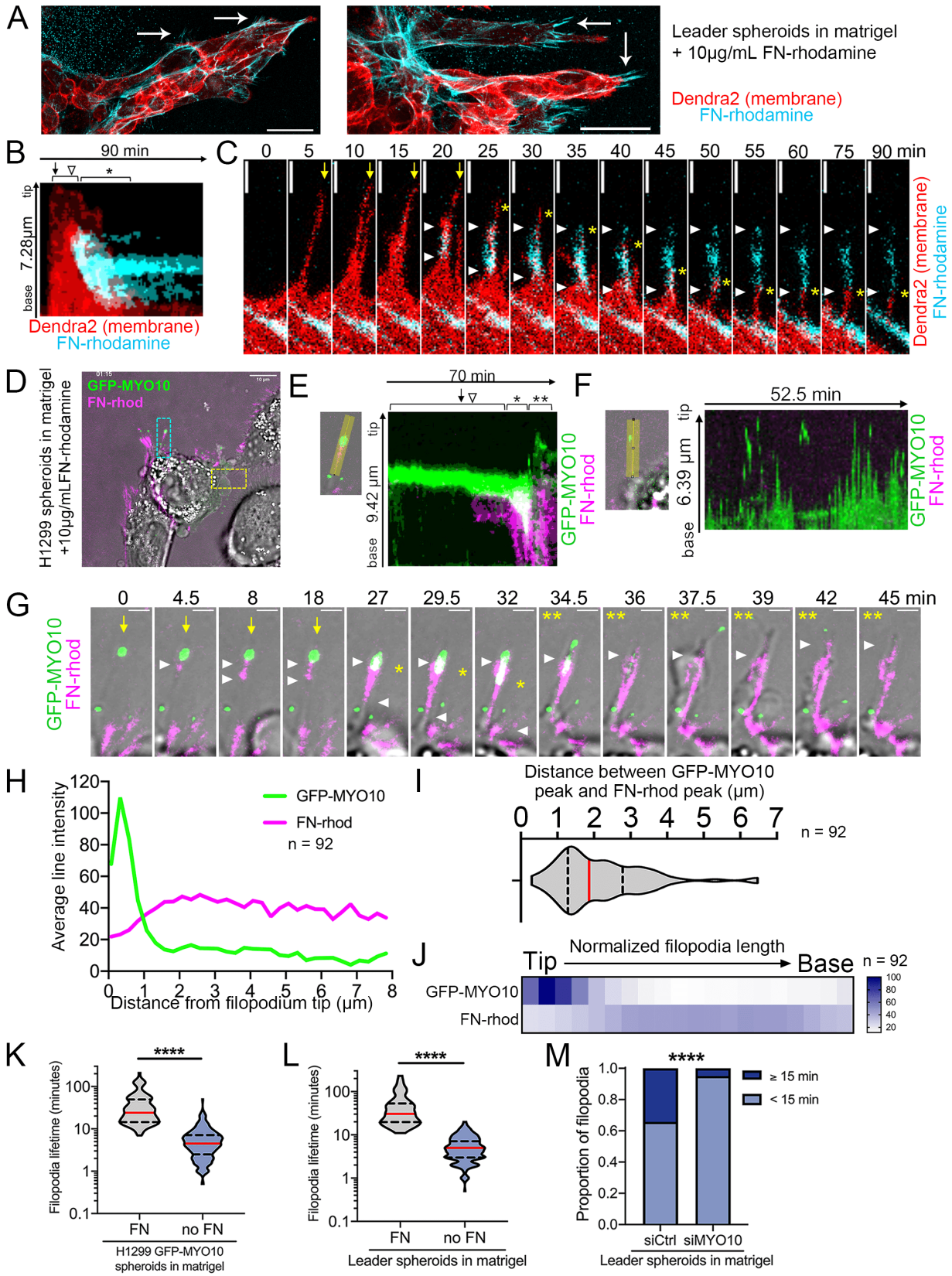
A
Leader spheroids in matrigel
+ 10µg/mL FN-rhodamine
Dendra2 (membrane)
FN-rhodamine
B
90 min
tip
7.28µm
base
Dendra2 (membrane)
FN-rhodamine
C
0 5 10 15 20 25 30 35 40 45 50 55 60 75 90 min
Dendra2 (membrane)
FN-rhodamine
D
H1299 spheroids in matrigel
+10µg/mLFN-rhodamine
GFP-MYO10
FN-rhod
E
70 min
tip
9.42 µm
base
GFP-MYO10
FN-rhod
F
52.5 min
tip
6.39 µm
base
GFP-MYO10
FN-rhod
G
0 4.5 8 18 27 29.5 32 34.5 36 37.5 39 42 45 min
GFP-MYO10
FN-rhod
H
Average line intensity
GFP-MYO10
FN-rhod
n = 92
Distance from filopodium tip (µm)
I
Distance between GFP-MYO10
peak and FN-rhod peak (µm)
n = 92
J
Normalized filopodia length
Tip
Base
n = 92
GFP-MYO10
FN-rhod
K
Filopodia lifetime (minutes)
****
FN
no FN
H1299 GFP-MYO10
spheroids in matrigel
L
Filopodia lifetime (minutes)
****
FN
no FN
Leader spheroids in matrigel
M
Proportion of filopodia
****
≥ 15 min
< 15 min
siCtrl
siMYO10
Leader spheroids in matrigel

**Figure 3.14: MYO10 drives leader cell filopodia persistence and fibronectin micropatterning.**

(**A**) Representative live cell image of a spheroid invasion assay of leader cells expressing membrane-bound Dendra2 (red) embedded into rBM mixed with 10 μg/mL FN-rhodamine (cyan). Arrows indicate linear FN micropatterning extending beyond the leading cells. n = 3 independent biological replicates. Scale bar, 50μm. (**B**) Representative kymograph spanning 90 minutes, showing line profile fluorescence intensity of Dendra2 and FN-rhodamine along a single leader cell filopodium forming a FN fibril during 3D collective spheroid invasion. x-axis = time and y-axis = length of the line profile (μm). Arrow indicates filopodium tip pause, arrowhead indicates when nascent FN fibril is first visible, and asterisk indicates filopodia retraction. (**C**) Time lapse montage of the filopodium in **(B)**. Time (min) above each image. Yellow arrow indicates filopodium tip pause, white arrowheads indicate the upper and lower boundaries of nascent FN puncta. Yellow asterisk indicates filopodia retraction. Scale bar, 2 μm. For (**A-C**), n = 5 biological replicates, and N = 112 filopodia line plots analyzed from 9 spheroids total. (**D**) Representative live cell image of a spheroid invasion assay of H1299 cells expressing GFP-MYO10 (green) embedded into rBM mixed with 10 μg/mL FN-rhodamine (magenta). n = 4 independent biological replicates. Cyan box indicates zoom shown in (**E**), yellow box indicates zoom shown in (**F**). Scale bar, 10 μm. (**G**) Time lapse montage from live cell imaging of the H1299 GFP-MYO10 filopodium seen in (**E**). Time in minutes indicated above each image. Yellow arrow indicates filopodium pause. White arrowheads indicate the upper and lower boundaries of the nascent FN puncta. Yellow asterisk indicates filopodia retraction. Double asterisk indicates a second extension of the filopodia and slight distal elongation of the FN fibril. Scale bar, 2μm. (**H**) Line plot of the average fluorescence intensity (8-bit grey value, arbitrary unit) of GFP-MYO10 and FN-rhodamine along

the length of individual H1299 GFP-MYO10 filopodia from tip to base during 3D collective invasion. n = 4 biological replicates, N = 92 filopodia. (**I**) Violin plot showing the distance (μm) between the peak of MYO10-GFP and the peak of FN-rhodamine for each of the 92 filopodia in (**H**). Red = median, and black dashed lines = interquartile range (IQR). (**J**) Heatmap showing the line plot intensity values (8-bit grey value, arbitrary unit) from the filopodia in (**H-I**), distance normalized from base to tip across all filopodia. For (**D-J**), n = 5 biological replicates, and N = 92 filopodia line plots analyzed from 10 spheroids total. (**K**) Violin plots displaying the lifetime of H1299 GFP-MYO10 filopodia during 3D collective invasion as seen in (**D-J**), comparing the lifetimes of filopodia associated with FN-rhodamine fibrillogenesis and filopodia that were not. n = 4 biological replicates, N = 347 filopodia. Red line = median, and black dashed lines = interquartile range (IQR). For filopodia associated with FN: N = 105 filopodia, median = 24.0 minutes, IQR = 14.5 – 49.5 minutes. For filopodia not associated with FN: N = 242 filopodia, median = 4.5 minutes, IQR = 2.5 – 7.125 minutes. Mann-Whitney U-test, two-tailed. (**L**) Violin plots displaying the lifetime of Dendra2-expressing leader cell filopodia during 3D collective invasion as seen in **(A-C),** comparing the lifetimes of filopodia that participated in FN-rhodamine fibrillogenesis and filopodia that did not. n = 3 biological replicates, N = 344 filopodia. Red line = median, and black dashed lines = interquartile range (IQR). For filopodia associated with FN: N = 110 filopodia, median = 30.5 minutes, IQR = 19.5 – 53.0 minutes. For filopodia not associated with FN: N = 234 filopodia, median = 5.0 minutes, IQR = 3.0 – 7.125 minutes. Mann-Whitney U-test, two-tailed. (**M**) Proportion of leader cell filopodia quantified with a lifetime < 15 minutes (light blue) or ≥ 15 minutes (dark blue) within invading spheroids of leader cells expressing siCtrl or siMYO10. Two-tailed Fisher's exact test. For all panels, * $p < 0.05$, ** $p < 0.01$, *** $p < 0.001$, and **** $p < 0.0001$.

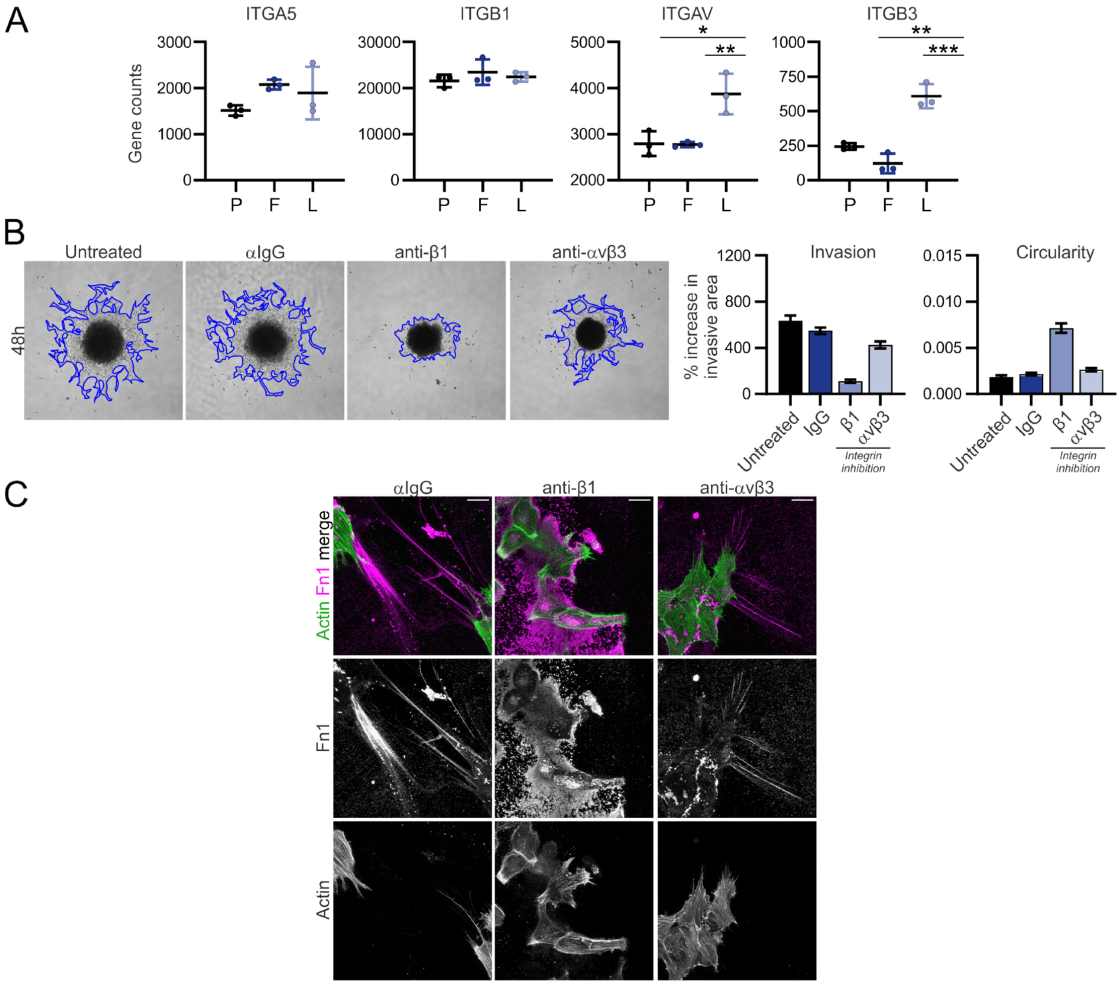


**Figure 3.15: Integrin β1 but not integrin αVβ3 facilitates fibronectin alignment during 3D collective invasion.**

(**A**) Normalized RNAseq gene counts for integrin expression within H1299 parentals, followers and leaders. n = 3 independent biological replicates. Ordinary one-way ANOVA with Tukey's correction for multiple comparisons. (**B**) Representative images and quantification of H1299 leader cell spheroid 3D invasion in rBM. Spheroids were either untreated or treated with 5ug/mL isotype-matched IgG, an inhibitory antibody against β1 integrin or an inhibitory antibody against αvβ3 and allowed to invade for 48h. (**C**) 3D immunofluorescence images showing Fn1 staining after antibody inhibition of β1 or αvβ3 integrin in the spheroids from (**B**).

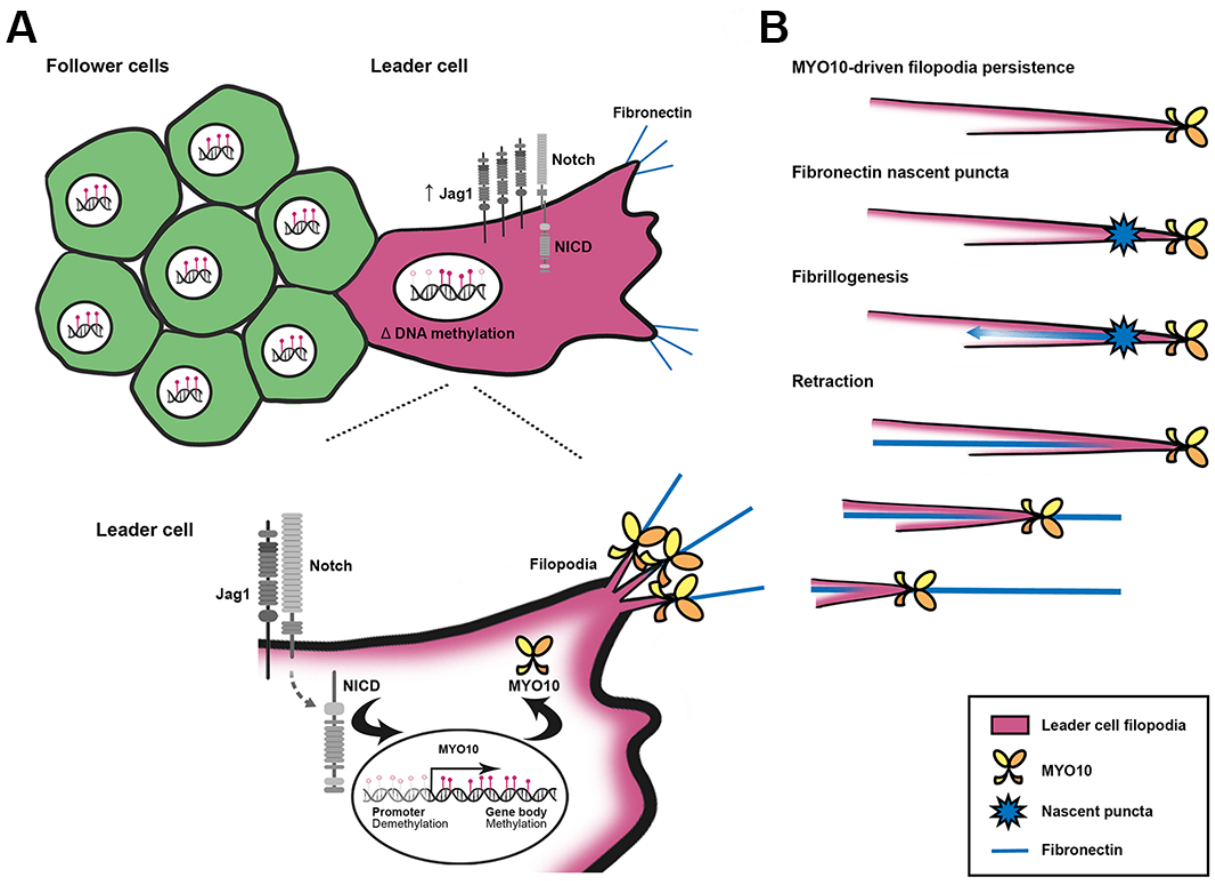


**Figure 3.16: Model of epigenetic heterogeneity within leader cells leading to MYO10-driven remodeling of fibronectin through filopodia.**

(**A**) A collective invasion pack containing two subpopulations of follower cells (green) and a leader cell (magenta), which show phenotypic and epigenetic heterogeneity. Compared to follower cells or the parental cells of origin, leader cells contain unique DNA methylation patterns and transcriptional programs, including enrichment for pathways related to Notch signaling, axon guidance, angiogenesis, and ECM-receptor interactions. In leader cells, the promoter of MYO10 is hypomethylated and the gene body is hypermethylated compared to follower cells and parental cells. The combination of permissive MYO10 DNA methylation and elevated JAG1 expression/Notch activation within leader cells results in overexpression of MYO10 in leader cells.

(**B**) MYO10, a filopodial motor protein, drives filopodia elongation and persistence over time during 3D collective invasion. Once a MYO10-expressing filopodia persists in one location for ≥15 minutes, a nascent puncta of fibronectin (FN) initiates in line with the filopodia shaft, approximately 1.8 μm proximal to the MYO10 puncta at the tip. Fibrillogenesis elongates the FN puncta towards the cell body while the distal end of the FN fibril remains in place. As the filopodia retracts into the cell body, MYO10 remains at the tip of the retreating filopodia, but the FN fibril remains in place, leaving behind discrete linear micropatterns of FN extending past the cellular leading edge during 3D collective invasion. Loss of MYO10 or JAG1 profoundly inhibits this filopodia-dependent FN fibrillogenesis.

### 3.6 Discussion

We identified myosin-X *(MYO10)* as a key gene at the intersection of differential DNA methylation and expression in leader cells (Figs. 2.4 and 3.1). MYO10 is an unconventional myosin that regulates the formation and elongation of filopodia as well as other actin-based protrusions that are important for cancer invasion, such as filopodia-like long protrusions and invadopodia (*143, 144*). MYO10 loss in mice leads to severe developmental defects in several collective migration-dependent processes (*162-164*), which suggests that MYO10 regulates collective migration in development as well as cancer. We show that MYO10 is enriched in leader cells across multiple NSCLC cell lines and a patient-derived lung NSCLC cell line, and we further demonstrate that MYO10-driven filopodia are critical for leader-driven lung cancer collective invasion (Figs. 3.1-3.2). In addition, MYO10 overexpression is sufficient to induce follower cell collective invasion (Figs. 3.2-3.3). Importantly, we show how MYO10 affects filopodia elongation and persistence in a 3D ECM (Fig. 3.2A-C). While MYO10-driven effects on filopodia have been well-documented on 2D surfaces (*143, 144*), we provide some of the first analysis of filopodia length and dynamics within 3D collective cancer invasion. In addition, while MYO10 has been shown to regulate cancer cell invasion and metastasis (*149, 163, 165*), we present the first evidence that MYO10 expression in only a rare subset of cells (*i.e.* leader cells) rather than the entire population is sufficient to induce tumor cell collective invasion.

Transcriptional regulation of *MYO10* is poorly understood, and our results support the model that both promoter DNA hypomethylation and JAG1/Notch transcriptional activity cooperate to drive *MYO10* expression in leader cells. We identify the Notch ligand, JAG1, as a leader-specific marker and as a transcriptional activator of *MYO10* (Figs. 3.4-3.5). JAG1 was detected in the rare leader cell population not only during spheroid collective invasion (Fig. 3.4B-

C), but it was also detected by flow cytometry within a small population of the parental H1299 cell line and within a rare subpopulation of a patient-derived NSCLC sample (Fig. 3.5C). JAG1 knockdown or inhibition significantly abrogated collective 3D invasion of several cell lines, the patient-derived sample, and mixed populations of leader and follower cells (Figs. 3.4J-K, 3.7B-C, 3.8A). In many cancers, JAG1 expression promotes cancer stem cells, tumor invasion, metastasis, and poor patient outcome (*206, 219*). JAG1 is also highly expressed in breast cancer leader cells (*50*), suggesting that JAG1 may regulate leader cells across other cancer types beyond breast and lung cancer.

Notch pathway signaling and downstream transcriptional targets are strongly enriched in leader cells compared to follower cells (Figs. 2.3, 3.4, 3.5), but JAG1 was the Notch family member most robustly upregulated in leader cells (Fig. 3.4A). We demonstrate that JAG1 upregulates *MYO10* expression; *JAG1* knockdown significantly decreased *MYO10* mRNA and protein expression, whereas *MYO10* knockdown did not affect *JAG1* expression (Figs. 3.4D-E, 3.7A), suggesting that JAG1 is upstream of MYO10. We also show that *JAG1* knockdown significantly decreased filopodia length, consistent with a loss of *MYO10* expression (Fig. 3.4H-I). Interestingly, *JAG1* overexpression in follower cells did not induce *MYO10* expression (Figs. 3.4F, 3.8C-D) and also did not demethylate the *MYO10* promoter (Fig. 3.4G). These data suggest that JAG1 expression without other subsequent epigenetic changes to chromatin availability observed in leader cells (*e.g.* MYO10 promoter DNA hypomethylation) is not sufficient to induce MYO10 expression. In addition, Notch signaling gene sets were significantly enriched in leaders compared to followers (Figs. 2.1G, 2.3, 3.5A-B), and JAG1 was strongly localized to cell-cell contacts between leader cells (Figs. 3.4C, 3.6). Since JAG1 was frequently present in clusters of 2-4 leader cells within invading parental spheroids (Fig. 3.4C), we propose that leader cells

participate in trans-activation of JAG1 and Notch across two adjacent leader cells, rather than between leader and follower cells (*205*). Notch signaling often undergoes context-dependent spatiotemporal regulation (*205, 220*) and therefore questions remain about how Notch/JAG1 interact to coordinate transcription within the collective invasion pack.

Cell-ECM interactions regulate several aspects of collective cancer invasion, including integrin-FAK motility signaling, MMP-driven proteolysis of the ECM, and deposition and remodeling of ECM components (*32, 51, 221*). Here, we show that leader cells but not follower cells secrete and align fibronectin into long linear fibrils extending past the leading edge (Figs. 3.9-3.14). Fibronectin fibrillogenesis is a complex process that involves integrin engagement with soluble FN dimers, reorganization of the actin cytoskeleton, and translocation of integrin-FN complexes along actin filaments to form mature fibrillar adhesions (*215, 222*). Studies of FN fibrillogenesis have focused primarily on adhesion sites within the cell body, but questions remain as to how the fibrillogenesis that we observed within the shafts of filopodia at the leading edge of 3D invasion differs from canonical fibrillogenesis along the basal surface of the cell body.

Cell-ECM adhesion sites can form within filopodia tips or shafts, but the core components of these nascent filopodia adhesions lack many proteins that transmit traction forces seen in canonical focal adhesions or mature fibrillar adhesions (*133*). Nascent filopodia adhesions can mature into focal adhesions after lamellipodial advancement (*136*). Our live cell imaging shows that while most FN fibrillogenesis occurred beneath the basal surface of the cell body in advancing leader cells, FN fibrillogenesis could catalyze within the shaft of stabilized MYO10-expressing filopodia (Figs. 3.9, 3.14). Concomitant with filopodia tip retraction, nascent FN puncta elongated from the proximal end of the fibril, while the distal end remained in place. In many cases, the distal end of the FN fibril remained anchored to the ECM while the proximal end of the FN fibril

continued to elongate under the cell body even after the filopodia completely retracted, leaving long FN "tracks" extending in front of the leading cell, parallel to the direction of collective invasion (Fig. 3.14A-G). This observation of multi-step FN fibril elongation is consistent with focal adhesions maturing into fibrillar adhesions during FN fibrillogenesis observed underneath the basal surface of the cell body (*222*). However, these nascent filopodial adhesions likely differ from canonical focal adhesions in their integrin and intracellular components (*133, 136*). Understanding how these filopodial adhesions mature into focal adhesions and how they transmit traction forces capable of remodeling the extracellular matrix (*i.e.* fibronectin fibrillogenesis) remain areas of keen interest.

Notably, nascent FN fibrils initiated approximately 1.8μm behind the filopodia tip and were not co-localized with MYO10-GFP in live cell imaging (Fig. 3.14H-J). This suggests that MYO10 does not directly interact with FN. However, MYO10+ leader cell filopodia had longer lifetimes than MYO10-knockdown filopodia during 3D invasion (Fig. 3.2C, 3.14M). We speculate that MYO10-driven filopodial persistence is necessary for forming nascent filopodial adhesions in the tip and/or shaft, engaging with FN, and maturing into larger focal adhesion sites capable of elongating nascent FN fibrils at the leading edge. Thus, in MYO10-knockdown cells, FN fibrillogenesis can still occasionally be seen beneath the cell body (Fig. 3.9D, 3.11-3.14), but MYO10-depleted cells form significantly fewer leading-edge FN tracks since these filopodia likely do not persist long enough to form nascent adhesions (Fig. 3.9D-E, 3.14M).

MYO10 induces filopodial longevity most likely in part through its ability to transport integrins into filopodia (*143, 150*). Structural studies confirm that MYO10 binds to β-integrins through its FERM domain, and functional studies suggest that MYO10 affects the localization of integrin α5 to filopodia tips as well (*148-150*). Since the integrin heterodimers α5β1 and αVβ3

are the predominant integrins responsible for FN fibrillogenesis (*215-217, 222*), we interrogated the expression and function of these four integrins within leader cells (Fig. 3.15). Leader cells expressed significantly more αV and β3 integrins compared to follower and parental cells, while all three cell types expressed comparable levels of α5 and β1 integrins (Fig. 3.15A). However, all three cell types expressed substantially more β1 integrin than any of the other three integrins. Integrin β1 in particular has long been implicated in cancer invasion and metastasis (*223*), so it is not entirely surprising that these cells express high levels of integrin β1. Furthermore, by functionally blocking each of these integrins separately with inhibitory antibodies, we determined that loss of integrin β1 function significantly abrogated both collective invasion and FN micropatterning, whereas inhibition of α5 alone (data not shown) or αVβ3 integrins did not affect either function (Fig. 3.15B-C). Thus, these data suggest that integrin β1, a MYO10 cargo protein, is a key component of filopodia-directed FN alignment. High-resolution microscopy would be necessary to identify whether integrin β1 localizes preferentially to the filopodia tip or shaft, as well as to identify additional molecular components of integrin β1 filopodial adhesion sites.

Even though integrin β1 directly binds to FN during fibrillogenesis (*213*), it is not yet known whether the same integrin β1-containing adhesion sites within filopodia that drive FN fibrillogenesis are the same adhesion sites that maintain filopodial stability, or whether different integrin heterodimers are responsible for this stability. Filopodia produce adhesion sites at both the tip and along the shaft that are unique in their protein composition compared to canonical focal adhesions (*133, 136*), but there has not yet been a thorough examination of which integrins localize to adhesion sites within one or both of these filopodial regions. Furthermore, it is possible that filopodial integrin composition varies depending on the microenvironment (2D vs 3D culture, differing matrix components, mechanical properties of the extracellular environment, etc.), and

elucidating the contributions of different integrins within filopodia remains an area of keen interest. In addition, further studies of traction forces within filopodia, how integrin activation and molecular components differ between filopodial tip and shaft adhesions, and how filopodial tip adhesions and shaft adhesions differentia affect filopodial dynamics and FN fibrillogenesis may elucidate how filopodia act not only as sensors of the extracellular environment but also as active participants in ECM remodeling. Ultimately, this study provides the first evidence that directly links MYO10 and stabilized filopodia to fibronectin alignment during 3D cancer invasion, which opens the intriguing possibility that filopodia may play a much more active role than previously thought during cancer invasion and metastasis.

# Chapter 4: Looking beyond the leading edge: Additional roles of MYO10 in regulating leader cell function

## 4.1 Author's Contribution and Acknowledgement of Reproduction

Portions of this chapter, including Figures 4.2-4.4 and associated text in the results and discussion, were reproduced with edits from: J. Konen, E. Summerbell, B. Dwivedi, K. Galior, Y. Hou, L. Rusnak, A. Chen, J. Saltz, W. Zhou, L. Boise, P. Vertino, L. Cooper, K. Salaita, J. Kowalski, A.I. Marcus. (2017). Image-guided genomics of phenotypically heterogeneous populations reveals vascular signaling during symbiotic collective cancer invasion. *Nature Communications* 8:15078.

For Figures 4.2-4.4: J.Konen and AIM designed the experiments. ES performed the experiments. J.Konen, ES, JS, WZ, LHB, PV, LC, KS, J.Kowalski, and AIM provided guidance on experimental design and wrote the manuscript.

For Figures 4.1 & 4.5-4.8 (unpublished data): ES and AIM designed the experiments. ES performed the experiments and analysis and wrote the associated parts of this chapter.

## 4.2 Abstract

In addition to localizing at the tips of long-lived leader cell filopodia at the front of collective invasion, MYO10 also localizes to additional subcellular compartments. Here, we show that MYO10 also localizes to retraction fibers and the cleavage midbody in mitotic cells but does not localize with the tubulin-rich spindle poles or centrosomes. Leader cells are poorly proliferative and frequently prone to mitotic errors compared to follower cells, but the mechanisms driving high mitotic error rates in leader cells are not yet known. When MYO10 was knocked down in leader cells, the rate of mitotic errors decreased significantly, most notably errors related to cell deformation leading to unstable cytokinesis. Thus, we predict that high MYO10 expression in mitotic leader cell retraction fibers and the cleavage furrow interfere with the mechanics of cell division. In addition, MYO10 localizes to filopodia at the rear of the cell where cell-cell adhesion with neighboring cells occurs. MYO10-expressing filopodia at both the front and rear of the cell co-localize with the vascular cell adhesion protein VE-cadherin but not N-cadherin. Thus, our data suggest that MYO10 acts not only within filopodia at the front of collective invasion and ECM remodeling but also regulates filopodia and filopodia-like structures during both mitosis and cell-cell adhesion within the collective invasion pack.

## 4.3 Introduction

Filopodia and filopodia-like structures occur not only along the dorsal edge of migrating cells, but also at the rear of the cell, at regions of cell-cell contact, and along the basal cell surface (*132*). Thus, it is likely that MYO10 contributes to the formation and stability of filopodia-like structures elsewhere beyond the leading edge. For example, MYO10 has been shown to localize to podosomes on the basal surface of osteoclasts (*224*) and also to the structurally similar invadopodia (*169*). Invadopodia are microtubule-containing filopodia-like structures that secrete matrix metalloproteases (MMPs) and are concentrated sites of ECM proteolysis; this function allows invading cancer cells to "bulldoze" a path through the ECM (*225*). In breast cancer cell lines, MYO10 localizes to the tips of invadopodia, and knockdown of MYO10 inhibits the formation of invadopodia and decreases ECM proteolysis (*165, 169*).

In addition, filopodia or filopodia-like structures play a role in forming cell-cell adhesions during both development and epithelial cell homeostasis. During the earliest stages of embryo development, long filopodia that contain E-cadherin are crucial for maintaining cell-cell contacts and compacting the embryo to the proper size and shape (*226*). Furthermore, when epithelial cells form new cell-cell contacts, cadherin complexes at the tips of filopodia in two neighboring cells form an interdigitated "zipper" that facilitates the formation of mature adherens junctions and complete cell-cell adhesion (*227*). Consistent with the fact that filopodia localize to sites of cell-cell adhesion, MYO10 also localizes to newly-forming regions of cell-cell adhesion in polarized epithelial cell monolayers, and loss of MYO10 delays the formation and disrupts the integrity of both adherens junctions and tight junctions (*228, 229*). In addition, MYO10 contributes to the integrity of newly-formed blood vessels during angiogenesis by transporting VE-cadherin to the tips of long filopodia in endothelial tip cells (similar to leader cells) (*230*).

Another filopodia-like structure that expresses MYO10 is retraction fibers. Retraction fibers are actin-rich filopodia-like structures that tether rounded-up mitotic cells to the extracellular substrate during mitosis to compensate for the lack of mature focal adhesions that normally anchor the cell body during interphase (*231, 232*). Retraction fibers play a critical role in properly orienting the spindle poles by connecting the detached cell body to the extracellular matrix (*130, 233*). In turn, proper spindle pole orientation is critical for maintaining the integrity of chromosome separation and preventing aneuploidy, which could lead to cancer-promoting genomic alterations or cell death (*234, 235*).

In addition to containing an actin-binding domain, MYO10 contains a MyTH4 domain that is capable of binding to microtubules, including binding to microtubule-based spindle poles (*141, 236*). MYO10 localizes to the spindle poles of *Xenopus laevis* embryos and has been implicated as a regulator of spindle assembly and mitotic progression in these cells *(236-238)*. MYO10 does not directly localize to the spindle poles in mammalian cells, yet loss of MYO10 leads to improper spindle pole orientation, most likely due to the role of MYO10 within retraction fibers (*228, 233*). Thus, many questions remain as to how MYO10 functionally coordinates spindle orientation in mammalian cells without localizing to the spindle poles themselves, whether by its actin-binding properties, its tubulin-binding properties, and/or transporting cargo proteins to retraction fibers.

Since filopodia and filopodia-like structures that express MYO10 perform a wide variety of roles in cells during cell migration, cell adhesion, cell division, development, and homeostasis, we hypothesized that MYO10 contributes to the leader cell phenotype in more ways than only by coordinating the stability of leading-edge filopodia. Here, we investigate the localization and potential functions of MYO10 within leader cells during mitosis and during cell-cell adhesion. Our work reveals that MYO10 does not localize to the mitotic spindle poles but does localize to

retraction fibers, the mitotic midbody, and at cell-cell junctions containing VE-cadherin, thus providing novel evidence that MYO10 coordinates multiple cellular activities within leader cells.

## 4.4 Methods

### Cell lines and transfections.

H1299 human NSCLC cells (ATCC, Manassas, VA) were cultured in Roswell Park Memorial Institute (RPMI-1640) media supplemented with 10% fetal bovine serum and 100 units $ml^{-1}$ of penicillin/streptomycin and maintained at 37 °C and 5% CO2. Cell lines were mycoplasma tested and authenticated using single nucleotide polymorphism analysis by the Emory Integrated Genomics Core (see cell line genotyping below). The gd2PAL-Dendra2 plasmid was obtained from the Gary Bassell lab (Emory University) and was stably transfected into H1299 cells using LT-1 transfection reagent (Mirus). Geneticin was used to select for Dendra2-expressing cells at 300 mg $ml^{-1}$ concentration.

### Cell line genotyping.

H1299 samples were processed according to the ABI AmpFLSTR Identifiler PCR Amplification Kit protocol and analyzed on the ABI 3130xl Genetic Analyzer according to the manufacturer's directions. Amplicons were electrophoresed with the appropriate allelic ladder on the 3130xl Genetic Analyzer. Identification analysis was performed using GeneMApper ID software version 3.2.1.

### Reagents and antibodies

*Primary and secondary antibodies for immunoblotting:* MYO10 (Novus Biologicals, NBP1-87748) was used at 1:2000. JAG1 (Cell Signaling, 70109) was used at 1:2000. IL13RA2 (Abcam, ab55275) was used at 1:2000. Cleaved Notch1 (Val1744)(Cell Signaling, 4147) was used at 1:2000. α-tubulin (Millipore, MAB1864) was used at 1:5000. Actin (Sigma A2066) was used at

1:5000. Gapdh (Cell Signaling, 2118) was used at 1:5000. Peroxidase AffiniPure Goat Anti-Mouse IgG (H+L) (Jackson ImmunoResearch, 115-035-003) was used at 1:10,000. Peroxidase AffiniPure Goat Anti-Rabbit IgG (H+L)(Jackson ImmunoResearch, 111-035-144) was used at 1:10,000. Peroxidase AffiniPure Goat Anti-Rat IgG (H+L) (Jackson ImmunoResearch, 112-035-003) was used at 1:10,000.

*Primary and secondary antibodies and reagents for immunostaining*: MYO10 (Novus Biologicals, NBP1-87748) was used at 1:1000. α-tubulin (Millipore, MAB1864) was used at 1:1000. γ-tubulin (Santa Cruz, sc-17787) was used at 1:100. VE-cadherin (mouse, BV9) (Novus Biologicals, NB600-1409) was used at 1:200. VE-cadherin (rabbit) (Cell Signaling, 2158) was used at 1:100. N-cadherin (mouse) (BD Transduction, 610,920) was used at 1:100. 4′,6-Diamidine-2′-phenylindole dihydrochloride (DAPI) (Sigma, D9542) was used as a nuclear counterstain at 300nM. Phalloidin-635 (Thermo Fisher, A34054) was dissolved in methanol and used at 1:100. The following IgG Highly Cross-Adsorbed secondary antibodies were each used at 1:1000: Goat anti-mouse Alexa Fluor 568 (Invitrogen, A11031), Goat anti-mouse Alexa Fluor 647 (Invitrogen, A21235), Goat anti-rabbit Alexa Fluor 568 (Invitrogen, A11036), Goat anti-rabbit Alexa Fluor 647 (Invitrogen, A21245), Goat anti-rat Alexa Fluor 555 (Invitrogen, A21434).

**3-D spheroid invasion and immunofluorescence microscopy**

Spheroids with 3000 cells each were generated as previously described (*112*) and embedded in Matrigel recombinant basement membrane (Corning, 356237). Brightfield images were taken using an Olympus CKX41 microscope with an Infinity 1-3C camera (×4 air, 0.13 NA, UPlanFLN). For immunostaining, cells in 2D or spheroids embedded in rBM were rinsed twice with 1X PBS containing calcium and magnesium pre-warmed to 37°C and then immediately fixed with

paraformaldehyde and glutaraldehyde (1X PBS containing calcium and magnesium with added 2% PFA and 0.001% glutaraldehyde; freshly prepared and warmed to 37°C) for 20 minutes at room temperature. For immunofluorescence staining, permeabilization, three glycine rinses, blocking, and antibody staining were performed as previously described (*203*). After primary and secondary antibody staining, cells in 2D or 3D spheroids were imaged with the Leica TCS SP8 inverted confocal microscope (×20 air HC PL APO CS2, 0.75 NA; ×40 oil HC PL APO CS2, 1.30 NA; ×63 oil HC PL APO CS2, 1.40 NA) using 1mm stack intervals for ×20 objective or 0.3 mm z-stack intervals for all other objectives, line scanning (405 nm DMOD Flexible, 488 nm argon, 561 nm DPSS, 633 nm Helium-Neon), 2x line averaging, and both Hyd GaAsP detectors and PMT detectors.

**Proliferation assays and mitosis analysis**

For the proliferation assays, H1299 leader and follower cells were plated in triplicate in a 24-well plate. At days 1–3, cells were counted using an automatic cell counter (BioRad). For mitotic event analyses, H1299 RFP-leader and follower cells (either alone or in co-culture) or H1299 siCtrl and siMYO10 leader cell were plated in an eight-well LabTek glass bottom slide. After 6 h, cells were imaged every 5 min for 21 h on the Leica SP8 inverted confocal microscope at ×10 using a 488 nm argon laser. Mitotic events were analyzed from these images using Leica Application Suite X software. Cell death events were counted based on morphological changes consistent with cell death phenotypes (loss of all cell motility and membrane dynamics, shrinkage of cell, nuclear fragmentation, formation of apoptotic bodies, phagocytosis by neighboring cells and so on). The length of time from prophase to anaphase and anaphase to cytokinesis was determined by morphological features. The beginning of prophase was defined as the first image where the cell

became spherical and increased Dendra2 fluorescence, the beginning of anaphase was defined as the first image where the chromosomes were visibly separated and the cell has begun elongating, and cytokinesis was defined as the first image where the two daughter cells are separated by a plasma membrane.

The presence of a variety of mitotic defects was defined by morphological abnormalities. Cytokinetic instability was defined as what appears to be initially greater than two daughter cells with excessive membrane blebbing and cell shape deformation during cytokinesis, but over time is corrected to two daughter cells. The severity of cytokinetic stability was rated on a scale of 0-3+, with 0 being no cytokinetic instability (i.e. cell continued through the final stages of mitosis to create two spherical daughter cells; no excess membrane blebbing visible), 1+ being mild cytokinetic instability (i.e. for greater than 5 minutes, the two emerging daughter cells elongate before separating and/or briefly form a second partial furrow at the center of the daughter cell, appearing as if the two daughter cells were going to further divide into 4 daughter cells total), 2+ being moderate cytokinetic instability (i.e. for greater than 5 minutes, the two emerging daughter cells elongate and form temporary second furrows to appear like 4 potential daughter cells, and the plasma membrane shows excess blebbing and deformation; the dividing cells must always be visibly recognizable as two daughter cells even if the shape is unusual), and 3+ being severe cytokinetic instability (i.e. for greater than 5 minutes, the dividing cell undergoes such severe membrane elongation, blebbing, and deformation that it is not possible to visually distinguish how many daughter cells are present or where the cleavage furrow is located).

**Cell cycle analysis**

H1299 follower and leader cells were plated in 100 mm tissue culture dishes. After 24 h, cells were

washed, and fresh RMPI-1640 media supplemented with 0 or 10% FBS was added to the cells. After 20 h, cells were collected and fixed in 95% ethanol at -20 °C. Cells were stored at 4 °C for 24 h before staining with DNA staining buffer (4 mg $ml^{-1}$ DAPI, 0.25% Triton-X 100 in 1× PBS). DAPI expression was analyzed by flow cytometry on a BD FACSCanto-II cytometer using FACSDiva software. FlowJo software was used to exclude doublets and determine the distribution of cells within G0/G1, S and G2 peaks.

**Colony formation assays**

H1299 parental, follower and leader cells, or H1792 follower and leader cells, were plated in 35 mm tissue culture dishes at 500 cells per plate. Cells were grown for 2 weeks, and media (RPMI-1640, 24-h follower conditioned media, or 24-h leader conditioned media) was refreshed every 3 days. To create conditioned media, $10x10^4$ leader cells or $7.2x10^4$ follower cells were seeded in a six- well plate so as to reach ~70% confluence. After 24 h, cells were washed twice with 1× PBS and then 1.5 ml of RPMI-1640 without FBS was added to each well. After another 24 h, media was centrifuged to remove cells and debris, and 24-h conditioned media was added to colony formation assays. After 2 weeks, colony formation assays were stained with crystal violet (6% glutaraldehyde, 0.5% crystal violet in 1× PBS) for 30 min before rinsing thoroughly with water. Colony surface area and the number of colonies with more than 50 cells were quantified using Fiji imaging software (ImageJ).

## 4.5 Results

### MYO10 localizes to filopodia-like structures within mitotic leader cells

To examine additional roles of MYO10 within leader cells, we performed MYO10 immunofluorescence and confocal imaging on fixed leader cells to identify the subcellular localization of MYO10 beyond the leading-edge filopodia (Figure 4.1). Since MYO10 has been implicated as a regulator of spindle assembly and mitotic progression in *Xenopus laevis (236-238)*, we investigated whether MYO10 localized to the tubulin-based spindle poles in our human lung cancer leader cells. When we examined MYO10 localization within metaphase leader cells in 2D culture, we did not see MYO10 localizing to the spindle poles (Fig. 4.1). Instead, MYO10 appeared diffusely localized to the cytoplasm in metaphase cells with only a slight enrichment along the encircling cortical actin ring (Fig. 4.1A, 4.1C), consistent with previous studies of MYO10 in mammalian cells during mitosis (*233*). However, MYO10 strongly localized to the midbody of cells in late-stage cytokinesis (Fig. 4.1B-C). The midbody is a specialized transient structure that forms during the final stages of cytokinesis as the two emerging daughter cells prepare for the final abscission, and the midbody structure resembles a bridge composed of overlapping microtubules and microtubule-binding proteins (*239*). As this is the first report of MYO10 localizing to the midbody, it is not yet known what function MYO10 utilizes within this structure, but these observations suggest that MYO10 could regulate the late stages of mitosis through its association with the midbody.

In addition, MYO10 puncta strongly localized to retraction fibers of metaphase cells (Fig. 4.1C). Retraction fibers orient the spindle poles in response to extracellular cues by connecting the detached cell body to the extracellular matrix (*130, 233*). In turn, proper spindle pole orientation

is critical for maintaining the integrity of chromosome separation and preventing aneuploidy, which could lead to cancer-promoting genomic alterations or cell death (*234, 235*). Taken together, these observations suggest that MYO10 does not localize to spindle poles or the microtubule aster as described in non-mammalian cells but instead may potentially regulate mitotic integrity through spindle-independent structures such as retraction fibers and/or the midbody.

**Follower cells are highly proliferative and rescue leader cell growth and mitotic defects**

The question remained as to whether high levels of MYO10 expression in leader cells affected cell growth and cell division. Before determining the effects of MYO10 expression on leader cell mitosis, we first examined whether proliferation and mitosis differed between leader cells and follower cells. During the initial collection and expansion of leader and follower clones, we observed that leader cells grew at slower rates compared to follower cells (not shown); therefore, to test if follower cells are more proliferative, a basic proliferation assay was performed, showing that follower cells had increased cell counts after 3 days compared to leader cells (Fig 4.2A). Similarly, colony formation assays showed that leader cells have little colony growth over time, whereas followers have a greater number of large colonies (Fig 4.2B). Cell cycle analysis 20 hours post-serum starvation showed a large G1 population in leader cells compared to follower cells (Fig. 4.2C, Fig. 4.3A-C); however, without serum starvation there are no differences in the cell cycle between these two populations (Fig. 4.3D).

To test the hypothesis that followers provide a growth or survival advantage to leader cells, leader cells were subjected to a colony formation assay in the presence of leader cell conditioned media (LCM) or follower cell conditioned media (FCM). Leader cells in LCM had low colony formation as measured by colony number and area (Fig 4.2D-E); in contrast, adding FCM to

leaders resulted in a significantly increased colony number and area. Strikingly, the addition of LCM to follower cells significantly inhibited colony growth as compared to followers grown in their own conditioned media (Fig 4.2D-E). Taken together, these data show that FCM can significantly increase colony growth of leader cells, whereas LCM inhibits colony growth of follower cells.

To probe why leader cells have growth defects, live cell imaging was used to assess mitosis in purified populations. Leader cells had a variety of mitotic defects compared to follower cells (Fig 4.4A), with the most prominent being cytokinetic instability (defined as initially having >2 daughter cells with excessive membrane blebbing and cell shape deformation during cytokinesis but over time corrected to 2 daughter cells; Fig 4.4B). Other defects include increased time from prophase through anaphase and eventual fusion of daughter cells. Overall, ~70% of all leader cells have mitotic defects, as compared to only 6% in follower cells (Fig. 4.4C).

To test if leader cell mitotic defects could be rescued by follower cells, follower cells were co-cultured with RFP-leader cells, and leader cell mitotic defects were nearly abolished (Fig 4.4C). Co-culture with follower cells specifically rescued the prophase-to-anaphase mitotic delay observed in leader cells (Fig 4.4D) and cytokinetic instability (Fig 4.4E); however, the mitotic fraction of leader cells, defined as the percentage of cells entering mitosis in a field of view, was not impacted by follower cells (Fig 4.4F). A similar effect on mitotic defects was observed using FCM on leader cell cultures where unsuccessful mitotic defects was significantly decreased as compared to leaders cultured in LCM (Fig 4.4G). In addition to effects on mitotic efficiency, FCM also impacted the percentage of cells undergoing cell death. The addition of FCM to leader cells significantly reduced cell death as compared to leaders cultured in LCM (Fig 4.4H). Conversely, LCM had the opposite impact on follower cells and increased cell death (Fig 4.4H). Interestingly,

follower cells when co-cultured with leader cells also have an increase in cytokinetic instability as well as a decrease in the overall mitotic fraction (Fig 4.4E-F), suggesting that leader cells may hinder follower cell growth. Taken together, these data support a model whereby follower cells decrease mitotic defects and leader cell death while supporting leader cell colony formation, whereas leader cells increase these defects in follower cells thereby hindering follower cell growth.

**Leader cells are prone to mitotic spindle pole misorientation and centrosome amplification**

Since leader cells display much higher rates of mitotic defects than follower cells, we investigated whether leader cells also displayed structural aberrations in mitotic spindle poles that could contribute to the gross morphological mitotic errors observed in live cell imaging. During mitosis, the centrosomes act as the organizing centers for the microtubule-based spindle poles that attach to each chromosome kinetochore, and proper bipolar organization of the spindle poles is necessary for accurate chromosome segregation (*240, 241*). Cells with more than exactly two spindle poles oriented in a single plane are prone to chromosome mis-segregation and genomic instability (*240*). Interestingly some cells with extranumerary centrosomes are able to prevent spindle multipolarity by clustering together excess centrosomes into two groups, forming a "pseudobipolar" orientation (*242*). However, pseudobipolar spindles are not as accurate as true bipolar spindles and may still lead to occasional cancer-promoting aneuploidy and chromosomal instability (*243, 244*).

We examined the number and orientation of mitotic spindles in metaphase leader and follower cells in 2D cell culture by immunofluorescence for α-tubulin, and we examined centrosome number and organization by immunofluorescence for γ-tubulin. Approximately 35% of leader cells displayed aberrant spindle pole numbers and/or orientation, including spindles that

were monopolar, multipolar, or pseudobipolar; in comparison, only about 10% of follower cells showed these same defects in spindle formation (Fig. 4.5A). In addition, over 50% of leader cells contained more than 2 centrosomes, arranged in both organized and disorganized geometries, whereas only 20% of followers contained additional centrosomes (Fig. 4.5B). Thus, these data demonstrate that leader cells are highly prone to centrosome amplification and spindle pole mis-orientation, consistent with leader cells displaying more mitotic defects overall.

In addition to cells in 2D culture, we examined spindle pole formation in leader and follower cells within collectively-invading 3D spheroids. Almost all metaphase follower cells that were observed contained properly formed bipolar spindles (Fig. 4.6A). In contrast, metaphase leader cells, although rare, commonly displayed multipolar spindles (Fig. 4.6A-B). Intriguingly, we observed two leader cells in the late stages of mitosis with gross blebbing aberrations in the membrane structure (Fig. 4.6B). These membrane blebs strongly resemble the misshapen plasma membranes of leader cells undergoing cytokinetic instability in 2D live cell imaging (Fig. 4.4B).

Much like mitotic leader cells in 2D culture, leader cells that underwent mitosis during 3D collective invasion in pure leader cell spheroids had unsuccessful mitotic events in about a third of all cases (Fig. 4.6C). However, leader cells within spheroids of a 1:1 mix of leader and follower cells underwent unsuccessful mitotic events only about 10% of the time (Fig. 4.6C), similar to the effect of follower cells on leader cell mitotic success in 2D culture (Fig. 4.4C-H). Therefore, these observations suggest that leader cells are more prone than follower cells to structural aberrations during mitosis in both 2D and 3D conditions, and that follower cells in co-culture with leader cells are capable of reducing leader cell mitotic errors in both 2D and 3D conditions through a yet-unknown mechanism.

Since MYO10 localizes to both retraction fibers and the midbody within mitotic leader cells (Fig. 4.1), and since MYO10 regulates spindle orientation and mitotic progression (*233, 236-238*), we hypothesized that the abnormally high expression of MYO10 in leader cells could contribute to the frequent mitotic errors seen within leader cells. Leader cells expressing a control siRNA underwent unsuccessful mitotic events in about one third of cells (Fig. 4.6D), consistent with earlier quantifications (Fig. 4.6C). However, MYO10-knockdown leader cells underwent unsuccessful mitotic events in only about 10% of cells, which is remarkably similar to the rescue effect of co-culturing leader cells with follower cells (Fig. 4.6D). When examining cytokinetic instability independently of other mitotic defects, siCtrl leader cells displayed cytokinetic instability in 80% of mitotic cells, while MYO10 knockdown cells displayed this aberrant phenotype in only 60% of cells (Fig. 4.6E). In addition, MYO10 knockdown decreased not only the frequency of cytokinetic instability but also the severity of the phenotype (Fig. 4.6E). These results suggest that high expression of MYO10 in leader cells may contribute to the high rates of mitotic defects in leader cells, and that MYO10 knockdown in leader cells can partially rescue mitotic integrity.

**MYO10 localizes to cell-cell contacts and co-localizes with VE-cadherin**

In addition to directing cell migration and mitotic progression, filopodia and filopodia-like structures also regulate cell-cell adhesion by creating the initial points of contact for two cells that are forming new cell-cell adhesions (*226-228*). Loss of filopodia through knockdown of MYO10 leads to a delay in forming new cell-cell adherens junctions and tight junctions in polarized epithelial cells (*228*). Since cell-cell adhesion is necessary for collective invasion, we hypothesized

that MYO10-expressing filopodia regulate cell-cell adhesion between leader cells and other cells within the collective invasion pack.

To determine if MYO10 localizes to filopodia at cell-cell contacts, we performed immunofluorescence for MYO10 in leader cells on a 2D substrate and examined regions where cells overlapped or were adjacent to each other. Strikingly, leader cells produced long filopodia with large MYO10 puncta at the tips in regions where one leader cell overlapped another (Fig. 4.7A). Specifically, these MYO10-expressing filopodia were on the basal surface of this cell-cell interface (*i.e.* within the cell closest to the cover slip; Fig. 4.7A insets), consistent with observations that MYO10 preferentially localizes to the basolateral surface of epithelial cells (*228*).

In addition, the role of filopodia during cell-cell adhesion is cadherin-dependent (*227, 228, 230*). The parental H1299 cells from which we derived our leader and follower cells do not express E-cadherin (the canonical epithelial cadherin), but they do express the mesenchymal cadherin N-cadherin (*112*). Our leader cells also express the endothelial cadherin VE-cadherin as part of a transcriptional program that mimics angiogenic signaling (*112*) Interestingly, VE-cadherin is a known cargo protein of MYO10 in endothelial cells, and MYO10 transport of VE-cadherin into long filopodia in tip cells facilitates the formation of new cell-cell adhesions during angiogenesis (*230, 245*). When we examined the localization of VE-cadherin within leader cells in 2D cell culture, we found VE-cadherin localized within regions of cell-cell adhesion, consistent with the canonical localization of VE-cadherin (Fig. 4.7B). Upon closer inspection, these regions of VE-cadherin co-localized with filopodia or filopodia-like structures that overlapped the region of cell-cell contact (Fig. 4.7B insets), reminiscent of filopodia-cadherin “zippers” at newly-forming cell-cell adhesions (*227*).

Furthermore, VE-cadherin localized to filopodia that were not in contact with neighboring cells, with larger puncta at the tips of many filopodia (Fig. 4.7B). Since VE-cadherin is a cargo protein of MYO10, this localization pattern is consistent with MYO10 transporting VE-cadherin into the tips of filopodia. To determine if VE-cadherin localized to MYO10-expressing filopodia during 3D collective invasion, we performed immunofluorescence of VE-cadherin and MYO10 in invading spheroids of leader cells and the H1299 parental cell line. In both leader cells and parental cells, VE-cadherin localized to MYO10-expressing filopodia at the invasive front (Fig. 4.8A). However, both VE-cadherin and MYO10 also localized to the extracellular region in front of leader cell dorsal filopodia in extended lines parallel to the filopodia (Fig. 4.8A). These extracellular parallel lines were highly reminiscent of the patterns formed by filopodia-driven FN remodeling (Figs. 3.9-3.15). These same VE-cadherin localization patterns could be seen when using a different primary and secondary antibody (Fig. 4.8B), suggesting that this localization pattern is not an artifact of nonspecific antibody binding.

Although MYO10 has been shown to transport VE-cadherin as a cargo protein, MYO10 is not known to transport any other cadherin. To determine if the extracellular localization of VE-cadherin was unique to VE-cadherin as a MYO10 cargo protein or if this localization pattern occurred with other non-MYO10-cargo cadherins, we compared the localization of N-cadherin and VE-cadherin within spheroids of H1299 leader cells or the H1792 cell line (Fig. 4.8B). While VE-cadherin localized as described above, N-cadherin was seen at cell-cell adhesions but did not localize to leading-edge filopodia nor to the extracellular space extending in front of the leading edge (Fig. 4.8B). Although additional functional studies will be needed to determine how and why VE-cadherin localizes to the extracellular space during 3D invasion, this patterning suggests that

the localization may be dependent up MYO10-expressing filopodia in leader cells, and perhaps dependent upon FN micropatterning induced by these filopodia as well.

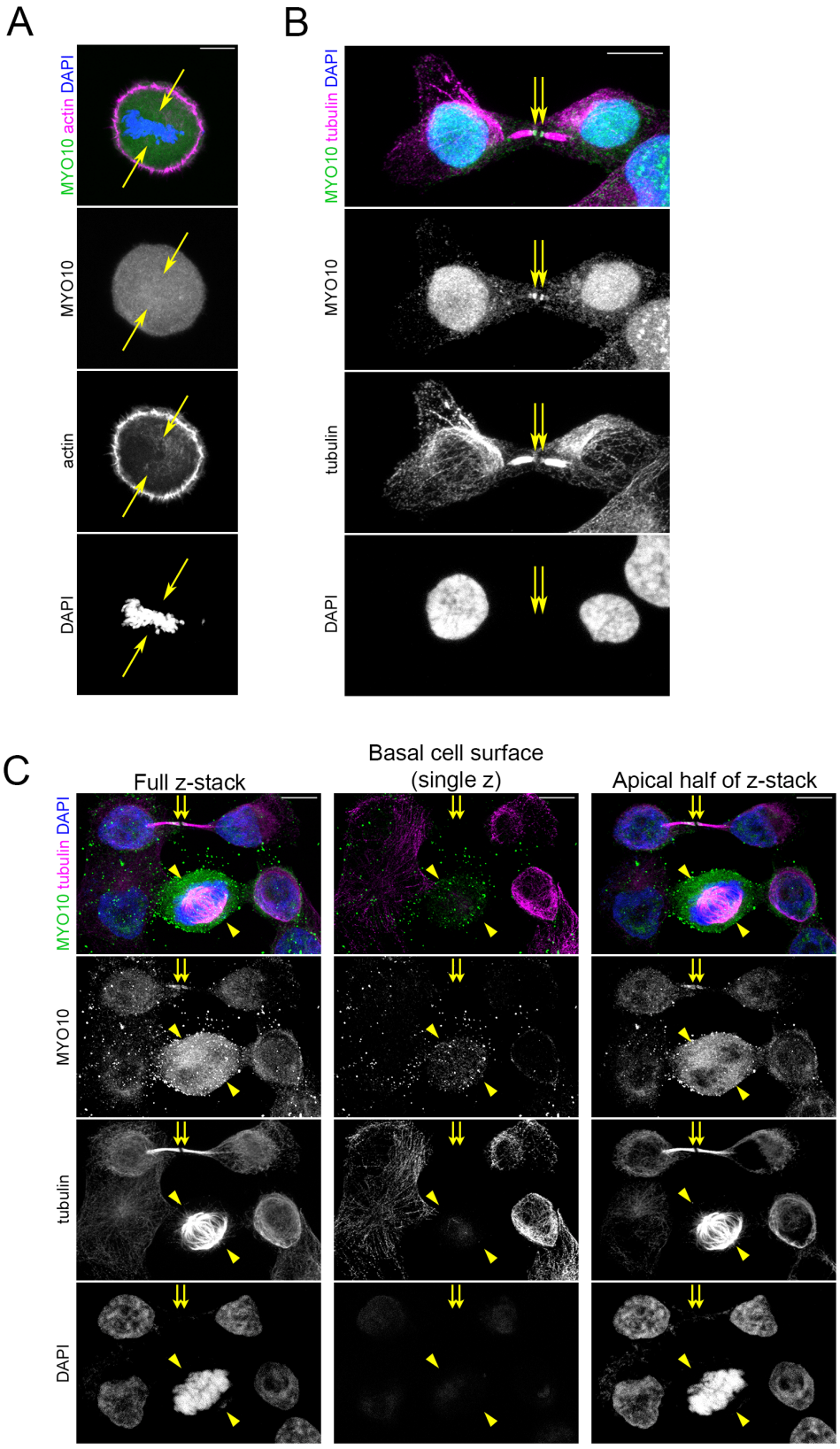
A
MYO10 actin DAPI
MYO10
actin
DAPI
B
MYO10 tubulin DAPI
MYO10
tubulin
DAPI
C
Full z-stack
Basal cell surface (single z)
Apical half of z-stack
MYO10 tubulin DAPI
MYO10
tubulin
DAPI

**Figure 4.1: MYO10 localization within mitotic leader cells.**

(**A**) Immunofluorescence imaging of MYO10 within a metaphase leader cell in 2D culture. Actin labeled by phalloidin; DNA labeled by DAPI. Arrows indicate presumed location of the spindle poles. Scale bar = 10μm. (**B**) Immunofluorescence imaging of MYO10 and α-tubulin within a telophase/cytokinesis leader cell in 2D culture. DNA labeled by DAPI. Arrows indicate the tips of the midbody within the cleavage furrow. Scale bar = 10μm. (**C**) Immunofluorescence imaging of MYO10 and α-tubulin within a telophase/cytokinesis leader cell and a metaphase leader cell in 2D culture. DNA labeled by DAPI. Arrows indicate the tips of the midbody within the cleavage furrow. Arrowheads indicate location of the spindle poles. Full z-stack depth = 8.1 μm, 0.3 μm per slice. Scale bar = 10μm.

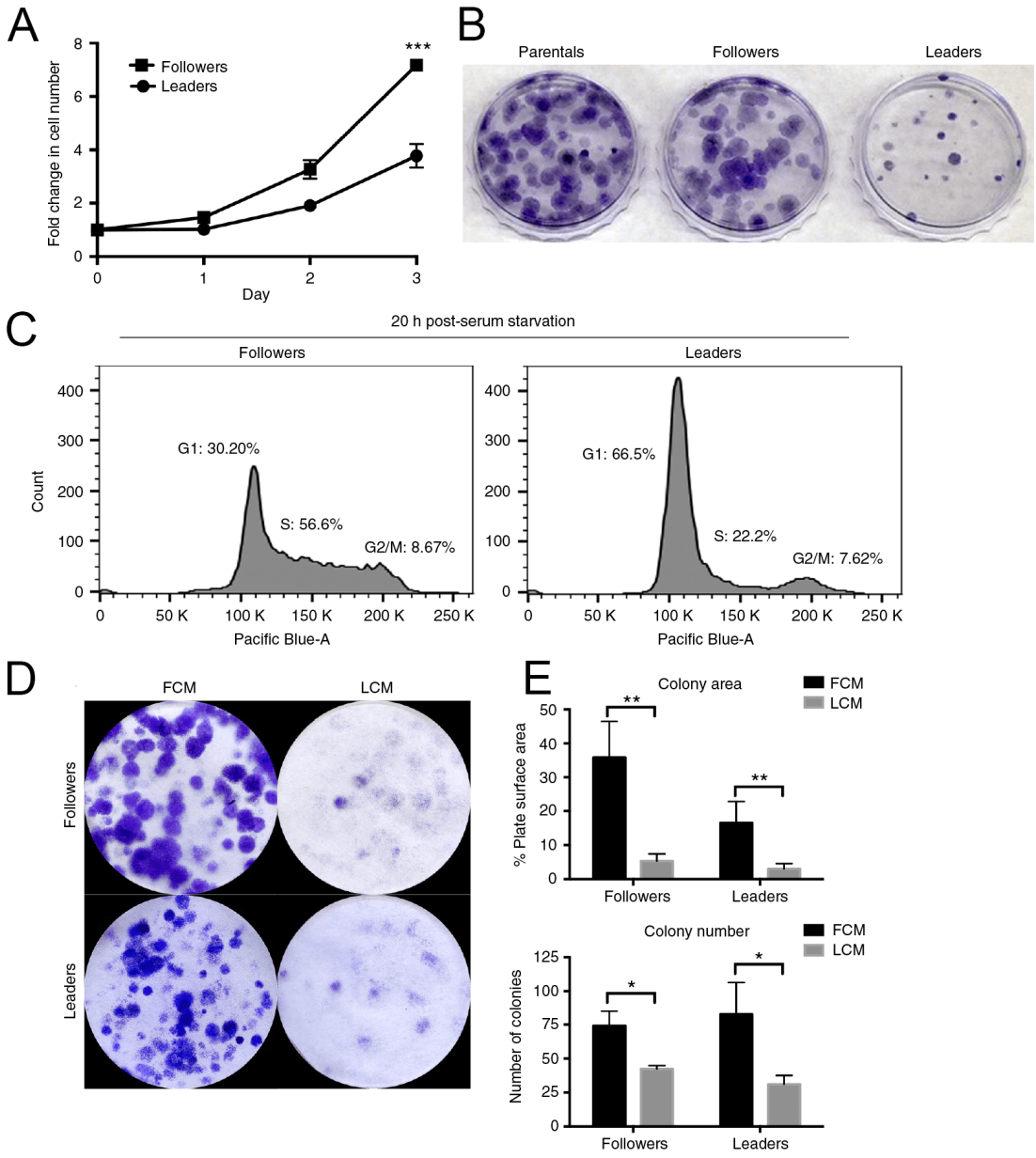


**Figure 4.2: Follower cells are a proliferative subpopulation promoting leader cell growth via a secreted factor.**

(**A**) Graph showing H1299 follower and leader cell growth over 3 days. ***p<0.001. (**B**) Colony formation assay of H1299 parental, follower and leader cells. (**C**) Cell cycle analysis of H1299 follower and leader cells that were serum starved, and then released for 20 h with normal growth

media. (**D**) Colony formation assay of H1299 follower and leader cells. Cells were plated in conditioned media from FCM or LCM. Images taken 2 weeks after plating. (**E**) The colony size and number of colonies from (**D**) were measured using ImageJ software. *$p<0.05$, **$p<0.01$ using a Student's t-test. Error bars denote the s.e.m.

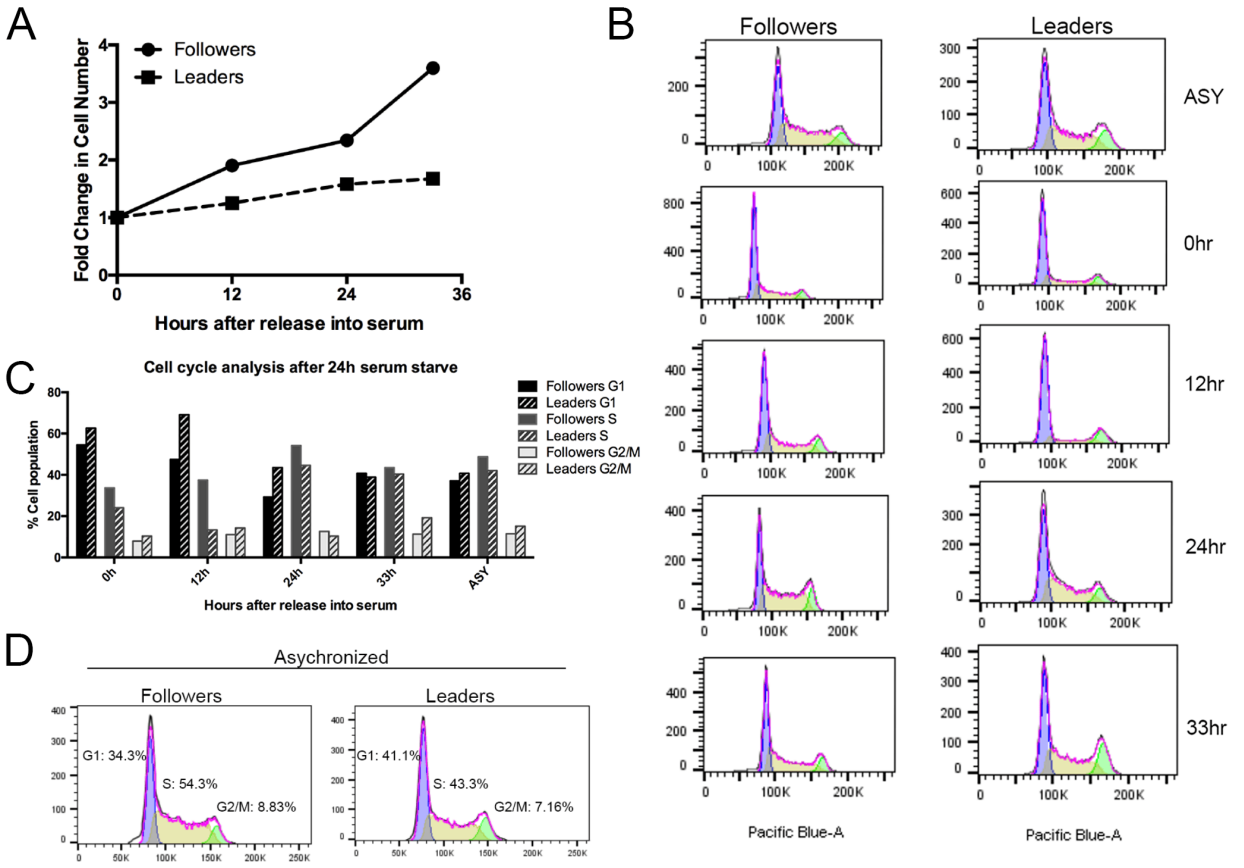


**Figure 4.3: Cell cycle analysis of follower and leader cells.**

(**A**) A sample of H1299 follower and leader cells were collected prior to fixation for the cell cycle analysis and counted using an automatic cell counting machine. Fold change in total cell number is shown over the time course. (**B-C**) H1299 follower and leader cells were serum started for 24 hours, then released by the addition of normal growth media for various lengths of time. Cells were collected for both cell growth (**A**) and cell cycle analysis. (**B**) Cells were fixed at various times after release from serum starvation and stained with DAPI for cell cycle analysis. (**C**) Quantification of each cell cycle phase from (**B**) in follower and leader cells. (**D**) H1299 follower and leader cells were fixed and stained with DAPI for cell cycle analysis using flow cytometry. Cells were not first synchronized before fixation.

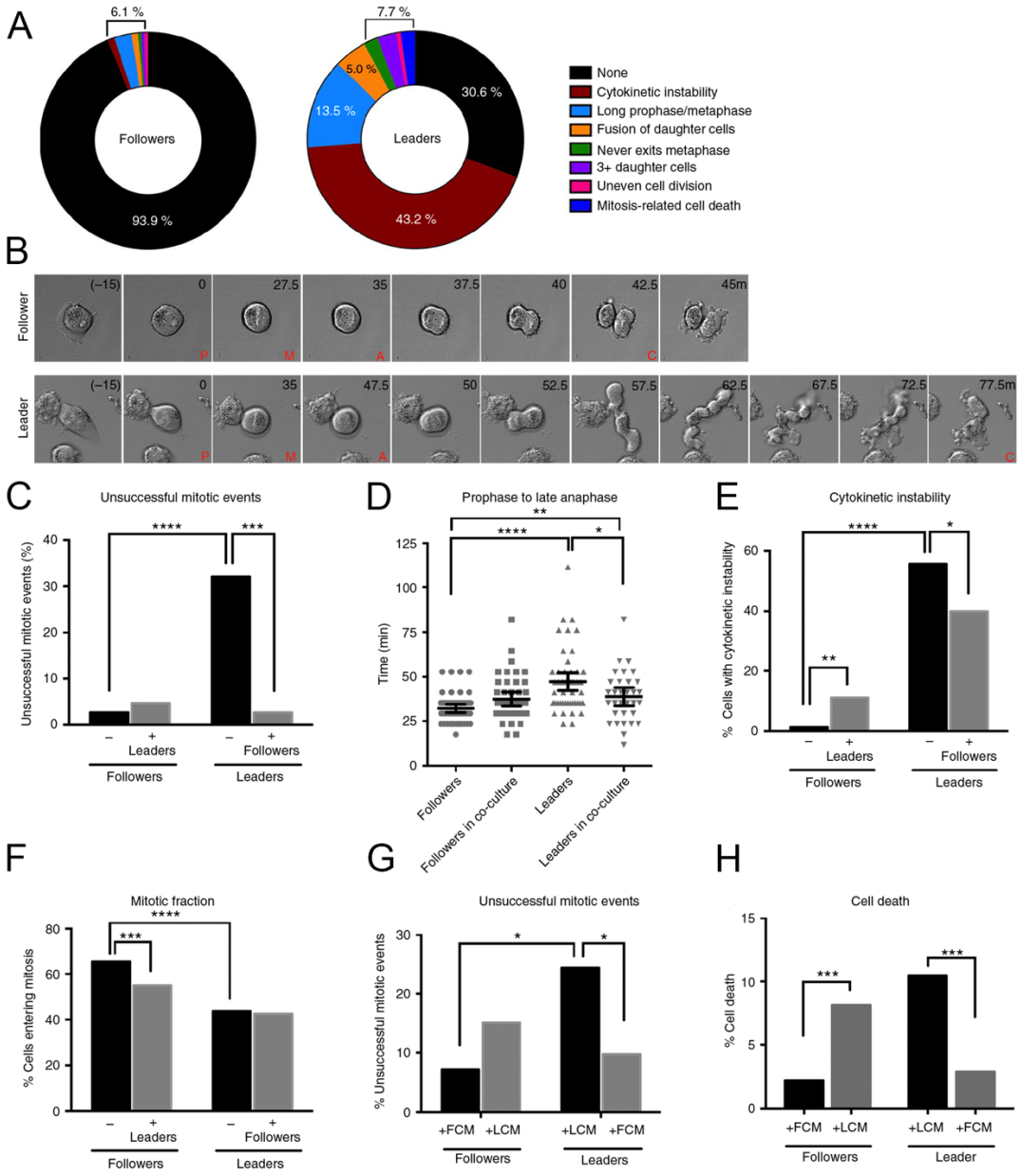


**Figure 4.4: Mitotic defects observed in leader cells are rescued by the addition of follower cells.**

(**A-F**) H1299 follower and RFP-leader cells were plated in 2D alone or in a 50:50 mixed co-culture then imaged using live cell confocal microscopy. Mitotic events were analyzed in each condition. (**A**) Graphs of each type of mitotic error noted during the live cell imaging as a percentage of all

mitotic events. N = 258 cells. (**B**) Still images of a mitotic event in a follower cell and a leader cell. Time in minutes. P, prophase; M, metaphase; A, anaphase; C, cytokinesis. (**C**) Unsuccessful mitotic events were classified and graphed as a percentage of total mitotic events seen in followers, leaders or each cell type in the co-culture condition. N = 506 cells. A two-tailed $X^2$-test was used to determine significance. (**D**) Dot plot of the amount of time each cell spent from prophase to the beginning of anaphase. N = 555 cells. A one-way ANOVA with Tukey's multiple comparisons test was used. Bars represent the median and 95% confidence intervals from 40 randomly selected cells per condition. (**E**) Cytokinetic instability events were graphed as a percentage of all dividing cells. A two-tailed $X^2$- analysis was used. N = 486 cells. (**F**) Bar graph of mitotic fraction, defined as the number of cells that undergo mitosis as a percentage of total cells in the field of view. A two-tailed $X^2$- analysis was used. N = 1,106 cells. (**G**) Unsuccessful mitotic events were counted and graphed from conditioned media from FCM or LCM. A two-tailed $X^2$- analysis was used. N = 185 cells. (**H**) Leader and follower cells were cultured in LCM or FCM and cell death events were graphed as a percentage of total cells in the field of view. A two-tailed $X^2$-analysis was used. N = 1782 cells. *$p<0.05$, **$p<0.01$ ***$p<0.001$, ****$p<0.0001$.

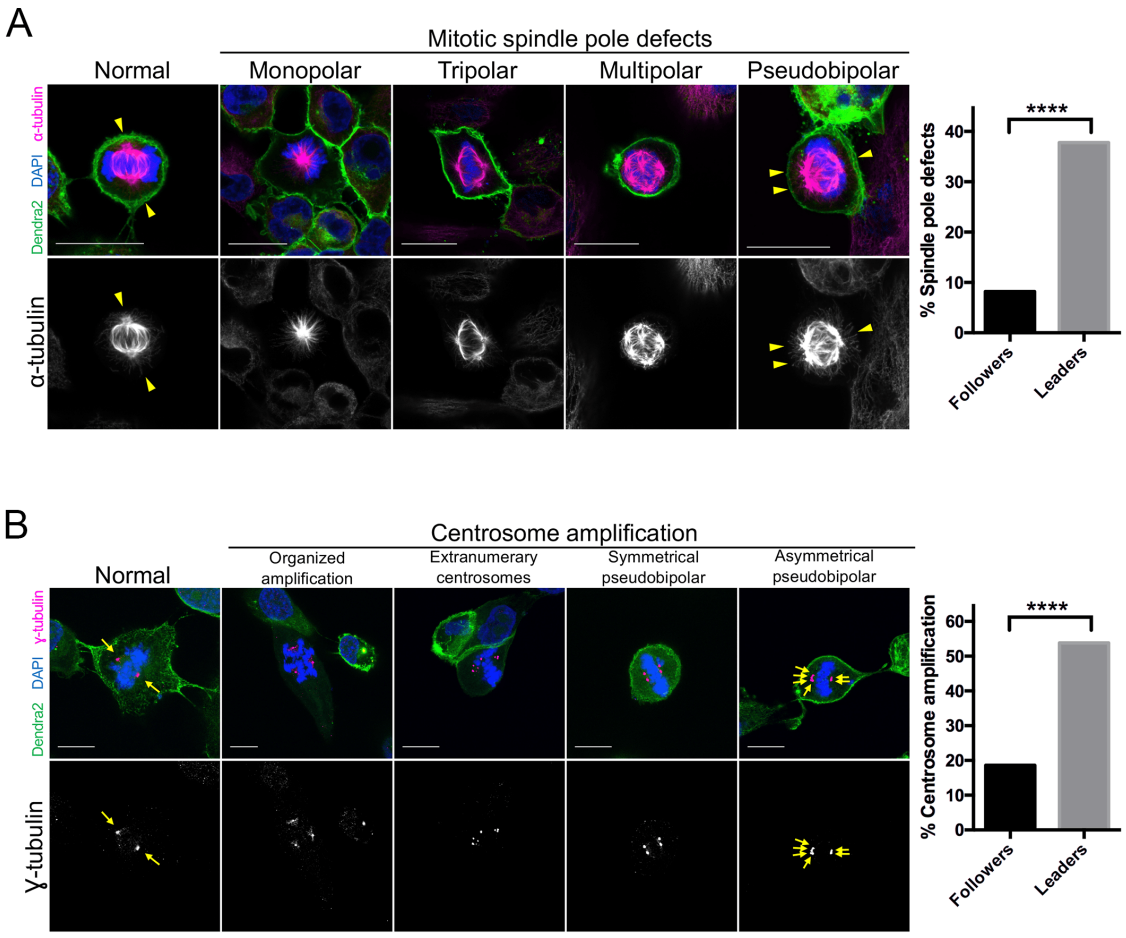


**Figure 4.5: Spindle pole defects and centrosome amplification in leader cells.**

(**A**) *Left:* Immunofluorescence imaging of leader cells in 2D cell culture to visualize mitotic spindles. Representative images of mitotic spindle defects are shown. Arrowheads indicate examples of microtubule organizing centers within mitotic spindles. *Right:* Quantification of spindle pole defects observed in metaphase follower and leader cells. N = 175 cells. (**B**) *Left*: Immunofluorescence imaging of leader cells in 2D cell culture to visualize centrosome number and organization. Representative images of centrosome amplification and classifications are shown. Arrows indicate examples of centrosomes. *Right:* Quantification of centrosome amplification in metaphase follower and leader cells. N = 209 cells. (**A-B**) Scale bars = 20μm; $X^2$-test, ****$p<0.0001$.

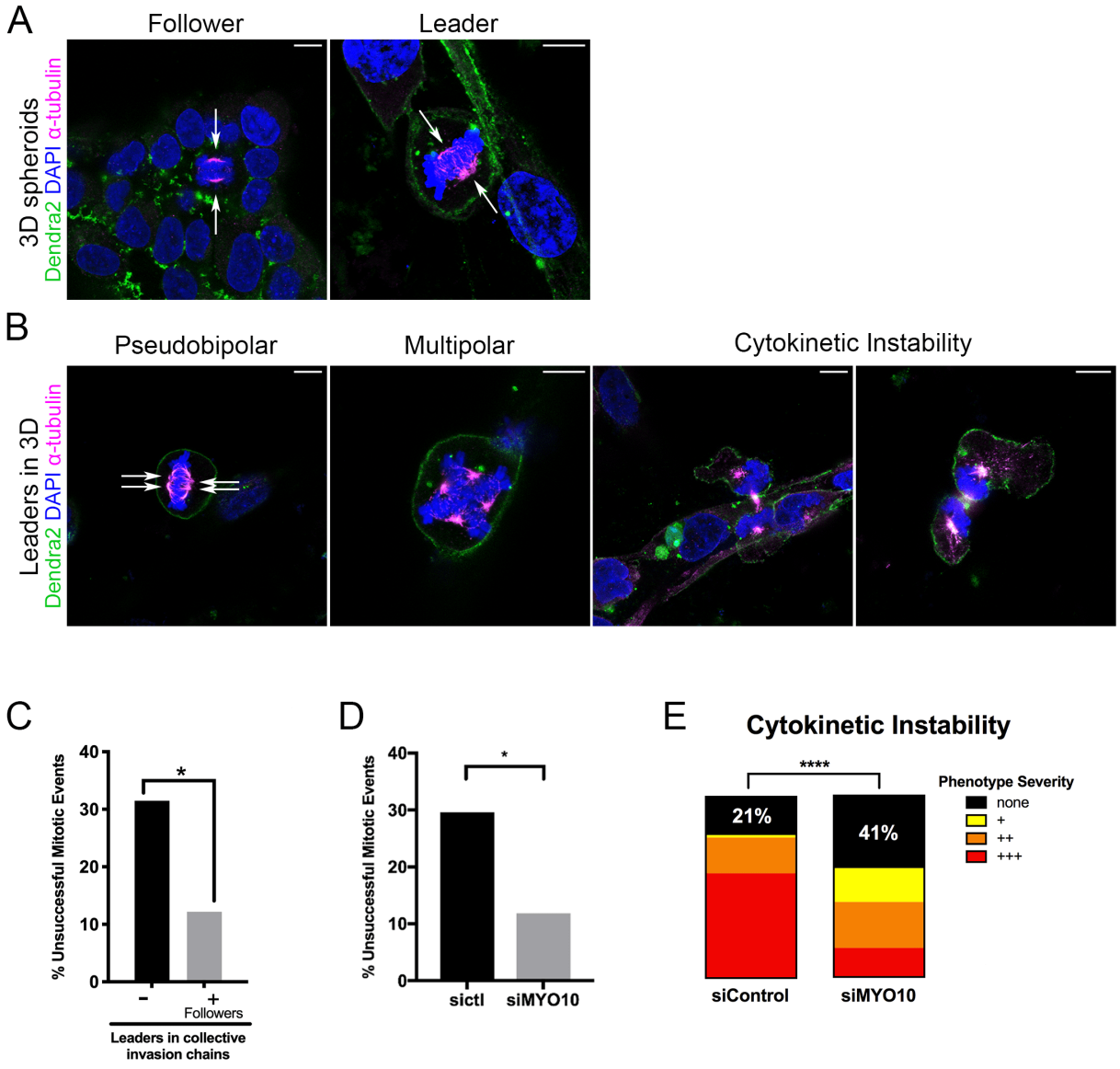


**Figure 4.6: Leader cell mitotic defects occur during 3D collective invasion and are mitigated by MYO10 knockdown.**

(**A**) Representative immunofluorescence images of a follower cell spheroid and leader cell spheroid 24 hours after embedding into recombinant basement membrane (rBM). (**B**) Immunofluorescence images of a leader cell spheroid 24 hours after embedding into recombinant

basement membrane. Representative images of pseudobipolar spindle poles, multipolar spindle poles, and cytokinetic instability (excess membrane blebbing and cell membrane deformation) seen in leader cells at the tip or within 3 cells of the tip of the collective invasion chains. (**A-B**) Dendra2-pal localizes to the plasma membrane. DNA labeled by DAPI. Arrows show location of spindle poles. Scale bar = 10μm. (**C**) Quantification from live cell imaging of leader cell unsuccessful mitotic events in spheroids of 100% leader cells or a 1:1 mix of leader cells and follower cells embedded into rBM. N = 95 cells. $X^2$-test, *$p<0.05$. (**D**) Quantification from live cell imaging of leader cells in 2D culture expressing either siCtrl or siMYO10. N = 146 cells. $X^2$-test, *$p<0.05$. (**E**) Quantification of the severity of cytokinetic instability seen in mitotic leader cells in (**D**). N = 146 cells. Fisher's exact test, ****$p<0.0001$.

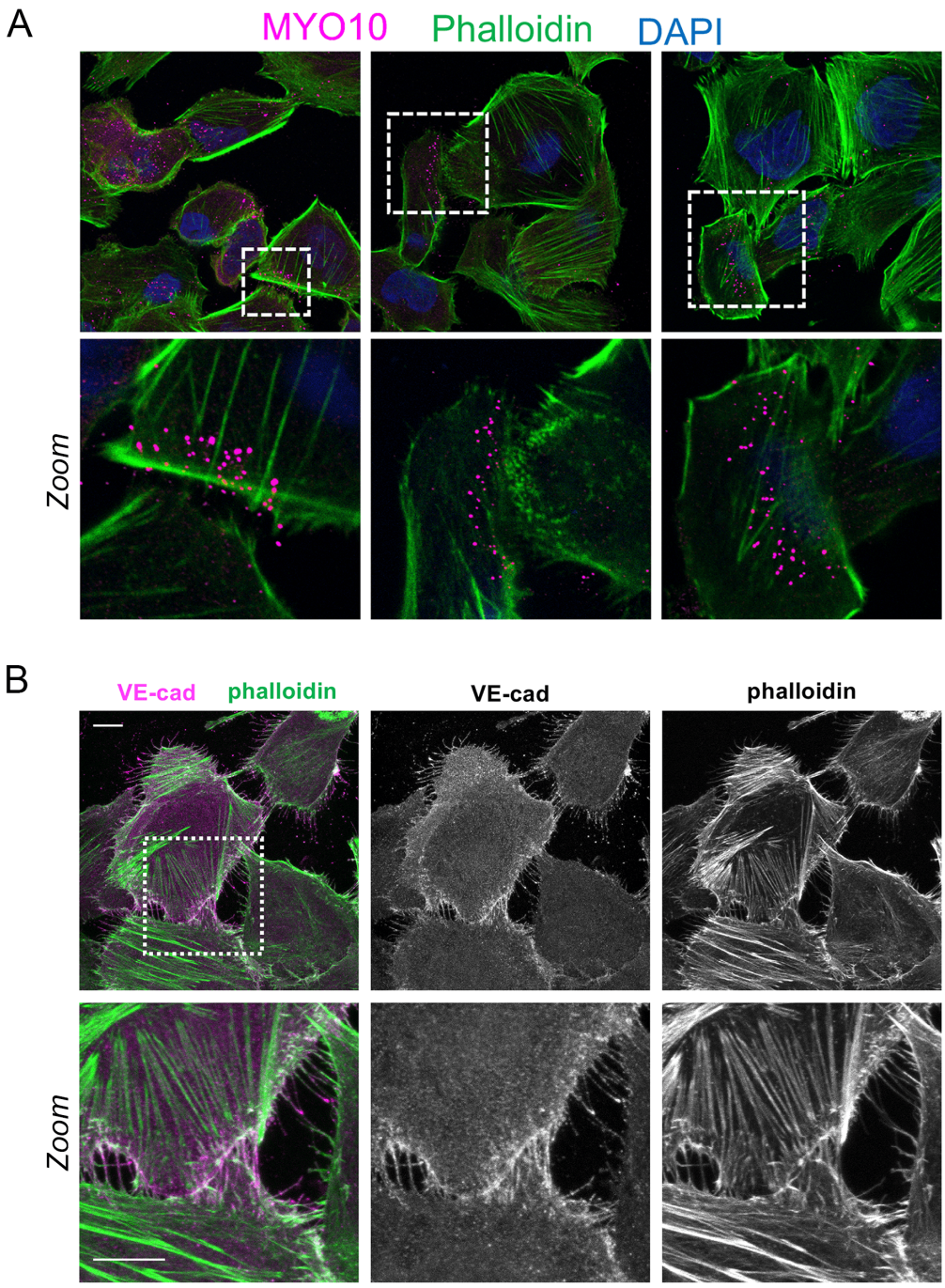


**Figure 4.7: MYO10 and VE-cadherin, a known cargo protein of MYO10, both localize to filopodia-like structures at cell-cell adhesion sites.**

(**A**) Representative MYO10 immunofluorescence images of leader cells in 2D cell culture. Actin marked by phalloidin; DNA marked by DAPI. White dashed box indicates area of zoom insert

below, showing regions of MYO10 in filopodia-like structures extending underneath the neighboring cell. (**B**) Representative VE-cadherin immunofluorescence images of leader cells in 2D cell culture. Actin marked by phalloidin. White dashed box indicates area of zoom insert below, showing VE-cad within a region of cell-cell adhesion. Scale bar = 10 μm.

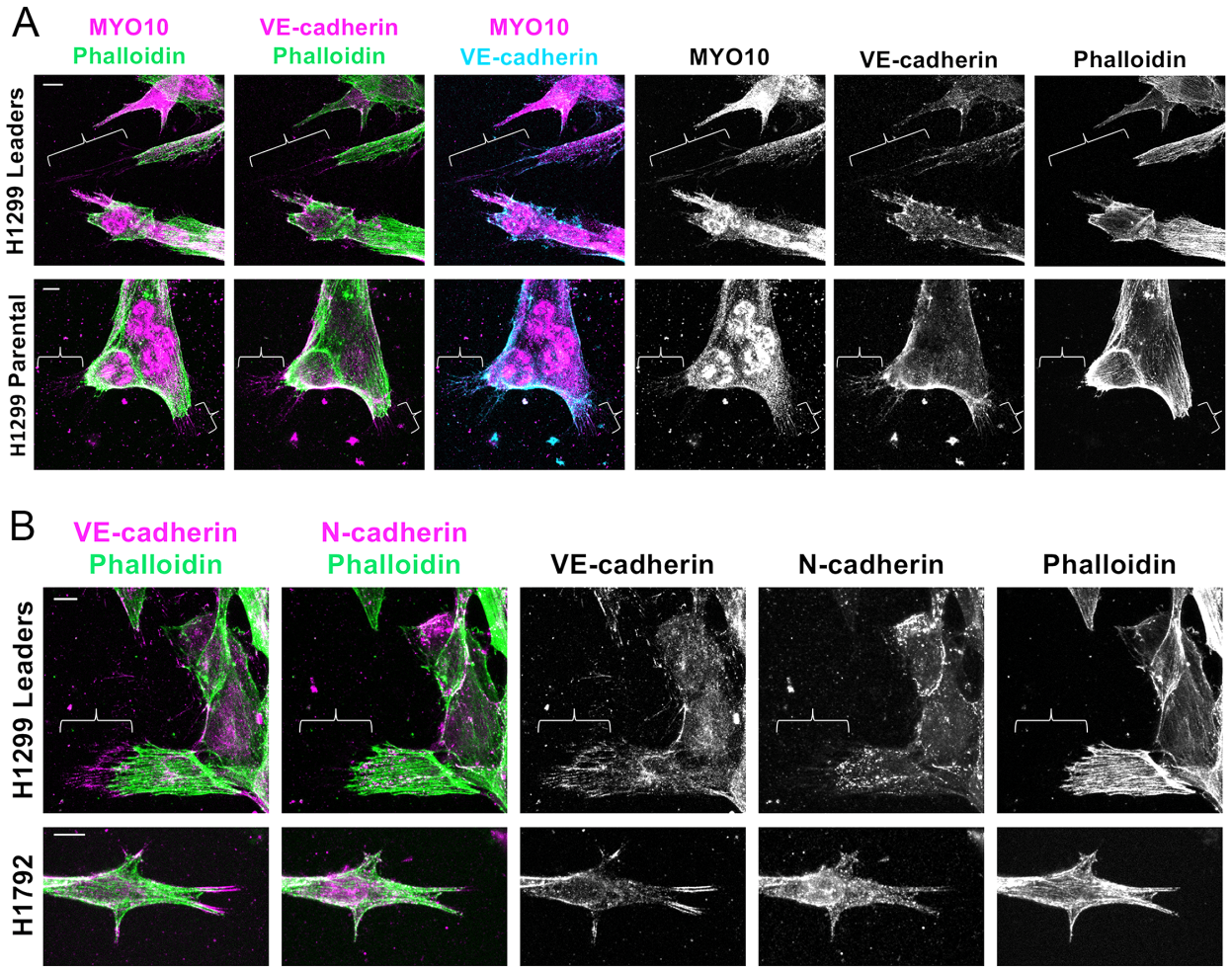


**Figure 4.8: VE-cadherin, but not N-cadherin, localizes to the leading edge of 3D collective invasion.**

(A) Representative MYO10 and VE-cadherin immunofluorescence images of H1299 leader cell spheroids or parental cell spheroids 24h after embedding into rBM. Actin marked by phalloidin. Bracket indicates region in the extracellular matrix extending past the ends of actin-containing filopodia. Scale bar = 10μm. (B) Representative VE-cadherin and N-cadherin immunofluorescence images of H1299 parental cell spheroids or H1792 spheroids 24h after embedding into rBM. Actin marked by phalloidin. Bracket indicates region in the extracellular matrix extending past the ends of actin-containing filopodia. Scale bar = 10μm.

**4.6 Discussion**

Although filopodia are most commonly studied in the context of the cellular leading edge during cell migration, these finger-like structures facilitate a wide variety of additional critical functions, such as cell-cell adhesion, invadopodia, cell-ECM adhesion during mitosis, and spindle alignment. Our leader cells depend upon MYO10-driven filopodia at the leading edge to direct cell migration and collective invasion (Chapter 3), but we show here that MYO10-driven filopodia also localize to certain mitotic structures and cell-cell junctions, providing evidence that MYO10 and filopodia may play additional roles to support leader cell function.

As a motor protein that is capable of binding to both actin microfilaments and tubulin microtubules, MYO10 can localize to cellular structures that contain both of these cytoskeletal components, such as invadopodia (*169*). However, several mitotic structures also contain both actin and tubulin and/or depend on the interaction of the two in order to impart pulling forces. Here, we show that MYO10 localizes to the midbody of cells during cytokinesis, but it does not localize to the mitotic spindle. Although MYO10 has been reported to localize to the mitotic spindle poles in *Xenopus laevis* cells (*236, 237*), our observations support prior studies that found no evidence that MYO10 localizes to the spindle poles, consistent of previous studies of MYO10 within mammalian cells undergoing mitosis (*228, 233*). It is not known why MYO10 localization at the spindle poles (or lack thereof) differs between non-mammalian and mammalian species, but it is clear that MYO10 regulates spindle pole orientation using mechanisms independent of direct binding to the mitotic spindle (*233, 237, 238*). In addition, this is the first report that MYO10 localizes to the midbody. Since the midbody contains overlapping bundles of both microfilaments and microtubules, we speculate that MYO10 may coordinate the bundling and/or pulling force of

the midbody by linking the two components. Further studies are needed in order to determine the function of MYO10 within this short-lived structure.

At the rear of the cell, MYO10-induced filopodia are a critical component of creating and maintaining cell-cell contacts (*227, 228*). Within our leader cells, MYO10 localized to filopodia and filopodia-like structures at regions of cell-cell contact, both in 2D and 3D cell culture (Fig. 4.7-4.8). Ultimately, this may prove to be one of the most important functions of MYO10 within the context of collective cancer cell invasion, since maintaining cell-cell adhesion is necessary for collective invasion; no cell-cell adhesion, by definition, is single cell invasion.

We also show that MYO10-expressing filopodia localize to regions of cell-cell contacts within 3D spheroid invasion as well as 2D cell culture (Fig. 4.7-4.8). Filopodia have been implicated in facilitating cell-cell adhesion during development and in normal epithelial cells, but very little is known about the role of filopodia within the context of cancer cell-cell adhesion (*132*). Although additional studies are needed to determine whether MYO10-expressing filopodia affect the formation of intercellular junctions between leader cells and follower cells at points of cell-cell contact (i.e. adherens junctions, tight junctions, gap junctions), the observations in this study encourage further studies into the role of filopodia in forming and maintaining cell-cell adhesion during collective invasion.

Filopodial regulation of cell-cell adhesion may potentially explain how cancer cells maintain physical contact during collective invasion, but the question remains as to why cancer cells preferentially invade as a collective pack as opposed to single cells. One potential answer is that the multicellular pack provides a survival or invasive advantage to escaping cells. In circulating tumor cells, cells that invaded as groups had greater success and worse clinical outcomes (*48, 246*). Furthermore, studies show that tumor cell clusters, rather than single cells,

seed polyclonal metastases in mouse models (*48-50, 247*), supporting the concept of collective invasion and/or metastasis. In both homotypic culture and co-culture, our leader and follower cells invade almost exclusively in a collective manner rather than as single cells, suggesting that collective invasion provides a favorable advantage to these cells (*112*).

We show that followers provide a growth advantage to poorly-proliferative leader cells by increasing leader cell colony formation (Figs. 4.2, 4.3) and by correcting leader cell mitotic defects in both 2D cell culture (Figs. 4.4, 4.5, 4.6) and also within 3D collectively invading spheroids (Fig. 4.6). These data argue for a symbiotic relationship between leader and follower cells, where the follower cell secretome improves leader cell mitotic success and leader cells provide followers with an escape mechanism. Interestingly, leader cell conditioned media caused follower cell death and inhibited their colony formation (Fig. 4.2, 4.4), suggesting that leader cells impact follower cell growth dynamics, perhaps to maintain the leader cell lineage within the greater cellular population. How follower cell secreted factors impact leader cell growth and mitosis remains an area of interest, where pathways related to growth factor signaling (*248-250*) could be candidates for impacting cell survival of collective invasion packs.

Although the specific mechanism(s) by which follower cells promote mitotic success in leader cells is not yet known, these data provide evidence that follower cells may serve a unique role as “support cells” for leader cells. This proposed role for follower cells is consistent with a concept from the field of tumor evolution known as clonal cooperation (*251*). As tumors grow and acquire new mutations, new clones of cancer cells will emerge. But what prevents the most robust clone from out-competing with the other cancer cell clones? Both computational and biological studies suggest that tumors frequently exhibit clonal cooperation, wherein two or more populations of cancer cells mutually support each other and thus ensure the survival of multiple different clones

within a single tumor (*66, 98, 172, 252*). As our exploration of leader/follower phenotype determination and cell-cell cooperation continues, we anticipate discovering additional layers of heterogeneity within cancer collective invasion packs that may provide clues as to how to effectively disrupt collective cancer invasion and metastasis.

## Chapter 5: Discussion and Future Directions

Basic and translational cancer biology research over the past few decades has revealed that tumors are far more complex, diverse, and adaptable structures than a mere accumulation of rapidly dividing cells. The rapid influx of knowledge about cancer has provided many new windows of opportunity for designing targeted and effective therapeutics, but it has also revealed several persistent challenges in achieving remission and survival for more patients. In particular, we now understand that tumors are highly heterogeneous, often composed of many different populations of cancer cells each with unique DNA mutations and phenotypic properties. Not only does genotypic and phenotypic heterogeneity limit the ability to therapeutically target all cancer cells within a tumor, but groups of heterogeneous cancer cells can cooperate to symbiotically support each other, as seen in the process of leader cells and follower cells working together to drive collective cancer invasion. The work presented in this dissertation aims to address gaps in the knowledge of how heterogeneous leader and follower cells regulate their unique transcriptional programs, as well as how specific changes in gene expression lead to downstream functional adaptations in leader cells that allow them to regulate collective cancer invasion.

### 5.1 Epigenetic heterogeneity functionally contributes to distinct leader and follower phenotypes

Collective invasion has been observed in patient tumors since at least 1960 (*46*), and histological studies of patient tumors and mouse models of cancer metastasis reveals that most solid tumors preferentially invade using collective invasion rather than single cell invasion (*44, 49, 50*). Recent studies now identify genotypically- and phenotypically-distinct leader and follower cell types within collective invasion packs, with leader cells being highly invasive and able to

coordinate the migration of less-invasive follower cells behind them (*44, 45, 105-107, 112*). Previously, we developed a novel method to isolate purified populations of leader cells and follower cells from collectively invading packs of lung cancer cells, which has allowed us to examine the unique genetic, epigenetic, metabolic, and phenotypic characteristics that drive the distinct leader and follower cell types as well as drive the cooperation between the two populations (*112, 114, 115*). Interestingly, our leader cells derived from collectively-invading lung cancer cell lines exist as a highly-stable highly-invasive cell population that can maintain their leader phenotype over the course of weeks in homotypic culture (*112*), while leader cells from various breast cancer models are a much more transient population that can readily "switch" phenotypes with follower cells and which do not maintain their leader cell status during extended cell culture (*105, 107*). This suggests that the molecular mechanisms that direct the emergence and plasticity of leader and follower phenotypes may differ between cancer types (i.e. breast cancer vs. lung cancer), and it also suggests that epigenetic regulation of gene expression without additional genetic mutations may be a critical component of leader/follower phenotype determination.

Despite a growing understanding of the underlying genetic and transcriptomic differences between tumor subpopulations such as leader cells and follower cells, little is known about the epigenetic factors that underlie heterogeneous phenotype determination and plasticity within the collective invasion pack. In Chapter 2 of this dissertation, we sought to utilize epigenetic heterogeneity to identify key regulators of phenotypic heterogeneity, cell-cell cooperation, and collective tumor invasion. To do this, we integrated DNA methylation array data with RNAseq expression data on purified populations of lung cancer leader and follower cells as well as the parental population of H1299 cells that they were derived from. We show here that lung cancer leader cells are an epigenetically distinct cell population with unique patterns of both DNA

methylation and gene expression, compared to follower cells and the parental population (Fig. 2.1-2.3). DNA methylation patterns that differed in leader cells compared to follower cells and parental cells correlated with a gene expression program enriched for pathways that drive collective invasion, such as Notch signaling, angiogenesis, and cell-ECM interactions (*32, 50, 51, 112, 172, 183*) (Fig. 2.1, 2.3). In contrast, follower cells and the parental population showed almost no significant differences in DNA methylation patterns despite maintaining differences in gene expression (Fig. 2.1-2.3). Together, these data suggest that the leader cell phenotype is characterized by a distinct epigenome regulated in part by genome-wide changes in DNA methylation, providing the first evidence of heritable epigenetic rewiring that differentiates leader and follower cells beyond gene expression alone.

In addition to broad genome-wide shifts in DNA methylation within leader cells, we identified several genes of interest whose expression in leader cells may be regulated by DNA methylation at the promoter (Fig. 2.1F). Here, we identified the genes *MYO10* and *HTATIP2* as two of the genes with the most significant differences in both promoter methylation and gene expression; *MYO10* is both highly expressed and is hypomethylated at the promoter in leader cells compared to follower cells, while *HTATIP2* is not expressed in leader cells and contains a hypermethylated promoter compared to follower cells (Fig. 2.4-2.5). Functional analyses of these two genes demonstrate that both high expression of *MYO10* and silencing of *HTATIP2* are necessary components of the leader cell invasive phenotype within lung cancer collective invasion (Fig. 2.5, and Chapters 3 and 4).

Interestingly, when examining the 123 differentially expressed genes with differentially methylated promoters in leaders versus follower, over 5 times as many genes were hypermethylated and “silenced” in leader cells (i.e. HTATIP2, 72 genes total) rather than

hypomethylated and overexpressed (i.e. MYO10, 13 genes total) (Fig. 2.1F). In comparison, genome-wide changes in DNA methylation followed similar proportions, wherein approximately 80% of differentially methylated CpG probes (DMPs) and 80% of differentially methylated regions (DMRs)were hypermethylated in leaders compared to followers, with the remaining 20% of probes or regions being hypomethylated in leaders compared to followers (Fig. 2.1, 2.2). Although not surprising that these ratios are similar, these data suggest that there may be many other potential genes of interest that are silenced in leader cells through DNA hypermethylation beyond HTATIP2. By probing the biological function and clinical presentation of the additional 71 candidate genes, we may identify additional tumor suppressor genes or invasion/metastasis suppressor genes that are silenced in leader cells.

Looking beyond changes in DNA methylation in these discrete loci, leader cells showed a genome-wide shift towards DNA hypermethylation. Leader cells displayed a 10% increase in the median beta value across all CpG probes in leader cells, i.e. a genome-wide shift towards DNA hypermethylation (Fig. 2.1C, 2.2A). Although the majority of these DMPs were within promoter regions or intragenic regions, approximately 30% of DMPs were within the sequences of enhancers, non-coding RNAs; since only 21% of the CpG probes designed for this array annotate to these non-coding regions, then it can be inferred that hypermethylation or hypomethylation in leader cells occurs disproportionately in non-coding regions (Fig. 2.1C). DNA methylation at distal regulatory elements is still poorly understood, but these data raise the intriguing question as to whether DNA methylation in leader cells within distal regulatory elements and intergenic regions plays a role in regulating leader cell gene expression. In order to evaluate DNA methylation within non-coding regions and non-annotated intergenic regions, bisulfite sequencing could be utilized to

provide true genome-wide analysis of DNA methylation beyond the subset of CpG sites sampled in the MethylationEpic 850K array.

Since leader cells showed an overall shift towards DNA hypermethylation, we hypothesized that this increase in DNA methylation was a necessary component of leader cell transcriptional regulation, and that consequently, leader cells would be more sensitive to the inhibition of DNA methylation. Although there are not currently any methods to reliably reduce DNA methylation at specific loci, there are several clinically-utilized inhibitors of DNA methyltransferases (DNMTs) (*79, 81*). These inhibitors act as mimetics of cysteine and are incorporated into nascent DNA during DNA replication, wherein they permanently bind to DNMTs to inhibit these proteins from adding 5mC to the nascent DNA strand (*77*). When parental, follower, and leader cells were treated with the DNMT inhibitor DAC, leader cell spheroids and parental cell spheroids significantly decreased collective invasion, while all three cell types treated with DAC showed approximately 90% viability across a wide range of doses compared to treatment with the vehicle control (Fig. 2.6). While we did not confirm that DAC decreased the overall levels of DNA methylation in these cells, increased expression of *HTATIP2* and *MYO10* after DAC treatment suggested that DAC had induced changes in gene expression through reduced promoter DNA methylation (Fig. 2.7).

Since alterations in DNA methylation are associated with cancer progression and poor patient prognosis across many tumor types, scientists have utilized DNMT inhibitors as part of chemotherapy regimens for certain cancer patients for many years (*83*). Clinically, these inhibitors are capable of causing global DNA hypomethylation as well as demethylating the promoters of tumor suppressor genes to re-activate expression these silenced genes (i.e. *HTATIP2*) (*80, 81, 253*). While these inhibitors are commonly utilized to treat several hematological malignancies, DNMT

inhibitors have shown only modest clinical results when used to treat solid tumors, potentially due to the short half-life of these inhibitors, poor bioavailability within solid tumors, or the necessity to inhibit additional molecular targets in order to elicit a clinical effect (*254*). However, recent and ongoing studies that combine DNMT inhibitors with additional inhibitors of histone modifiers and/or inhibitors of immune checkpoints show great promise in eliciting a stronger antitumor response in patients (*78, 82, 255, 256*). One recent study demonstrates that DNMT inhibitors induce an interferon-dependent innate immune response in tumors by triggering expression of evolutionarily-conserved dsRNAs and hypermethylated endogenous retroviruses; thus, DNA methylation inhibitors may provide an exciting new avenue to induce an anti-tumor immune response in tumors that would otherwise fail to benefit from immune checkpoint inhibitors (*255*). Thus, while it may not be feasible to target leader cells and decrease tumor invasion with DNMT inhibitors alone, it is worth investigating whether a combination of these DNA demethylating agents with additional therapeutic compounds such as histone methyltransferase/deacetylase inhibitors, immune checkpoint inhibitors, or even traditional DNA-damaging agents could create a sustained epigenetic blockade of leader cells and a bolstered anti-tumor response in patients.

### 5.2 The uncharted waters of the genome: Future avenues for examining how chromatin regulation contributes to tumor phenotypic heterogeneity

The work presented here provides a solid basis to suggest that epigenetic regulation of leader/follower transcriptional programs is critical for inducing and maintaining the specific functional roles of leader cells and follower cells, but many questions concerning the transcriptional regulation of these cell populations remain unanswered. Although this study focused primarily on differential DNA methylation at gene promoters, less than 20% of DMPs

between leaders and followers occurred within gene promoters, whereas approximately 12% of DMPs occurred within distal regulators of gene expression such as enhancer regions or non-coding RNAs and an additional 20% of DMPs occurred within intergenic regions with no known functional annotations (Fig. 2.1C). Enhancers are uniquely dynamic distal regulatory elements that can regulate the transcription of their target genes up to several megabases away by chromatin looping and recruitment of transcription factors and various co-activator proteins (*182, 257*). The highly variable activity of enhancers has been hypothesized to play a crucial role in the spatiotemporal control of cell type differentiation during development and homeostasis (*257*). Active enhancers are strongly associated with the active histone marks H3K27ac and H3K4me1, while DNA methylation at active enhancers is far more variable (*258*).

DNA methylation at enhancers is a complicated and poorly-understood process. DNA methylation at some enhancers but not all can reduce transcription factor binding, potentially by maintaining a bivalent state with certain histone modifications, but a complete understanding of how DNA methylation at enhancers affects downstream gene expression is lacking (*259, 260*). DNA methylation at enhancer regions has been observed in multiple cancer types and is hypothesized to play a role in regulating the vast changes in gene expression that occur in cancer (*261*). Since an outsized portion of differential DNA methylation in our leader cells occurred at enhancers and other distal regulatory elements, we hypothesize that differential DNA methylation at these sites could play an important role in regulating gene expression changes during leader/follower phenotype determination, or potentially in regulating phenotypic plasticity during collective invasion (i.e. follower cells that transition to leader cells). Thus, probing the role of variable DNA methylation at enhancers in regulating divergent leader/follower cell transcription warrants further study.

Although DNA methylation is a critical component of epigenetic regulation, it is by no means the only regulator of chromatin architecture. For example, histone modifying enzymes add or remove a variety of post-translational modifications to change the ability of histones to bind to DNA and to recruit various molecular components of transcriptional complexes (*262-264*), and histone modifications and DNA methylation show extensive interplay in regulating gene expression (*265*). Many questions remain as to what additional chromatin regulators participate in leader/follower phenotype determination, but we expect there will be additional transcriptional regulators that functionally regulate phenotype determination during collective invasion. For example, RNAseq analysis showed that leaders and followers expressed differing amounts of several genes responsible for writing, erasing, or maintaining DNA methylation (Fig. 2.2E) as well as several genes related to histone modifications (data not shown). Functional studies of these differentially expressed chromatin regulators would reveal which ones are necessary for maintaining the leader and follower phenotypes. In addition, more nuanced epigenomic analysis, such as whole genome bisulfite sequencing of DNA methylation combined with ChIP-seq or Cut-and-Run analysis of histone modifications would provide a more detailed map of the chromatin landscape in leader and follower cells.

Additional analysis of our RNAseq data, although limited, provides clues as to other potential epigenetic regulators of interest that are differentially expressed between leader and follower cells. From this RNAseq data, we showed that follower cells express a mutation in lysine demethylase 5B (*KDM5B* L685W) that leads to a significant loss of KDM5B protein expression in follower cells; expression of wild-type KDM5B promoted collective invasion while expression of KDM5B L685W inhibited collective invasion in both leader cells and follower cells (*114*). KDM5B removes di- and trimethylation from lysine 4 of histone 3 (H3K4me2 and H3K4me3)

(*266*). H3K4 methylation marks regions of active transcription and is commonly enriched at the promoter and transcription start site (*267*). Not only do H3K4 methylation and DNA methylation have opposite effects on transcriptional activity, but also DNA methylation and H3K4me2/H3K4me3 are mutually exclusive within the same chromatin regions (*268, 269*). Therefore, it is possible that loss of KDM5B in follower cells "protects" them from an increase of DNA methylation (as seen in leader cells) in order to maintain follower-related transcriptional activity, although additional studies are needed to test this hypothesis.

Another interesting avenue of transcriptional regulation that may contribute to tumor heterogeneity are proteins that can induce big structural changes in the 3D chromatin architecture. For example, leader cells express high levels of the chromatin regulator CTCFL, while followers show almost no expression (and parental cells express an intermediate amount of CTCFL) (Fig. 2.1E). CTCFL, or CCCTC Binding Factor Like, is a paralog for the gene CTCF; CTCF promotes chromatin insulation and 3D chromatin structures called chromatin loops that play a role in bringing distal enhancers in close proximity to their target genes (*270*). While CTCF is ubiquitously expressed in all cells, CTCFL is expressed almost exclusively in the testis during spermatogenesis (*271*). While the function of CTCFL is not yet fully understood, as its role in regulating 3D chromatin structures does not perfectly match that of CTCF (*270, 272*), it has been shown that CTCFL rewires the epigenomic landscape of cancer cells to induce a more germ-like or stem cell-like state (*273-275*). Aberrant CTCFL expression has also been found in multiple cancer types, including urogenital cancers, ovarian cancer, and esophageal cancer (*271, 274, 276-278*). Thus, the intriguing possibility remains that aberrant CTCFL expression in leader cells could regulate substantial chromatin structural changes that contribute to the unique epigenetic landscape of leader cells.

**5.3 MYO10 promotes collective invasion through long, stable filopodia in leader cells**

In Chapter 2 of this dissertation, we identified myosin-X *(MYO10)* as a key gene at the intersection of differential DNA methylation and expression in leader cells, and in Chapters 3 and 4, we demonstrate how MYO10 promotes the invasive properties of leader cells during collective invasion by driving the formation and stability of long filopodia. MYO10 is an unconventional myosin that regulates the formation and elongation of filopodia as well as other actin-based protrusions that are important for cancer invasion, such as filopodia-like long protrusions and invadopodia (*143, 144*). We show that MYO10 is enriched in leader cells across multiple NSCLC cell lines and a patient-derived lung NSCLC cell line, and we further demonstrate that MYO10 expression in filopodia is critical for leader-driven lung cancer collective invasion (Figs. 3.1-3.2). Importantly, we show how MYO10 affects filopodia elongation and persistence in a 3D ECM (Fig. 3.2A-C). While MYO10-driven effects on filopodia have been well-documented on 2D surfaces (*143, 144*), we provide some of the first analysis of filopodia length and dynamics within 3D collective cancer invasion. In addition, while MYO10 has been shown to regulate cancer cell invasion and metastasis (*149, 163, 165*), we present the first evidence that MYO10 expression in only a rare subset of cells (*i.e*. leader cells) rather than the entire population is sufficient to induce tumor cell collective invasion.

Interestingly, MYO10 appears to regulate collective migration not only during cancer invasion but also during development. Two independently-created MYO10 knockout mouse models showed that MYO10 loss in mice lead to severe developmental defects in several collective migration-dependent processes, such as angiogenesis, melanocyte migration from the neural crest, axon guidance, and digit formation (*162-164*). Our observations and the observations within

MYO10 knockout mouse models suggest that filopodia may play a surprisingly important role in regulating multicellular functions (*e.g.* collective cancer invasion or angiogenesis) despite the fact that most research on filopodia function has been conducted on single cells on 2D substrates. In particular, MYO10 is responsible for facilitating the elongation of filopodia and promoting filopodial stability over time. Filopodial stability is achieved at least in part by a combination of MYO10 transport of the actin anti-capping proteins MENA/VASP to the tips of filopodia that prevent the collapse of the supporting actin microfilament bundles (*151*) and by the creation of nascent filopodial adhesion sites that adhere to the ECM and prevent the passive retraction of filopodia back into the cell body (*132, 134*). Understanding the unique components of filopodial adhesion sites within cancer cells, such as MYO10 and the integrins it transports, may provide new opportunities for targeted inhibition of cancer invasion and metastasis.

**5.4 JAG1/Notch regulates MYO10 expression**

Transcriptional regulation of *MYO10* is poorly understood, and our results support the model that both promoter DNA hypomethylation and JAG1/Notch transcriptional activity cooperate to drive *MYO10* expression in leader cells. We identify the Notch ligand, JAG1, as a leader-specific marker and as a transcriptional activator of *MYO10* (Figs. 3.4-3.5). JAG1 was detected in the rare leader cell population not only during spheroid collective invasion (Fig. 3.4B-C), but it was also detected by flow cytometry within a small population of the parental H1299 cell line and within a rare subpopulation of a patient-derived NSCLC sample (Fig. 3.5C). JAG1 knockdown or inhibition significantly abrogated collective 3D invasion of several cell lines, the patient-derived sample, and mixed populations of leader and follower cells (Figs. 3.4J-K, 3.7B-C, 3.8A). In many cancers, JAG1 expression promotes cancer stem cells, tumor invasion, metastasis,

and poor patient outcome (*206, 219*). JAG1 is also highly expressed in breast cancer leader cells (*50*), suggesting that JAG1 may regulate leader cells across other cancer types beyond breast and lung cancer.

Notch pathway signaling and downstream transcriptional targets are strongly enriched in leader cells compared to follower cells (Figs. 2.3, 3.4, 3.5), but JAG1 was the Notch family member most robustly upregulated in leader cells (Fig. 3.4A). Out of all the Notch ligands and receptors, JAG1 is also the Notch family member that is most frequently indicated as a poor prognostic indicator in cancer patients; studies across several cancer types including breast cancer, lung cancer, cervical cancer, head and neck cancer, ovarian cancer, and medulloblastoma show that high JAG1 expression promotes cancer cell survival, chemoresistance, cancer stem cell activity, and metastasis, and ultimately high JAG1 expression correlates with poor patient prognosis (*206, 279-285*). We demonstrate here that JAG1 is upstream of *MYO10* expression in leader cells; *JAG1* knockdown significantly decreased *MYO10* mRNA and protein expression, whereas *MYO10* knockdown did not affect *JAG1* expression (Figs. 3.4D-E, 3.7A). We also show that *JAG1* knockdown significantly decreased filopodia length, consistent with a loss of *MYO10* expression (Fig. 3.4H-I). Interestingly, *JAG1* overexpression in follower cells did not induce *MYO10* expression (Figs. 3.4F, 3.8C-D) and also did not demethylate the *MYO10* promoter (Fig. 3.4G). These data suggest that JAG1 expression without other subsequent epigenetic changes to chromatin availability observed in leader cells (*e.g.* MYO10 promoter DNA hypomethylation) is not sufficient to induce MYO10 expression. This is also the first report that links JAG1 to transcriptional regulation of MYO10. Only one previous study has implicated Notch1 signaling as an upstream regulator of MYO10 expression (*208*). However, this study examined Notch1 ICD activity independent of any Notch ligands, and the study was performed in endothelial cells in

mice. As mentioned above, Notch signaling is highly variable depending on the biological context, so our identification of JAG1 as the key Notch family regulator upstream of MYO10 in leader cells provides important novel insight into how MYO10 is transcriptionally regulated in cancer cells, as well as providing a new example of the many pro-tumor functions of JAG1.

Looking beyond JAG1 alone, multiple Notch signaling gene sets were significantly enriched in leaders compared to followers (Figs. 2.1G, 2.3, 3.5A-B). The Notch signaling pathway is highly evolutionarily conserved and plays critical roles in many facets of development and cancer (*205, 220*). And yet, this single signaling pathway is capable of inducing incredibly variable consequences in cell function; depending on when and where in an organism Notch signaling occurs, different combinations of receptor/ligand interactions at cell-cell contacts as well as combinations of additional transcription factors within Notch ICD transcriptional complexes can promote very different transcriptional programs (*220*). Due to the complexities of the Notch pathway, Notch signaling likely undergoes different spatiotemporal regulation within collective invasion packs than it does during developmental processes, such as angiogenesis.

JAG1 was strongly localized to cell-cell contacts between leader cells (Figs. 3.4C, 3.6). Since JAG1 was frequently present in clusters of 2-4 leader cells within invading parental spheroids (Fig. 3.4C), we propose that leader cells participate in trans-activation of JAG1 and Notch across two adjacent leader cells, rather than between leader and follower cells (*205*). Notch signaling often undergoes context-dependent spatiotemporal regulation (*205, 220*), and a recent study suggests that Notch may occasionally undergo cis-activation with Notch receptors and

ligands on the same cell (*286*). Therefore, much remains to be explored in terms of how Notch/JAG1 interact to coordinate transcription within the collective invasion pack.

### 5.5 MYO10 promotes FN micropatterning at the invasive front of 3D collective invasion by inducing filopodial stability

In Chapter 3 of this dissertation, we also show that MYO10-expressing filopodia play a unique and surprising role in ECM alignment at the invasive front of collective invasion. Cell-ECM interactions regulate several aspects of collective cancer invasion, including integrin-FAK motility signaling, MMP-driven proteolysis of the ECM, and deposition and remodeling of ECM components (*32, 51, 221*). Here, we show that leader cells but not follower cells secrete and align fibronectin into long linear fibrils extending past the leading edge (Figs. 3.9-3.14). Fibronectin fibrillogenesis is a complex process that involves integrin engagement with soluble FN dimers, reorganization of the actin cytoskeleton, and translocation of integrin-FN complexes along actin filaments to form mature fibrillar adhesions (*215, 222*). Studies of FN fibrillogenesis have focused primarily on adhesion sites within the cell body, but questions remain as to how the fibrillogenesis that we observed within the shafts of filopodia at the leading edge of 3D invasion differs from canonical fibrillogenesis along the basal surface of the cell body.

Cell-ECM adhesion sites can form within filopodia tips or shafts, but the core components of these nascent filopodia adhesions lack many proteins that transmit traction forces, such as tensin, that are seen in canonical focal adhesions or mature fibrillar adhesions (*133*). Nascent filopodia adhesions can mature into focal adhesions after lamellipodial advancement (*136*). Our live cell imaging shows that while most FN fibrillogenesis occurred beneath the basal surface of the cell body in advancing leader cells, FN fibrillogenesis could catalyze through a multi-step

process within the shaft of stabilized MYO10-expressing filopodia, leaving long parallel FN "tracks" extending in front of the leading cell after filopodial retraction (Figs. 3.9, 3.14). This observation of multi-step FN fibril elongation is consistent with focal adhesions maturing into fibrillar adhesions during FN fibrillogenesis observed underneath the basal surface of the cell body (*222*). However, these nascent filopodial adhesions likely differ from canonical focal adhesions in their integrin and intracellular components (*133, 136*). Understanding how these filopodial adhesions mature into focal adhesions and how they transmit traction forces capable of remodeling the extracellular matrix (*i.e.* fibronectin fibrillogenesis) remain areas of keen interest.

Notably, nascent FN fibrils initiated approximately 1.8μm behind the filopodia tip and were not co-localized with MYO10-GFP in live cell imaging (Fig. 3.14H-J). This suggests that MYO10 does not directly interact with FN. However, MYO10+ leader cell filopodia had longer lifetimes than MYO10-knockdown filopodia during 3D invasion (Fig. 3.2C, 3.14M). We speculate that MYO10-driven filopodial persistence is necessary for forming nascent filopodial adhesions in the tip and/or shaft, engaging with FN, and maturing into larger focal adhesion sites capable of elongating nascent FN fibrils at the leading edge. Thus, in MYO10-knockdown cells, FN fibrillogenesis can still occasionally be seen beneath the cell body (Fig. 3.9D, 3.11-3.14), but MYO10-depleted cells form significantly fewer leading-edge FN tracks since these filopodia likely do not persist long enough to form nascent adhesions (Fig. 3.9D-E, 3.14M).

MYO10 induces filopodial longevity most likely in part through its ability to transport integrins into filopodia (*143, 150*). Structural studies confirm that MYO10 binds to β-integrins through its FERM domain, and functional studies suggest that MYO10 affects the localization of integrin α5 to filopodia tips as well (*148-150*). Since the integrin heterodimers α5β1 and αVβ3 are the predominant integrins responsible for FN fibrillogenesis (*215-217, 222*), we interrogated

the expression and function of these four integrins within leader cells (Fig. 3.15). Leader cells expressed significantly more αV and β3 integrins compared to follower and parental cells, while all three cell types expressed comparable levels of α5 and β1 integrins (Fig. 3.15A). However, all three cell types expressed substantially more β1 integrin than any of the other three integrins. Integrin β1 in particular has long been implicated in cancer invasion and metastasis (*223*), so it is not entirely surprising that these cells express high levels of integrin β1. Furthermore, by functionally blocking each of these integrins separately with inhibitory antibodies, we determined that loss of integrin β1 function significantly abrogated both collective invasion and FN micropatterning, whereas inhibition of α5 alone (data not shown) or αVβ3 integrins did not affect either function (Fig. 3.15B-C). Thus, these data suggest that integrin β1, a MYO10 cargo protein, is a key component of filopodia-directed FN alignment. High-resolution microscopy would be necessary to identify whether integrin β1 localizes preferentially to the filopodia tip or shaft, as well as to identify additional molecular components of integrin β1 filopodial adhesion sites.

Even though integrin β1 directly binds to FN during fibrillogenesis (*213*), it is not yet known whether the same integrin β1-containing adhesion sites within filopodia that drive FN fibrillogenesis are the same adhesion sites that maintain filopodial stability, or whether different integrin heterodimers are responsible for this stability. Filopodia produce adhesion sites at both the tip and along the shaft that are unique in their protein composition compared to canonical focal adhesions (*133, 136*), but there has not yet been a thorough examination of which integrins localize to adhesion sites within one or both of these filopodial regions. Furthermore, it is possible that filopodial integrin composition varies depending on the microenvironment (2D vs 3D culture, differing matrix components, mechanical properties of the extracellular environment, etc.), and elucidating the contributions of different integrins within filopodia remains an area of keen

interest. In addition, further studies of traction forces within filopodia, how integrin activation and molecular components differ between filopodial tip and shaft adhesions, and how filopodial tip adhesions and shaft adhesions differentia affect filopodial dynamics and FN fibrillogenesis may elucidate how filopodia act not only as sensors of the extracellular environment but also as active participants in ECM remodeling. Ultimately, this study provides the first evidence that directly links MYO10 and stabilized filopodia to fibronectin alignment during 3D cancer invasion, which opens the intriguing possibility that filopodia may play a much more active role than previously thought during cancer invasion and metastasis.

Another surprising finding was that JAG1 knockdown in leader cell spheroids abrogated globular FN localization, suggesting that JAG1 may impact FN secretion independently of MYO10 expression (Fig. 3.13). Knockdown of JAG1 in leader cell spheroids inhibits MYO10 expression (Fig. 3.4), so the loss of leading-edge linear FN micropatterning in JAG1 knockdown spheroids is consistent with JAG1 transcriptional regulation of MYO10 (Fig. 3.13). However, the appearance of globular FN in JAG1 knockdown cells (Fig. 3.13) is strikingly different from that of globular FN in MYO10 knockdown cells (Fig. 3.9). In MYO10 knockdown cells, some minimal amount of FN fibrillogenesis still occurs beneath the cell body, and globular FN dimers are diffusely localized, so that there is a slight “haze” of FN immunofluorescence signal in the extracellular matrix. However, in JAG1 knockdown cells, huge clumps of FN with very bright immunofluorescence intensities can be seen within the cytoplasm of cells, clustering near cell-cell contacts, but almost no globular FN can be seen in the extracellular space. This observation suggests that JAG1 may regulate FN secretion, and so loss of JAG1 leads to an excess accumulation of globular FN within the cell. Quantification of extracellular FN by Western blot or proteomic analysis in JAG1 knockdown leader cells compared to knockdown-control leader

cells will be necessary to confirm if this unusual FN localization is due to a loss of FN secretion or due to aberrant subcellular localization. There are currently no known direct signaling events that link JAG1 to FN1 secretion, but future examination of signaling events downstream of JAG1 may elucidate a novel connection between the two.

### 5.6 MYO10 utilizes additional functions beyond the leading edge to regulate mitotic integrity and cell-cell adhesion in leader cells

Filopodia act as far more than the "sticky fingers" at the front of directed cell migration; filopodia and filopodia-like structures facilitate a wide variety of additional critical cellular functions, such as cell-cell adhesion, invadopodia, cell-ECM adhesion during mitosis, and spindle alignment (*132*). In Chapter 4 of this dissertation, we show that MYO10-driven filopodia also localize to certain mitotic structures and cell-cell junctions, providing evidence that MYO10 and filopodia may play additional roles to support leader cell function.

Since MYO10 is capable of binding to both actin microfilaments and tubulin microtubules, MYO10 can localize to cellular structures that contain both of these cytoskeletal components. Highly dynamic interactions between actin and tubulin are critical for driving huge cytoskeletal restructuring events that occur during mitosis (*287-289*). Although MYO10 has been reported to localize to the mitotic spindle in non-mammalian cells (*236, 237*), we show that MYO10 does not localize to the mitotic spindle (Fig. 4.1), consistent of previous studies of MYO10 within mammalian cells undergoing mitosis (*228, 233*). It is not known why MYO10 localization at the spindle poles (or lack thereof) differs between non-mammalian and mammalian species, but it is clear that MYO10 regulates spindle pole orientation using mechanisms independent of direct binding to the mitotic spindle (*233, 237, 238*). Although MYO10 did not localize to the spindle

pole in our leader cells, MYO10 did localize to the midbody during cytokinesis, a previously unreported localization of MYO10 (Fig. 4.1). Since the midbody contains overlapping bundles of both microfilaments and microtubules, we speculate that MYO10 may coordinate the bundling and/or pulling force of the midbody by linking the two components. Further studies are needed in order to determine the function of MYO10 within this short-lived structure.

Previous studies suggest that MYO10-induced filopodia are also a critical component of creating and maintaining cell-cell contacts (*227, 228*). We show that MYO10 localized to filopodia and filopodia-like structures at regions of cell-cell contact, both in 2D and 3D leader cell culture (Fig. 4.7-4.8). Filopodia facilitate cell-cell adhesion during development and in normal epithelial cells, but very little is known about the role of filopodia within the context of cancer cell-cell adhesion (*132*). Additional live cell imaging studies utilizing fluorescent fusion proteins are needed to determine whether MYO10-expressing filopodia affect the timing and structure of new intercellular junctions between leader cells and follower cells at points of cell-cell contact (i.e. adherens junctions, tight junctions, gap junctions). Ultimately, facilitating cell-cell adhesion may prove to be one of the most important functions by which MYO10 regulates collective invasion of leader and follower cells, since maintaining cell-cell adhesion is necessary by definition for collective cancer invasion.

Although it is difficult to determine the direction of lateral migration in fixed 2D cells, MYO10 in leader cells localized to the basal side of regions of cell-cell overlap. These observations suggest that either the leading edge of the leader cell with MYO10-expressing filopodia "wedges" beneath another cell, or that the leading edge of another leader cell moves over the "tail" end of a leader cell with ventral MYO10-expressing filopodia. In either scenario, the MYO10-expressing filopodia were unidirectional, i.e. MYO10-expressing filopodia were present within this region of

overlap in the bottom cell but not in the top cell. It is not clear whether there is any functional significance to MYO10-expressing filopodia being present on only one side of the cell-cell contact, but it suggests that there may be some sense of molecular polarity at the cell-cell interface, meaning that the molecular components of the top cell and the bottom cell may not be identical and could potentially orient the direction of collective invasion.

Filopodial regulation of cell-cell adhesion may potentially explain *how* cancer cells maintain physical contact during collective invasion, but the question remains as to *why* cancer cells preferentially invade as a collective pack as opposed to single cells. One potential answer is that the multicellular pack provides a survival or invasive advantage to escaping cells. In circulating tumor cells, cells that invaded as groups had greater success and worse clinical outcomes (*48, 246*). Furthermore, studies show that tumor cell clusters, rather than single cells, seed polyclonal metastases in mouse models (*48-50, 247*), supporting the concept of collective invasion and/or metastasis. In both homotypic culture and co-culture, our leader and follower cells invade almost exclusively in a collective manner rather than as single cells, suggesting that collective invasion provides a favorable advantage to these cells (*112*).

We show that followers provide a growth advantage to poorly-proliferative leader cells by increasing leader cell colony formation (Figs. 4.2, 4.3) and by correcting leader cell mitotic defects in both 2D cell culture (Figs. 4.4, 4.5, 4.6) and also within 3D collectively invading spheroids (Fig. 4.6). These data argue for a symbiotic relationship between leader and follower cells, where the follower cell secretome improves leader cell mitotic success and leader cells provide followers with an escape mechanism. Interestingly, leader cell conditioned media caused follower cell death and inhibited their colony formation (Fig. 4.2, 4.4), suggesting that leader cells impact follower cell growth dynamics, perhaps to maintain the leader cell lineage within the greater cellular

population. How follower cell secreted factors impact leader cell growth and mitosis remains an area of interest, where pathways related to growth factor signaling (*248-250*) could be candidates for impacting cell survival of collective invasion packs.

Although the specific mechanism(s) by which follower cells promote mitotic success in leader cells is not yet known, these data provide evidence that follower cells may serve a unique role as "support cells" for leader cells. This proposed role for follower cells is consistent with a concept from the field of tumor evolution known as clonal cooperation (*251*). As tumors grow and acquire new mutations, new clones of cancer cells will emerge. But what prevents the most robust clone from out-competing with the other cancer cell clones? Both computational and biological studies suggest that tumors frequently exhibit clonal cooperation, wherein two or more populations of cancer cells mutually support each other and thus ensure the survival of multiple different clones within a single tumor (*66, 98, 172, 252*). As our exploration of leader/follower phenotype determination and cell-cell cooperation continues, we anticipate discovering additional layers of heterogeneity within cancer collective invasion packs that may provide clues as to how to effectively disrupt collective cancer invasion and metastasis.

## 5.7 Conclusions

In summary, the research in this dissertation provides new insight into how heterogeneous epigenetic regulation of gene expression facilitates the unique transcriptional landscape and invasive properties of leader cells, as well as providing new evidence that MYO10 regulates filopodia and filopodia-like structures in leader cells within multiple cellular functions that are important for collective invasion, including ECM remodeling, mitotic integrity, and cell-cell adhesion. The work in this dissertation also highlights the importance of rethinking how cellular

processes “normally” happen. For example, filopodia have long been regarded as merely sensors of the ECM, but we provide evidence that filopodia are not just passive sensors but instead directly contribute to FN alignment at the invasive front of collective cancer invasion. This is some of the first evidence that MYO10 and filopodia as a whole have been shown to play a direct role in ECM alignment. Perhaps by similarly re-examining the canonical components of cancer cell biology, we may discover new and clinically-actionable ways in which cancer flaunts the rules of normal cell biology.

Importantly, the studies within this dissertation are limited by a lack of *in vivo* data. While tumor spheroid models are a highly effective tool for probing and imaging the complex cellular and molecular dynamics during collective cancer invasion, away from the primary tumor, it is impossible to assess the role of collective invasion during metastasis without a whole living organism. Metastasis research in genetically-engineered mouse models could provide crucial insight into how the 3D extracellular environment at both the primary and secondary site affect the behavior of collective invasion packs, as well as how additional confounding factors effect collective invasion, such as hypoxic conditions, tumor cell circulation, and immune surveillance. Murine and human studies of breast cancer collective invasion show that polyclonal multicellular clusters have an advantage in completing the metastatic cascade compared to single-clone clusters or single cells (*44, 48-50, 105*). Thus, we hypothesize that tumor cell clusters containing both leader cells and follower cells would be more successful at establishing metastases compared to either the follower or leader cells alone, and we aim to create both xenograft models and genetically-engineered mouse models to explore these questions. Although the work presented in this dissertation provides new insight into the complex molecular regulation of collective cancer cell invasion, many questions remain as to how tumor heterogeneity, phenotypic plasticity, and

clonal cooperation fit into the larger context of cancer metastasis. Ultimately, this work provides one small step forward in our path to understanding and effectively eliminating the insidious process of cancer metastasis.

## Chapter 6: References


1. R. L. Siegel, K. D. Miller, A. Jemal, Cancer statistics, 2019. *CA Cancer J Clin* **69**, 7-34 (2019).
2. E. National Cancer Institute Surveilance, and End Results (SEER) Program. (2020).
3. I. J. Fidler, The pathogenesis of cancer metastasis: the 'seed and soil' hypothesis revisited. *Nat Rev Cancer* **3**, 453-458 (2003).
4. L. Wan, K. Pantel, Y. Kang, Tumor metastasis: moving new biological insights into the clinic. *Nat Med* **19**, 1450-1464 (2013).
5. P. S. Steeg, Tumor metastasis: mechanistic insights and clinical challenges. *Nat Med* **12**, 895-904 (2006).
6. C. Zappa, S. A. Mousa, Non-small cell lung cancer: current treatment and future advances. *Transl Lung Cancer Res* **5**, 288-300 (2016).
7. A. M. Alizadeh, S. Shiri, S. Farsinejad, Metastasis review: from bench to bedside. *Tumour Biol* **35**, 8483-8523 (2014).
8. A. F. Chambers, A. C. Groom, I. C. MacDonald, Dissemination and growth of cancer cells in metastatic sites. *Nat Rev Cancer* **2**, 563-572 (2002).
9. M. D. Cameron *et al.*, Temporal progression of metastasis in lung: cell survival, dormancy, and location dependence of metastatic inefficiency. *Cancer Res* **60**, 2541-2546 (2000).
10. A. F. Chambers, G. N. Naumov, S. A. Vantyghem, A. B. Tuck, Molecular biology of breast cancer metastasis. Clinical implications of experimental studies on metastatic inefficiency. *Breast Cancer Res* **2**, 400-407 (2000).
11. P. Subarsky, R. P. Hill, The hypoxic tumour microenvironment and metastatic progression. *Clin Exp Metastasis* **20**, 237-250 (2003).
12. Q. T. Le, N. C. Denko, A. J. Giaccia, Hypoxic gene expression and metastasis. *Cancer Metastasis Rev* **23**, 293-310 (2004).
13. J. T. Chi *et al.*, Gene expression programs in response to hypoxia: cell type specificity and prognostic significance in human cancers. *PLoS Med* **3**, e47 (2006).
14. R. Blanco, H. Gerhardt, VEGF and Notch in tip and stalk cell selection. *Cold Spring Harb Perspect Med* **3**, a006569 (2013).
15. M. Boareto, M. K. Jolly, E. Ben-Jacob, J. N. Onuchic, Jagged mediates differences in normal and tumor angiogenesis by affecting tip-stalk fate decision. *Proc Natl Acad Sci U S A* **112**, E3836-3844 (2015).
16. H. M. Eilken, R. H. Adams, Dynamics of endothelial cell behavior in sprouting angiogenesis. *Curr Opin Cell Biol* **22**, 617-625 (2010).
17. H. Gerhardt *et al.*, VEGF guides angiogenic sprouting utilizing endothelial tip cell filopodia. *J Cell Biol* **161**, 1163-1177 (2003).
18. J. W. Rak, B. D. St Croix, R. S. Kerbel, Consequences of angiogenesis for tumor progression, metastasis and cancer therapy. *Anticancer Drugs* **6**, 3-18 (1995).
19. P. Rouhi *et al.*, Pathological angiogenesis facilitates tumor cell dissemination and metastasis. *Cell Cycle* **9**, 913-917 (2010).
20. S. P. Chiang, R. M. Cabrera, J. E. Segall, Tumor cell intravasation. *Am J Physiol Cell Physiol* **311**, C1-C14 (2016).
21. V. Plaks, C. D. Koopman, Z. Werb, Cancer. Circulating tumor cells. *Science* **341**, 1186-1188 (2013).

22. C. L. Chaffer, R. A. Weinberg, A perspective on cancer cell metastasis. *Science* **331**, 1559-1564 (2011).
23. P. Friedl, K. Wolf, Tumour-cell invasion and migration: diversity and escape mechanisms. *Nat Rev Cancer* **3**, 362-374 (2003).
24. P. Friedl, K. Wolf, Plasticity of cell migration: a multiscale tuning model. *J Cell Biol* **188**, 11-19 (2010).
25. J. E. Bear, J. M. Haugh, Directed migration of mesenchymal cells: where signaling and the cytoskeleton meet. *Curr Opin Cell Biol* **30**, 74-82 (2014).
26. S. V. Plotnikov, A. M. Pasapera, B. Sabass, C. M. Waterman, Force fluctuations within focal adhesions mediate ECM-rigidity sensing to guide directed cell migration. *Cell* **151**, 1513-1527 (2012).
27. L. S. Havel, E. R. Kline, A. M. Salgueiro, A. I. Marcus, Vimentin regulates lung cancer cell adhesion through a VAV2-Rac1 pathway to control focal adhesion kinase activity. *Oncogene* **34**, 1979-1990 (2015).
28. K. Burridge, K. Fath, T. Kelly, G. Nuckolls, C. Turner, Focal adhesions: transmembrane junctions between the extracellular matrix and the cytoskeleton. *Annu Rev Cell Biol* **4**, 487-525 (1988).
29. V. Petit, J. P. Thiery, Focal adhesions: structure and dynamics. *Biol Cell* **92**, 477-494 (2000).
30. M. Larsen, V. V. Artym, J. A. Green, K. M. Yamada, The matrix reorganized: extracellular matrix remodeling and integrin signaling. *Curr Opin Cell Biol* **18**, 463-471 (2006).
31. P. Friedl, K. S. Zanker, E. B. Brocker, Cell migration strategies in 3-D extracellular matrix: differences in morphology, cell matrix interactions, and integrin function. *Microsc Res Tech* **43**, 369-378 (1998).
32. C. Bonnans, J. Chou, Z. Werb, Remodelling the extracellular matrix in development and disease. *Nat Rev Mol Cell Biol* **15**, 786-801 (2014).
33. I. Stamenkovic, Extracellular matrix remodelling: the role of matrix metalloproteinases. *J Pathol* **200**, 448-464 (2003).
34. B. Eckes *et al.*, Fibroblast-matrix interactions in wound healing and fibrosis. *Matrix Biol* **19**, 325-332 (2000).
35. B. Erdogan, D. J. Webb, Cancer-associated fibroblasts modulate growth factor signaling and extracellular matrix remodeling to regulate tumor metastasis. *Biochem Soc Trans* **45**, 229-236 (2017).
36. E. Sahai, Mechanisms of cancer cell invasion. *Curr Opin Genet Dev* **15**, 87-96 (2005).
37. A. F. Maree, P. Hogeweg, How amoeboids self-organize into a fruiting body: multicellular coordination in Dictyostelium discoideum. *Proc Natl Acad Sci U S A* **98**, 3879-3883 (2001).
38. P. Friedl, S. Borgmann, E. B. Brocker, Amoeboid leukocyte crawling through extracellular matrix: lessons from the Dictyostelium paradigm of cell movement. *J Leukoc Biol* **70**, 491-509 (2001).
39. K. Wolf, R. Muller, S. Borgmann, E. B. Brocker, P. Friedl, Amoeboid shape change and contact guidance: T-lymphocyte crawling through fibrillar collagen is independent of matrix remodeling by MMPs and other proteases. *Blood* **102**, 3262-3269 (2003).
40. J. Konen *et al.*, LKB1 kinase-dependent and -independent defects disrupt polarity and adhesion signaling to drive collagen remodeling during invasion. *Mol Biol Cell* **27**, 1069-1084 (2016).

41. M. Yilmaz, G. Christofori, Mechanisms of motility in metastasizing cells. *Mol Cancer Res* **8**, 629-642 (2010).
42. N. V. Krakhmal, M. V. Zavyalova, E. V. Denisov, S. V. Vtorushin, V. M. Perelmuter, Cancer Invasion: Patterns and Mechanisms. *Acta Naturae* **7**, 17-28 (2015).
43. A. G. Clark, D. M. Vignjevic, Modes of cancer cell invasion and the role of the microenvironment. *Curr Opin Cell Biol* **36**, 13-22 (2015).
44. P. Friedl, J. Locker, E. Sahai, J. E. Segall, Classifying collective cancer cell invasion. *Nat Cell Biol* **14**, 777-783 (2012).
45. P. Friedl *et al.*, Migration of coordinated cell clusters in mesenchymal and epithelial cancer explants in vitro. *Cancer Res* **55**, 4557-4560 (1995).
46. J. Leighton, R. L. Kalla, J. M. Turner, Jr., R. H. Fennell, Jr., Pathogenesis of tumor invasion. II. Aggregate replication. *Cancer Res* **20**, 575-586 (1960).
47. O. Ramos Gde *et al.*, Fibronectin Modulates Cell Adhesion and Signaling to Promote Single Cell Migration of Highly Invasive Oral Squamous Cell Carcinoma. *PLoS One* **11**, e0151338 (2016).
48. N. Aceto *et al.*, Circulating tumor cell clusters are oligoclonal precursors of breast cancer metastasis. *Cell* **158**, 1110-1122 (2014).
49. K. J. Cheung, A. J. Ewald, A collective route to metastasis: Seeding by tumor cell clusters. *Science* **352**, 167-169 (2016).
50. K. J. Cheung *et al.*, Polyclonal breast cancer metastases arise from collective dissemination of keratin 14-expressing tumor cell clusters. *Proc Natl Acad Sci U S A* **113**, E854-863 (2016).
51. R. Mayor, S. Etienne-Manneville, The front and rear of collective cell migration. *Nat Rev Mol Cell Biol* **17**, 97-109 (2016).
52. A. Patsialou *et al.*, Intravital multiphoton imaging reveals multicellular streaming as a crucial component of in vivo cell migration in human breast tumors. *Intravital* **2**, e25294 (2013).
53. E. Theveneau, R. Mayor, Cadherins in collective cell migration of mesenchymal cells. *Curr Opin Cell Biol* **24**, 677-684 (2012).
54. A. J. Ewald, A. Brenot, M. Duong, B. S. Chan, Z. Werb, Collective epithelial migration and cell rearrangements drive mammary branching morphogenesis. *Dev Cell* **14**, 570-581 (2008).
55. A. Haeger, M. Krause, K. Wolf, P. Friedl, Cell jamming: collective invasion of mesenchymal tumor cells imposed by tissue confinement. *Biochim Biophys Acta* **1840**, 2386-2395 (2014).
56. S. Lehmann *et al.*, Hypoxia Induces a HIF-1-Dependent Transition from Collective-to-Amoeboid Dissemination in Epithelial Cancer Cells. *Curr Biol* **27**, 392-400 (2017).
57. C. Revenu, D. Gilmour, EMT 2.0: shaping epithelia through collective migration. *Curr Opin Genet Dev* **19**, 338-342 (2009).
58. T. Tsuji, S. Ibaragi, G. F. Hu, Epithelial-mesenchymal transition and cell cooperativity in metastasis. *Cancer Res* **69**, 7135-7139 (2009).
59. J. P. Thiery, H. Acloque, R. Y. Huang, M. A. Nieto, Epithelial-mesenchymal transitions in development and disease. *Cell* **139**, 871-890 (2009).
60. X. Zheng *et al.*, Epithelial-to-mesenchymal transition is dispensable for metastasis but induces chemoresistance in pancreatic cancer. *Nature* **527**, 525-530 (2015).

61. K. R. Fischer *et al.*, Epithelial-to-mesenchymal transition is not required for lung metastasis but contributes to chemoresistance. *Nature* **527**, 472-476 (2015).
62. V. Padmanaban *et al.*, E-cadherin is required for metastasis in multiple models of breast cancer. *Nature* **573**, 439-444 (2019).
63. N. M. Aiello *et al.*, Metastatic progression is associated with dynamic changes in the local microenvironment. *Nat Commun* **7**, 12819 (2016).
64. J. J. Christiansen, A. K. Rajasekaran, Reassessing epithelial to mesenchymal transition as a prerequisite for carcinoma invasion and metastasis. *Cancer Res* **66**, 8319-8326 (2006).
65. N. M. Aiello *et al.*, EMT Subtype Influences Epithelial Plasticity and Mode of Cell Migration. *Dev Cell* **45**, 681-695 e684 (2018).
66. D. Neelakantan, D. J. Drasin, H. L. Ford, Intratumoral heterogeneity: Clonal cooperation in epithelial-to-mesenchymal transition and metastasis. *Cell Adh Migr* **9**, 265-276 (2015).
67. W. L. Tam, R. A. Weinberg, The epigenetics of epithelial-mesenchymal plasticity in cancer. *Nat Med* **19**, 1438-1449 (2013).
68. R. Holliday, Epigenetics: a historical overview. *Epigenetics* **1**, 76-80 (2006).
69. C. H. Waddington, The epigenotype. 1942. *Int J Epidemiol* **41**, 10-13 (2012).
70. P. A. Jones, Overview of cancer epigenetics. *Semin Hematol* **42**, S3-8 (2005).
71. P. A. Jones, S. B. Baylin, The fundamental role of epigenetic events in cancer. *Nat Rev Genet* **3**, 415-428 (2002).
72. H. Easwaran, H. C. Tsai, S. B. Baylin, Cancer epigenetics: tumor heterogeneity, plasticity of stem-like states, and drug resistance. *Mol Cell* **54**, 716-727 (2014).
73. K. Hinohara, K. Polyak, Intratumoral Heterogeneity: More Than Just Mutations. *Trends Cell Biol* **29**, 569-579 (2019).
74. O. G. McDonald *et al.*, Epigenomic reprogramming during pancreatic cancer progression links anabolic glucose metabolism to distant metastasis. *Nat Genet* **49**, 367-376 (2017).
75. A. Marusyk, M. Janiszewska, K. Polyak, Intratumor Heterogeneity: The Rosetta Stone of Therapy Resistance. *Cancer Cell* **37**, 471-484 (2020).
76. S. A. Patel, S. Vanharanta, Epigenetic determinants of metastasis. *Mol Oncol* **11**, 79-96 (2017).
77. J. K. Christman, 5-Azacytidine and 5-aza-2'-deoxycytidine as inhibitors of DNA methylation: mechanistic studies and their implications for cancer therapy. *Oncogene* **21**, 5483-5495 (2002).
78. S. A. Belinsky *et al.*, Inhibition of DNA methylation and histone deacetylation prevents murine lung cancer. *Cancer Res* **63**, 7089-7093 (2003).
79. J. P. Issa *et al.*, Phase 1 study of low-dose prolonged exposure schedules of the hypomethylating agent 5-aza-2'-deoxycytidine (decitabine) in hematopoietic malignancies. *Blood* **103**, 1635-1640 (2004).
80. B. Brueckner *et al.*, Epigenetic reactivation of tumor suppressor genes by a novel small-molecule inhibitor of human DNA methyltransferases. *Cancer Res* **65**, 6305-6311 (2005).
81. J. P. Issa, DNA methylation as a therapeutic target in cancer. *Clin Cancer Res* **13**, 1634-1637 (2007).
82. P. A. Jones, J. P. Issa, S. Baylin, Targeting the cancer epigenome for therapy. *Nat Rev Genet* **17**, 630-641 (2016).
83. S. B. Baylin, P. A. Jones, A decade of exploring the cancer epigenome - biological and translational implications. *Nat Rev Cancer* **11**, 726-734 (2011).

84. E. Vidal *et al.*, A DNA methylation map of human cancer at single base-pair resolution. *Oncogene* **36**, 5648-5657 (2017).
85. J. R. Edwards, O. Yarychkivska, M. Boulard, T. H. Bestor, DNA methylation and DNA methyltransferases. *Epigenetics Chromatin* **10**, 23 (2017).
86. M. Klutstein, D. Nejman, R. Greenfield, H. Cedar, DNA Methylation in Cancer and Aging. *Cancer Res* **76**, 3446-3450 (2016).
87. T. H. Bestor, The DNA methyltransferases of mammals. *Hum Mol Genet* **9**, 2395-2402 (2000).
88. A. Merlo *et al.*, 5' CpG island methylation is associated with transcriptional silencing of the tumour suppressor p16/CDKN2/MTS1 in human cancers. *Nat Med* **1**, 686-692 (1995).
89. S. B. Baylin, DNA methylation and gene silencing in cancer. *Nat Clin Pract Oncol* **2 Suppl 1**, S4-11 (2005).
90. A. Bird, M. Taggart, M. Frommer, O. J. Miller, D. Macleod, A fraction of the mouse genome that is derived from islands of nonmethylated, CpG-rich DNA. *Cell* **40**, 91-99 (1985).
91. D. Brocks *et al.*, Intratumor DNA methylation heterogeneity reflects clonal evolution in aggressive prostate cancer. *Cell Rep* **8**, 798-806 (2014).
92. C. C. Oakes *et al.*, Evolution of DNA methylation is linked to genetic aberrations in chronic lymphocytic leukemia. *Cancer Discov* **4**, 348-361 (2014).
93. R. G. Gupta, R. A. Somer, Intratumor Heterogeneity: Novel Approaches for Resolving Genomic Architecture and Clonal Evolution. *Mol Cancer Res* **15**, 1127-1137 (2017).
94. R. A. Hlady *et al.*, Initiation of aberrant DNA methylation patterns and heterogeneity in precancerous lesions of human hepatocellular cancer. *Epigenetics* **12**, 215-225 (2017).
95. S. Liu *et al.*, Multi-omics Analysis of Primary Cell Culture Models Reveals Genetic and Epigenetic Basis of Intratumoral Phenotypic Diversity. *Genomics Proteomics Bioinformatics* **17**, 576-589 (2019).
96. D. R. Caswell, C. Swanton, The role of tumour heterogeneity and clonal cooperativity in metastasis, immune evasion and clinical outcome. *BMC Med* **15**, 133 (2017).
97. N. McGranahan, C. Swanton, Biological and therapeutic impact of intratumor heterogeneity in cancer evolution. *Cancer Cell* **27**, 15-26 (2015).
98. R. Rosenthal, N. McGranahan, J. Herrero, C. Swanton, Deciphering Genetic Intratumor Heterogeneity and Its Impact on Cancer Evolution. *Annual Review of Cancer Biology* **1**, 223-240 (2017).
99. S. Yachida *et al.*, Distant metastasis occurs late during the genetic evolution of pancreatic cancer. *Nature* **467**, 1114-1117 (2010).
100. A. P. Makohon-Moore *et al.*, Limited heterogeneity of known driver gene mutations among the metastases of individual patients with pancreatic cancer. *Nat Genet* **49**, 358-366 (2017).
101. J. G. Reiter *et al.*, Minimal functional driver gene heterogeneity among untreated metastases. *Science* **361**, 1033-1037 (2018).
102. D. C. Wang, W. Wang, B. Zhu, X. Wang, Lung Cancer Heterogeneity and New Strategies for Drug Therapy. *Annu Rev Pharmacol Toxicol* **58**, 531-546 (2018).
103. R. T. Davis *et al.*, Transcriptional diversity and bioenergetic shift in human breast cancer metastasis revealed by single-cell RNA sequencing. *Nat Cell Biol* **22**, 310-320 (2020).
104. W. C. Lee *et al.*, Multiregion gene expression profiling reveals heterogeneity in molecular subtypes and immunotherapy response signatures in lung cancer. *Mod Pathol* **31**, 947-955 (2018).

105. K. J. Cheung, E. Gabrielson, Z. Werb, A. J. Ewald, Collective invasion in breast cancer requires a conserved basal epithelial program. *Cell* **155**, 1639-1651 (2013).
106. K. J. Cheung, A. J. Ewald, Invasive leader cells: metastatic oncotarget. *Oncotarget* **5**, 1390-1391 (2014).
107. J. M. Westcott *et al.*, An epigenetically distinct breast cancer cell subpopulation promotes collective invasion. *J Clin Invest* **125**, 1927-1943 (2015).
108. S. P. Carey, A. Starchenko, A. L. McGregor, C. A. Reinhart-King, Leading malignant cells initiate collective epithelial cell invasion in a three-dimensional heterotypic tumor spheroid model. *Clin Exp Metastasis* **30**, 615-630 (2013).
109. P. B. Gupta *et al.*, Stochastic state transitions give rise to phenotypic equilibrium in populations of cancer cells. *Cell* **146**, 633-644 (2011).
110. J. Sangodkar, S. Katz, H. Melville, G. Narla, Lung adenocarcinoma: lessons in translation from bench to bedside. *Mt Sinai J Med* **77**, 597-605 (2010).
111. T. Goto, Y. Hirotsu, K. Amemiya, H. Mochizuki, M. Omata, Understanding Intratumor Heterogeneity and Evolution in NSCLC and Potential New Therapeutic Approach. *Cancers (Basel)* **10**, (2018).
112. J. Konen *et al.*, Image-guided genomics of phenotypically heterogeneous populations reveals vascular signalling during symbiotic collective cancer invasion. *Nat Commun* **8**, 15078 (2017).
113. D. M. Chudakov, S. Lukyanov, K. A. Lukyanov, Tracking intracellular protein movements using photoswitchable fluorescent proteins PS-CFP2 and Dendra2. *Nat Protoc* **2**, 2024-2032 (2007).
114. E. L. Zoeller *et al.*, Genetic heterogeneity within collective invasion packs drives leader and follower cell phenotypes. *J Cell Sci*, (2019).
115. R. Commander *et al.*, Subpopulation targeting of pyruvate dehydrogenase and GLUT1 decouples metabolic heterogeneity during collective cancer cell invasion. *Nat Commun* **11**, 1533 (2020).
116. B. Pedro *et al.*, Prognostic significance of an invasive leader cell-derived mutation cluster on chromosome 16q. *Cancer*, (2020).
117. J. Zhang *et al.*, Energetic regulation of coordinated leader-follower dynamics during collective invasion of breast cancer cells. *Proc Natl Acad Sci U S A* **116**, 7867-7872 (2019).
118. A. J. Ewald *et al.*, Mammary collective cell migration involves transient loss of epithelial features and individual cell migration within the epithelium. *J Cell Sci* **125**, 2638-2654 (2012).
119. K. J. Cheung, A. J. Ewald, Illuminating breast cancer invasion: diverse roles for cell-cell interactions. *Curr Opin Cell Biol* **30**, 99-111 (2014).
120. E. R. Shamir, K. Coutinho, D. Georgess, M. Auer, A. J. Ewald, Twist1-positive epithelial cells retain adhesive and proliferative capacity throughout dissemination. *Biol Open* **5**, 1216-1228 (2016).
121. V. Padmanaban, Y. Tsehay, K. J. Cheung, A. J. Ewald, J. S. Bader, Between-tumor and within-tumor heterogeneity in invasive potential. *PLoS Comput Biol* **16**, e1007464 (2020).
122. S. P. Carey, T. M. D'Alfonso, S. J. Shin, C. A. Reinhart-King, Mechanobiology of tumor invasion: engineering meets oncology. *Crit Rev Oncol Hematol* **83**, 170-183 (2012).
123. D. D. Tang, B. D. Gerlach, The roles and regulation of the actin cytoskeleton, intermediate filaments and microtubules in smooth muscle cell migration. *Respir Res* **18**, 54 (2017).

124. T. D. Pollard, J. A. Cooper, Actin, a central player in cell shape and movement. *Science* **326**, 1208-1212 (2009).
125. S. Tojkander, G. Gateva, P. Lappalainen, Actin stress fibers--assembly, dynamics and biological roles. *J Cell Sci* **125**, 1855-1864 (2012).
126. S. Pellegrin, H. Mellor, Actin stress fibres. *J Cell Sci* **120**, 3491-3499 (2007).
127. M. Krause, A. Gautreau, Steering cell migration: lamellipodium dynamics and the regulation of directional persistence. *Nat Rev Mol Cell Biol* **15**, 577-590 (2014).
128. P. K. Mattila, P. Lappalainen, Filopodia: molecular architecture and cellular functions. *Nat Rev Mol Cell Biol* **9**, 446-454 (2008).
129. J. Albuschies, V. Vogel, The role of filopodia in the recognition of nanotopographies. *Sci Rep* **3**, 1658 (2013).
130. M. Thery *et al.*, The extracellular matrix guides the orientation of the cell division axis. *Nat Cell Biol* **7**, 947-953 (2005).
131. N. O. Alieva *et al.*, Myosin IIA and formin dependent mechanosensitivity of filopodia adhesion. *Nat Commun* **10**, 3593 (2019).
132. G. Jacquemet, H. Hamidi, J. Ivaska, Filopodia in cell adhesion, 3D migration and cancer cell invasion. *Curr Opin Cell Biol* **36**, 23-31 (2015).
133. G. Jacquemet *et al.*, Filopodome Mapping Identifies p130Cas as a Mechanosensitive Regulator of Filopodia Stability. *Curr Biol* **29**, 202-216 e207 (2019).
134. M. B. Steketee, K. W. Tosney, Three functionally distinct adhesions in filopodia: shaft adhesions control lamellar extension. *J Neurosci* **22**, 8071-8083 (2002).
135. G. Jacquemet *et al.*, L-type calcium channels regulate filopodia stability and cancer cell invasion downstream of integrin signalling. *Nat Commun* **7**, 13297 (2016).
136. W. Hu, B. Wehrle-Haller, V. Vogel, Maturation of filopodia shaft adhesions is upregulated by local cycles of lamellipodia advancements and retractions. *PLoS One* **9**, e107097 (2014).
137. P. G. Gillespie *et al.*, Myosin-I nomenclature. *J Cell Biol* **155**, 703-704 (2001).
138. J. S. Berg, B. C. Powell, R. E. Cheney, A millennial myosin census. *Mol Biol Cell* **12**, 780-794 (2001).
139. R. E. Cheney, M. S. Mooseker, Unconventional myosins. *Curr Opin Cell Biol* **4**, 27-35 (1992).
140. T. N. Oliver, J. S. Berg, R. E. Cheney, Tails of unconventional myosins. *Cell Mol Life Sci* **56**, 243-257 (1999).
141. J. S. Berg, B. H. Derfler, C. M. Pennisi, D. P. Corey, R. E. Cheney, Myosin-X, a novel myosin with pleckstrin homology domains, associates with regions of dynamic actin. *J Cell Sci* **113 Pt 19**, 3439-3451 (2000).
142. J. S. Berg, R. E. Cheney, Myosin-X is an unconventional myosin that undergoes intrafilopodial motility. *Nat Cell Biol* **4**, 246-250 (2002).
143. M. L. Kerber, R. E. Cheney, Myosin-X: a MyTH-FERM myosin at the tips of filopodia. *J Cell Sci* **124**, 3733-3741 (2011).
144. A. B. Bohil, B. W. Robertson, R. E. Cheney, Myosin-X is a molecular motor that functions in filopodia formation. *Proc Natl Acad Sci U S A* **103**, 12411-12416 (2006).
145. O. Sato *et al.*, Activated full-length myosin-X moves processively on filopodia with large steps toward diverse two-dimensional directions. *Sci Rep* **7**, 44237 (2017).
146. V. Ropars *et al.*, The myosin X motor is optimized for movement on actin bundles. *Nat Commun* **7**, 12456 (2016).

147. B. L. Ricca, R. S. Rock, The stepping pattern of myosin X is adapted for processive motility on bundled actin. *Biophys J* **99**, 1818-1826 (2010).
148. Y. Hirano *et al.*, Structural basis of cargo recognition by the myosin-X MyTH4-FERM domain. *EMBO J* **30**, 2734-2747 (2011).
149. A. Arjonen *et al.*, Mutant p53-associated myosin-X upregulation promotes breast cancer invasion and metastasis. *J Clin Invest* **124**, 1069-1082 (2014).
150. H. Zhang *et al.*, Myosin-X provides a motor-based link between integrins and the cytoskeleton. *Nat Cell Biol* **6**, 523-531 (2004).
151. H. Tokuo, M. Ikebe, Myosin X transports Mena/VASP to the tip of filopodia. *Biochem Biophys Res Commun* **319**, 214-220 (2004).
152. X. D. Ju *et al.*, Both Myosin-10 isoforms are required for radial neuronal migration in the developing cerebral cortex. *Cereb Cortex* **24**, 1259-1268 (2014).
153. A. D. Sousa, J. S. Berg, B. W. Robertson, R. B. Meeker, R. E. Cheney, Myo10 in brain: developmental regulation, identification of a headless isoform and dynamics in neurons. *J Cell Sci* **119**, 184-194 (2006).
154. A. N. Raines, S. Nagdas, M. L. Kerber, R. E. Cheney, Headless Myo10 is a negative regulator of full-length Myo10 and inhibits axon outgrowth in cortical neurons. *J Biol Chem* **287**, 24873-24883 (2012).
155. W. H. Lin, J. T. Hurley, A. N. Raines, R. E. Cheney, D. J. Webb, Myosin X and its motorless isoform differentially modulate dendritic spine development by regulating trafficking and retention of vasodilator-stimulated phosphoprotein. *J Cell Sci* **126**, 4756-4768 (2013).
156. N. Umeki *et al.*, Phospholipid-dependent regulation of the motor activity of myosin X. *Nat Struct Mol Biol* **18**, 783-788 (2011).
157. Q. Lu, J. Yu, J. Yan, Z. Wei, M. Zhang, Structural basis of the myosin X PH1(N)-PH2-PH1(C) tandem as a specific and acute cellular PI(3,4,5)P(3) sensor. *Mol Biol Cell* **22**, 4268-4278 (2011).
158. A. Naguib, Following the trail of lipids: Signals initiated by PI3K function at multiple cellular membranes. *Sci Signal* **9**, re4 (2016).
159. L. Plantard *et al.*, PtdIns(3,4,5)P(3) is a regulator of myosin-X localization and filopodia formation. *J Cell Sci* **123**, 3525-3534 (2010).
160. K. He, T. Sakai, Y. Tsukasaki, T. M. Watanabe, M. Ikebe, Myosin X is recruited to nascent focal adhesions at the leading edge and induces multi-cycle filopodial elongation. *Sci Rep* **7**, 13685 (2017).
161. D. S. Courson, R. E. Cheney, Myosin-X and disease. *Exp Cell Res* **334**, 10-15 (2015).
162. A. C. Bachg *et al.*, Phenotypic analysis of Myo10 knockout (Myo10(tm2/tm2)) mice lacking full-length (motorized) but not brain-specific headless myosin X. *Sci Rep* **9**, 597 (2019).
163. H. Tokuo, J. Bhawan, L. M. Coluccio, Myosin X is required for efficient melanoblast migration and melanoma initiation and metastasis. *Sci Rep* **8**, 10449 (2018).
164. E. G. Heimsath, Jr., Y. I. Yim, M. Mustapha, J. A. Hammer, R. E. Cheney, Myosin-X knockout is semi-lethal and demonstrates that myosin-X functions in neural tube closure,

pigmentation, hyaloid vasculature regression, and filopodia formation. *Sci Rep* **7**, 17354 (2017).
165. R. Cao *et al.*, Elevated expression of myosin X in tumours contributes to breast cancer aggressiveness and metastasis. *Br J Cancer* **111**, 539-550 (2014).
166. G. Bidkhori *et al.*, Reconstruction of an integrated genome-scale co-expression network reveals key modules involved in lung adenocarcinoma. *PLoS One* **8**, e67552 (2013).
167. Y. Sun, X. Ai, S. Shen, S. Lu, NF-kappaB-mediated miR-124 suppresses metastasis of non-small-cell lung cancer by targeting MYO10. *Oncotarget* **6**, 8244-8254 (2015).
168. K. A. Makowska, R. E. Hughes, K. J. White, C. M. Wells, M. Peckham, Specific Myosins Control Actin Organization, Cell Morphology, and Migration in Prostate Cancer Cells. *Cell Rep* **13**, 2118-2125 (2015).
169. M. Schoumacher, R. D. Goldman, D. Louvard, D. M. Vignjevic, Actin, microtubules, and vimentin intermediate filaments cooperate for elongation of invadopodia. *J Cell Biol* **189**, 541-556 (2010).
170. L. G. Morris *et al.*, Pan-cancer analysis of intratumor heterogeneity as a prognostic determinant of survival. *Oncotarget* **7**, 10051-10063 (2016).
171. Q. Wei *et al.*, Multiregion whole-exome sequencing of matched primary and metastatic tumors revealed genomic heterogeneity and suggested polyclonal seeding in colorectal cancer metastasis. *Ann Oncol* **28**, 2135-2141 (2017).
172. M. Janiszewska *et al.*, Subclonal cooperation drives metastasis by modulating local and systemic immune microenvironments. *Nat Cell Biol* **21**, 879-888 (2019).
173. M. Gilbert-Ross *et al.*, Targeting adhesion signaling in KRAS, LKB1 mutant lung adenocarcinoma. *JCI Insight* **2**, e90487 (2017).
174. E. Wagenblast *et al.*, A model of breast cancer heterogeneity reveals vascular mimicry as a driver of metastasis. *Nature* **520**, 358-362 (2015).
175. C. I. Schnegg, M. H. Yang, S. K. Ghosh, M. Y. Hsu, Induction of Vasculogenic Mimicry Overrides VEGF-A Silencing and Enriches Stem-like Cancer Cells in Melanoma. *Cancer Res* **75**, 1682-1690 (2015).
176. Y. Tian *et al.*, ChAMP: updated methylation analysis pipeline for Illumina BeadChips. *Bioinformatics* **33**, 3982-3984 (2017).
177. X. Ren, P. F. Kuan, methylGSA: a Bioconductor package and Shiny app for DNA methylation data length bias adjustment in gene set testing. *Bioinformatics* **35**, 1958-1959 (2019).
178. S. Anders, P. T. Pyl, W. Huber, HTSeq--a Python framework to work with high-throughput sequencing data. *Bioinformatics* **31**, 166-169 (2015).
179. S. Anders, W. Huber, Differential expression analysis for sequence count data. *Genome Biol* **11**, R106 (2010).
180. M. Rupji, B. Dwivedi, J. Kowalski, NOJAH: NOt Just Another Heatmap for genome-wide cluster analysis. *PLoS One* **14**, e0204542 (2019).
181. A. Subramanian *et al.*, Gene set enrichment analysis: a knowledge-based approach for interpreting genome-wide expression profiles. *Proc Natl Acad Sci U S A* **102**, 15545-15550 (2005).
182. E. P. Consortium, An integrated encyclopedia of DNA elements in the human genome. *Nature* **489**, 57-74 (2012).
183. J. B. Long, S. M. Jay, S. S. Segal, J. A. Madri, VEGF-A and Semaphorin3A: modulators of vascular sympathetic innervation. *Dev Biol* **334**, 119-132 (2009).

184. Q. Raza, J. R. Jacobs, Guidance signalling regulates leading edge behaviour during collective cell migration of cardiac cells in Drosophila. *Dev Biol* **419**, 285-297 (2016).
185. N. Shenker, J. M. Flanagan, Intragenic DNA methylation: implications of this epigenetic mechanism for cancer research. *Br J Cancer* **106**, 248-253 (2012).
186. M. P. Ball *et al.*, Targeted and genome-scale strategies reveal gene-body methylation signatures in human cells. *Nat Biotechnol* **27**, 361-368 (2009).
187. X. Yu, Z. Li, W. K. Wu, TIP30: A Novel Tumor-Suppressor Gene. *Oncol Res* **22**, 339-348 (2014).
188. F. W. King, E. Shtivelman, Inhibition of nuclear import by the proapoptotic protein CC3. *Mol Cell Biol* **24**, 7091-7101 (2004).
189. M. Ito *et al.*, TIP30 deficiency increases susceptibility to tumorigenesis. *Cancer Res* **63**, 8763-8767 (2003).
190. Y. Hu *et al.*, Overexpression of TIP30 inhibits the growth and invasion of glioma cells. *Mol Med Rep* **13**, 605-612 (2016).
191. T. Xu *et al.*, Tat-Interacting Protein 30 (TIP30) Expression Serves as a New Biomarker for Tumor Prognosis: A Systematic Review and Meta-Analysis. *PLoS One* **11**, e0168408 (2016).
192. E. Shtivelman, A link between metastasis and resistance to apoptosis of variant small cell lung carcinoma. *Oncogene* **14**, 2167-2173 (1997).
193. X. Dong *et al.*, Downregulation of HTATIP2 expression is associated with promoter methylation and poor prognosis in glioma. *Exp Mol Pathol* **98**, 192-199 (2015).
194. Y. Kumtepe *et al.*, High serum HTATIP2/TIP30 level in serous ovarian cancer as prognostic or diagnostic marker. *Eur J Med Res* **18**, 18 (2013).
195. F. Bu *et al.*, TGF-beta1 induces epigenetic silence of TIP30 to promote tumor metastasis in esophageal carcinoma. *Oncotarget* **6**, 2120-2133 (2015).
196. B. Lu *et al.*, Methylation of Tip30 promoter is associated with poor prognosis in human hepatocellular carcinoma. *Clin Cancer Res* **14**, 7405-7412 (2008).
197. J. T. Robinson *et al.*, Integrative genomics viewer. *Nat Biotechnol* **29**, 24-26 (2011).
198. W. Dong, R. Shen, S. Cheng, Reduction of TIP30 in esophageal squamous cell carcinoma cells involves promoter methylation and microRNA-10b. *Biochem Biophys Res Commun* **453**, 772-777 (2014).
199. S. Shuai *et al.*, TIP30 nuclear translocation negatively regulates EGF-dependent cyclin D1 transcription in human lung adenocarcinoma. *Cancer Lett* **354**, 200-209 (2014).
200. Y. S. DeRose *et al.*, Patient-derived models of human breast cancer: protocols for in vitro and in vivo applications in tumor biology and translational medicine. *Curr Protoc Pharmacol* **Chapter 14**, Unit14 23 (2013).
201. D. Montezuma *et al.*, A panel of four immunohistochemical markers (CK7, CK20, TTF-1, and p63) allows accurate diagnosis of primary and metastatic lung carcinoma on biopsy specimens. *Virchows Arch* **463**, 749-754 (2013).
202. B. G. Barwick, C. D. Scharer, A. P. R. Bally, J. M. Boss, Plasma cell differentiation is coupled to division-dependent DNA hypomethylation and gene regulation. *Nat Immunol* **17**, 1216-1225 (2016).
203. J. Debnath, S. K. Muthuswamy, J. S. Brugge, Morphogenesis and oncogenesis of MCF-10A mammary epithelial acini grown in three-dimensional basement membrane cultures. *Methods* **30**, 256-268 (2003).

204. N. T. Seyfried *et al.*, A Multi-network Approach Identifies Protein-Specific Co-expression in Asymptomatic and Symptomatic Alzheimer's Disease. *Cell Syst* **4**, 60-72 e64 (2017).
205. R. Kopan, M. X. Ilagan, The canonical Notch signaling pathway: unfolding the activation mechanism. *Cell* **137**, 216-233 (2009).
206. C. M. Grochowski, K. M. Loomes, N. B. Spinner, Jagged1 (JAG1): Structure, expression, and disease associations. *Gene* **576**, 381-384 (2016).
207. T. Donnem *et al.*, Prognostic impact of Notch ligands and receptors in nonsmall cell lung cancer: coexpression of Notch-1 and vascular endothelial growth factor-A predicts poor survival. *Cancer* **116**, 5676-5685 (2010).
208. Y. Li, M. A. Hibbs, A. L. Gard, N. A. Shylo, K. Yun, Genome-wide analysis of N1ICD/RBPJ targets in vivo reveals direct transcriptional regulation of Wnt, SHH, and hippo pathway effectors by Notch1. *Stem Cells* **30**, 741-752 (2012).
209. M. J. Oudin *et al.*, Tumor Cell-Driven Extracellular Matrix Remodeling Drives Haptotaxis during Metastatic Progression. *Cancer Discov* **6**, 516-531 (2016).
210. J. E. Schwarzbauer, D. W. DeSimone, Fibronectins, their fibrillogenesis, and in vivo functions. *Cold Spring Harb Perspect Biol* **3**, (2011).
211. B. Erdogan *et al.*, Cancer-associated fibroblasts promote directional cancer cell migration by aligning fibronectin. *J Cell Biol* **216**, 3799-3816 (2017).
212. M. W. Conklin *et al.*, Aligned collagen is a prognostic signature for survival in human breast carcinoma. *Am J Pathol* **178**, 1221-1232 (2011).
213. A. van der Flier, A. Sonnenberg, Function and interactions of integrins. *Cell Tissue Res* **305**, 285-298 (2001).
214. R. O. Hynes, Integrins: bidirectional, allosteric signaling machines. *Cell* **110**, 673-687 (2002).
215. E. H. Danen, P. Sonneveld, C. Brakebusch, R. Fassler, A. Sonnenberg, The fibronectin-binding integrins alpha5beta1 and alphavbeta3 differentially modulate RhoA-GTP loading,

organization of cell matrix adhesions, and fibronectin fibrillogenesis. *J Cell Biol* **159**, 1071-1086 (2002).
216. C. Wu, P. E. Hughes, M. H. Ginsberg, J. A. McDonald, Identification of a new biological function for the integrin alpha v beta 3: initiation of fibronectin matrix assembly. *Cell Adhes Commun* **4**, 149-158 (1996).
217. M. R. Morgan, A. Byron, M. J. Humphries, M. D. Bass, Giving off mixed signals--distinct functions of alpha5beta1 and alphavbeta3 integrins in regulating cell behaviour. *IUBMB Life* **61**, 731-738 (2009).
218. C. A. Lowell, T. N. Mayadas, Overview: studying integrins in vivo. *Methods Mol Biol* **757**, 369-397 (2012).
219. D. Li, M. Masiero, A. H. Banham, A. L. Harris, The Notch ligand Jagged1 as a target for anti-tumor therapy. *Frontiers in Oncology* **4**, 254 (2014).
220. S. J. Bray, Notch signalling in context. *Nat Rev Mol Cell Biol* **17**, 722-735 (2016).
221. C. H. Stuelten, C. A. Parent, D. J. Montell, Cell motility in cancer invasion and metastasis: insights from simple model organisms. *Nat Rev Cancer* **18**, 296-312 (2018).
222. R. Pankov *et al.*, Integrin dynamics and matrix assembly: tensin-dependent translocation of alpha(5)beta(1) integrins promotes early fibronectin fibrillogenesis. *J Cell Biol* **148**, 1075-1090 (2000).
223. A. F. Blandin *et al.*, beta1 Integrins as Therapeutic Targets to Disrupt Hallmarks of Cancer. *Front Pharmacol* **6**, 279 (2015).
224. B. K. McMichael, R. E. Cheney, B. S. Lee, Myosin X regulates sealing zone patterning in osteoclasts through linkage of podosomes and microtubules. *J Biol Chem* **285**, 9506-9515 (2010).
225. D. A. Murphy, S. A. Courtneidge, The 'ins' and 'outs' of podosomes and invadopodia: characteristics, formation and function. *Nat Rev Mol Cell Biol* **12**, 413-426 (2011).
226. J. C. Fierro-Gonzalez, M. D. White, J. C. Silva, N. Plachta, Cadherin-dependent filopodia control preimplantation embryo compaction. *Nat Cell Biol* **15**, 1424-1433 (2013).
227. V. Vasioukhin, C. Bauer, M. Yin, E. Fuchs, Directed actin polymerization is the driving force for epithelial cell-cell adhesion. *Cell* **100**, 209-219 (2000).
228. K. C. Liu, D. T. Jacobs, B. D. Dunn, A. S. Fanning, R. E. Cheney, Myosin-X functions in polarized epithelial cells. *Mol Biol Cell* **23**, 1675-1687 (2012).
229. S. Yonezawa *et al.*, Possible involvement of myosin-X in intercellular adhesion: importance of serial pleckstrin homology regions for intracellular localization. *Dev Growth Differ* **45**, 175-185 (2003).
230. S. Almagro *et al.*, The motor protein myosin-X transports VE-cadherin along filopodia to allow the formation of early endothelial cell-cell contacts. *Mol Cell Biol* **30**, 1703-1717 (2010).
231. M. Thery, M. Bornens, Get round and stiff for mitosis. *HFSP J* **2**, 65-71 (2008).
232. L. P. Cramer, T. J. Mitchison, Investigation of the mechanism of retraction of the cell margin and rearward flow of nodules during mitotic cell rounding. *Mol Biol Cell* **8**, 109-119 (1997).
233. M. Kwon, M. Bagonis, G. Danuser, D. Pellman, Direct Microtubule-Binding by Myosin-10 Orients Centrosomes toward Retraction Fibers and Subcortical Actin Clouds. *Dev Cell* **34**, 323-337 (2015).
234. W. T. Silkworth, D. Cimini, Transient defects of mitotic spindle geometry and chromosome segregation errors. *Cell Div* **7**, 19 (2012).

235. J. C. Pease, J. S. Tirnauer, Mitotic spindle misorientation in cancer--out of alignment and into the fire. *J Cell Sci* **124**, 1007-1016 (2011).
236. K. L. Weber, A. M. Sokac, J. S. Berg, R. E. Cheney, W. M. Bement, A microtubule-binding myosin required for nuclear anchoring and spindle assembly. *Nature* **431**, 325-329 (2004).
237. J. C. Sandquist, M. E. Larson, K. J. Hine, Myosin-10 independently influences mitotic spindle structure and mitotic progression. *Cytoskeleton (Hoboken)* **73**, 351-364 (2016).
238. J. C. Sandquist, M. E. Larson, S. Woolner, Z. Ding, W. M. Bement, An interaction between myosin-10 and the cell cycle regulator Wee1 links spindle dynamics to mitotic progression in epithelia. *J Cell Biol* **217**, 849-859 (2018).
239. C. K. Hu, M. Coughlin, T. J. Mitchison, Midbody assembly and its regulation during cytokinesis. *Mol Biol Cell* **23**, 1024-1034 (2012).
240. K. Fukasawa, Centrosome amplification, chromosome instability and cancer development. *Cancer Lett* **230**, 6-19 (2005).
241. J. B. Manneville, S. Etienne-Manneville, Positioning centrosomes and spindle poles: looking at the periphery to find the centre. *Biol Cell* **98**, 557-565 (2006).
242. N. J. Quintyne, J. E. Reing, D. R. Hoffelder, S. M. Gollin, W. S. Saunders, Spindle multipolarity is prevented by centrosomal clustering. *Science* **307**, 127-129 (2005).
243. A. Ogden, P. C. Rida, R. Aneja, Let's huddle to prevent a muddle: centrosome declustering as an attractive anticancer strategy. *Cell Death Differ* **19**, 1255-1267 (2012).
244. A. Milunovic-Jevtic, P. Mooney, T. Sulerud, J. Bisht, J. C. Gatlin, Centrosomal clustering contributes to chromosomal instability and cancer. *Curr Opin Biotechnol* **40**, 113-118 (2016).
245. H. Yamamoto *et al.*, Integrin beta1 controls VE-cadherin localization and blood vessel stability. *Nat Commun* **6**, 6429 (2015).
246. J. M. Hou *et al.*, Circulating tumor cells as a window on metastasis biology in lung cancer. *Am J Pathol* **178**, 989-996 (2011).
247. R. Maddipati, B. Z. Stanger, Pancreatic Cancer Metastases Harbor Evidence of Polyclonality. *Cancer Discov* **5**, 1086-1097 (2015).
248. S. E. Alcala *et al.*, Mitotic asynchrony induces transforming growth factor-beta1 secretion from airway epithelium. *Am J Respir Cell Mol Biol* **51**, 363-369 (2014).
249. C. A. Duckworth *et al.*, Progastrin-induced secretion of insulin-like growth factor 2 from colonic myofibroblasts stimulates colonic epithelial proliferation in mice. *Gastroenterology* **145**, 197-208 e193 (2013).
250. J. Gregori *et al.*, Enhancing the Biological Relevance of Secretome-Based Proteomics by Linking Tumor Cell Proliferation and Protein Secretion. *J Proteome Res* **13**, 3706-3721 (2014).
251. K. Polyak, A. Marusyk, Cancer: Clonal cooperation. *Nature* **508**, 52-53 (2014).
252. A. S. Cleary, T. L. Leonard, S. A. Gestl, E. J. Gunther, Tumour cell heterogeneity maintained by cooperating subclones in Wnt-driven mammary cancers. *Nature* **508**, 113-117 (2014).
253. S. B. Baylin, W. Y. Chen, Aberrant gene silencing in tumor progression: implications for control of cancer. *Cold Spring Harb Symp Quant Biol* **70**, 427-433 (2005).
254. C. Gros *et al.*, DNA methylation inhibitors in cancer: recent and future approaches. *Biochimie* **94**, 2280-2296 (2012).
255. K. B. Chiappinelli *et al.*, Inhibiting DNA Methylation Causes an Interferon Response in Cancer via dsRNA Including Endogenous Retroviruses. *Cell* **162**, 974-986 (2015).

256. N. S. Azad *et al.*, Combination epigenetic therapy in metastatic colorectal cancer (mCRC) with subcutaneous 5-azacitidine and entinostat: a phase 2 consortium/stand up 2 cancer study. *Oncotarget* **8**, 35326-35338 (2017).
257. C. J. Coppola, C. R. R, E. M. Mendenhall, Identification and function of enhancers in the human genome. *Hum Mol Genet* **25**, R190-R197 (2016).
258. E. Calo, J. Wysocka, Modification of enhancer chromatin: what, how, and why? *Mol Cell* **49**, 825-837 (2013).
259. A. Angeloni, O. Bogdanovic, Enhancer DNA methylation: implications for gene regulation. *Essays Biochem* **63**, 707-715 (2019).
260. J. Charlet *et al.*, Bivalent Regions of Cytosine Methylation and H3K27 Acetylation Suggest an Active Role for DNA Methylation at Enhancers. *Mol Cell* **62**, 422-431 (2016).
261. R. Ordonez, N. Martinez-Calle, X. Agirre, F. Prosper, DNA Methylation of Enhancer Elements in Myeloid Neoplasms: Think Outside the Promoters? *Cancers (Basel)* **11**, (2019).
262. O. Galm, J. G. Herman, S. B. Baylin, The fundamental role of epigenetics in hematopoietic malignancies. *Blood Rev* **20**, 1-13 (2006).
263. K. P. Nightingale, L. P. O'Neill, B. M. Turner, Histone modifications: signalling receptors and potential elements of a heritable epigenetic code. *Curr Opin Genet Dev* **16**, 125-136 (2006).
264. S. B. Hake, A. Xiao, C. D. Allis, Linking the epigenetic 'language' of covalent histone modifications to cancer. *Br J Cancer* **90**, 761-769 (2004).
265. T. Vaissiere, C. Sawan, Z. Herceg, Epigenetic interplay between histone modifications and DNA methylation in gene silencing. *Mutat Res* **659**, 40-48 (2008).
266. B. Xhabija, B. L. Kidder, KDM5B is a master regulator of the H3K4-methylome in stem cells, development and cancer. *Semin Cancer Biol* **57**, 79-85 (2019).
267. A. Shilatifard, The COMPASS family of histone H3K4 methylases: mechanisms of regulation in development and disease pathogenesis. *Annu Rev Biochem* **81**, 65-95 (2012).
268. C. Y. Okitsu, C. L. Hsieh, DNA methylation dictates histone H3K4 methylation. *Mol Cell Biol* **27**, 2746-2757 (2007).
269. M. Weber *et al.*, Distribution, silencing potential and evolutionary impact of promoter DNA methylation in the human genome. *Nat Genet* **39**, 457-466 (2007).
270. F. Sleutels *et al.*, The male germ cell gene regulator CTCFL is functionally different from CTCF and binds CTCF-like consensus sites in a nucleosome composition-dependent manner. *Epigenetics Chromatin* **5**, 8 (2012).
271. E. M. Pugacheva *et al.*, The cancer-associated CTCFL/BORIS protein targets multiple classes of genomic repeats, with a distinct binding and functional preference for humanoid-specific SVA transposable elements. *Epigenetics Chromatin* **9**, 35 (2016).
272. P. Bergmaier *et al.*, Choice of binding sites for CTCFL compared to CTCF is driven by chromatin and by sequence preference. *Nucleic Acids Res* **46**, 7097-7107 (2018).
273. P. Nguyen *et al.*, CTCFL/BORIS is a methylation-independent DNA-binding protein that preferentially binds to the paternal H19 differentially methylated region. *Cancer Res* **68**, 5546-5551 (2008).
274. L. Alberti, L. Losi, S. Leyvraz, J. Benhattar, Different Effects of BORIS/CTCFL on Stemness Gene Expression, Sphere Formation and Cell Survival in Epithelial Cancer Stem Cells. *PLoS One* **10**, e0132977 (2015).

275. K. R. Garikapati *et al.*, Down-regulation of BORIS/CTCFL efficiently regulates cancer stemness and metastasis in MYCN amplified neuroblastoma cell line by modulating Wnt/beta-catenin signaling pathway. *Biochem Biophys Res Commun* **484**, 93-99 (2017).
276. K. Okabayashi *et al.*, Cancer-testis antigen BORIS is a novel prognostic marker for patients with esophageal cancer. *Cancer Sci* **103**, 1617-1624 (2012).
277. A. Woloszynska-Read *et al.*, DNA methylation-dependent regulation of BORIS/CTCFL expression in ovarian cancer. *Cancer Immun* **7**, 21 (2007).
278. M. J. Hoffmann, M. Muller, R. Engers, W. A. Schulz, Epigenetic control of CTCFL/BORIS and OCT4 expression in urogenital malignancies. *Biochem Pharmacol* **72**, 1577-1588 (2006).
279. M. X. Liu *et al.*, Epigenetic silencing of microRNA-199b-5p is associated with acquired chemoresistance via activation of JAG1-Notch1 signaling in ovarian cancer. *Oncotarget* **5**, 944-958 (2014).
280. M. Reedijk *et al.*, High-level coexpression of JAG1 and NOTCH1 is observed in human breast cancer and is associated with poor overall survival. *Cancer Res* **65**, 8530-8537 (2005).
281. B. C. Dickson *et al.*, High-level JAG1 mRNA and protein predict poor outcome in breast cancer. *Mod Pathol* **20**, 685-693 (2007).
282. W. H. Chang *et al.*, JAG1 Is Associated with Poor Survival through Inducing Metastasis in Lung Cancer. *PLoS One* **11**, e0150355 (2016).
283. G. Zhao *et al.*, MiR-153 reduces stem cell-like phenotype and tumor growth of lung adenocarcinoma by targeting Jagged1. *Stem Cell Res Ther* **11**, 170 (2020).
284. Z. Y. Liu *et al.*, Notch Signaling Components: Diverging Prognostic Indicators in Lung Adenocarcinoma. *Medicine (Baltimore)* **95**, e3715 (2016).
285. N. G. Yousif *et al.*, Notch1 ligand signaling pathway activated in cervical cancer: poor prognosis with high-level JAG1/Notch1. *Arch Gynecol Obstet* **292**, 899-904 (2015).
286. N. Nandagopal, L. A. Santat, M. B. Elowitz, Cis-activation in the Notch signaling pathway. *Elife* **8**, (2019).
287. O. C. Rodriguez *et al.*, Conserved microtubule-actin interactions in cell movement and morphogenesis. *Nat Cell Biol* **5**, 599-609 (2003).
288. L. M. Griffith, T. D. Pollard, Evidence for actin filament-microtubule interaction mediated by microtubule-associated proteins. *J Cell Biol* **78**, 958-965 (1978).
289. T. D. Pollard, S. C. Selden, P. Maupin, Interaction of actin filaments with microtubules. *J Cell Biol* **99**, 33s-37s (1984).